Developing and Implementing Advanced Optical Diagnostics for the Investigation of Fuel and Flow Effects on Impinging Jet Flames

Miss Chloe Jo McDaid

Combustion and Flow Diagnostics Research Group

Department of Mechanical Engineering

This thesis is submitted to the University of Sheffield for the degree of Doctor of Philosophy, September 2013.

Declaration

The work presented in this thesis is that of the Author and has not been submitted for any other award or degree at the University of Sheffield or any other university or institution. Where other sources of information or help from other parties has been used this has been acknowledged.

Dedication

For my late great nephew: Giovanni, **my great niece:** Isabella, **and my nieces and nephews:** Adam, Somma, Mason, Aidan, Elise, Sophia, Sonny and Tommy and those yet to come.

Acknowledgements

I would first of all like to thank my supervisor, Prof. Yang Zhang, for his continued support and expertise throughout my PhD studies with regards to experimentation, writing and organisation. Without his assistance this would not have been possible. In addition, I would like to thank my second supervisor, Dr Robert Woolley for his additional support and for his computational expertise. I would also like to thank my colleagues in the Combustion and Flow Diagnostics research group; Hua Wei Kevin Huang, Hussain Saeed, Qian Wang, Li-Wei Chen, Jason Yang, Paco Carranza Ch and Zhen Ma for their support and cooperation in laboratory work and for making my time during my PhD very enjoyable. I would like to thank the University technicians for helping me with the design and building of laboratory equipment and safety aspects of the laboratory, and the University staff for their help with placing orders and general difficulties encountered. In addition, I would like to thank the undergraduate and MSc students, Jie Zhao, Xuan Jiang and Yiran Wang who assisted me with some experiments.

I would like to thank my parents Annette and Julian Dunn, who have given me constant love, support and encouragement throughout my PhD studies and before, and without whom this thesis could not have been written. I would also like to thank my partner Aidan for always believing in me, and my siblings, step-siblings and siblings-in-law; Ella, Alex, Rowena, Layla, Melissa, Sammie, Verena, Jimmy, Joe, Benjamin, Katie, Mark, Steve, Laura, Chloe and Emily, for always supporting and encouraging me and giving me advice and care when I needed it. I would also like to thank all of my family and friends for their encouragement.

I would like to thank the project's collaborative partners at the University of Lancaster (Prof. Xi Jiang, Ranga Dinesh and Daniel Mira Martinez), Xi'an Jiaotong University (Prof. Zuohua Huang and Jin Fu), Tsinghua University (Prof. Min Zhu) and Eindhoven University of Technology (Prof. Jeroen van Oijen), and industrial partners Siemens, Eon and BP. Finally I would like to thank EPSRC for funding through the grant No. EP/G063044/1 and for the loaning of equipment. It is part of the Energy Programme which is an RCUK cross-council initiative led by EPSRC and contributed to by ESRC, NERC, BBSRC and STFC.

Publications

C. McDaid, and Y. Zhang, "Wall temperature measurements using a thermal imaging camera with temperature dependent emissivity corrections," *Meas. Sci. Technol.* Vol. 22**,** 125503 (8pp), 2011.

C. McDaid, J. Zhou, and Y. Zhang, "Experimental observations of the complex flame propagations initiated at different locations of an impingement configuration," *Fuel*, Vol. 103**,** pp. 783-791, 2013.

Abstract

Experimental diagnostic techniques have been utilised and developed to investigate the flame wall interaction for impinging flames of propane, methane, hydrogen and syngas. Thermal imaging has been used to evaluate the plate temperatures and radiation losses at steady state. A methodology has been developed for temperature dependent emissivity materials. Schlieren and direct imaging have been used to visualise flame shapes and flow structure. A methodology has been developed to quantify the relative effects of visual turbulent structures on the flame wall interaction. High speed schlieren has been used to assess the time dependent flame front propagation following ignition at various ignition locations.

The combination of these techniques has allowed the flame wall interaction to be analysed for fuel composition, thermal loading, equivalence ratio, nozzle-to-plate distance, Reynolds number, geometry and fuel exit velocity. It has been found that fuel composition significantly affects the wall temperature profiles even at similar nozzle conditions. Mixing in different regions of the impingement configuration caused significant differences in the wall temperature profiles for the different fuels due to differences in diffusivity and laminar flame speed. Syngas premixed flames produce similar wall temperature profiles near the lift-off limit but at different equivalence ratios and Reynolds numbers, due to the similar turbulence shown in the schlieren images. Plate material and nozzle-to-plate distance significantly affected the wall temperature profiles. Radiation losses from the plate helped to explain the differences in heat transfer for the different conditions.

Delays in the initial downwards propagation were observed for the hydrogen flames. The competing factors of the upstream propagation and heat production, causing decelerations and accelerations of the flame front respectively, differed significantly for different fuels and conditions. The propagation of the flame front immediately after ignition was observed to be very complex, changing significantly for relatively small changes in nozzle conditions.

Table of Contents

Nomenclature

Uppercase Roman Letters

A	Position A
A_c	Cross sectional area
A_D	Reference Area
A_f	Flame surface area
B	Position B
C_D	Drag coefficient
D	Mass diffusivity
E	Energy
ΔE	Threshold energy
E_s	Seebeck voltage
F	Flow rate
F_D	Drag force
K	Gladstone-Dale coefficient
Ka	Karlovitz number
L	Characteristic length scale
Le	Lewis number
L_M	Markstein length
M	Molecular weight
Ma	Markstein Number
N	Total number of species
Nu	Nusselt Number
Pr	Prandtl number
$\dot{Q}$	Heat loss
R	Universal gas constant
Re	Reynolds number
Sc	Schmidt number
S_L	Laminar flame speed
S_{L0}	Unstretched laminar flame speed
S_T	Turbulent burning velocity
S_U	Laminar burning velocity
T	Temperature

U_I	Integral scale
U_θ	Vortex maximum rotational velocity
V	Characteristic velocity
V_i	Diffusion velocity of species i
X	Volume fraction inputs
Y	Mass fraction

Lowercase Roman Letters

c	Speed of light
c_p	Specific heat
c_{pg}	Constant pressure heat capacity
d	Nozzle diameter
f	Fuel to air mass ratio
f_{ap}	Aperture size
h	Nozzle-to-plate height
h_c	Convective heat transfer coefficient
h_i	Specific enthalpy of species i
h_p	Planck's constant
Δh	Change in height
k	Thermal conductivity
m	Mass
n	Number of moles
n_x	Refractive index
p	Pressure
q	Heat flux
r	Radius
t	Time
u	Velocity
v	Nozzle exit velocity
x	Volume fraction
x_{01}, x_{02}	x – coordinates (nozzle)
x_1, x_2	x – coordinates
x_f	Spatial coordinate
y	Distance in the y-direction

y_{01}	y – coordinate (nozzle)
y_1	y – coordinate
z	Distance in the z-direction

Lowercase Greek Letters

α	Number of carbon atoms
$\alpha_{A,B}$	Seebeck coefficient
α_λ	Spectral absorptivity
β	Number of hydrogen atoms
γ	Number of oxygen atoms
δ	Small change/perturbation
δ_L	Flame thermal thickness
δ_{L0}	Unstretched flame thickness
δ_V	Vortex core diameter
ε	Emissivity
ε_d	Rate of energy dissipation
η	Kolmogorov length scale
θ	Angle or spreading rate
κ	Flame stretch factor
λ	Wavelength
λ_T	Taylor microscale
μ	Dynamic viscosity
ν	Kinematic viscosity
ρ	Density
σ	Stefan-Boltzmann constant
ϕ	Equivalence ratio
φ_{ij}	Viscosity calculation parameter
ω	Molecular rate production

Subscripts

∞	Ambient
a	Air
ae	Aerodynamic (diameter)

as	Stoichiometric air
c	Curvature
cd	Conductive
circ	Circumference
con	Conduction band
cone	Cone
cut	Cut-off
cv	Convective
e1	Ground state electron
e2	Excited electron
f	Fuel
ge	Geometric (diameter)
h1	Ground state electron hole
h2	Excited electron hole
i	Component i
j	Component j
m	Mass (flow rate)
mix	Mixture
p	Plate
p1, p2, p3	Photons 1, 2 and 3
rad	Radiative
s	strain
st	Stoichiometric
val	Valence band
W	Surface/wall
λ	Spectral

Superscripts

0	One-dimensional, unstretched
d	Directional

Acronyms

1D	One-dimensional
2D	Two-dimensional

3D	Three-dimensional
CCD	Charge Coupled Device
CCGT	Combined-Cycle Gas Turbine
CEA	Chemical Equilibrium with Applications
CFD	Computational Fluid Dynamics
CMOS	Complimentary metal-oxide-semiconductor
CV	Calorific Value
DAQ	Data acquisition
DDT	Deflagration to detonation
DF	Diffusion flame
DFCD	Digital Flame Colour Discrimination
DNS	Direct Numerical Simulation
emf	electromotive force
FLIR	Forward Looking Infrared
fps	Frames per second
GFC	Gas Flow Control (Model)
GRI	Gas Research Institute
IGCC	Integrated Gasification Combined Cycle
IR	Infrared
ISO	International Standards Organisation
LDV	Laser Doppler Velocimetry
LES	Large Eddy Simulation
LPF	Lean premixed flame
LPG	Liquefied petroleum gas
LWIR	Long wave infrared
MP	Mega Pixel
MWIR	Medium wave infrared
NASA	The National Aeronautics and Space Administration
NTP	Normal temperature and pressure
PIV	Particle Image Velocimetry
PLIF	Planar Laser Induced Florescence
RPF	Rich premixed flame
QWIP	Quantum Well Infrared Photodetector
TCHR	Thermochemical heat release

USC	University of Southern California
VI	Virtual Instrument

Abbreviations

CHEMKIN	Chemical Kinetics (Computer program)
Gaseq	Gas Equilibrium (computer program)
LabVIEW	Laboratory Virtual Instrumentation Engineering Workbench (computer program)
MATLAB	Matrix Laboratory (computer program)
Mech	Mechanism
SP01	Spot number 1
SP02	Spot number 2
SP03	Spot number 3
Wobbe No.	Wobbe Number

Chemical Symbols

Al_2O_3	Aluminium Oxide
C	Carbon element
C_3H_8	Propane
CH	CH radical
CH_4	Methane
CO	Carbon Monoxide
CO_2	Carbon Dioxide
H	Hydrogen element
H_2	Hydrogen
H_2O	Water
N	Nitrogen element
N_2	Nitrogen
NO	Nitrous Oxide
NOx	Nitrous oxides
O	Oxygen element
O_2	Oxygen
OH	OH radical

List of Tables

List of Tables

List of Figures

1. Introduction

1.1. Motivations

The first examples of combustion experienced by man originated from forest fires; the ignition source was provided by lightning storms and the forest wood acted as the fuel source [1]. Around 600,000 years ago, man pioneered the use of natural fire from forest fires or volcanic lava to light camp fires; using sticks with fire to ignite larger fuel supplies, determining that the heat produced by combustion is greater than the energy required to ignite the fuel [2, 3]. Since then, combustion has been used as a source of heat and light, and the use of combustion has developed into more complex systems and has been used for powering engines, pumping water and direct heating by flame jets.

Modern gas turbines have been used in aircraft as exhaust turbo chargers since 1918, for aircraft propulsion since the Whittle engine, which first ran in 1937 [4], and in power plants since 1939 [5]. Gas turbines are used in power plants, aeroplane jet engines, agricultural and industrial tractors and off-shore power plants, and are used with various fuels, such as natural gas, diesel, fuel oils and biomass gases [6]. Steam engines mainly used coal as their primary fuel source, and can be quite inefficient; coal has been used in power stations since Thomas Edison's first coal burning generation station in 1882, which only had an efficiency of 2.5 % [7]. In 1997, around 50 % of the world's coal usage was in large coal-fired power plants [8].

Much effort has been made to increase the efficiency of fossil fuelled power plants, and since the 1990s, Combined-Cycle Gas Turbine (CCGT) power plants have been used [6]. Due to the growing need for emission reductions and carbon capture, Integrated Gasification Combined Cycle (IGCC) power plants are in operation, which convert the solid fuel feedstock into syngas (a mixture of hydrogen and carbon dioxide) by partial oxidation with oxygen and steam, which is then purified and used as the fuel source for the gas turbines [9]. These power plants can be used for carbon capture and to create high hydrogen content syngas for use in the CCGTs [9, 10], which reduces carbon emissions compared to coal fuelled power plants. Industrial developments in combustion have been fuelled by the need to create more efficient heating, power generation and propulsion methods and more recently by the growing demand to keep emissions low. The development of cleaner fuels, such as hydrogen and syngas, is

integral to the future advancement of combustion systems. However, the properties of hydrogen are vastly different to the properties of other fuels such as propane and methane, and the various compositions of syngas also differ greatly in their properties. Therefore, the continuing research on the properties of these fuels is integral to the design and maintenance of many industrial systems that may use syngas as a fuel. In addition, when flames impinge directly onto surfaces in gas turbine combustors or furnaces, the flame wall interaction can cause areas of high heat transfer, which can affect the combustor performance or cause damage to the combustor walls. Hydrogen has a very high thermal diffusivity and a high flame temperature compared to hydrocarbon fuels, and so the effects of the flame wall interaction for hydrogen and syngas can be very different than for hydrocarbon fuels. Laboratory scale experiments can provide much useful information into the interaction between the flame and wall, and can allow hydrogen and syngas to be studied meaningfully in terms of the flame wall interaction so that information and data can be provided for new combustor designs that may use these new cleaner fuels.

Impinging flames occur often in industry, for example in the heating of glass and metals and on combustor walls in furnaces and gas turbines. Direct flame impingement can cause advantages and disadvantages, due to the higher heat transfer rates and non-uniform heat flux respectively [11]. Impinging flames provide a simple geometric configuration for the study of flame wall interactions. The configurations allow optical access to the flame and allow various aspects of the flame wall interactions to be studied. They provide a controlled environment where different parameters may be compared. In addition, there is much literature concerning impinging flames and they are well understood. However, the principle focus of impinging flame studies has usually been hydrocarbon fuels rather than hydrogen and syngas fuels. Therefore, this thesis aims to look into the flame wall interactions for impinging flames of hydrogen and syngas fuels.

Although combustion has been economically and technically important throughout history, the scientific study of combustion is relatively recent [2]. This is due to the science behind combustion phenomena, including thermodynamics and fluid mechanics, and the more recent developments in chemical kinetics and transport processes, not being understood until recently, so that combustion science did not

properly develop until the early 20th Century [2]. More recently, advances in computational ability and power have led to combustion simulations being possible which has greatly improved scientific knowledge of combustion phenomena. Alongside this, increased experimental ability has led to advances in research at high pressure and high speed, allowing a greater range of experimental conditions to be explored. Therefore, this thesis will use advanced experimental techniques and some computations in order to look into the combustion of fuels that are being studied more and more due to their clean combustion nature, in an impinging flame configuration so that meaningful results can be obtained and compared.

Technological advances have made it possible for combustion to be studied in a wide variety of methods, and consequently, much is being discovered regarding flow structure, heat transfer and combustion characteristics of many types of flame. New fuels that are being developed for the purposes of cleaner combustion mean that various aspects of combustion must be studied for these fuels and this thesis is concerned with the particular interaction between jet flames and a flat impingement surface. Computational and experimental advances will be utilised in this thesis by using Gaseq and CHEMKIN to calculate the adiabatic temperatures and laminar flame speeds of the various mixtures for use with the experimental results. Advanced experimental techniques will be used to study the wall temperature, flame structure and propagation characteristics in order to better understand the flame wall interactions. Various fuel and flow conditions will be studied to test their effect on the flame wall interactions and experimental diagnostic techniques will be utilised and improved upon for this purpose.

1.2. Aims and Objectives

Advances in experimental methods and instrumentation mean that measurements of flame and surface temperature, flame structure, fluid velocity, particle size and species concentration can be performed with greater accuracy and efficiency and for a larger range of experimental conditions [12]. High speed cameras, lasers, thermal imaging and other diagnostic tools are constantly being developed, and along with the computational and theoretical combustion advances allow more and more combustion phenomena to be understood. It is the aim of this thesis to use and develop diagnostic and

visualisation techniques in order to evaluate flame wall interactions in the following ways:

- Use a simple geometric configuration to compare impinging flames of hydrogen, syngas, propane and methane.
- Combine the use of schlieren and thermal imaging to evaluate the heat transfer and flow characteristics.
- Develop these techniques for use with impinging flames; particularly to use the thermal imaging to evaluate the non-uniform temperature of the heated impingement plate, and to use schlieren to evaluate flow and turbulence characteristics.
- Vary flow conditions, fuel parameters and geometric properties in order to test the effect of the nozzle exit conditions on the flame wall interactions.
- Calculate the laminar flame speeds and adiabatic temperatures of the syngas compositions in order to test their effects on the flame wall interactions.
- Evaluate the flame propagation characteristics of impinging flames using the advanced diagnostic tools.

The objective of this thesis is to develop the experimental diagnostic techniques so that the interaction between the flame and wall for hydrogen and hydrocarbon fuels can be meaningfully evaluated and compared. The results presented are specific to the configurations used; however, the techniques that have been developed can be applied to industry. The heat transfer and flame wall interactions in many industrial setups can be evaluated and monitored, including measuring the temperature and flame wall interaction in furnace walls and gas turbine combustors. The next section will give a brief outline of the thesis.

1.3. Thesis Outline

Following this introduction, a detailed literature review will be given in Chapter 2. This will consist of background information, a review of experimental techniques and a review of literature pertaining to impinging flames, heat transfer and flame propagation. Chapter 3 will discuss the rig setup and the experimental techniques and methodologies, along with error analyses. Chapter 4 will discuss the adiabatic flame temperature and laminar flame speed calculations for the various compositions. Chapters 5 and 6 will

contain all of the results and discussions; Chapter 5 will look into the wall temperature comparisons, comparing flames of propane, hydrogen and syngas at various experimental conditions using thermal imaging, schlieren and direct imaging and Chapter 6 will look into the flame propagation of hydrogen mixtures and methane, using the high speed schlieren imaging. Chapter 7 will give a brief conclusion to the results and outline the major findings of the thesis, which will be followed by the scope for future work in Chapter 8, where improvements on the methods used and possibilities for further research will be discussed.

2. Literature Review

2.1. Introduction

Combustion is a very complex phenomenon, with various factors and parameters affecting flames of many kinds. Therefore, it is necessary to define in clear terms the combustion and flow properties of certain types of flames, and present a review of the literature. The review will begin with an outline of the basic properties of combustion, heat transfer and impinging flames. A review of experimental diagnostic techniques used in combustion studies will then be given, followed by a comprehensive review of impinging flame studies; in particular the configurations, heat transfer and flow properties thereof, including a review of how the various experimental techniques may be utilised and improved in an impinging flame configuration, as these are the main focus of this thesis. Following that, a review of ignition and flame propagation phenomena will be given, as the flame propagation in impinging flames is also a focus of this thesis. In this way, a clear overview of combustion characteristics and ways in which these can be measured, along with a review of the literature pertaining to combustion and impinging flames will be given in this chapter.

2.2. Combustion Theory

This section will give a comprehensive discussion of the background theory of combustion in order to define various terms, look into the specific properties of jet flames and impinging flames, including flow structure and heat transfer mechanisms and to compare properties of various fuels.

2.2.1. Flames

2.2.1.1. Flame Definition

A flame, by definition, is an exothermic chemical reaction, whereby reactants (or fuel) react with an oxidant, usually air or oxygen, to form products of a different chemical composition. The reaction is demonstrated mathematically by the *stoichiometric* chemical equation. For a reaction to be stoichiometric, the oxygen content must be of the exact amount to convert all of the reactants into products. For stoichiometric hydrocarbon reactions, the reactants will contain elements of carbon (C) and hydrogen (H), and perhaps other elements such as nitrogen (N). The oxidiser will contain oxygen

(O) and, if reacting in air, 79 % nitrogen. The products will contain carbon dioxide (CO_2), water (H_2O) and possibly nitrogen. An example for propane (C_3H_8) reacting in pure oxygen is shown in Fig. 2.1. C_3H_8 requires 5 times the (molar) amount of oxygen (O_2) than reactant to burn stoichiometrically. The *reaction rate* is defined as the rate of decrease of the concentration of a reactant or equally as the rate of increase of a reaction product [13].

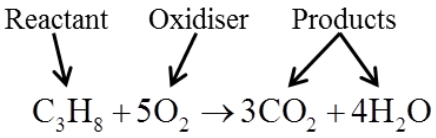

Figure 2.1: Chemical equation for propane reacting in stoichiometric oxygen.

The reaction requires some initial stimulant to begin the process. This stimulant is normally the addition of heat, with a large enough thermal energy to kick-start the reaction. This is called the *activation energy* or *ignition energy* and often takes different values depending on the fuel. Table 2.1 shows the minimum ignition energies for the fuels used in this thesis. It can be seen that hydrogen requires much less energy to ignite than carbon monoxide and the hydrocarbon fuels.

Fuel	Minimum Ignition Energy (mJ)	Flammability Limits in Air (% Fuel)
Hydrogen	0.02	4 - 74
Carbon Monoxide	< 0.3	10.9 - 76
Propane	0.25	1.7 - 10.9
Methane	0.28	4.4 - 17

Table 2.1: Ignition energy and flammability limits in air of the fuels used in this thesis [14-18].

The *fire triangle* (Fig. 2.2a) has often been used to demonstrate the requirements of a stable fire; in order for a fire to burn, three elements are needed; fuel, oxygen and heat [19]. If one or more of these factors are taken away, then the flame cannot burn. Moreover, the ratio of fuel to oxidiser must be sufficient to support combustion. The percentages of fuel in the fuel-air or fuel-oxygen mixture that will support combustion are called the *flammability limits*. The flammability limits in air of the fuels used in this thesis are given in Table 2.1. Hydrogen and carbon monoxide both have quite a large

range of flammability limits in air, whereas the hydrocarbon fuels require more air in the mixture for the fuel to ignite.

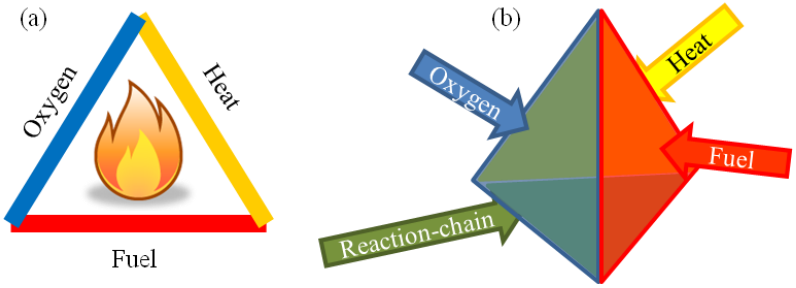

Figure 2.2: Diagrams to illustrate (a) The 'fire triangle' and (b) The 'combustion tetrahedron'.

The flame exists in the *reaction zone*, where the change of chemical composition takes place and where high temperatures are produced. In the reaction zone, many complex reactions occur, inducing other chain reactions. Many factors affect these complex reactions. More recently, an element has been added to the fire triangle to make the *combustion tetrahedron*, whereby, it is stated that a *reaction chain* is also required to sustain combustion (Fig. 2.2b) [20]. The reaction chain occurs after initiation of the flame and before the formation of the final products and the reaction processes are many and complex. The process involves the formation of *free radicals*, such as C, O, H and combinations of the form OH and CH for example, which facilitate other reactions in the reaction zone [21]. The radicals eventually combine, after many reaction steps, to form the final products. In addition to the requirements for a flame to ignite, there are many classifications to describe the type of flame, which will be discussed in the next section.

2.2.1.2. Flame Classifications

Fire is usually referred to as an uncontrolled combustion reaction, whereas a *flame* is a controlled reaction, usually in a regulated environment. The latter is the subject of this thesis, and in particular flames produced by gaseous fuels, which can be easily controlled; parameters may be altered by simply changing the flow rate for example. In this way many different parameters can be studied experimentally. Gaseous flames can be classified according to their state before and during combustion. These classifications can be split into combustion related properties and flow properties.

2.2.1.2.1. Combustion Properties

The main combustion related property used to classify a gaseous flame is whether the fuel and oxidiser are initially mixed or separated. Combining the fuel and oxidiser before combustion is known as premixing. The flames can be classified into three categories; *diffusion* (or *non-premixed*), *partially premixed* and *premixed* flames.

Diffusion Flames

For a diffusion flame (Fig. 2.3a), the flame exists in a reaction zone located in between the reactants and the products, which mix by molecular and thermal diffusion. In this case, the mixing rate is lower than the chemical reaction rate [22], and so the reaction is controlled by the diffusion mixing process. A typical example of a diffusion flame is a candle flame, where the wax evaporates to form a zone containing reactants, which combust in the reaction zone; observed by a yellow flame. In the reaction zone, diffusion occurs between the reactants and the surrounding air. This process is slower than the reaction process causing a wide region where the gas composition and amount of products/reactants are variable [13].

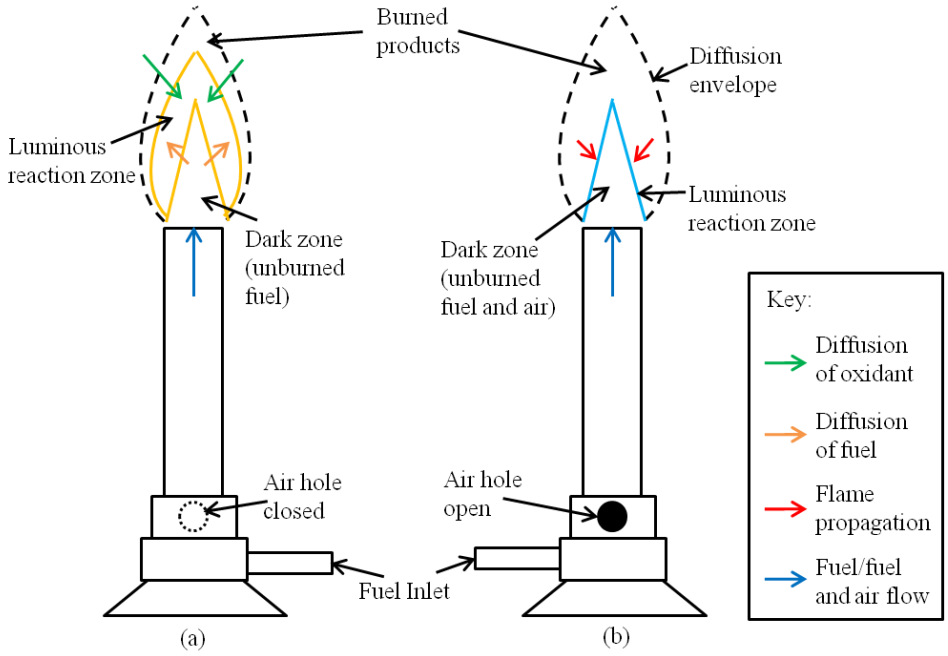

Figure 2.3: Schematics of Bunsen burner flames for (a) Diffusion flames and (b) Premixed flames (adapted from [22]).

The Bunsen burner, invented by Robert Bunsen in 1985 [22], is able to produce gaseous flames of all three classifications by allowing the input of air to be adjusted. Figure 2.3a

shows a schematic of a Bunsen burner with the air hole closed, producing a diffusion flame. The diffusion of the fuel and air are shown by the orange and green arrows respectively. The structure of diffusion flames has been investigated extensively [23-28], in particular, *buoyancy*; the rising of the hot gases due to gravitational forces, plays a large part in diffusion flame structure, causing the convection of vortical structures and flame flickering [29-31].

Premixed Flames

In a premixed flame, the reaction occurs within the fuel and air mixture, and the flame propagates through the mixture, for example, in a petrol engine. The flame propagates through the unburned mixture at the *laminar flame speed* (S_L); which is the flame propagation rate relative to the unburned gas [22], and depends on the fuel type and mixing ratio. Figure 2.3b shows the Bunsen burner with the air hole open, producing a premixed flame. In a Bunsen flame, the premixed flame propagation is stabilised by the fuel flow velocity in the opposite direction. In this case the flame exists between the unburned fuel-air mixture and the burned reaction products. The mixing rate is considered to be very fast and so it is the chemical reaction that dominates the reaction rate, in contrast to diffusion flames. Partially premixed flames are flames that do not contain enough oxidiser in the unburned mixture so that combustion is facilitated by the diffusion of the fuel-air mixture and the surrounding air. This creates a flame with premixed and diffusion flame characteristic features.

The *laminar burning velocities*; which are the rates of consumption of unburned fuel, of various gas mixtures have been calculated using CHEMKIN [32, 33], and the flame structure of premixed [34-37] and partially premixed flames [38-40] has been studied by many researchers.

Equivalence Ratio

The amount of mixing for premixed flames can be characterised by the *equivalence ratio, ϕ,* defined by Eq. 2.1 as the ratio of the actual fuel to air mass ratio, *f*, to the stoichiometric fuel to air mass ratio, f_{st}, which is calculated from Eq. 2.2:

$$\phi = f / f_{st}, \tag{2.1}$$

$$f_{st} = \frac{m_f}{m_{as}} = \frac{M_f n_f}{M_a n_{as}} = \frac{M_f}{29.0(\alpha + \beta/4 - \gamma/2)(4.76)}, \quad (2.2)$$

where m_f and m_{as} represent the mass of the fuel and the stoichiometric air respectively and M_f and M_a are the molecular weights of the fuel and air respectively (M_a = 29.0). n_{as}/n_f is the number of moles of stoichiometric air per mole of fuel, calculated from the stoichiometric *atom balance equation* (Eq. 2.3), equal to 4.76 ($\alpha + \beta/4 - \gamma/2$):

$$C_\alpha H_\beta O_\gamma + (\alpha + \beta/4 - \gamma/2)(O_2 + 3.76N_2) \rightarrow$$

$$\alpha CO_2 + (\beta/4)H_2O + 3.76(\alpha + \beta/4 - \gamma/2)N_2, \quad (2.3)$$

where α, β and γ are the number of carbon, hydrogen and oxygen atoms respectively in the fuel components. For propane (C_3H_8) reacting in air, the stoichiometric atom balance equation (adapted from Fig. 2.1 for the addition of nitrogen) is given by Eq. 2.4, and the value of ($\alpha + \beta/4 - \gamma/2$) is (3 + 8/4 – 0) = 5. This means that 5 moles of oxygen are needed to react 1 mole of propane stoichiometrically. For methane, the value of ($\alpha + \beta/4 - \gamma/2$) is 2. For hydrogen and carbon monoxide the value of ($\alpha + \beta/4 - \gamma/2$) is 0.5. This means that a much lower amount of air per fuel is required to burn these gases stoichiometrically than for propane and methane.

$$C_3H_8 + 5(O_2 + 3.76N_2) \rightarrow 3CO_2 + 4H_2O + 18.8N_2. \quad (2.4)$$

When the fuel to air ratio is changed, the value of the equivalence ratio (Eqs. 2.1 and 2.2) changes accordingly; a value of $\phi = 1$ indicates that the mixture is stoichiometric, whereas $\phi < 1$ indicates a *fuel lean* flame (there is more oxidiser than is needed to combust the fuel) and $\phi > 1$ indicates a *fuel rich* flame (there is not enough oxidiser to fully combust the reactants). The equivalence ratio characterises the initial premixing conditions, which have been described in the previous paragraphs.

There are many differences between diffusion ($\phi = \infty$), fuel rich (partially premixed), and fuel lean (premixed) flames. The temperature of diffusion flames is much lower due to the lack of oxygen and slow mixing rates. They experience *incomplete combustion;* where much of the carbon in the reactants takes the form of CO in the products, due to lack of available oxygen to form CO_2. Diffusion hydrocarbon flames generally produce

soot particles, which cause a bright yellow flame, whereas premixed flames are generally blue in colour due to the high temperature induced oxidation of the fuel and *complete combustion*, where the products are in the form of the stoichiometric reaction equation (Eq. 2.4 for propane). Partially premixed flames will produce some soot but will also exhibit a blue flame at the base, due to air entrainment at the base providing sufficient oxygen, and incomplete combustion towards the tip where the oxygen cannot mix fast enough with the reactants.

The equivalence ratio also affects the laminar flame speed and consequently the stability of the flame on the burner nozzle. If the flame speed is much higher than the nozzle exit velocity of the fuel then the flame will propagate into the nozzle, causing *flashback*. Flashback can also be caused by turbulence and acoustic instabilities and in swirl combustors [41-43]. If the nozzle is small and cold enough, the nozzle pipe will *quench* the flashback; the cool pipes will cause the flame to be extinguished, causing no damage, but flashback can be very dangerous if the flame is able to propagate further into the nozzle and fuel pipes. On the other hand, if the nozzle exit velocity is higher than the flame speed, the flame will *lift off* from the burner nozzle. In some cases the flame can be stabilised during lift-off so that it becomes a stable *lifted flame*. However, if the flow velocity becomes too high, then *blow-out* will be observed and the flame will be extinguished. For the cases where the flame does not lift off but becomes extinguished when the flow velocity is increased, this is called *blow-off* [44]. The laminar flame speed of hydrogen is much faster than that of propane and other hydrocarbon fuels, and so the risk of flashback is much higher for hydrogen and hydrogen enriched fuels. The laminar flame speeds for the fuels used in this thesis will be determined using CHEMKIN and will be discussed further in Chapter 4.

Heat Release

Other combustion properties of gaseous fuels are related to energy release in the form of heat. The local temperature of a flame depends on many factors such as equivalence ratio, soot formation, reactants, pressure and the complex reactions that take place within the flame. A property used to describe flame temperature is the *adiabatic temperature*. This is the maximum temperature that a flame will reach if all combustion processes are completed and there is no heat loss, and hence is an idealised temperature.

The adiabatic temperatures of propane, methane, hydrogen and the syngas compositions will be determined by Gaseq and CHEMKIN and will be discussed further in Chapter 4.

A common parameter used to assess the energy that can be gained from a specific fuel is the *calorific value* of that fuel. The calorific value is a measure of the amount of potential energy per kg of fuel, i.e. the amount of heat energy that can be gained by combusting all reactants into products. The *gross calorific value* is that calculated when the water in the fuel is considered to be a liquid, whereas the *net calorific value* is used for when the water is assumed to be already vaporised, and so does not take into account the energy required to vaporise the water. From the calorific value, a term called the *Wobbe number* can be calculated (Eq. 2.5). The Wobbe number is a measure of the interchangeability of different fuels and takes into account the *specific density* (the denominator in Eq. 2.5) and calorific value of the fuel. However, the Wobbe number does not take into account factors such as adiabatic temperature, which may cause large differences in heat transfer effects and other factors that relate to the interchangeability of fuels.

$$\text{Wobbe No.} = \frac{\text{Gross } CV}{\sqrt{\rho / \rho_a}}, \tag{2.5}$$

where Gross *CV* is the gross calorific value of the fuel, ρ is the fuel density and ρ_a is the density of air. It can be seen from Table 2.2 that the Wobbe numbers for propane, methane, hydrogen and carbon monoxide are vastly different and this implies that the fuels cannot be interchanged. However, when the fuels are mixed together, the Wobbe numbers will change quite quickly due to the changes in calorific value and specific density.

Thermal loading can also be used to characterise the heat energy in the fuel. It is a measure of the thermal power available in the flame and can be calculated from Eq. 2.6:

$$\text{Thermal loading} = CV \times \text{mass flow rate}, \tag{2.6}$$

where *CV* is the calorific value of the fuel in kJ kg^{-1}, the mass flow rate is in m^3 s^{-1} and the thermal loading is calculated in kW. It can be used to compare fuels in specific burners, and for heat transfer studies with flame impingement [45-47]. The thermal

loading can be used to compare fuels in the same combustor as the same thermal power could be achieved by simply altering the flow rate although other factors relating to the flow properties must also be taken into consideration.

Fuel	Gross *CV* ($MJ\ kg^{-1}$)	Wobbe Number ($MJ\ kg^{-1}$)
Methane	55.53	74.7
Propane	50.35	40.9
Hydrogen	141.79	537.8
Carbon Monoxide	10.11	10.3

Table 2.2: Calorific value and Wobbe number of various fuels at normal temperature and pressure (NTP) [48].

The next section deals with the properties related to the flow structure, and can be applied to cold flows as well as combusting gases. The flow properties may change the specific effects of the combustion related properties due to the fluid dynamics and aerodynamics of the fuel, and the effects of flow structure and flow properties on the heat transfer and flame wall interaction are a large focus of this thesis.

2.2.1.2.2. Flow Properties

Turbulence

The main flow related property used to describe gaseous flames is the degree of *turbulence* in the flow. *Laminar* flow is that which does not exhibit turbulence and can be characterised by a smooth flow without any fluctuations or disturbances. Turbulent flow contains eddies, which are small scale or large scale vortices, and other fluctuations within the flow. Turbulent structures increase the mixing rates of the fluid and so cause fluids that are initially separated to mix more quickly with one another. Increasing the flow velocity will cause the turbulence to increase and in nature most fluids will become turbulent as flow velocity is increased and obstacles are placed in the flow [49]. The simplest way to visualise turbulence is to observe flow within pipes. Figures 2.4a and b show examples of laminar and turbulent flow in a pipe respectively. Laminar flow will exhibit a parabolic profile due to resistance from the walls of the pipe. Turbulent flow will display vortices and disturbances within the flow. Turbulent [34, 36, 37, 40, 50-55] and laminar [23, 32, 56-61] flows in jet flames have been studied at length.

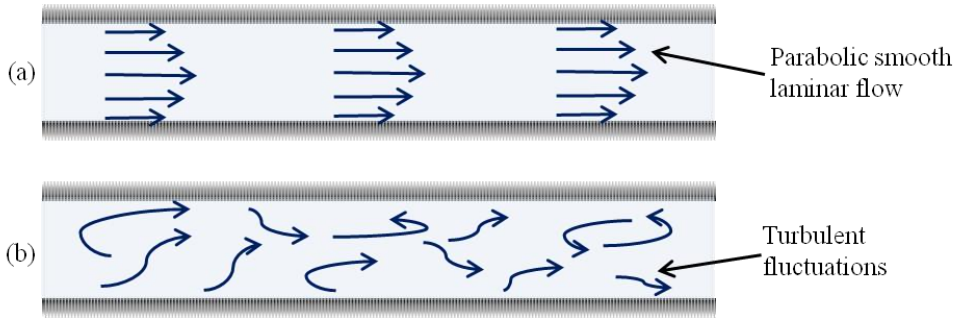

Figure 2.4: Example profiles of (a) Laminar and (b) Turbulent flow within a pipe.

Reynolds Number

The *Reynolds number* (Re) is used to characterise the degree of turbulence and the effect of the viscous forces of the fluid, and is defined as the ratio of inertial forces to viscous forces [62]. This means that for low Re, the flow is dominated by viscous forces, but for higher Re, the flow is dominated by the inertial forces, causing more resistance to changes in motion. The higher the Reynolds number, the higher the turbulence degree. It was first introduced in 1883 by Osborn Reynolds, who observed that the laminar and turbulent characteristics of a stream of dye within a tube of flowing water were dependent upon the velocity of the water [49]. Figure 2.5 shows an example of this experiment; at low velocities, the stream of dye was distinctly separate from the water flow and followed a straight flow without mixing with the water. When the velocity was increased above a certain value, the dye would mix with the water due to the turbulent nature of the flow.

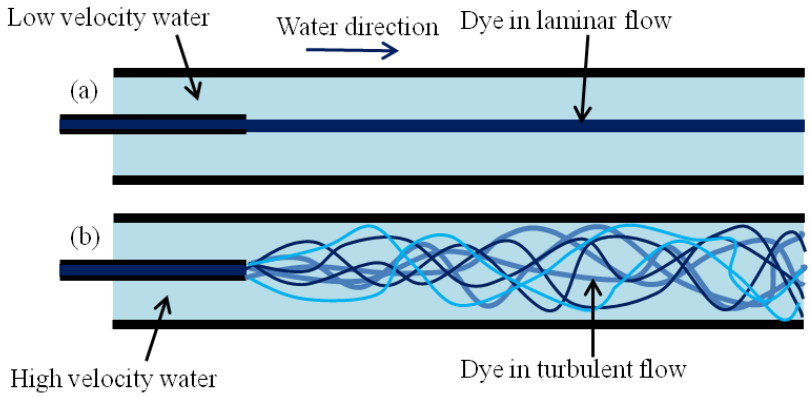

Figure 2.5: Example of Reynolds' experiment to demonstrate laminar and turbulent flow (adapted from [49]).

The Reynolds number (Eq. 2.7 [62]) takes a dimensionless form, using a characteristic length scale, L, the fluid density, ρ, dynamic viscosity, μ, and a characteristic velocity V:

$$\mathrm{Re} = \frac{\text{Inertial forces}}{\text{Viscous forces}} = \frac{\rho V^2 L^2}{\mu V L} = \frac{\rho V L}{\mu}. \tag{2.7}$$

For flow exiting a burner nozzle (Eq. 2.8), L is taken as the nozzle diameter, d, and V is taken as the nozzle exit flow velocity, v, so that:

$$\mathrm{Re} = \frac{\rho v d}{\mu}. \tag{2.8}$$

Values of density and viscosity of the pure fuels used in this thesis are given in Table 2.3. The densities and viscosities of the fuel mixtures were calculated using LabVIEW (see Appendix A). For a certain fuel and burner geometry, the flow velocity can be adjusted to vary the Reynolds number. For free circular jets, Reynolds numbers below 1000 are considered to be laminar, those between 1000 and 3000 in the *turbulent transitional* regime, or semi-turbulent, and those above 3000 to be turbulent [11]. The effects of Reynolds number in jet flames have been studied in depth [63-65]; in particular Re significantly affects heat transfer characteristics of impinging jets [61, 66-68]. Impinging flames are the subject of Sections 2.2.2 (for background information) and 2.4 (for a detailed review) and heat transfer will be discussed in more detail there.

Gas	Density (kg m^{-3})	Viscosity (kg m^{-1} s^{-1} x 10^{-5})
Air	1.19	1.84
C_3H_8	1.80	0.80
CO	1.15	1.74
CO_2	1.80	1.48
CH_4	0.66	1.03
H_2	0.08	0.87
N_2	1.15	1.75

Table 2.3: Viscosities and densities at NTP of the gases used in this Thesis [69].

Turbulent Length Scales

For high Re flows, the turbulence scales can be represented by an energy cascade; where energy is transferred from larger scale eddies to form smaller scale eddies, driven by the large inertial forces present in high Re cases [70]. When Re (based on the size of the eddies) becomes of the order of unity, the smallest scale eddies are driven by viscous forces and dissipation of kinetic energy is significant at these length scales [70]. The smallest turbulence scales can be characterised by the *Kolmogorov length scale, η*:

$$\eta \sim \left(\frac{\nu^3}{\varepsilon_d}\right)^{1/4} \sim L\,\mathrm{Re}^{-3/4}, \tag{2.9}$$

where ν is the kinematic viscosity, ε_d is the rate of energy dissipation and L is the characteristic length scale of the largest eddies [70]. Other length scales include the *Integral scale*, U_I, and the *Taylor microscale*, λ_T, which characterise the largest turbulence scales and the smallest turbulence scales before dissipation comes into effect respectively, and are represented by Eq. 2.10 [71]:

$$\varepsilon_\mathrm{d} \sim \nu \frac{U_I^2}{\lambda_T^2}\ . \tag{2.10}$$

Along with the turbulent properties such as Re and the premixing conditions, which are important for stable flame analysis, many important flame properties also relate to the ignition of the fuels, which, with the development of high speed cameras, has been studied more in recent years. The time dependent propagation of flames is also important when dealing with factors such as burning velocity. The next section deals with some important parameters related to the ignition and propagation of gaseous fuels.

2.2.1.3. Ignition and Flame Propagation

2.2.1.3.1. Ignition Definition

Ignition is the process by which unburned fuel begins to combust with the addition of a heat source. For a spark ignition, the process begins when the mixture reaches a high enough temperature, producing a *flame kernel* [72]. A flame kernel is the period between ignition and either a self-sustaining flame (growth of the kernel) or extinction (death of the kernel), and typically moves from a cylindrical shape to a spherical shape

approximately 0.01 m in diameter [72, 73]. After ignition, the flame will either reach a state of steady combustion, where the flame can exist without an additional heat source, or become extinguished and may need a pilot flame to keep the flame ignited.

Ignition phenomena are very important in internal combustion engines, where design factors, such as ignition location with respect to fuel/air compositions, will influence how quickly the combustion processes are completed and how easily the mixture is ignited [39], and in gas turbine combustion the fuel mixture may need to be quickly re-ignited or a steady state flame established quickly. Design factors, ignition location and fuel composition can all affect the ability of the mixture to ignite and also the ignition time, which is related to the propagation of the flame immediately after ignition and before a stable flame is reached. The propagation of the flame kernel and subsequent flame are important in ignition studies, and flame propagation phenomena are essential to some analytical and computational models [74] and to the understanding of ignition processes. Some important parameters relating to flame propagation will now be discussed.

2.2.1.3.2. Flame Propagation Parameters

Burning Velocity and Flame Speed

The laminar flame speed (S_L) has been defined in Section 2.2.1.2.1 as the rate of flame propagation relative to the unburned gas. For example, fuel propagating along a tube at a velocity equal to the laminar flame speed will produce a stationary flame. If the fuel velocity is lower than the laminar flame speed then the flame will propagate into the unburned mixture, but if the fuel velocity is higher than S_L then the flame will propagate away from the unburned fuel. The burning velocity (S_U) is a measure of how fast reactants are consumed into products, and the turbulent burning velocity (S_T) is for flames where there exists turbulence in the unburned gases, causing an increase in the flame surface area due to wrinkling and flame front distortions, and increasing the overall mass consumption rate (Fig. 2.6) [75].

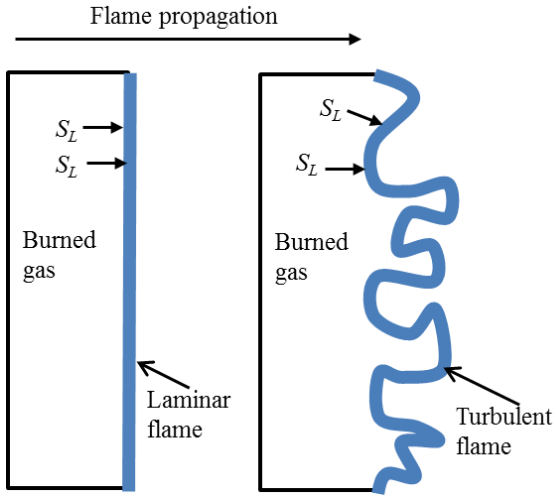

Figure 2.6: Diagram showing the increase in flame surface area due to turbulence (adapted from [75]).

Lewis Number

For gaseous fuels, the fuel must be within a certain range of conditions for ignition to be viable (see Section 2.2.1.1), but other factors such as turbulence, the interaction of the flame kernel with the flow field and the Lewis number (Eq. 2.11) may also affect the ignition process.

$$\mathrm{Le} = \frac{\text{Thermal Diffusivity}}{\text{Mass Diffusivity}} = \frac{\mathrm{Sc}}{\mathrm{Pr}}, \tag{2.11}$$

where Le is the Lewis number, Sc is the Schmidt number and Pr is the Prandtl number (Eq. 2.12):

$$\mathrm{Sc} = \frac{\mu}{\rho D}, \qquad \mathrm{Pr} = \frac{c_p \mu}{k}, \tag{2.12}$$

where μ is the dynamic viscosity, ρ is the density, D is the mass diffusivity, c_p is the specific heat and k is the thermal conductivity. The Prandtl number is a relation of the relative thicknesses of the hydrodynamic and thermal boundary layers, and represents the ratio of momentum and heat diffusion within the fluid, connecting the velocity and temperature fields, whereas the Schmidt number is significant when both convection and mass transfer are important [76]. The Lewis number controls flame stability; premixed flames with Le < 1 tend to develop cellular structures and instabilities, which

cause turbulent flames to be more wrinkled for lower Le. This is because of the continuous distortion of the flow field due to inhomogeneities in the flow [77]. The Lewis number also affects local flame temperatures and reaction rates due to the effects of curvature and strain rates, or flame stretch, which affect the flame propagation and ignition phenomena [77].

Flame Stretch

For non-uniform flow fields, a propagating flame surface is subjected to effects of strain and curvature [22]. For fluids, the shear stress is proportional to the rate of angular deformation, or the strain rate, through Stokes' law, and it is dependent on the specific fluid and the thermodynamic state of that fluid [22]. Flame curvature may be positive or negative depending on whether the flame is curved towards or away from the unburned mixture respectively, for example in expanding and collapsing spherical flames (Figs. 2.7a and b respectively) [78].

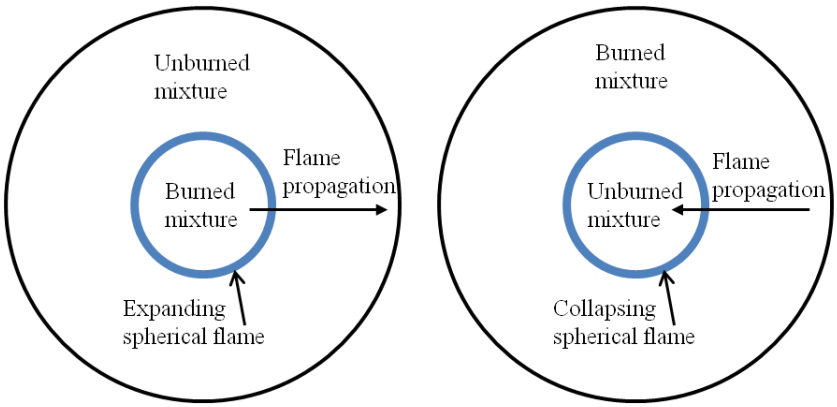

Figure 2.7: (a) Positive curvature for expanding spherical flame and (b) Negative curvature for collapsing spherical flame.

For Le = 1, positive curvature reduces the flame speed and negative curvature increases the flame speed (due to the heat entering a control volume via a smaller/larger surface respectively), but does not affect the burning velocity [78]. The effects of strain and curvature lead to changes in the flame front area, and are characterized by the flame stretch factor κ, defined as the relative rate of change of the flame surface area due to flame stretch [22]:

$$\kappa \equiv \frac{1}{\delta A_f}\frac{\mathrm{d}\left(\delta A_f\right)}{\mathrm{d}t} = \frac{1}{A_f}\frac{\mathrm{d}A_f}{\mathrm{d}t}, \tag{2.13}$$

where κ is the flame stretch factor, A_f is the flame surface area and t is time.

Flame stretch reduces the thickness of the flame front and the flame speed, and influences the flame structure due to the effects of heat and mass diffusion [22]. The flame stretch factor is made up of contributions from the strain rate tensor, dilatation (volume expansion of the fluid) and curvature effects [22]. Taking stretch into account, the laminar flame speed (S_L) becomes:

$$S_L = S_{L0} - L_M \kappa, \tag{2.14}$$

where S_{L0} is the unstretched laminar flame speed, κ is the flame stretch factor and L_M is the Markstein length, which characterises the hydrodynamic 'size' of the flame, taking the non-dimensional form of the Markstein number, Ma (Eq. 2.15):

$$\mathrm{Ma} = \frac{L_M}{\delta_L}, \tag{2.15}$$

where δ_L characterises the thermal thickness of the flame. The Karlovitz number, Ka, (Eq. 2.16) is a non-dimensional stretch factor using the thickness of the unstretched flame, δ_{L0}, and the unstretched laminar flame speed S_{L0}, and is made up of contributions from the strain and curvature (Eq. 2.17) [22]:

$$\mathrm{Ka} = \frac{\text{Residence time for crossing an unstretched flame}}{\text{Characteristic time for flame stretching}} = \frac{\delta_{L0}}{S_{L0}}\kappa, \tag{2.16}$$

$$\mathrm{Ka} = \mathrm{Ka_s} + \mathrm{Ka_c}, \tag{2.17}$$

where $\mathrm{Ka_s}$ and $\mathrm{Ka_c}$ are the strain and curvature components respectively. Combining Eqs. 2.14 to 2.16, the apparent flame speed is related to Ma and Ka by Eq. 2.18 [22]:

$$\frac{S_{L0}}{S_L} = 1 + \mathrm{MaKa}. \tag{2.18}$$

The burning velocity is also affected by the flame stretch in a similar way (Eq. 2.19) [22]:

$$S_U = S_U^0 - L_M \kappa, \tag{2.19}$$

where S_U is the burning velocity associated with the reference flame surface, S_U^0 is the one-dimensional (1D), unstretched burning velocity, L_M is the Markstein length and κ is the stretch factor.

Flame stretch is present in the stagnation region of opposed jets and impinging flames [79], and laminar flame speeds and burning velocities are affected by flame stretch due to strain and curvature of the flame front, and can have significant effects on flame propagation.

Background information for various properties of jet flames, including premixing, turbulence and ignition has been given. The flame propagation characteristics of impinging flames have not been widely studied and will be looked into in this thesis, along with other properties and flame wall interactions of impinging flames. The next section deals with the background information integral to any study of impinging flames and flame wall interactions. A detailed review of impinging flame studies will be given in Section 2.4.

2.2.2. Impinging Flames

An *impinging flame* is one in which part of the flame experiences direct contact with a surface or wall. Impinging flames exist in many areas of combustion, including inside combustor chambers, where the flame will impinge onto the combustor walls, or in heating processes where flame jets may be used to heat materials, melt glass or forge metals. Impinging flames may be desirable, for high heat transfer rates, or undesirable, where flame wall interactions may cause hot spots or flame quenching. Temperature gradients on wall surfaces may also cause uneven heating which can lead to damage.

2.2.2.1. Structure

The structure of a jet flame impinging upon a surface will be different to the non-impinging (free) jet structure due to the obstruction of the flow. In addition, the combustion properties will change the structure when compared to a non-reacting jet.

The effect of an impingement plate and combustion on the jet structure will be discussed here.

Free Non-Reacting Jet

The structure of a free, non-reacting jet is shown in Fig. 2.8. It consists of a *potential core zone*, which has a constant velocity, equal to the nozzle exit velocity, and the length of which depends on the turbulence in the nozzle exit and the initial velocity profile [11]. Downstream of that is the *developing zone*, in which air is entrained due to turbulence caused by large shear stresses at the jet boundary, and the axial velocity profile decays [11]. Following that is the *fully developed zone*, where linear jet broadening with axial velocity decay and also a Gaussian velocity distribution have been observed [11].

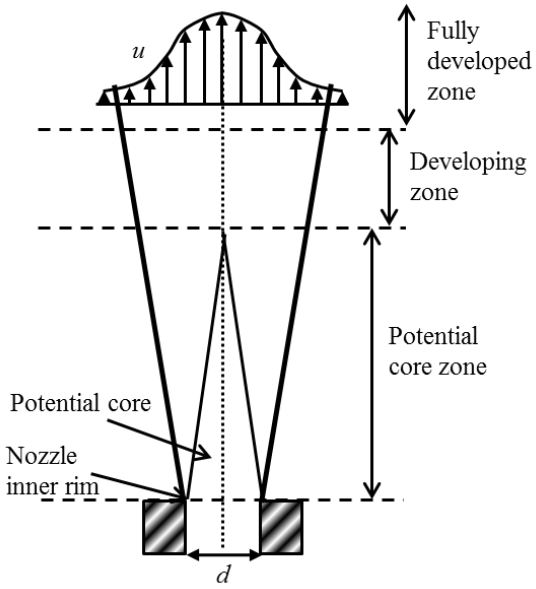

Figure 2.8: Structure of a free non-reacting jet (adapted from [11]). The symbols *d* and *u* are the nozzle diameter and developed velocity profile respectively.

Impinging Non-Reacting Jet

Impinging flame jet aerodynamics are very similar to those of impinging non-reacting jets [11]. Viskanta [11] has described the structure of impinging jets as follows: In an impinging jet, there are three distinct regions; the *free jet region*, *stagnation region* and *wall jet region* (Fig. 2.9). In the free jet region, the fuel initially exits the nozzle in a near-uniform velocity, *v*, before mixing with the ambient air in the *shear layer*, causing entrainment of mass, momentum and energy. The amount of entrainment depends upon

the velocity and turbulence within the flow. This entrainment causes an increase in mass flow, due to the increase in air amount within the flow, non-uniform velocity distribution, a change in jet temperature and an increase in the width of the jet, as for the free jet [11]. The stagnation region is where the jet changes direction upon coming into contact with the plate, and at the stagnation point, the velocity is zero due to the gas flowing in opposite directions away from the stagnation point. Following this is the transition to the wall jet region, which is a bulk flow radially outward, away from the stagnation region (Fig. 2.9) [11].

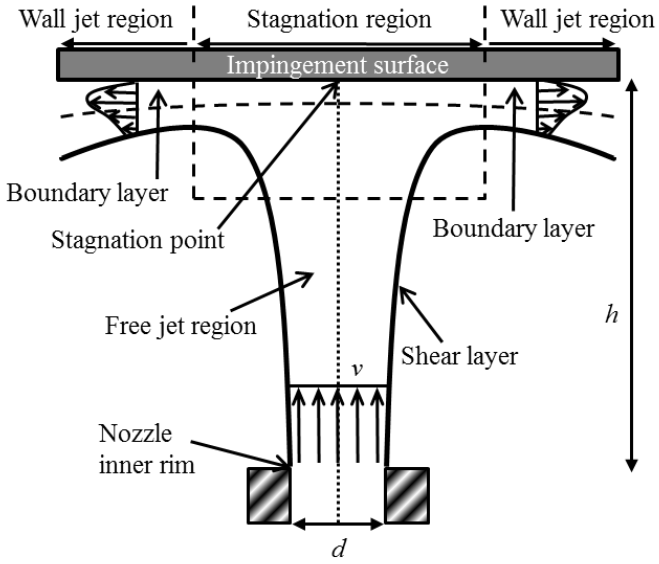

Figure 2.9: Structure of impinging isothermal jet (adapted from [11]). The symbols *d*, *h*, and *v* are the nozzle diameter, nozzle-to-plate distance and nozzle exit velocity respectively.

Impinging Reacting Jet

However, for impinging flame jets, the reaction zones and temperature gradients cause the structure to be different than for impinging isothermal jets [11]. In particular, there exists an intense reaction zone slightly away from the stagnation point, and for low enough nozzle-to-plate distances/nozzle diameters (*h*/*d*) there is a cool central core consisting of unburned gases, causing the stagnation point temperature to be lower than the temperature just away from the stagnation point (Fig. 2.10). Also, the air entrainment that causes jet widening in non-reacting jets causes the local equivalence ratio to become lower with widening jet diameter due to air entrainment.

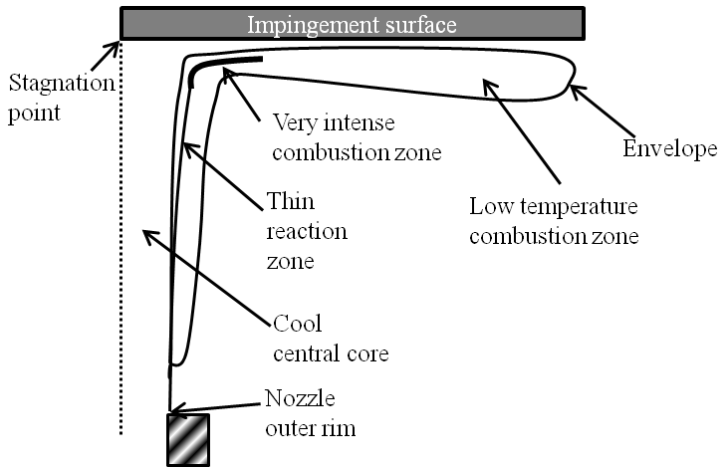

Figure 2.10: Diagram showing reaction zones and cool central core for typical methane-air flame, Re = 7000, $\phi = 2$, $h/d = 10$ (adapted from [11]).

In addition to the intense combustion zones, various impinging flame modes can be observed, being stabilised either on the nozzle rim or the plate, depending on the flow conditions, nozzle exit velocity, nozzle-to-plate distance and place of ignition [34, 80]. These include the ring flame, conic flame, disc flame, envelope flame and cool central core flame (Figs. 2.11a to e respectively) [80]. In addition, blown ring, detached conic and complex flames can be observed [34]. The ring flame, blown ring flame and disc flame are stabilised by the impingement plate and are detached from the nozzle, due to the high flow velocity. The ring flame has a core of unburned gases but the disc flame has burning at the stagnation point. The blown ring flame occurs at higher jet velocities than the ring flame and cannot be ignited in the centre, whereas the ring flame can be ignited at the centre to form a disc flame. The conical flame has a low axial velocity near the plate due to the large nozzle-to-plate distance, and the detached conic flame exists at fuel rich conditions, is lifted from the nozzle and can be formed from a disc flame. The cool central core flame has unburned fuel impinging on the stagnation point due to the low nozzle-to-plate distance, but the envelope flame, formed with less rich mixtures, has combustion occurring at the stagnation point. Both the envelope and cool central core flames have cellular structures that need high shutter speeds to be observed. The complex flame is made up of different types of flame and occurs in fuel rich mixtures and at large *h/d*.

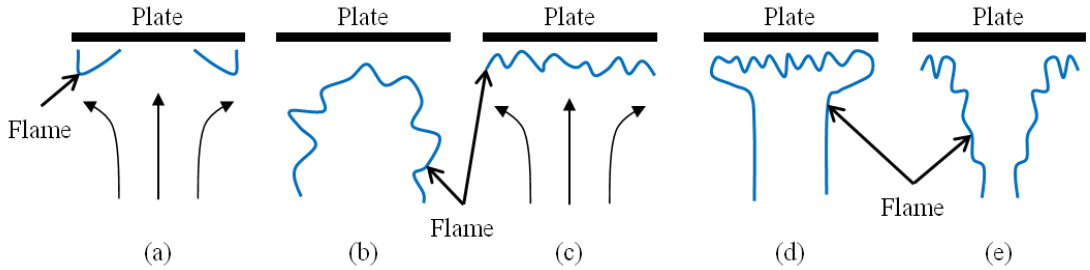

Figure 2.11: Flame modes: (a) Ring flame, (b) Conic flame, (c) Disc flame, (d) Envelope flame and (e) Cool central core flame (adapted from [80]).

The various flame modes and flow structures will greatly affect the heat transfer to the impingement plate, due to whether unburned fuel, flame or hot combustion products are impinging on the plate. The turbulence, gas velocity and flame temperature will also affect the heat transfer, along with the mechanisms by which heat is transferred to the plate. The heat transfer mechanisms relevant to impinging flame studies will be discussed in the next section.

2.2.2.2. Heat Transfer Mechanisms

An important area of study in impinging flames, along with the flame structure, is the heat transfer between the flame and the plate. This section deals with the mechanisms whereby heat can be transferred to and from the impingement surface and with the importance of each mechanism in heat transfer impingement studies. Heat can be transferred to and from impingement surfaces via *conduction*, *forced* or *natural convection*, *radiation* and *thermochemical heat release* (TCHR).

Conduction

Conduction heat transfer is the transfer of heat energy resulting from interaction between particles, and so occurs when substances of different temperatures are in contact with one another. For fluids, it is described by the net transfer of thermal energy by random molecular motion [81] and always moves from states of higher to lower energy, i.e. hotter to colder substances. *Heat flux* (which is the rate of heat energy transfer) due to conduction, $\vec{q}_{cd}$ (units W m^{-2}), is proportional to the temperature gradient, ∇T, and the thermal conductivity, k, of the material, and can be represented by Eq. 2.20 [81]:

$$\vec{q}_{cd} = -k\nabla T \,. \tag{2.20}$$

In impinging flames, conductive heat transfer occurs when the flame is in direct contact with the surface, thereby heating the surface and also removing heat from the flame if the surface is cold. However, in general there exists a layer of hot gases between the flame and the plate, causing the heat conduction to the plate to be minimal. The main mechanism of conduction is generally through the impingement surface, whereas a large amount of heat may be transferred to the plate from the gases via convection.

Convection

Convection is the motion of fluid particles across a surface or within an enclosure. When fluid particles are heated up, they will become less dense and will rise above the surrounding particles, creating *convection currents*. Heat transfer by convection can be either forced or natural. Natural convection is caused by the heat/mass transfer itself. Natural convection will be present on the top side of a flame impinged plate, if it is not insulated, caused by the high temperature plate heating the ambient air and producing convection currents. Buoyancy induced natural convection on the underside of the plate may increase or decrease the heat transfer to the plate depending on plate location with respect to the flame structure [82]. Forced convection is that for which the motion of the fluid is caused by something other than the heat/mass transfer, for example by a fan or pump [81, 83]. So, for example, in an impinging flame configuration, there exists forced convection of the gas on the wall, due to the motion of the gas from the nozzle. *Mixed convection* occurs when both natural and forced convection are present, for example, a high temperature material cools by natural convection due to the temperature gradient between it and cooler surrounding air, but would also cool by forced convection if a fan was blowing cool air over the surface. Convective heat flux is given by Newton's law of cooling (Eq. 2.21) [81]:

$$\vec{q}_{cv} = -h_c \left(T_w - T_\infty\right), \tag{2.21}$$

where $\vec{q}_{cv}$ is the convective heat flux (units W m^{-2}), h_c is the convective heat transfer coefficient (units W m^{-2} K^{-1}), T_w is the temperature of the surface and T_∞ is the temperature of the surrounding fluid.

For turbulent flow past a solid boundary, contained in the boundary layer (Fig. 2.9) and very close to the wall, there is a *laminar sublayer*; where the flow slows down due to resistance from the wall. In the laminar sublayer, macroscopic fluid motion no longer contributes to the heat transfer, and the heat is only transferred by molecular conduction [81]. The laminar boundary layer resists the heat transfer depending upon the fluid and the thickness; for thicker boundary layers, the heat transfer will be lower. The more turbulent the flow, the smaller the boundary layer, and so turbulence increases the conductive heat transfer to a solid surface [81]. Forced convection contributes to a large amount of the heat transfer from flames to impingement surfaces, particularly in relation to the radiation effects [59, 84-86], and in modern furnaces (with direct flame impingement) it can account for 70 - 90 % of the total heat transferred [85, 87], and higher temperature flames will produce higher forced convection heat transfer rates [88].

Nusselt Number

The Nusselt number represents heat exchange between a fluid and surface, and is defined by Eq. 2.22, combining conductive and convective heat transfer (Eqs. 2.20 and 2.21 respectively):

$$\mathrm{Nu} = \frac{h_c L}{k}, \tag{2.22}$$

where Nu is the Nusselt number, h_c is the convective heat transfer coefficient, L is a characteristic length scale and k is the thermal conductivity of the fluid [76, 89]. However, Eq. 2.22 applies only if the surface temperature is constant, and so is often used for isothermal boundaries/flows [90-92]. The local Nusselt number can be applied to problems with constant surface heat flux [93-95] using Eq. 2.23:

$$\mathrm{Nu} = \frac{qL}{k(T_w - T_\infty)}, \tag{2.23}$$

where q is the surface heat flux, T_w is the surface temperature and T_∞ is the fluid temperature [76, 89]. For impinging jets, the stagnation point heat transfer is often characterised by the local Nusselt number at the stagnation point, using local radial velocity gradients or local heat flux measurements to calculate the Nusselt number [96-98]. The radial velocity in the stagnation region of low Re turbulent flames is significant

to the stagnation point heat transfer [96, 98]. However, large uncertainties arise from heat flux measurements in impinging jets (up to 6 %) and flame temperature measurements in impinging flames (up to 10 %) [96-98]. The Nusselt number is more commonly used in impinging air jet studies [99, 100].

Radiation

Heat can also be transferred to the impingement surface via radiation from the flame. In particular, if the flame is luminous, i.e. a sooty, yellow flame, then heat will radiate from the soot particles via approximate *black body radiation* [101]. A black body is a perfect absorber/emitter of electromagnetic radiation. Black body radiation is an idealised concept but objects may be approximated as black bodies if they emit/absorb nearly all electromagnetic radiation. A common visualisation of a black body is a cavity with a small hole (Fig. 2.12). When light is shone on the hole, many internal reflections will take place, but the probability of the light escaping through the small hole is very low. Therefore, the object absorbs nearly all of the light that is incident upon it. In terms of thermal radiation, the radiation emitted by black bodies is dependent solely upon the temperature of the body, due to the electromagnetic radiation emitted from the charged particles in the object. The thermal *emissivity* of a material is defined as the ratio of thermal energy emitted by the material to that emitted by a black body at the same temperature.

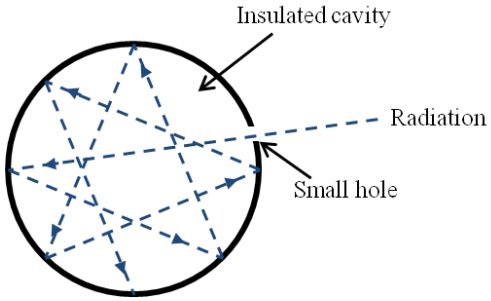

Figure 2.12: Visualisation of black body radiation using a cavity with a small hole.

The soot in flames can be approximated as black body particles and therefore radiate heat from the flame dependent on their temperature. For non-luminous flames, such as hydrogen flames or premixed hydrocarbon flames, the radiation from the flame is minimal, due to the lack of soot particles, although radiation can still be transferred from CO_2 and H_2O particles in the products [101]. When the soot deposition on the

plate is small, due to the non-luminosity of the flames, the effects of heat transfer to the impingement surface due to radiation from the flame can generally be neglected [84]. However, thermal radiation may also be emitted from the plate to the flame and, if it reaches high enough temperatures, could possibly increase the temperature of the flame and facilitate combustion. The higher the emissivity of the plate, the more radiation will be emitted from it at a particular temperature. If the configuration is enclosed, for example in a furnace, then the radiation heat transfer to the flame from the surroundings will be significant.

In addition, heat may be radiated away from an impingement surface if not cooled. The radiative heat transfer from a solid circular surface can be calculated using Eq. 2.24. It is highly dependent on the surface temperature (T^4 dependence) and so temperature measurements must be accurate in order to achieve accurate radiation calculations from Eq. 2.24.

$$\dot{Q}_{\text{rad}} = \int_0^{r_p} 2\pi r \sigma \varepsilon(r)\left(T(r)_w^4 - T_\infty^4\right)\mathrm{d}r, \tag{2.24}$$

where $\dot{Q}_{rad}$ is the radiative heat loss (units W), r_p is the total radius of the surface/plate, r is the variable radius of the plate, σ is the Stefan-Boltzmann constant, equal to 5.67 x 10^{-8} W m^{-2} K^{-4}, $\varepsilon(r)$ is the emissivity at radius r, $T(r)_w$ is the temperature of the surface at radius r and T_∞ is the ambient temperature.

Thermochemical Heat Release

Heat can also be transferred to the plate by thermochemical heat release, otherwise known as *convection vive*. This occurs in high temperature flames when radicals in the flame, which have not been converted into final products due to chemical equilibrium, impinge on the cool surface of the wall and consequently recombine with other dissociated products to form more thermodynamically stable species [85, 102, 103]. The recombination process is exothermic and so the reactions heat the wall surface further. Above temperatures of 1600 K radicals (such as CO and H_2) are preferred but when the temperatures are below 1600 K products (such as CO_2 and H_2O) are preferred [101]. TCHR is mainly significant to the heat transfer for those flames burned with oxygen or oxygen enriched air due to the high temperatures of these flames [102].

2.2.3. Conclusions

Various combustion properties have been defined and a background to combustion has been given, with particular regards to flame jet structure, premixing, turbulence, ignition and heat transfer characteristics. The conditions needed to support combustion, along with flow and combustion properties of jet flames have been described and the structure and heat transfer mechanisms relating to impinging flames have been discussed. It has been shown that flow and fuel properties are important in flame jet impingement studies. Premixing and turbulence are significant properties of jet flames and affect both flame structure and heat transfer characteristics. A more detailed review of impinging flame studies will be given in Section 2.4.

These characteristics are studied widely for combusting flows using various experimental diagnostic and visualisation techniques. The next section gives a comprehensive review of these techniques in order to highlight the advantages of each technique and how they can be utilised in combustion and impinging flame studies. Following this, a detailed review of the literature relevant to impinging flames, including a discussion of how the aforementioned techniques may be utilised and improved in impinging flame configurations, will be given, as this is the focus of this thesis.

2.3. Experimental Diagnostic Techniques

2.3.1. Introduction

The development of imaging techniques is integral to advances in combustion experimentation. In particular digital and high speed imaging, lasers and thermal imaging techniques have made it possible to study combustion in greater detail.

Digital Imaging

The use of digital cameras has led to increased experimental power, partly due to a reduction in the time it takes to process images. With digital cameras, the images can be viewed, stored and processed immediately, so that any mistakes can be quickly resolved and viewing angle, exposure and frame rate issues can be dealt with immediately. Camera quality is constantly increasing so that better spatial resolution is available. This allows smaller features to be studied with greater accuracy. The development of Charge

Coupled Device (CCD) chips has been important to the development of digital cameras, and are used for many scientific purposes due to the high sensitivity, good responsiveness, low noise and large dynamic range [104]. A CCD chip consists of an array of light-sensitive capacitors that store charge depending on the amount of light incident on each cell (or pixel), using electron-hole pairs (see Section 2.3.2.1.2) [104, 105]. A colour filter or prism is used to separate the red, green and blue signals in each cell so that colour images can be processed. The spatial resolution of the CCD device depends on the numbers of pixels, and high resolution digital cameras are widely in use [105].

High Speed Imaging

High speed cameras record images at a high frame rate so that the images can be played back in slow motion, giving a high temporal resolution and allowing detail to be seen that would otherwise happen too quickly. Early high speed imaging in the 1870s utilised a sequence of still frame cameras, which progressed to using film strips capturing up to 200 frames per second (fps) in the 1970s and up to 2000 fps in the 1980s [106]. Digital imaging devices with CCD chips and complementary metal–oxide–semiconductor (CMOS) sensors are used today, saving on materials such as film and offering advantages such as quick start up time, immediate playback and quick triggering capability [106]. CCD cameras can record frame rates up to 1000 fps and CMOS cameras over 650,000 fps at reduced resolution [107, 108]. High speed cameras are constantly being developed to record at higher and higher frame rates.

In combustion, high speed cameras can be used to visualise rapid fluid motion and flame structures [34, 109-112]. Flickering frequencies can be observed [113] and detailed information can be gained about flame structures. High speed cameras can be used with a triggering device that can record data before the trigger is pressed, so that spontaneous events can be recorded without using up lots of memory in anticipation of the event. This allows ignition and explosion characteristics to be recorded easily at high speed [112, 114-116]. (A more detailed review of ignition and flame propagation studies will be given in Sections 2.2.1.3 and 2.5). High speed cameras in combustion are often combined with other techniques such as schlieren and Particle Image Velocimetry (PIV) (which will be described in more detail in Section 2.3.3) to obtain better temporal resolution with these techniques.

Lasers

The use of lasers in combustion has been integral in determining velocity fields, turbulent structures, vorticity fields, species concentration and flame structure. Before lasers, probes were used in combustion studies for measuring velocity, temperature and species concentration [117]. Lasers and other flow visualisation techniques, unlike probing techniques, have made it possible to obtain quantitative information about two-dimensional (2D) flow fields in one set of images and without disturbing the flow [118], and the understanding of turbulent flows has greatly improved since the introduction of these techniques. In addition, laser based methods tend to have very good spatial and temporal resolution (~ 10-50 μm and < 10 ns respectively) [119]. Lasers are used for many applications in combustion, including using PIV to study turbulence and vorticity [120-123] and combustion flow velocity fields [51, 122, 124, 125]. Flame front positions can be studied using Planar Laser Induced Florescence (PLIF); where a laser is used to excite molecules, usually OH or CH radicals, in the flow into a higher energy state. These radicals will then re-emit the radiation, via fluorescence, which can be detected [119]. The radiation emitted depends on the species and in this way, the flame front position can be determined; OH radicals are prominent in the burned gas, showing the flame front, but for more turbulent flames, the flame front becomes distorted and so it is better to use CH radicals, which are produced in the flame front and represent the reaction zone [123]. PLIF is often combined with PIV studies to simultaneously measure flame characteristics, in particular the flame front position, and velocity fields [51, 54, 126].

Thermal Imaging

Advances in optics have also led to the use of thermal imaging cameras (which will be discussed in greater detail in Section 2.3.2.1) for surface temperature measurements. Surface temperature measurements are important for heat transfer and flame wall interaction studies, as well as for finding hot-spots or regions of low temperature to prevent damage and/or flame quenching. Previously, thermocouples were mainly used to measure wall temperature, requiring drilling into the surface to install the thermocouples and only giving single-point temperature measurements. Thermal imaging allows 2D, non-intrusive temperature measurements and can also be used to measure a material's emissivity (discussed in Sections 2.2.2.2, 2.3.2.1.1 and 2.4.8) if the

temperature is known. However, in general, thermal imaging cannot be used to investigate flame temperature due to the large spectral range of emissions from the flame, and has not been used widely in combustion studies. Thermal imaging techniques will be utilised and developed in this thesis to measure the temperature distributions of flame impinged walls.

A review of these techniques will be given in this section with particular relevance to impinging flames. The section will explore the main principles and science behind each technique. Firstly, the techniques used to measure heat transfer will be discussed. Following this, the techniques used to measure flow structure and flow properties will be looked into.

2.3.2. Heat Transfer

In order to evaluate flame wall interactions, the heat transfer to the wall must be studied. Heat transfer to and from a surface depends highly on the temperature of that surface. Therefore, this section deals with ways to accurately measure the temperature of flame impinged walls in order to evaluate the flame wall interactions.

2.3.2.1. Thermal Imaging

Thermal imaging takes advantage of the thermal radiation emitted by objects depending on their temperature. However, various factors affect the emission of radiation from these objects as will be examined in this section.

2.3.2.1.1. Thermal Radiation

Electromagnetic spectrum

All objects emit thermal radiation depending on their thermal energy. Thermal radiation is radiation in the infrared (IR) range of the electromagnetic spectrum, but can also include radiation from the visible and ultra-violet ranges, and lies in the intermediate range of the electromagnetic spectrum; 0.1 to 1000 μm [127]. Figure 2.13 shows the wavelength ranges for the IR section of the electromagnetic spectrum, displaying the short, medium and long wave bands [128] and the *near* and *far infrared* bands [127].

Thermal radiation is transmitted from objects, without requiring any intermediate matter, due to the temperature of the object [129]. The higher the temperature of the object, the shorter the wavelength of the radiation, with objects above the *Draper point*

of 798 K [127] emitting radiation in the visible spectrum, visualised as red, blue and then white light and known as *incandescence*. This means that the temperature of an object may be determined by the wavelength of radiation emitted from it. However, various factors affect thermal radiation from a surface, including temperature, emissivity, viewing angle and reflection and transmission properties of the surface. If these properties depend on the wavelength of the radiation then they are called *spectral* properties. In addition, the emissivity (defined in Section 2.2.2.2) of a particular surface may also depend on the surface temperature, viewing angle and radiation wavelength. Surface properties that affect the emission of thermal radiation will now be discussed.

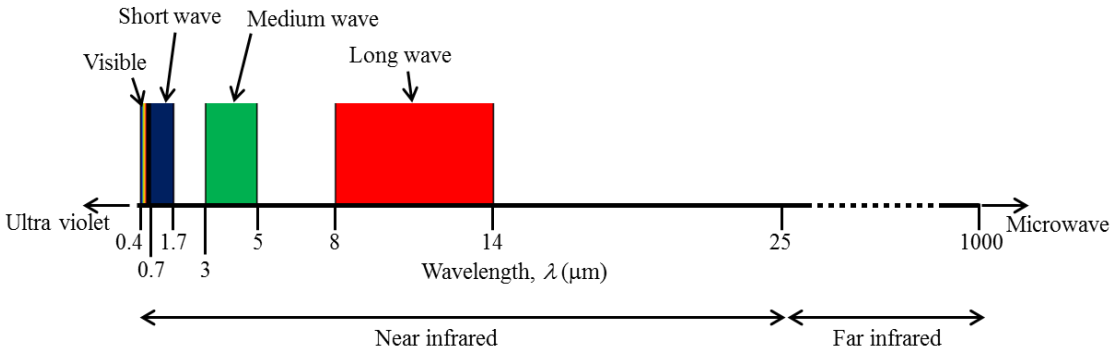

Figure 2.13: Thermal radiation part of the electromagnetic spectrum.

Temperature Dependent Emissivity

Many surfaces have an emissivity that changes with temperature. For these surfaces, infrared absorption bands (*Reststrahlen bands*), which are narrow energy bands through which electromagnetic radiation cannot propagate, tend to increase in width and decrease in strength with an increase in temperature. Also, the wavelength of peak absorption shifts towards higher values. This generally increases the emissivity in the near infrared and decreases it for shorter wavelengths [130]. A method for dealing with the problems encountered in measuring the temperature of a surface whose emissivity depends on that temperature will be explored in this thesis, using a quartz plate, and more detail will be given in Chapter 3.

Spectral Emissivity

Surfaces with spectral emissivity have different emissivities depending on the wavelength being observed, and are called *selective emitters*. If these emissivities are averaged over all wavelengths, this is called *total emissivity*. A *grey body* is one whose

emissivity does not depend on wavelength, but is lower than that of a black body. Figure 2.14 shows examples of spectral emissivity curves for a black body, grey body and selective emitter.

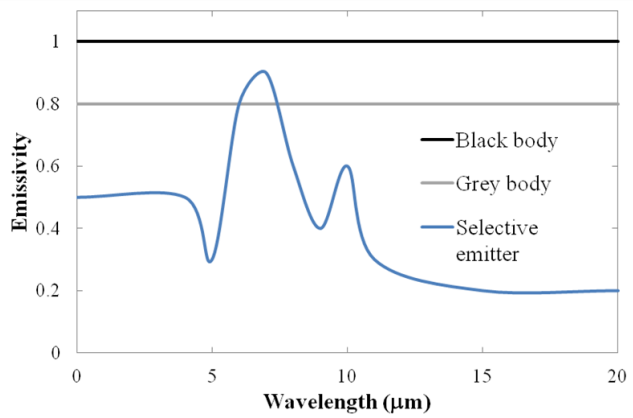

Figure 2.14: Graph to show examples of spectral emissivity for a black body, grey body, and selective emitter (adapted from [128]).

Directional Emissivity

Surfaces may also have varying emissivity depending on the viewing angle. A *diffuse emitter* is one that emits radiation uniformly in all directions. *Directional* emissivity is the emissivity in a chosen direction, and emissivity averaged over all directions is called the *hemispherical emissivity* [127]. A black body is a diffuse emitter but, in general, real surfaces have emissivity depending on the viewing angle, θ (Fig. 2.15). For non-conductors, the directional emissivity is generally constant for angles up to 70° to the normal, and for conductors up to 40° (Fig. 2.16) [131, 132]. The hemispherical emissivity may also be represented by the emissivity normal to the surface ($\theta = 0$) [131].

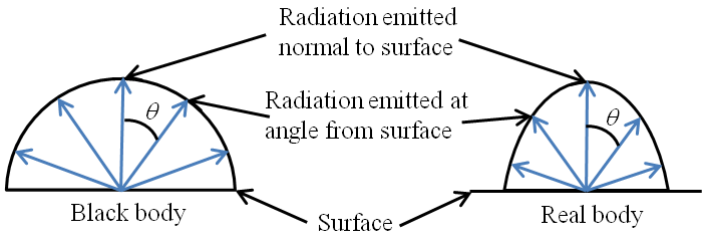

Figure 2.15: Directional dependence of radiation emitted by a diffuse emitter (black body) and a real surface, (length of arrows represents radiation intensity and θ is the angle from the normal).

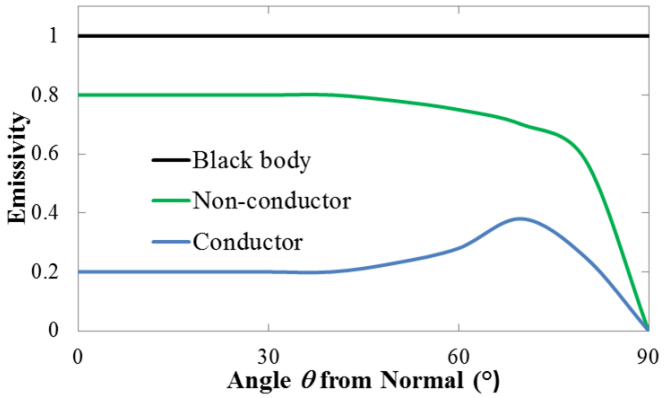

Figure 2.16: Examples of emissivity dependence on viewing angle for a black body, non-conductor and conductor (adapted from [128, 131]).

Reflection, Absorption and Transmission

As well as emitting thermal radiation due to its temperature, an object will also reflect, absorb and/or transmit incident radiation (Fig. 2.17). Most solid objects are *opaque* to (do not transmit) thermal radiation. The *absorptivity* of a material is related to the emissivity by *Kirchhoff's law* (Eq. 2.25) [127]:

$$\varepsilon_{\lambda}^{\mathrm{d}}(\lambda, \theta_{\mathrm{cone}}, \theta_{\mathrm{circ}}, T) = \alpha_{\lambda}^{\mathrm{d}}(\lambda, \theta_{\mathrm{cone}}, \theta_{\mathrm{circ}}, T), \tag{2.25}$$

where $\varepsilon_{\lambda}^{d}$ and α_{λ}^{d} are the spectral, directional emissivity and absorptivity respectively, λ is the wavelength, θ_{cone} and θ_{circ} are the cone and circumference angles respectively and T is the surface temperature. This means that the absorptivity of radiation at wavelength λ from a particular direction from a black body at the same temperature will be the same as the emissivity of that surface.

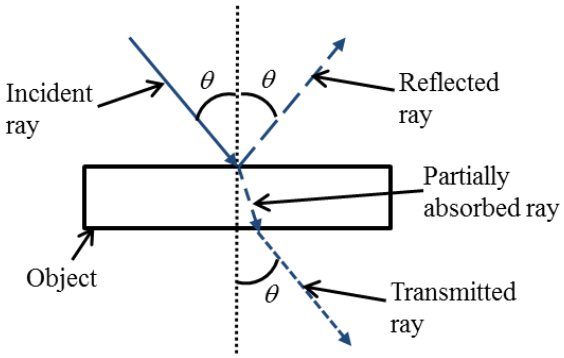

Figure 2.17: Diagram showing the reflection, absorption and transmission of incident radiation through a semi-transparent, reflective object.

The reflectivity of a surface generally depends on the roughness of that surface. Smooth surfaces are called *specular*; they reflect incident radiation in one direction, at an angle equal to the angle of incidence, θ (Fig. 2.18a). For example a mirror is a specular reflector. Lambertian reflectors reflect radiation according to Lambert's cosine law; the intensity of reflected radiation is proportional to the cosine of the viewing angle with the normal of the surface (Fig. 2.18c). Most surfaces exhibit a combination of both specular and diffuse reflection (Fig. 2.18b) [128].

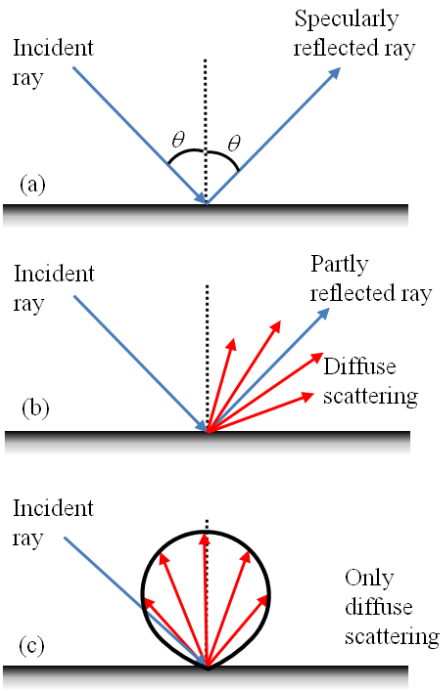

Figure 2.18: Reflection characteristics for (a) A very smooth reflecting surface, (b) A reflecting surface with partial roughness and (c) A Lambertian (rough) surface (adapted from [128]).

The mechanisms and applications of thermal imaging cameras will now be discussed. Emissivity and reflection, and their spectral and directional dependence, of surfaces must be taken into consideration when using thermal imaging cameras to measure surface temperature and this will be discussed in more detail in Chapter 3.

2.3.2.1.2. Thermal Imaging Cameras

Thermal imaging cameras are able to detect portions of thermal radiation and convert the information into a *thermogram*; a visual image of the temperature distribution of the object based on the wavelength of the detected radiation. In principle, a thermal imaging

detector works much in the same way as a typical digital camera in that it consists of a number of cells that interact with incoming radiation, creating an electric current that is converted into an image relative to the wavelengths of the radiation at each pixel. There are different types of thermal imaging detectors; the main distinction being whether the detector is cooled or uncooled.

Cooled Detectors

Cooled detectors use *semiconductors*; materials that have very low conductivity and whose electrical resistivity falls with increasing temperature, to detect thermal radiation. The *internal photoelectric effect* occurs in semiconductors; incoming photons above the required threshold energy, ΔE, to excite an electron from the valence band (bound to the atoms) to the conduction band (free to move within the semi-conductor) are absorbed, creating electron and electron hole pairs (Fig. 2.19). This changes the free carrier concentration, that is the concentration of electrons free to move in the semi-conductor, which causes a change in the electronic energy distribution, which can be converted into the thermal image [128].

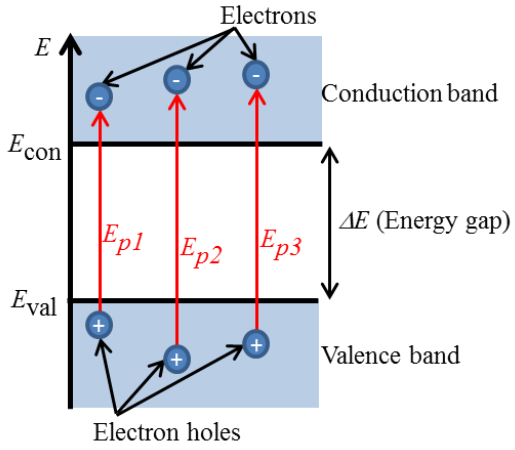

Figure 2.19: Internal photoelectric effect; photons (with energies E_{p1}, E_{p2} and $E_{p3} > \Delta E$) excite electrons from the valence band ($E < E_{val}$) to the conduction band ($E > E_{con}$) creating electron holes (adapted from [128]).

Due to the quantum nature of the internal photoelectric effect, the detectors are only sensitive below a certain cut-off wavelength, proportional to the inverse of the threshold energy (Eq. 2.26) [128]:

$$\lambda_{\text{cut}} = \frac{h_p c}{\Delta E}, \tag{2.26}$$

where λ_{cut} is the cut-off wavelength, h_p is Planck's constant, c is the speed of light and ΔE is the threshold energy. This means that the detectors will not detect thermal radiation above the cut-off wavelength. ΔE can be altered by changing the semiconductor alloy material and can be varied by using an alloy with varying composition [133]. Atmospheric transmission of IR radiation is highest in the medium wave infrared (MWIR) and long wave infrared (LWIR) bands (3-5 μm and 8-14 μm respectively), with the maximum emissivity of objects at 300 K being at 10 μm [134].

The detectors must be cooled to avoid noise from the semiconductors themselves; the thermally excited free charge carrier concentration in semiconductors is much higher than the increased concentration caused by the radiation excitation. Therefore, the background noise from the semiconductor itself would drown out that of the thermal radiation being measured. However, cooling the semiconductor reduces the noise significantly. Detectors operating in LWIR bands are Stirling cooled to 77 K, but with increasing cut-off wavelengths, the cooling temperature needs to be lower [128]. This means that the cameras have a cooling down period before they can be operated.

The Forward Looking Infrared (FLIR) SC3000 thermal imaging camera used in this thesis has a self-cooling detector, with a cooling down time of less than 6 minutes [135]. It uses *Quantum Well Infrared Photodetector* (QWIP) technology, so that longer wavelength radiation can be detected with larger energy band gap materials, which are easier to produce than small band gap materials. Figure 2.20 shows the bands in a quantum well; ground state electrons (E_{e1}) or holes (E_{h1}) in the conduction or valence bands respectively are excited into higher energy states (E_{e2} and E_{h2} respectively) in the same band, without crossing the energy gap [133]. The QWIP can then be designed so that the charge carrier can escape from the quantum well and be detected. The quantum well allows the absorption spectrum to be altered and allows for easier production with high accuracy, large area and low cost arrays. The SC3000 also has very high thermal sensitivity along with accurate temperature measurements up to 2298 K in the 8-9 μm spectral range [136].

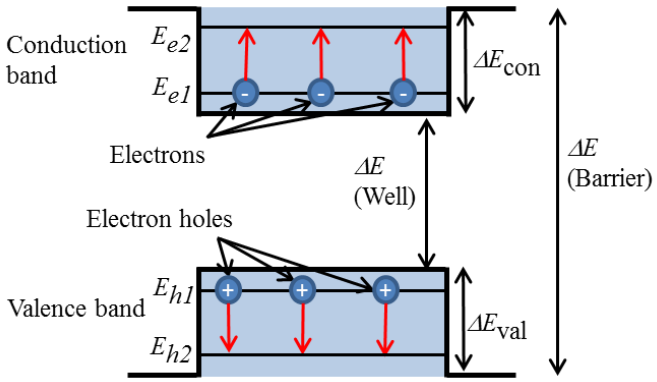

Figure 2.20: Band structure in a quantum well (adapted from [133]).

Uncooled Detectors

Microbolometer devices have been used in thermal imaging since the 1990s in order to avoid the bulky and expensive cooling systems required in the semiconductor device thermal imaging cameras [128]. A bolometer is a sensor that detects thermal radiation using the change in electrical conductivity that results from a temperature increase in the sensor [137]. A microbolometer consists of an IR absorbing plate with a thin film resistor. An electrical bias voltage is applied across the resistor so that as the incident IR radiation varies, so does the electric current [138]. Figure 2.21 shows a schematic of a typical microbolometer pixel. It consists of a square plate of electrically insulating silicon which is held above semiconducting silicon nitrate by thin silicon nitrate legs. The silicon nitrate contains electrical readout circuits. A thin conducting film is placed over the silicon nitrate plate and the legs to carry metal film conductors between the plate and substrate, while minimising the thermal contact. A thin reflecting metal film is placed on the substrate to enhance the IR absorption [138]. Although not as thermally sensitive as the QWIP devices discussed above, the microbolometer devices allow good sensitivity for practical applications without the need for expensive, bulky cooling systems, and the silicon technology allows for inexpensive production costs [138]. The FLIR SC640 used in this thesis uses an uncooled microbolometer array.

The next section will discuss typical applications of thermal imaging cameras and limitations faced in combustion and impinging flame studies.

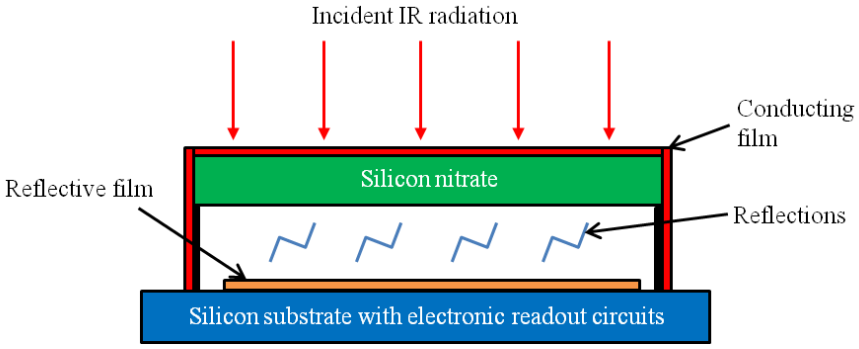

Figure 2.21: Schematic of a silicon based microbolometer.

2.3.2.1.3. Applications and Limitations

Thermal imaging cameras have been used in many practices, including military use, medical systems, climatology, law enforcement and fire services [139-142]. They can be used for testing the thermal efficiency of heating/cooling devices, and for finding hot spots in electrical systems. Thermal imaging can also provide a way for constant monitoring of time dependent temperature in various systems so that changes or component failure can be tracked [143, 144]. Thermal imaging provides a non-intrusive temperature measurement system that can view 2D areas. It can also be used to test the emissivity of materials provided the temperature is known.

In combustion research, thermal imaging can be used to test the time dependent wall temperature on the outside of furnaces or ducts for example, at various sizes including mesoscale [145-147], and for finding hot spots or cool areas where damage or flame quenching respectively may occur, in order to increase efficiency and prevent damage. Thermal imaging has also been used to test the temperature of air jet impinged walls [148, 149] and of the impinged side of flame impinged walls [150]. However, thermal imaging cameras cannot be used to accurately measure flame temperature due to the high spectral range of emissions from flames, although thin filament pyrometry; where the radiation from a thin filament placed in the flame can be detected for temperature measurements, and flame structure can be visualised with thermal imaging cameras [151, 152].

Problems also occur due to the need for accurate emissivity input values and the problems related to the dependence of the emissivity on temperature and viewing angle. As such, thermal imaging cameras are not widely used in combustion systems due to the

large ranges and variable temperatures of surfaces, and the many types of surfaces involved. However, thermal imaging has been used to measure wall boundary conditions for validation with computer simulations [153].

Therefore, this thesis explores solutions to these problems in order that thermal imaging may be used more widely in impinging flame configurations, to allow plate temperature distributions to be more easily visualised and quantitatively analysed. This thesis deals with measuring the temperature of flame impinged walls using a flame switch off method, developed from [150]. Thermal imaging will be used to measure temperature distributions of flame impinged walls and to calculate radiation heat loss using Eq. 2.24 (p. 30). An iterative method is also proposed to deal with temperature measurements of surfaces with temperature dependent emissivity. The methodologies will be discussed further in Chapter 3. Many impinging flame studies use thermocouples to measure wall temperature, which will be described in the next section.

2.3.2.2. Thermocouples

Principles

Thermocouples have been used since early developments of thermodynamics in the 19th Century [154]. Thermocouples work on the basis that when junctions of two different conducting metals of different temperature are placed together, an electric current will flow between them, known as the *Seebeck electromotive force (emf)* [155]. In this way, thermal energy is converted to electrical energy. If the Seebeck coefficient of the conducting metals is known, and one of the junctions is kept at a reference temperature, then the temperature of the other junction may be calculated, using the voltage produced (Eq. 2.27) [154]:

$$\mathrm{d}E_s = \alpha_{A,B}\,\mathrm{d}T\,, \tag{2.27}$$

where E_s is the Seebeck voltage, $\alpha_{A,B}$ is the Seebeck coefficient (depending only on the materials used), and T is the temperature. So the temperature difference between the two metals is directly proportional to the voltage produced. If the reference temperature is known, then the temperature of the 'hot' point can be calculated. Figure 2.22 shows a schematic of a thermocouple. An extension wire, usually copper, can be used at the reference temperature side as it is cheaper to use and as long as the temperatures at

either end of the copper wire are the same, it will not affect the emf produced by the temperature difference in the other metals. Common types of thermocouple materials are shown in Table 2.4. The K-type is the most commonly used in practical systems.

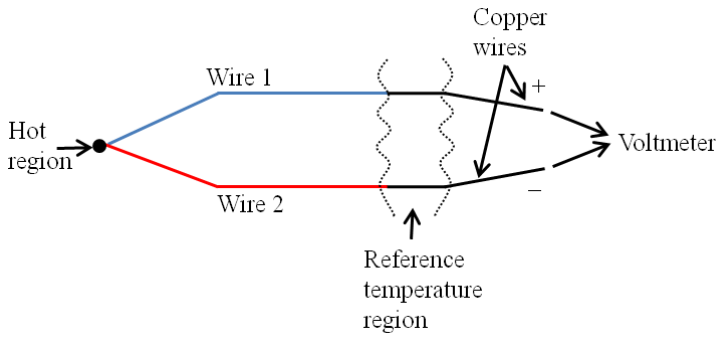

Figure 2.22: Schematic of a typical thermocouple.

Thermocouple Type	Wire 1 (Positive Charge)	Wire 2 (Negative Charge)
B	70% Platinum, 30 % rhodium.	94 % Platinum, 6 % rhodium.
E	90 % Nickel, 10 % chromium.	Constantan.
J	Iron.	Constantan.
K	90 % Nickel, 10 % chromium.	95 % Nickel, 5 % silicon/aluminium.
R	87 % Platinum, 13 % rhodium.	Platinum.
S	90 % Platinum, 10 % rhodium.	Platinum.
T	Copper.	Constantan.

Table 2.4: Materials for various thermocouple types [154].

Applications and Limitations

Thermocouples need to be in direct contact with the material in order to measure its temperature. Therefore drilling holes in the materials, in order to have the thermocouple flush with the surface, is often necessary to get an accurate reading of the temperature. Also, the presence of the thermocouple may affect the surface temperature. If the wires are placed in hot air for example, this may also affect the emf and so it is necessary to have insulated wires. However, if the thermocouple has good contact with the surface and causes minimal effect to the surface temperature, then thermocouples can be a good

and accurate way to measure spot temperatures. Thermocouples will not be used in this thesis due to time restraints, the necessity for drilling and the problems associated with insulating the thermocouples against the high temperatures of the flames, and so that the thermocouples do not interfere with the thermal imaging measurements, which are a main focus of the thesis.

Thermal imaging will be used to measure the surface temperature of flame impinged walls in order to evaluate the flame wall interaction. In addition, flow visualisation techniques can significantly aid the understanding of the flame wall interaction and will be used alongside the wall temperature measurements. Flow visualisation techniques will now be discussed.

2.3.3. Flow Visualisation

In order to evaluate the physical mechanisms related to the heat transfer and flame wall interaction, the flow structure must be visualised. This section deals with various methods that may be used to visualise and diagnose flame and flow structures of impinging flames.

2.3.3.1. Schlieren

Schlieren (from the German for streaks) is an experimental technique used to visualise density gradients in inhomogeneous, transparent materials; that is materials that exhibit variable densities and allow light to pass through. It takes advantage of the process of light refraction in order to visualise the density gradients.

2.3.3.1.1. Light Refraction

When light passes through materials of variable density, the light will bend according to Snell's Law of Refraction (Eq. 2.28):

$$n_{xi} \sin\theta_i = n_{xj} \sin\theta_j , \tag{2.28}$$

where n_{xi} and n_{xj} are the refractive indices of materials *i* and *j* respectively, and θ_i and θ_j are the angles of incidence of light in materials *i* and *j* with the normal between the materials respectively (shown in Fig. 2.23).

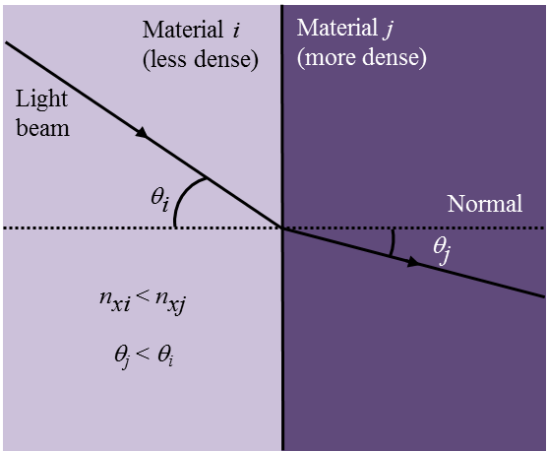

Figure 2.23: Light refraction between two media of different densities.

The density of a gas is proportional to its refractive index, as shown by the Gladstone-Dale relation (Eq. 2.29) [118]:

$$n_x - 1 = K\rho\,, \tag{2.29}$$

where $(n_x\text{-}1)$ is called the refractivity of the gas, ρ is the density and K is the Gladstone-Dale coefficient, which depends on gas characteristics and the wavelength of light being used. In an inhomogeneous gas, the variation of refractive index, caused by variation in ρ, will cause light to be refracted by various degrees throughout the fluid; the higher the change in density, the more the light will be refracted, and light will bend towards the normal when passing into a region of higher density (Fig. 2.23).

Optical visualisation of the change in refractive index with density can be applied to gaseous combustion, and in particular jet flames, due to mixing and high temperature flows [118]; when two or more gases mix with each other, the local concentration of gases will cause density variations in the mixing zone. Convection currents caused by temperature variations within the gas will also cause a density distribution proportional to the temperature gradients. The convective plumes of jet flames are often visualised using schlieren, along with flame front positions, and propagation rates and laminar flame speeds can also be measured. Shock waves may also be visualised due to rapid changes in velocity and density. The shadowgraph and schlieren optical techniques take advantage of this fact, creating a visual image of the density gradient distributions, and the principles of these techniques will now be discussed, followed by configurations, applications and limitations of the schlieren technique.

2.3.3.1.2. Principles

Shadowgraphy

Shadowgraphy is a simple experimental technique that can be best visualised using convection currents above a candle flame. Robert Hooke pointed out in the 17th Century that the convective plume of a candle can be seen simply by its shadow in sunlight, but the first published shadowgraph photographs (or *shadowgrams*) were by Boys in 1893 [156]. When the plume rises and sunlight is shining through the air, shadows can be seen on the wall behind the currents. This is due to the light refracting through the convection currents by different degrees, causing light and dark areas to be seen. The dark areas are due to the net amount of light being refracted away from those areas (causing a shadow), whereas the light areas are where more light has been refracted towards them.

Figure 2.24 shows a simple shadowgraph setup with a point light source and a disturbance. The disturbance causes light that would initially travel to point A to refract by an angle θ and hit the wall at point *B*, a distance δz from point *A*. This would cause point *B* to be lighter and point *A* to be darker than if there were no disturbance. The shadowgraph technique is simply a recording of these shadows caused by density variations in inhomogeneous, transparent media that has been illuminated by a light source.

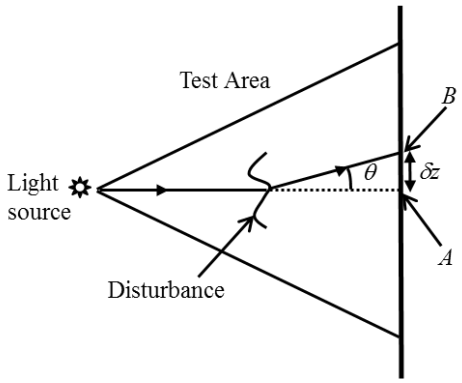

Figure 2.24: Simple shadowgraph setup (adapted from [156]).

Schlieren

The schlieren technique is a little more complex than shadowgraphy. While the shadowgraph technique is sensitive to changes in the second derivative of the density, the schlieren technique is sensitive to changes in the first derivative [118]. It utilises the

cutting off of part of the light in order to make the density variations more distinct. The first demonstration of schlieren was shown by Hooke, using two candles and a lens (Fig. 2.25). Light from the first, distant candle illuminated the lens to the eye, observing from the other side. When a second candle was placed close to the lens, some of the light from the first candle was refracted strongly enough by the convective plume to fall outside of the range of the eye and the transparent convective plume of the candle could be seen [156].

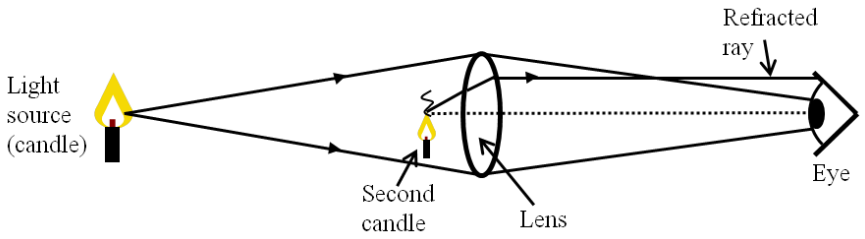

Figure 2.25: Schematic of Hooke's original schlieren experiment (adapted from [156]).

The principles for this phenomenon are illustrated in Fig. 2.26 using a modern schlieren system. A parallel beam of light is shone through the test area and focused towards a lens and camera. A knife edge is placed at the focal point and used as the cut-off device, similar to the edge of the eye in Hooke's experiment. If there are no disturbances in the test area, the image will lose a uniform degree of intensity due to the knife edge (dotted lines in Fig. 2.26). However, when light is refracted towards the normal of the knife edge, it will be cut off by it, causing darks regions in the image (red lines in Fig. 2.26). Similarly, when light is bent away from the knife edge, it will not be cut off at all, and will appear brighter in the image (blue lines in Fig. 2.26). By removing the knife edge, shadowgrams may be recorded with the same setup as for the schlieren imaging.

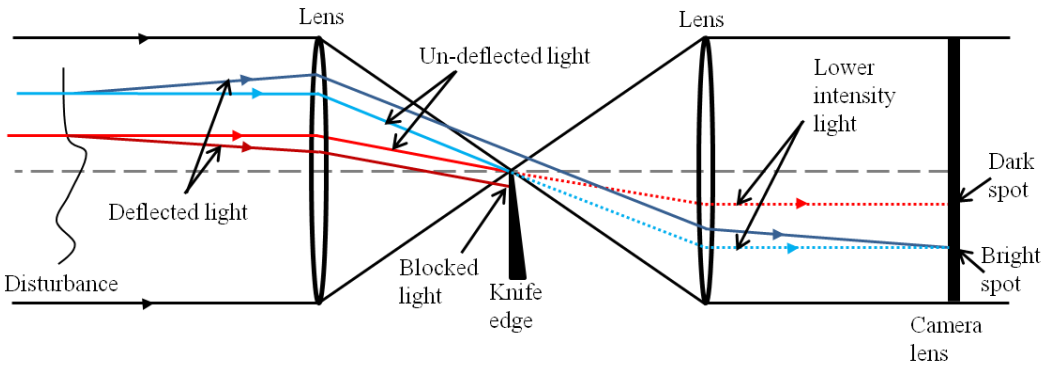

Figure 2.26: Function of the knife edge in the schlieren technique.

Configurations

A variety of setups for schlieren imaging can be used, depending on whether lenses or mirrors are used. When using lenses (Fig. 2.27a), the setup tends to require more space, whereas using parabolic mirrors allows a smaller space to be used. With mirrors, the most common types of setup are the Z-type alignment (Fig. 2.27b) and the *double pass* alignment, coincident or non-coincident (Figs. 2.27d and c respectively). For the lens arrangement (Fig. 2.27a), the light diverges from the light source onto the first lens, creating a parallel beam of light. The light then passes through the test region, where refraction occurs, and converges through the second lens onto the knife edge and to the camera. The principle is the same for the Z-type schlieren arrangement (Fig. 2.27b), with the exception that parabolic mirrors are implemented to converge the light beams. This means that less space needs to be used in the setup. Also, parabolic mirrors tend to have fewer irregularities and are less expensive than lenses of similar size and quality [157].

The double pass alignments (Figs. 2.27c and d) use only one parabolic mirror, so that the light diverges through the test area onto the mirror, where it converges back through the test area and onto the knife edge as before. There is no parallel beam of light, and so a smaller teat area is required, although only one mirror needs to be used. The coincident double pass setup uses a beam splitter in order to allow the light to reach the mirror without obscuring the camera (Fig. 2.27d). In this setup the incident and refracted rays occupy the same space. In the non-coincident setup (Fig. 2.27c) the camera and light source are at an angle to one another, so that they overlap in the test area but not near the camera or light source.

Three dimensional (3D) shadowgraphy is also being developed whereby two sets of mirrors may be used to view the test area from different directions, and the image is reconstructed using stereoscopic reconstruction techniques, allowing depth information to be obtained [158]. Colour schlieren may also be applied; a colour filter is used in place of the knife edge. This gives a colour image of the density gradient distribution whereby different colours are observed instead of the light and dark regions as previously discussed [159].

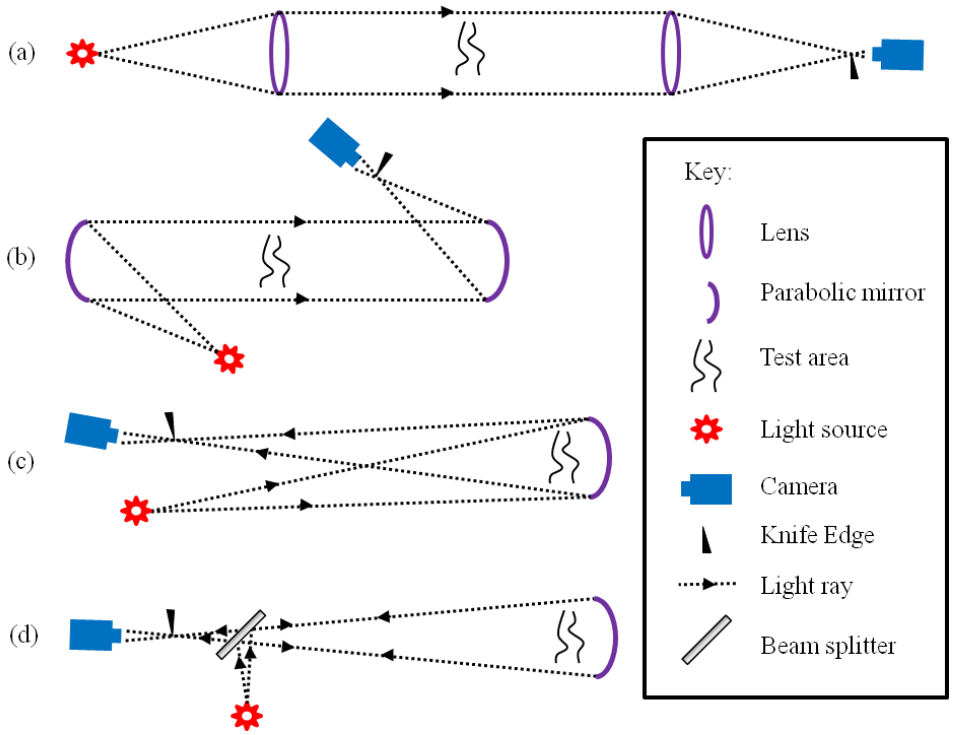

Figure 2.27: Schematics of (a) Lens, (b) Z-type, (c) Double pass and (d) Double pass coincident schlieren alignments.

The experiments in this thesis will use the Z-type alignment so that a large test area with a parallel beam may be used while conserving space and cost. The applications and limitations of the schlieren technique for combustion studies will now be discussed.

2.3.3.1.3. Applications and Limitations

Schlieren can be used to gain visual images of the integrated density distributions within transparent inhomogeneous materials. It is particularly useful in gaseous flows, where the local mixing dictates the density distribution, but can also be used to detect cracks and other imperfections in glass, and for liquid flows. It is often used for jet flames [24, 29, 55], where schlieren allows visualisation of hot combustion gases, flame structures and convective plumes of flames extending past the visual flame area, which digital photography cannot see alone. Flickering frequencies can also be observed with high speed schlieren [30, 160]. It can also depict unburned gases in the cool central core of flames since the density of these gases differs greatly from that of the combustion products. It can pick up the air entrainment in flame jets and can show a clear line between the flame edge and the surrounding air. Laminar and turbulent properties can

also be picked up due to the changes in density caused by turbulent structures and mixing of the burned and unburned gases [24].

Schlieren has been used to measure the laminar burning velocity, flame stretch and instabilities of mixtures using the spherical bomb method [161-163]. This is where mixtures are enclosed in a sphere and ignited at the centre (see Fig. 2.7, p. 20). The flame spreads through the mixture in a spherical shape and the laminar burning velocity can be calculated using the radius of the flame sphere and specific heats of the unburned gases. However, it is difficult to attain high accuracy in this method due to the variation of the unburned gases, temperature and burning velocity throughout the explosion [13]. Schlieren is good for visualising flame front positions and flame propagation characteristics [55], particularly when used with high speed cameras, and shock waves may also be visualised [164].

Good optical access is required for the schlieren method, therefore it cannot be used on enclosed areas, unless optical quality windows, of quartz for example, are used, which may disturb the experiment. Also, if obstacles were required in the flow, they would block the schlieren view. In addition, the image shows an integrated density gradient distribution, rather than a 2D 'slice' of the flow in question. Therefore, it is not particularly suited to thick areas with many density changes. In vertically impinging flames, the wall jet region and hot combustion products spread across the plate. Therefore, when viewed horizontally, wall jet region features will be obscured by the hot gases. However, some information can still be gained from the schlieren images, such as the free jet region and some features in the stagnation and wall jet regions.

In this thesis, schlieren will be used to visualise the flow structure in gaseous impinging flame jets. The thickness of hot gas regions below the plate will be evaluated for various fuels, and unburned fuel regions and mixing regions in the free jet and stagnation regions will be visualised. A quantitative method using schlieren to analyse turbulent structures within the impinging flames will be developed. The flame wall interactions will also be analysed by comparing the schlieren images with the thermograms in order to gain more understanding about flame wall interactions for propane, hydrogen and syngas. The laminar and turbulent nature of the flows at various Reynolds numbers, thermal loadings and equivalence ratios will be evaluated to test their effect on the

flame wall interactions. Schlieren will also be used to evaluate flame propagation immediately after ignition at various locations of the impinging flame configuration for various fuel and flow conditions. The methodologies for these applications of the schlieren technique will be described in Chapter 3. The use of Particle Image Velocimetry (PIV) for flow visualisation will now be discussed.

2.3.3.2. Particle Image Velocimetry

Schlieren may be used for flow visualisation, but in order to gain more quantitative results regarding the structure of the flow within the flames, other methods need to be used. PIV is a technique that can gain information about the velocity flow field and local velocity distributions within the flow.

2.3.3.2.1. Principles

Seeding the Flow

PIV uses the principle of seeded flow to examine flow fields; when objects that are able to follow the fluid motion are introduced into a flow field, the movement of the objects represents the movement of the surrounding flow, for example leaves on the surface of a stream, or balloons in the air. If objects can be selected that follow the flow closely and can be observed individually, then the motion of the fluid can be visualised. An early example of using seeding particles is an experiment performed by Ludwig Prandtl in 1904. Prandtl used a suspension of mica particles on the surface of water in a tunnel, with disturbances in the water caused by obstacles, and tracked their streamlines [108, 165]. More recently, developments in laser and optical technology and computing and electronics have made it possible to obtain quantitative measurements of instantaneous velocity vector fields in a number of flows [165]. In modern PIV, a laser sheet is shone through a test area and scatters off the seeding particles so that the camera can pick up their position. The camera is positioned perpendicularly to the laser sheet so that a 2D slice of the flow field can be visualised (Fig. 2.28).

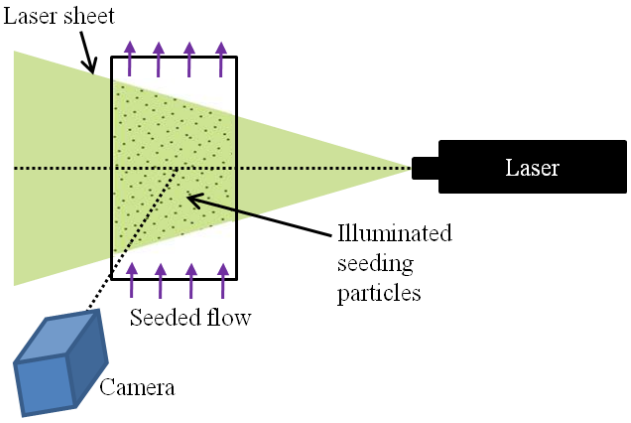

Figure 2.28: Example of a typical PIV setup with the laser sheet illuminating seeding particles.

Particle Tracking

The camera and laser are synchronised so that the camera shutter will open at the same time that the laser pulse fires. The laser pulse, fired twice in quick succession, is used, giving two images; frames A and B respectively, δt apart. The software can map groups of particles in each image and correlate these groups to find the velocity distribution. Each group of particles represents a 'fingerprint' which can be identified in both images. Small interrogation regions are defined in frame A, where a fingerprint is recorded. This interrogation region is then correlated with each area in frame B, pixel by pixel, where the maximum correlation defines a match between frame A and B. The displacement of this interrogation region can then be given a velocity vector depending on the particle group displacement and time interval, δt, between frames A and B. A velocity vector is then assigned (Fig. 2.29). This is repeated for each small interrogation region in frame A until a 2D velocity field is achieved. In order that the correlation values can be as high as possible, the interrogation area size can be adjusted so that each interrogation area contains 5 – 15 particles and so that the maximum displacement is approximately 25 % the size of the interrogation region [166]. The seeding density and time between each laser pulse may also be adjusted prior to recording in order to satisfy these values, however, it is not always possible to satisfy all of these required conditions [166].

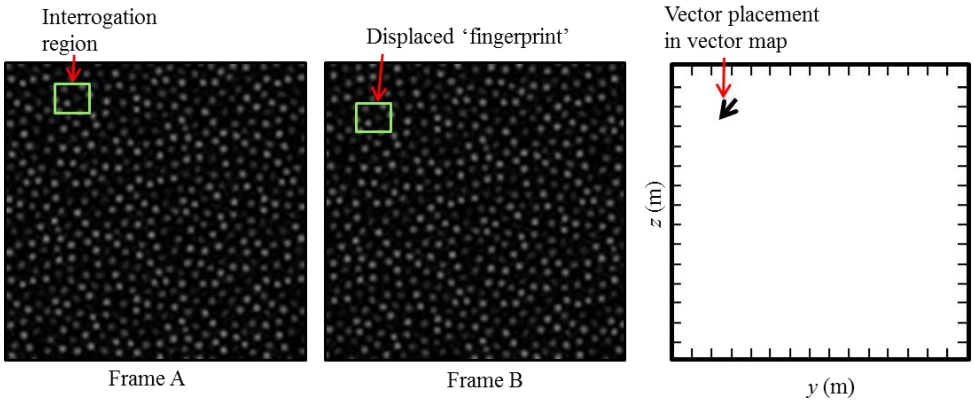

Figure 2.29: Examples of interrogation region in Frame A and matched displaced region in Frame B, along with the corresponding displacement vector in the *y* and *z* directions.

2.3.3.2.2. Seeding

Seeding Conditions

The seeding used in PIV is very important as it must be small enough to follow the flow while still being large enough to scatter the laser light effectively. The ability of a particle to follow flow fluctuations depends on the aerodynamic diameter (Eq. 2.30):

$$d_{ae}=d_{ge}\sqrt{\rho}\,, \tag{2.30}$$

where d_{ae} is the aerodynamic diameter, d_{ge} is the particle diameter and ρ is the density. The smaller the aerodynamic diameter the better the particle's ability to follow rapid fluctuations, and the higher the frequency response [167]. The ability of a particle to scatter laser light depends on the refractive index and surface properties of the particles; particles with irregular or metallic surfaces tend to scatter light well [167]. The scattering of light occurs in the *Mie regime*; this means that the wavelength of the incident light is smaller than the particle diameter (typically 1μm for gases and 10μm for liquid flows) [168]. Other considerations are the particle lifetime in the flow, particularly the resistance to thermal breakdown in high temperature/reacting flows, and toxicity and disposal of the seeding particles [167]. Depending on the type of flow (for example, liquid, gaseous or reacting), various types of seeding may be used as outlined in Table 2.5.

Seeding Particle	Aerodynamic Diameter (x 10^{-4} $kg^{1/2}$ $m^{3/2}$)	Scattering Ability	Type of Fluid
Vegetable/olive oil	Typically 0.3 to 0.9	Depends on droplet size.	Low temperature gases and liquids.
Aluminium oxide power	1.8	Irregular shapes => Good scattering in all directions. Refractive index = 1.79.	Reacting/high temperature gases; melting point = 2288 K.
Titanium dioxide power	1.9 to 3.2	Irregular shapes => Good scattering in all directions, Refractive index = 2.6 – 2.9.	Reacting/high temperature gases; melting point = 1750 K. .
Silicon carbide	0.85	Irregular shapes => Good scattering in all directions, Refractive index = 2.65.	Reacting/high temperature gases; melting point = 2700 K..
Hollow glass spheres	2.6 to 4.1	Large geometric diameter => High scattering intensity.	Liquids.
Metallic coated particles	4.6	Good scattering intensity.	Liquids.

Table 2.5: Properties of various seeding particles used for PIV [167, 168].

Powder particles may typically be used for reacting gaseous flows due to their high scattering intensity produced by their irregular shapes and to their resistance to high temperatures. However problems arise when generating the seeding, due to coagulation caused by humidity in the air flow, moisture in the powder bed and the flow rate of air through the seeder, and so dry gas and powder must be used [168, 169]. Agglomeration also increases with the flow rate, causing the powder bed to become non-uniform, with bubbles or slugs of air disturbing it, leading to an erratic generation rate [169]. Oil droplets are more commonly used in lower temperature gaseous flows or liquid flows, as they are non-toxic, will remain in air for long periods of time and remain of constant

size [108]. Hollow glass spheres and metallic coated particles are also used in liquid flows due to their high scattering ability.

Seeding Generators

A common type of seeding generator using powder is the cyclone aerosol generator, which utilises a powder bed with a cyclone of gas and an outlet for the aerosol (Fig. 2.30a). The cyclone disperses the powder and also separates the large from the small particles, depending on the size of the outlet tube [168], and also reduces the fluctuations in particle concentration [169]. Other seeders are the rotating brush seeder (Fig. 2.30b), which uses a rotating brush to take off the top layer of a column of power and introduce it into high speed flow, which breaks up coagulated particles [168]. Sonic jets may also be used to create high shear flow fields that break up powder while being dispensed in an outer chamber, reducing particle agglomeration [170] (Fig. 2.30c). However, measures must be taken to reduce the amount of coagulation in seeding powders, and other factors will also affect the ability to adequately seed the flow.

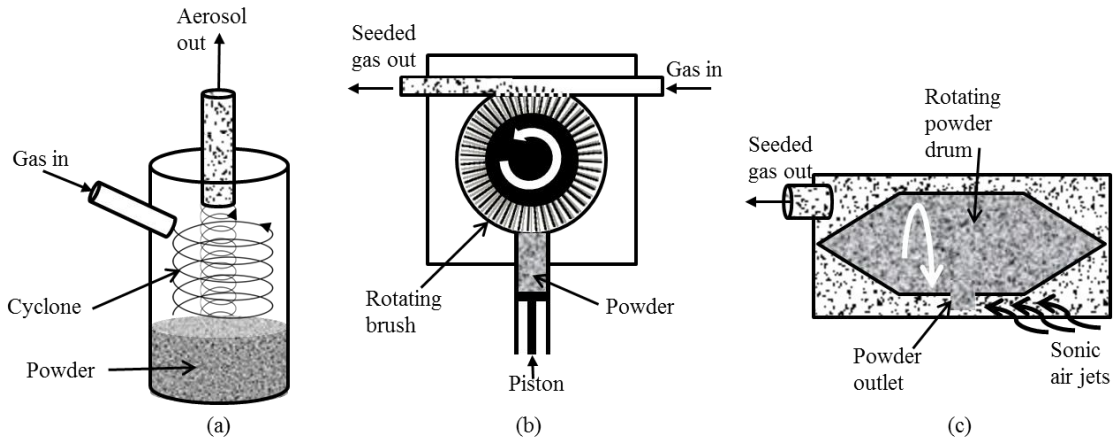

Figure 2.30: Images of solid particle seeders; (a) Cyclone aerosol generator [169], (b) Rotating brush seeder [168] and (c) Sonic air jet seeder.

Oil droplets can be generated by an *atomiser*, the most common type of which is the twin fluid or air assist atomiser [168]. Figure 2.31a shows a schematic of this type of atomiser; oil is drawn from a reservoir into a high speed gas jet, undergoing atomisation using *Laskin nozzles* (Fig. 2.31b). The Laskin nozzles cause small oil droplets to be carried inside air bubbles, due to the shear stress induced by the small sonic jets (Fig. 2.31b) [108]. An impactor plate or separator is used to separate larger droplets, allowing only the small droplets to get past the edges of the plate [108, 168]. A cascade of

nozzles can be used to vary the concentration at constant flow rates and bypass air can be used to dilute the seeded flow if necessary [168].

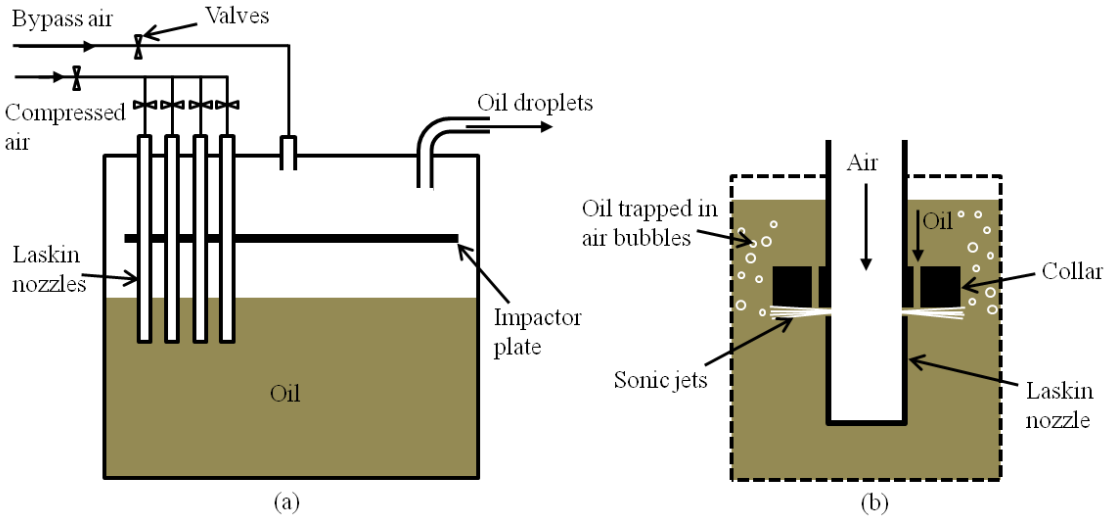

Figure 2.31: (a) Air assist atomiser and (b) Laskin nozzle, adapted from [108, 168].

2.3.3.2.3. Applications and Limitations

PIV may be used for a variety of flows, including liquid and gaseous, reacting and non-reacting. The seeding method and particles used must be such that the particles follow the flow as closely as possible and can be illuminated enough by the laser to be picked up by the camera. In addition, the seeding density must be consistent and large enough to give good statistical evaluation of the flow while being small enough that the camera can pick up individual particles. PIV can be used for high temperature reacting flows as long as the seeding particles have a high enough resistance to thermal breakdown. PIV has been used for calculating vorticity and analysing turbulent flame structures [54, 120-123, 126, 171]. Flow velocity distributions can be obtained [51, 122] and flame vortex interactions can be analysed [120, 172]. PIV has been used for studying vortex structure in an impinging jet on a protruded surface [173], impinging jets on a planar surface using polyamide tracer particles [174] and oil droplets [175], and impinging water jets on a planar surface [176, 177].

For impinging flame jets; the flow characteristics of opposed propane-air [126] and opposed hydrogen-air [178] impinging jets have been studied. For a methane-air flame impinging on a flat plate (using alumina particles and a cyclone seeder), velocity maps and flame contours near the plate were recorded and many statistical parameters were

found [179]. However, there is a lack of research for hydrogen flames impinging upon a flat plate. In impinging flames, density variations and high values of acceleration in stagnation regions, for example, may cause the particles to not follow the flow properly. A sonic jet powder seeding generator was used in this thesis with aluminium oxide particles. However, problems such as particle coagulation, inconsistent seeding density, not being able to achieve certain flow conditions due to the air velocity required to adequately seed the flow, pipe blockage, leakage and high accelerations in the stagnation region caused the PIV to be unsuccessful. This will be discussed in more detail in Chapter 3.

2.3.4. Conclusions

Various diagnostic techniques used for impinging flame analysis have been reviewed. It has been shown that thermal imaging can be a useful tool for visualising temperature distributions of 2D solid surfaces. However, problems arise due to the surface emissivity, and its dependence on temperature and viewing angle. Also, the flame temperature cannot be measured due to the high spectral emissions from the flames. Thermal imaging will be used in this thesis to record the temperature distributions of flame impinged plates using a flame switch off method, and temperature dependent emissivity problems will be explored using an iterative methodology so that the wall temperature can be evaluated. Radiation losses from the plate will also be analysed using the thermal images and the flame wall interactions of various fuel and flow conditions will be examined and compared.

This will be used alongside schlieren and direct photography. Direct photography is often used in impinging flame studies and will be used in this thesis for analysing the flame shapes. It will also be used for comparisons with the schlieren technique. The schlieren technique is well known for its use in visualising flame structure and is extensively used for jet flames. However, when using it with impinging flames, the layer of hot gases that spread across the plate partly obscure the view. Nevertheless, useful information on the flow structure in the free jet region and features such as unburned fuel, where there is a very distinct density gradient, can still be gained. Turbulent structures can also be visualised, and the images can be compared to the

direct images. Schlieren will be useful for analysing the flame wall interactions of various fuels and flow conditions when combined with the thermal imaging techniques.

Schlieren can also be used for flame edge visualisation, and when used with a high speed camera, can be useful for analysing ignition phenomena. The effect of an impingement plate on the ignition and propagation characteristics will be explored in this thesis. In addition, a quantitative method for analysing the turbulent structures in impinging flames will be developed using the schlieren technique.

Particle Image Velocimetry is a very useful tool for obtaining velocity distributions within fluids. However, very specific seeding and flow conditions need to be met. PIV was attempted in this thesis but was unsuccessful in the current setup. This will be discussed more in Chapter 3, along with the other experimental techniques and methodologies mentioned in the above paragraphs.

The techniques discussed will be used for analysing flame wall interactions of impinging jet flames of various fuels and flow conditions, and ignition and flame propagation phenomena in an impinging flame configuration. A detailed review of impinging flame studies is given in the next section, which will be followed by a review of ignition and flame propagation studies.

2.4. Impinging Flames

2.4.1. Introduction

Background information regarding the structure and heat transfer of impinging flames has been given in Section 2.2.2. This section will give a detailed review of the literature pertaining to impinging flames, including looking at different configurations used, common fuels and flow conditions studied. Common experimental techniques used to measure flame structure and flame wall interactions will be discussed including their relevance to the work in this thesis.

2.4.2. Impinging Flame Research

Many researchers look experimentally at the effects of impinging air jets [93, 95, 97, 99, 149, 157, 173-176, 180-184], or perform computational/analytical studies of impinging air jets [90, 92, 100, 173, 184] and flame jets [25, 58, 59, 68, 79, 98, 159,

185-201]. However, this thesis concerns the experimental investigation of impinging flame jets, where the effects of fuel, flame structure, equivalence ratio, reactions and flame impingement affect the flame wall interactions, along with the factors that also affect impinging air jets. Limited information in the literature means that a complete understanding of impinging jet flames and their heat transfer characteristics is not yet possible and due to the complex nature of impinging flames a lot more work needs to be done [84] (and references therein). In addition, the detailed coupling effects between fuel and flow configuration have not been investigated thoroughly. This chapter deals with the research concerned with impinging flame jets of various configurations, fuels and flow parameters, and the flame wall interactions thereof.

Various review papers have been written with regards to impinging flames [11, 84, 101, 202]. In general it is concluded that the effects of Reynolds number, equivalence ratio and nozzle-to-plate distance have been studied extensively. Chander and Ray [84] concluded in 2005 that some aspects of combustion that still needed attention included testing: H_2/air and CO/air flames impinging normal to a plane surface and multi-component mixtures of fuels, particularly with hydrogen addition, which will be explored in this thesis.

Table 2.6 gives a summary of experimental impinging flame studies, including configurations, parameters studied, fuels and measurement techniques. These will be discussed in Sections 2.4.3 to 2.4.8.

Authors	Fuels	Configurations	Re	ϕ	Parameters Varied	Techniques Used ⇒ Parameters Measured
Baukal and Gebhart, 1997 **[103]**.	Oxygen-enhanced natural gas.	Flame-working torch burner, impinging vertically normal to a water-cooled metal disc, at constant firing rate.		Diffusion flame with premixed characteristics.	Surface condition.	• Calorimetric rings. ⇒ Heat flux. • Polished, untreated, and blackened surfaces. ⇒ Emissivity effects. • Alumina-coated, untreated, and platinum-coated surfaces. ⇒ Catalytic effects.
Baukal and Gebhart, 1998 **[203]**.	Oxygen-enhanced natural gas.	Flame-working torch burner, impinging vertically normal to a water-cooled metal disc.		Diffusion flame with premixed characteristics.	Burner firing rate, oxidiser composition and axial and radial surface positions.	• Calorimetric rings. ⇒ Heat flux. • Thermocouples. ⇒ Temperature.

Authors	Fuels	Configurations	Re	ϕ	Parameters Varied	Techniques Used ⇒ Parameters Measured
Beer and Chigier, 1968 **[85]**.	Coke oven gas.	Impinging at 20° onto the hearth of a furnace.	Turbulent.	Premixed.	Impingement angle (20° and 0°), velocity, Re and distance to hearth.	• Impact tubes and suction pyrometer. ⇒ Velocity and temperature profiles in the flame. • Sampling. ⇒ Gas/soot concentration. • Heat flow meters. ⇒ Heat flux. • Radiometers. ⇒ Radiation. • Thermocouples. ⇒ Hearth temperature.
Chander and Ray, 2007 **[204]**.	Methane-air.	3 jets in a triangular configuration, impinging on a flat, water cooled copper plate.	Laminar.	Stoichiometric.	Inter-jet spacing, *h/d* and single/multiple jets.	• Calorimeter with heat flux micro- sensor. ⇒ Heat flux distribution. • Thermocouples. ⇒ Surface temperature. • Direct imaging. ⇒ Flame shapes.
Chander and Ray, 2007 **[57]**.	Methane-air.	Impinging normally to cylindrical, water cooled brass surface.	Laminar.	0.8-1.3	Re, ϕ and *h/d*.	• Calorimeter with heat flux micro- sensor. ⇒ Heat flux and surface temperature. • Direct imaging. ⇒ Flame shapes.

Authors	Fuels	Configurations	Re	ϕ	Parameters Varied	Techniques Used ⇒ Parameters Measured
Chander and Ray, 2008 **[98]**.	Methane-air.	Impinging normally to a flat, water cooled copper surface.	Laminar.	Premixed.	Re, ϕ and burner diameter.	• Calorimeter with heat flux micro- sensor. ⇒ Stagnation point heat flux.
Chander and Ray, 2011 **[186]**.	Methane-air.	Impinging normally to a flat, water cooled copper surface.	Laminar.	Stoichiometric.	Burner diameter and firing rate.	• Calorimeter with heat flux micro- sensor. ⇒ Radial heat flux profiles.
Dong et al, 2002 **[205]**.	Butane-air.	Round flame jet inclined onto flat, water cooled copper plate.	2500	Stoichiometric.	Plate inclination angle.	• Calorimeter with thermocouples. ⇒ Total heat transfer and maximum point of heat flux.
Dong et al, 2002 **[66]**	Butane-air.	Slot flame jet and circular flame jet impinging on a flat, rectangular, water cooled copper plate.	800-1700	Stoichiometric.	Re and *h/d*.	• Calorimeter with ceramic heat flux transducer. ⇒ Heat flux. • Thermocouples. ⇒ Plate temperature (flame side) and flame temperature.

Authors	Fuels	Configurations	Re	ϕ	Parameters Varied	Techniques Used ⇒ Parameters Measured
Dong et al, 2003 **[206]**.	Butane-air.	Row of 3 jets impinging on a flat, rectangular, water cooled copper plate.	900	Stoichiometric.	*h/d* and jet-to-jet spacing.	• Calorimeter with ceramic heat flux transducer. ⇒ Heat flux. • Thermocouples. ⇒ Plate temperature. • Direct imaging. ⇒ Flame shapes.
Dong et al, 2004 **[207]**.	Butane-air.	Twin jets impinging vertically on a square, water cooled copper plate.	800-1200	Stoichiometric.	Re, *h/d*, jet-to-jet spacing.	• Calorimeter with ceramic heat flux transducer. ⇒ Heat flux. • Pressure taps. ⇒ Wall pressure characteristics. • Direct imaging. ⇒ Flame shapes.
Dong et al, 2007 **[208]**.	Butane-air.	Inverse diffusion flame impinging vertically onto a rectangular, water cooled copper plate.	3,000-8,000	0.8-2.1	*h/d* (air), Re (air) and ϕ.	• Coated micro-sensor. ⇒ Local heat flux. • Pressure tap. ⇒ Wall pressure. • Direct imaging. ⇒ Flame shapes.

Authors	Fuels	Configurations	Re	ϕ	Parameters Varied	Techniques Used ⇒ Parameters Measured
Durox et al, 2002 **[209]**.	Methane-air.	Impinging from a water cooled converging nozzle onto a water cooled copper disc, with a loudspeaker.	Laminar.	0.95	Burner size and flow velocity.	• Thermocouple. ⇒ Plate temperature. • Laser Doppler Velocimetry (LDV). ⇒ Axial velocity. • Photomultiplier (CH* emission). ⇒ Global heat release. • Microphone. ⇒ Sound pressure.
Fairweather et al, 1984 **[59]**.	Oxygen enriched methane-air/ oxygen.	Impinging on a hemispherical brass probe.	Laminar.	Premixed.	Fuel/oxidiser ratio and ϕ.	• Calorimetric heat flux probe. ⇒ Stagnation point heat flux and probe surface temperature. • Sodium D line reversal method. ⇒ Flame temperature. • Pitot tube. ⇒ Velocity. • Direct imaging. ⇒ Flame diameter.

Authors	Fuels	Configurations	Re	ϕ	Parameters Varied	Techniques Used ⇒ Parameters Measured
Foat et al, 2001 **[34]**.	Propane-air.	Impinging vertically on flat, water cooled and uncooled plates.	Turbulent.	Premixed.	Turbulence generator, cooled/uncooled plate, flame mode and *h/d*.	• Hot wire anemometry. ⇒ Velocity profiles. • Colour video camera at high shutter speed. ⇒ Flame structure. • High speed digital imaging. ⇒ Time resolved consecutive images.
Hargrave et al, 1987 **[188]**.	Methane-air.	Impinging onto a hemispherical-nosed body and a cylindrical body.	2,000-12,000	0.8-1.2	Re, ϕ and heat receiving body type.	• Calorimeter with conductivity type heat flow meter. ⇒ Stagnation point heat flux for hemi-nosed body. • Transient slug-type calorimeter. ⇒ Stagnation point heat flux for cylindrical body.
Hou and Ko, 2004 **[210]**.	Methane-air.	Bunsen flame impinging vertically on a water cooled, horizontal steel plate.	365	Fuel rich (ϕ = 1.9) and diffusion.	Heating height.	• Thermocouples. ⇒ Jet flame temperature fields. • Thermal input to cooling water. ⇒ Efficiency. • (Not stated). ⇒ Flame appearance.

Authors	Fuels	Configurations	Re	ϕ	Parameters Varied	Techniques Used ⇒ Parameters Measured
Hou and Ko, 2005 **[211]**.	Methane-air.	Bunsen flame impinging vertically and at an angle to a water cooled stainless steel plate.	365	Fuel rich and diffusion.	Heating height and oblique angle.	• Thermocouples. ⇒ Jet flame temperature fields. • Thermal input to cooling water and a heating cup. ⇒ Efficiency. • CCD camera and imaging tool. ⇒ Flame structure.
Hsieh et al, 2005 **[79]**.	Methane-air.	Conical Bunsen flame with concave potential core impinging on a water cooled stainless steel plate.	Laminar.	Fuel lean – fuel rich.	Reacting/non-reacting jet and the transition from lean to rich flames.	• High resolution CCD camera. ⇒ Flame height. • Thermocouples. ⇒ Flame temperature distributions.
Huang et al, 2006 **[65]**.	Butane-air.	Circular flame jet with induced swirl impinging on a water cooled copper plate.	800-1700	Stoichiometric.	Swirl/no swirl, Re and *h/d*.	• Heat flux sensor. ⇒ Local heat flux.

Authors	Fuels	Configurations	Re	ϕ	Parameters Varied	Techniques Used ⇒	Parameters Measured
Huang et al, 2013 **[212]**.	Methane and Propane.	Impinging vertically onto a flat, steel plate.		Diffusion.	Fuel and flow rate.	• Multi-dimensional Digital Flame Colour Discrimination (DFCD) and schlieren.	⇒ Ignition and flame propagation characteristics.
Katta et al, 1998 **[213]**.	Hydrogen-nitrogen-air.	Opposing air and fuels jets with vortex interaction.		Diffusion.		• PLIF.	⇒ OH distributions.
Katta et al, 2004 **[214]**.	Hydrogen-nitrogen-air.	Opposing air and fuel jets with injected vortices.		Diffusion.		• PLIF.	⇒ OH distributions.
Kim et al, 2013 **[215]**.	High pressure hydrogen.	Extension tubes of different lengths and burst pressures interacting with a wall.			Wall height, distance from wall and burst pressure.	• High speed imaging. • Pressure transducers and photodiodes.	⇒ Ignition and flame propagation characteristics. ⇒ Burst pressure and flame generation inside the tube.

Authors	Fuels	Configurations	Re	ϕ	Parameters Varied	Techniques Used ⇒ Parameters Measured
Kwok et al, 2003 **[216]**.	Butane-air.	Round and slot jets impinging vertically onto a flat, water cooled copper plate.	1,000-1,700	0.5-1.3	Round/slot jet, Re and ϕ.	• Heat flux transducer. ⇒ Heat flux.
Kwok et al, 2005 **[217]**.	Butane-air.	Flame jets impinging vertically onto a flat, water cooled copper plate.	1,000	Stoichiometric.	Round/slot jet, single/multiple jets, *h/d* and jet-to-jet spacing.	• Heat flux transducer. ⇒ Heat flux distribution. • Digital camera. ⇒ Flame shapes.
Li et al, 2010 **[218]**.	Liquid Petroleum Gas (LPG) (70 % butane, 30 % propane)-air.	Circular jet impinging vertically onto a flat, water cooled rectangular plate.	Laminar.	Premixed.	Plate temperature, Re, *h/d* and ϕ.	• Cooling water. ⇒ Plate temperature control. • Heat flux sensor. ⇒ Heat flux and flame side plate temperature. • CO/CO_2 and NO_x analyser. ⇒ CO/CO_2 and NO_x emissions.

Authors	Fuels	Configurations	Re	ϕ	Parameters Varied	Techniques Used ⇒ Parameters Measured
Makmool et al, 2011 **[219]**.	LPG-air.	Cooker top burner flame impinging on the bottom surface of a pan.		Premixed.	Burner thermal efficiency.	• PIV. ⇒ Average velocity. • OH-PLIF. ⇒ OH radicals.
Malikov et al, 2001 **[189]**.	Natural gas-air.	Large size industrial Direct Flame Impingement furnace.		Premixed.	Nozzle arrangement, firing rate, nozzle exit velocity, ϕ and gas and surface temperature.	• Cylindrical calorimeter. ⇒ Heat flux. • Suction pyrometer and thermocouples. ⇒ Gas temperature.
Milson and Chigier, 1973 **[87]**.	Methane-air.	Impinging vertically onto a cold steel square plate with the upper surface coated in lamp black.	7,000-35,300	Premixed and diffusion.	Re, *h/d* and ϕ.	• Thermocouples. ⇒ Surface and flame temperature. • Direct imaging. ⇒ Flame structure.

Authors	Fuels	Configurations	Re	ϕ	Parameters Varied	Techniques Used ⇒ Parameters Measured
Mohr et al, 1996 **[220]**.	Natural gas-air.	Radial Jet Reattachment and coaxial jet flames impinging on a water cooled copper plate.	7,000	Partially premixed.	Burner type and ϕ.	• Thermocouples. ⇒ Surface temperature. • Pressure tap. ⇒ Pressure distribution. • Gas analyser. ⇒ CO, CO_2 and O_2 concentrations in exhaust gases.
Ng and Zhang, 2005 **[221]**.	Propane.	Impinging star-shape flames on a circular steel plate.	Turbulent.	Diffusion (with coflow).	Viewing angle.	• Stereoscopic imaging with a single camera. ⇒ Stereoscopic flame shapes.
Ng et al, 2007 **[67]**.	LPG (70 % butane and 30 % propane)-air.	Inverse diffusion and circular premixed flames impinging vertically onto a water cooled copper plate.	2,000-3,000	0.8-1.8	Re, ϕ and h/d.	• Heat flux sensor. ⇒ Local heat flux. • Direct imaging. ⇒ Flame shapes.

Authors	Fuels	Configurations	Re	ϕ	Parameters Varied	Techniques Used ⇒ Parameters Measured
Niu et al, 2008 **[222]**.	Diesel oil (for producing syngas).	Impinging entrained-flow gasifier with two opposed burners.			Oxygen/carbon content ratio.	• Mass spectrometry. ⇒ Gas concentration distribution. • Flame image detector. ⇒ Flame shapes. • Thermocouple. ⇒ Combustor wall temperature.
Remie et al, 2008 **[196]**.	Methane-oxygen and hydrogen-oxygen.	Single circular jet impinging vertically normal to a flat quartz plate.	Laminar.	Stoichiometric.	Fuel type.	• Thermographic phosphor YAG:Dy. ⇒ Temperature on top side of plate.
Singh et al, 2012 **[223]**.	Natural gas-air.	Swirling flames impinging on a flat water cooled surface.	3,500-6,000	1-1.5	Re, ϕ, h/d and swirling angle.	• Calorimeter with a heat flux sensor. ⇒ Heat flux and plate temperature distribution. • Thermocouples. ⇒ Flame temperature. • Direct imaging. ⇒ Flame shapes.
Su and Liu, 2002 **[28]**.	Methane-nitrogen.	Jet-to-jet impingement, with 144° between jets).	90-225	Diffusion.	CH_4/N_2 ratio.	• Thermocouple. ⇒ Flame temperature. • Schlieren and direct imaging. ⇒ Flame shapes.

Authors	Fuels	Configurations	Re	ϕ	Parameters Varied	Techniques Used ⇒ Parameters Measured
Sullivan et al, 2000 **[159]**.	Methane-air.	Array of flame jets impinging on a water cooled rotating cylinder.	Laminar.	Premixed.		• Colour bulls-eye schlieren. ⇒ Flow fields. • Thermocouples. ⇒ Surface temperature.
Takagi et al, 1996 **[197]**.	Hydrogen-nitrogen-air.	Counterflow flames strained by impinging micro fuel or air jet.	Laminar.	Diffusion.	Micro fuel or air jet.	• Laser Rayleigh scattering. ⇒ 2D temperature fields. • Direct imaging. ⇒ Flame shapes.
Tuttle et al, 2005 **[224]**.	Methane-air.	Enclosed jet flames impinging normal to a water cooled polished aluminium plate.	1,500-5,600	Stoichiometric to fuel rich.	Re, ϕ and h/d.	• Heat flux sensor. ⇒ Local heat flux and plate temperature. • Thermocouples. ⇒ Water and flame temperature. • Direct imaging. ⇒ Flame shapes.
Tuttle et al, 2005 **[225]**.	Methane-air.	Enclosed jet flames impinging normal to a water cooled polished aluminium plate.	1,500-5,600	Stoichiometric to fuel rich.	Re, ϕ and h/d.	• Heat flux sensor. ⇒ Local heat flux and plate temperature. • Thermocouples. ⇒ Water and flame temperature. • Direct imaging. ⇒ Flame shapes.

Authors	Fuels	Configurations	Re	ϕ	Parameters Varied	Techniques Used ⇒ Parameters Measured
Wehrmeyer et al, 2002 **[226]**.	Hydrogen-propane.	Opposing hydrogen and propane jets.		Hydrogen: 0.4. Propane: 0.6-1.25.	ϕ.	• Spontaneous Raman spectroscopy. ⇒ Species concentration and flame temperature.
Yoshida et al, 1998 **[201]**.	Hydrogen-nitrogen-air.	Counterflow flames unsteadily strained by impinging micro jet.	Laminar.	Diffusion.	Unsteadiness, flame curvature and preferential diffusion.	• Laser Rayleigh scattering. ⇒ 2D temperature fields.
Zhang and Bray, 1999 **[80]**.		Jet flames impinging vertically on a water cooled plate.			Nozzle exit velocity, *h/d* and ignition location.	• Direct imaging. ⇒ Flame shapes.
Zhao et al, 2004 **[61]**.	Butane-air.	Circular flame jet impinging on flat, square, water cooled brass and stainless steel plates.	500-1,800	0.9-1.2	Re, *h/d*, ϕ, surface emissivity, roughness and conductivity.	• Minolta spot infrared thermometer and thermocouples. ⇒ Surface emissivity. • Calorimeter with heat flux transducer. ⇒ Local heat flux. • Thermocouple. ⇒ Plate temperature.

Authors	Fuels	Configurations	Re	ϕ	Parameters Varied	Techniques Used ⇒ Parameters Measured
Zhao et al, 2006 **[227]**.	Butane-air.	Impinging vertically upwards onto a flat, water cooled plate.	1,200	Stoichiometric.	Plate material (brass, bronze and stainless steel) and surface emissivity for the bronze plate.	• Minolta spot infrared thermometer and thermocouples. ⇒ Surface emissivity. • Calorimeter with heat flux transducer. ⇒ Local heat flux. • Thermocouple. ⇒ Plate temperature.
Zhao et al, 2009 **[228]**.	Butane-air.	Array of three jets with/without swirl impinging onto the base of a water tank.	500-2,500	1-1.8	With/without swirl, Re, *h/d* and ϕ.	• High speed digital imaging. ⇒ Flame shapes. • Thermocouple. ⇒ Water temperature. • Heating the water to a fixed temperature rise. ⇒ Heating efficiency.
Zhen et al, 2009 **[229]**.	LPG (70 % butane, 30 % propane)-air.	Swirling inverse diffusion flame impinging on a flat water cooled copper plate.	6,000-10,000	1-2	Swirl number, Re, *h/d* and ϕ.	• Heat flux sensor. ⇒ Heat flux distributions. • Direct imaging. ⇒ Flame shapes.

Authors	Fuels	Configurations	Re	ϕ	Parameters Varied	Techniques Used ⇒ Parameters Measured
Zhen et al, 2012 **[230]**.	LPG (70 % butane, 30 % propane)-air.	Annular and round flame jets impinging vertically on a flat, water cooled copper plate.	1,300-1,700	1-1.5	With/without swirl, Re, *h/d* and ϕ.	• Heat flux transducer. ⇒ Local heat flux. • Direct imaging. ⇒ Flame shapes.

Table 2.6: Summary of impinging flame studies.

2.4.3. Impinging Flame Configurations

In combustion research, simple configurations are used to perform controlled experiments. For closed configurations, furnaces are usually used [85, 231, 232], but the most common configuration for open impinging flames is to have a flame jet impinge vertically onto a flat plate (Fig. 2.32a) [34, 61, 66, 67, 80, 87, 98, 103, 186, 195, 196, 203, 204, 208, 210, 211, 216, 218, 221, 227, 229, 230]. This allows for simple setup and data acquisition and symmetry. Other configurations are to change the angle of incidence of the flame on the plate or the orientation of the burner nozzle (Figs. 2.32b and d respectively) [85, 102, 185, 205, 211]. This allows buoyancy effects to be studied due to the unsymmetrical nature of the setup. Configurations may also use a hemi-spherical or cylindrical impingement surfaces (Fig. 2.32c) [57, 59, 188], or use an opposing jet of flame or air to create impinging flames without an impingement surface (Fig. 2.32e) [197, 201, 213, 214, 226]. In this case, the stagnation point is the point where the flow velocity is zero, due to the change in direction on either side caused by the flame impingement (Fig. 2.32e).

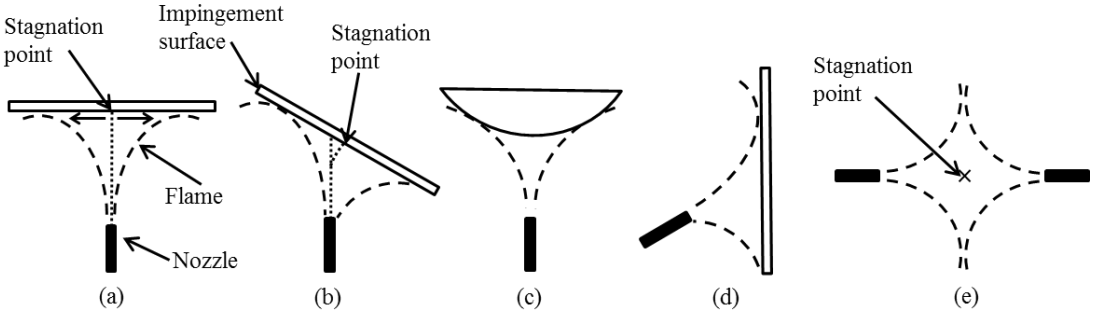

Figure 2.32: Diagrams of impinging flame configurations for flame jets impinging vertically upwards onto (a) A horizontal flat plate, (b) An angled flat plate and (c) A hemi-spherical plate, (d) At an angle upwards onto a vertical flat plate and (e) Opposing flame jets.

For vertically impinging symmetrical flames, the stagnation point is directly above the nozzle, but for other configurations, such as with an angled plate, it can be off-centre to the jet axis (Fig. 2.32b) [205]. For an angled plate, the heat flux in the uphill part (left side of Fig. 2.32b) is higher than the downhill part, and for the downhill part, the heat flux increases with inclination angle [185]. Different nozzle shapes, such as annular and flat, and multiple interacting jets may also be used [66, 159, 204, 206, 207, 216, 217,

228, 230]. Dong et al looked at the heat transfer of round jet flames on an inclined plate [205], slot jet flames on a flat plate [66] and a row of three jets on a flat plate [206] for butane-air flames, and Chander and Ray looked at the heat flux distributions for methane-air flames impinging normal to a flat surface [98] and a cylindrical surface [57] and in a triangular three-jet configuration on a flat surface [204]. It was found that the heat transfer characteristics were very closely related to the flame shapes and whether or not the reaction zone impinged on the target.

This thesis concerns only singular round nozzles impinging vertically onto a flat plate (Fig. 2.32a), since this configuration gives a symmetrical setup for the thermal imaging and schlieren techniques and it is the flame wall interaction that is of interest rather than the burner-plate geometry. The next section deals with flame wall interaction effects specific to the impingement plates.

2.4.4. Plate Effects

Plate Cooling

Water cooled plates cause both the hot and cold sides of the plate to be approximately constant at steady state, causing linear conduction though the plate, whereas uncooled plates experience a non-linear temperature gradient [233]. Water cooling takes heat from the non-impinged side of the plate and the flow rate and temperature rise of the coolant can be used to measure the total heat flux (called a heat flux calorimeter) due to the energy gained by the water. They are commonly applied in impinging flame studies, using the water temperature rise to obtain a steady state condition, and using a heat flux sensor to measure the local heat flux; moving the burner position relative to a single heat flux sensor attached to the plate [57, 61, 66, 98, 103, 186, 204-207, 223, 233]. Water cooled plates can also be used to approximate the plate as isothermal; cooling the plate evenly over the surface, reducing the temperature gradients within the plate [86, 204]. If the plate is not insulated or cooled, then heat will be radiated away from the other side of the plate, along with convection heat transfer to the surroundings [87].

A flame impinged plate has high radiation loss if not cooled and so far the radiation loss from a flame impinged plate has rarely been investigated. In addition, an uncooled plate represents a higher, more realistic temperature, and temperature distributions of uncooled plates have not commonly been investigated. The real temperature distribution

along the plate can be measured in this way, as the plate temperature will not be reduced due to the forced cooling. Uncooled impingement surfaces have been used to measure flame structures and corresponding temperature distributions for methane-air flames [87] and propane-air flames [34], heat transfer from buoyant diffusion flames to an unconfined ceiling [199], flame temperature and heat transfer coefficients [234], heat transfer to furnace walls [85] and stagnation point heat transfer [59]. However, uncooled plates have not been extensively studied, as for water cooled plates. The plate temperature for uncooled plates will be higher, which will also change the flame properties near the plate when compared to cooled plates. In addition, large temperature variations across the plate radius will occur, which will affect the radiation losses. Uncooled plates will be used in this thesis to study the wall temperature distributions across the plate for impinging flames. The variable temperatures across the plate surface will affect the radiation losses, which will also be evaluated and compared.

Surface Material

Various surface materials have been used in impinging flame studies. In order for the surface to be close to isothermal in the water cooled configurations, materials with high conductivity are used. Surface properties such as roughness, emissivity and conductivity will affect the flame wall interaction. Many researchers use copper plates [65-67, 98, 186, 204-209, 216, 217, 220, 229, 230] due to its high thermal conductivity, and steel [61, 79, 87, 210, 211, 221, 227], aluminium [224, 225], brass [59, 61, 227], bronze [227] and quartz [196] surfaces have also been used, but not as extensively.

Some studies have focused on the effects of surface roughness on the flame wall interaction, using surfaces with brass and stainless steel with different roughness properties [61], or using protrusions or dimples in the impingement target for air jets [99, 173], but mostly smooth flat surfaces are used for flame wall interaction studies.

In order to study emissivity effects for flame radiation heat transfer, polished, untreated and blackened surfaces have been used, as these give very different emissivities [103]. Catalytic effects were also studied by the same authors [103] by using alumina and platinum coated and untreated surfaces. It was found that the polished and blackened surfaces gave a maximum difference in heat flux of 9.8 % and the alumina and platinum coated surfaces gave a maximum difference of 12 %, showing that the non-luminous

radiation from the flame and TCHR were relatively small fractions of the total heat flux. Brass and stainless steel surfaces have also been used to compare emissivity and conductivity effects [61] and it was found that the plate material significantly affected the heat flux in the stagnation region, but not in the wall jet region. However, no studies so far have looked at the effects of temperature dependent emissivity in impingement surfaces, which will be a focus of this thesis, using a quartz plate for the impingement surface.

Oxidised steel has the property of high thermal inertia [150], and constant emissivity (of 0.79) with respect to temperature [235, 236]. Therefore, it makes for an excellent surface for measuring the wall temperature of flame impinged walls using a 'flame switch off' method, which will be discussed in Chapter 3. In addition, surfaces covered in soot produced by hydrocarbon flames generally have a constant emissivity of 0.96 [237, 238] and so the method can be applied to the surfaces heated by propane diffusion flames. Quartz has the property of temperature dependent emissivity, where the emissivity of the material changes depending on its temperature. This allows for a methodology to be developed for use with the thermal imaging cameras, which will also be discussed in Chapter 3. The differences in the properties of steel and quartz will also allow for comparison of flame wall interactions depending on plate material since they have significantly different emissivity and conductivity properties.

Nozzle-to-Plate Distance

The distance between the burner nozzle and the impingement plate has large effects on the flame wall interactions. The nozzle-to-plate distance normalised by the nozzle diameter (*h/d*) has been studied extensively for various impinging flame fuels and configurations [34, 57, 61, 65-67, 80, 87, 204, 206-208, 217, 218, 223-225, 228-230]. These studies mainly use methane, butane and LPG. In general, the flame wall interaction and heat transfer to the plate is greatly affected by the flame shape, and depends on whether or not the inner reaction zone or unburned fuel impinges on the plate at the stagnation region. In addition, the flame modes are affected by the nozzle-to-plate distance [80]. At smaller *h/d*, the plate has a greater influence on the stagnation point velocity and heat flux, and also, for smaller *h*/*d*, the dip in the heat flux at the stagnation region is more pronounced. The average heat flux tends to increase with increasing *h/d* up to a point and then decreases, due to the section of the flame that

impinges on the plate. The plate temperature follows the same pattern as the heat flux; a dip in the stagnation region when the cool central core impinges on the plate [87].

The effect of nozzle-to-plate distance on the wall temperature for propane impinging flames and on the ignition characteristics for hydrogen impinging flames will be studied in this thesis, since these aspects of the effect of nozzle-to-plate distance have not yet been studied in detail. However, the majority of the results will be at a constant h/d. The next section deals with parameters that are commonly studied for impinging flames and that, along with the plate effects, have large effects on the flame wall interactions.

2.4.5. Parameters Affecting Flame Wall Interactions

Reynolds Number

Impinging flames of varying Reynolds number have been studied with focus on the heat transfer characteristics and heat flux. Many studies do not vary the Reynolds number, but choose either laminar [59, 79, 196, 204, 206, 209-211, 217], transitional [205, 227] or turbulent [220, 221] flames. However, the effects of varying the Reynolds number on the heat flux and flow characteristics of laminar [57, 61, 65, 66, 98, 207, 216, 218, 228], transitional [61, 65-67, 216, 224, 225, 228, 230] and turbulent [85, 87, 188, 208, 223-225, 229] impinging flames has also been studied at length.

The effect of Re on the heat transfer of impinging flames is significant. For laminar flames, increasing Re tends to increase the heat flux to the plate while making it less uniform [65, 228], and for transitional flames, the enhancement of the heat flux with Re is more evident in the impinging and early wall jet regions [66]. For turbulent flames, an increase in Re causes the dip in the heat flux at the stagnation region to be more pronounced and increases the zone of influence of the cool central core [87, 223]. However, the effect of Re on the wall temperature profiles has not been studied in as much depth as the effect on the heat flux to the wall.

Foat et al [34] concluded that the nozzle exit Reynolds number was a less useful variable in describing the flame structure of reacting impinging flows than ignition location, stoichiometry, heat transfer, global stretch rate and turbulence scales. This thesis will look at both laminar and turbulent flames of various fuels and flow properties, focusing on the flame impinged wall temperature rather than the heat flux to

the wall and the effect of Re along with other properties such as equivalence ratio, thermal loading, ignition location, fuel and flame structure.

Equivalence Ratio

Most impinging flame studies are performed with premixed flames at a stoichiometric equivalence ratio [65, 66, 186, 196, 204-207, 217, 227], or varying between fuel rich and fuel lean flames [57, 61, 79, 98, 188, 208, 216, 239] or stoichiometric and fuel rich flames [223-225, 228-230]. Some studies have been performed for diffusion flames [28, 213, 214, 221] and comparing diffusion and premixed flames [87, 210, 211] but these are much fewer in number since most processes in industry use premixed flames, and diffusion flames tend to be sooty which can interfere with heat flux measurements. For the premixed studies, when moving from stoichiometric to lean or rich flames, the combustion efficiency decreased [239] and the maximum rate of heat transfer decreased with a shift of the maximum heat flux downstream [188]. When moving from stoichiometric to rich flames, the wall jet region increased in size but the free jet and stagnation zone remained unchanged [224] and the effect of the equivalence ratio on the heat flux for rich swirling flames was less than the effect of the Reynolds number [223].

This thesis will look at diffusion flames and fuel rich flames, since these types of flames are not as widely studied and experimental constraints such as blow-out mean that stoichiometric and fuel lean flames could not be studied. The diffusion and premixed flames of propane, hydrogen and syngas will be compared in terms of the flame wall interaction of these flames, and the effects of soot on the wall temperature of propane diffusion flames will be explored. The ignition characteristics of hydrogen diffusion and rich impinging flames, hydrogen plus carbon dioxide impinging flames and methane diffusion impinging flames will also be studied and compared.

Thermal Loading/Burner Firing Rate

Most studies do not consider the burner firing rate (or thermal loading) in impinging flame studies. Studies that have used the firing rate as a parameter to vary have used a flame working torch burner [203], a large size industrial Direct Flame Impingement furnace [189] and jet flames impinging on flat plates [186, 240, 241]. For the torch burner study, the wall temperature increased by 35 % - 59 % when the firing rate was increased from 5 to 25 kW. The effects of thermal loading on the flame wall interaction

of impinging jet flames has generally not been studied, however the firing rate is an important property of industrial burners. When using new fuels and designing new burners, the thermal loading is an important parameter for consideration. This thesis is concerned with testing the flame wall interaction of various fuel compositions, and the effects of thermal loading will be looked into, along with the effects of Re, ϕ, h/d and fuel composition.

2.4.6. Fuel Effects

Most impinging flame studies use only one fuel type and compare the Reynolds number, h/d, configuration and ϕ as discussed in Sections 2.4.3 to 2.4.5. Many studies use methane [57, 59, 68, 79, 98, 159, 186, 188, 204, 209-211, 224, 225, 241], butane [61, 65, 66, 205-208, 216, 217, 227, 228] or natural gas [103, 189, 203, 220, 223], and other studies use propane [34, 221], LPG [67, 218, 219, 229, 230], hydrogen [215] and hydrogen-nitrogen mixtures [197, 201, 213, 214], methane-nitrogen mixtures [28], coke oven gas [85] and diesel oil for syngas production [222]. However, experimental papers rarely compare the effect of different fuels on the flame wall interaction of impinging flames. Remie et al [196] compared temperatures of a quartz plate heated by methane-oxygen and hydrogen-oxygen flames for validation of numerical results. However, the fuels were not compared to each other; rather the experimentation was compared to the numerical results separately for the different fuels. Huang et al [212] compared the ignition characteristics of propane and methane impinging diffusion flames, which is related to the work in this thesis and will be discussed in Section 2.5. Saha et al [242] explored the effects of methane and ethylene impinging flames and found that the flame luminosity for the different fuels affected the heat transfer to the plate. Some numerical studies have been performed that compare the effects of fuel variability in impinging flames [190, 194]. Other studies compare the effects of oxidiser composition experimentally [59, 203] and numerically [58, 59, 192].

The effect of fuel variability on the heat transfer and flame wall interaction of impinging flames is lacking. The majority of research of impinging jet flames has concerned methane and butane, but with the increasing use of hydrogen and hydrogen based fuels such as syngas, a growing need for research on these fuels has come about, particularly because hydrogen is vastly different from these mainstream fuels in its combustion and

flow properties. These differences will greatly affect the flame wall interaction of impinging flames. The adiabatic flame temperature and thermal diffusivity of hydrogen are much higher than for propane or methane, which will cause heat transfer rates to be higher. In addition, the molecular diffusivity of hydrogen is higher than for hydrocarbon fuels, which will cause faster mixing rates between the unburned fuel and ambient air. The composition of syngas often varies between sources and so the effect of syngas composition on impinging flame heat transfer should be studied. This thesis will look at four different compositions of syngas and will compare the flame wall interaction experimentally for these fuels. This work has been performed in conjunction with the University of Lancaster [190, 191, 193, 194] who have performed Direct Numerical Simulations (DNS) and Large Eddy Simulations (LES) of the syngas impinging flames of the same compositions.

In addition to the above mentioned differences between hydrogen and hydrocarbon fuels, the laminar flame speed is also much larger for hydrogen, and flame curvature effects are much different due to the differences in density between the burned and unburned gases. When experimenting with hydrogen it was noticed that the ignition propagation characteristics were very different to those of methane and propane (studied by Huang et al [212]) and so the flame propagation after ignition, along with the heat transfer characteristics, of hydrogen impinging flames at various ignition locations will also be reported in this thesis, and will be discussed further in Section 2.5.

2.4.7. Flame Structure

The heat flux to an impingement surface depends heavily on the flame shapes and the section of flames that impinge on the wall, and the flame shapes and flow fields can be visualised and measured in different ways. This section deals with the literature pertaining to the interaction of the flame shapes and flow fields with impingement surfaces, and will be followed by heat transfer and wall temperature studies.

Flame Shape Visualisation

Many researchers use direct imaging for visualisation of impinging flame shapes [34, 59, 67, 79, 80, 87, 197, 204, 206-208, 210, 211, 215, 217, 221, 223-225, 228-230]. With direct imaging, the visual flame edge and inner reaction zone can be observed, along with the flame colour and flame modes. Foat et al [34] and Zhang and Bray [80] used

direct imaging to visualise flame modes ignited at various locations of an impinging flame configuration, and Ng and Zhang [221] used a novel stereoscopic technique with one camera to visualise the 3D structure of impinging flames.

Direct imaging has often been used with heat flux and wall temperature measurements. Chander and Ray [204] found that the heat transfer characteristics depended heavily on whether the inner reaction zone was impinging on the target surface. Milson and Chigier [87] used direct imaging to show the effect of the cool central core of premixed and diffusion methane impinging flames, which caused the stagnation region temperature to be lower. Taufiq et al [239] showed that the heating efficiency is maximised when the tip of the inner reaction cone is slightly higher than the heating height. Tuttle et al [224] used direct imaging to show the diffusion and premixed flame structure and vortices in the wall jet and free jet regions and their effect on the heat transfer. In this way, direct imaging can provide information about the flame wall interaction when used with other techniques such as heat flux and wall temperature measurements.

Schlieren imaging is not used as often as direct imaging in impinging flame studies. Schlieren has been used to visualise the structure of free jets [88] and schlieren showed that the presence of a hemispherical nosed cylinder probe in the second part of the study did not significantly affect the visible flame appearance [188]. Huang et al [212] used schlieren along with DFCD to visualise the ignition and flame propagation characteristics in flames impinging on a flat plate, and schlieren has been used for flow visualisation of methane flames impinging on a rotating cylinder [159].

When using schlieren in impinging flames the view can be obscured by the layer of hot gases in the impingement region, however many aspects can still be observed when there is a large variation in the density field, such as unburned fuel impinging on the plate, turbulent structures and the flame edge position. These features can give information into the flame wall interaction, particularly when used with wall temperature measurements. Therefore, schlieren will be used in this thesis, along with direct imaging, combined with wall temperature measurements to examine the flame wall interaction of impinging flames.

Flow Field Measurements

In addition to visualising flame and flow structure, techniques are used to measure the velocity and temperature profiles within impinging flames. Impact tubes [85], pitot tubes [59], hot wire anemometry [34], Laser Doppler Velocimetry (LDV) [209] and PIV [219] have been used to measure the velocity profiles in impinging flames. Thermocouples [79, 210, 211, 223-225], suction pyrometers [85, 189], laser Rayleigh scattering [197, 201], Rayman spectroscopy [226] and a sodium D line reversal method [59] have been used to measure the temperature profiles within impinging flames. PLIF has also been used to measure the flame front position in impinging flames [213, 214, 219].

These techniques have advantages over visualisation techniques due to the quantitative nature of the measurements. Velocity fields can provide information about flow vorticity and the flow structure in the presence of an obstacle or impingement plate. Flame temperature measurements can provide information regarding high temperature regions and temperature distributions to be compared to computational studies. PIV was attempted in this thesis but was unsuccessful and will be discussed in more detail in Chapter 3. The schlieren technique will be used to develop a quantitative method for analysing turbulent structures within impinging flames and thermal imaging will be used for quantitative measurements of the impingement wall temperature. The next section deals with the literature relevant to the use of thermal imaging in impinging flames.

2.4.8. Thermal Imaging

Surface Temperature Measurements

Most studies look at the convective heat transfer to an impingement plate using water cooled plates and heat flux sensors as discussed in Section 2.4.4. However, wall temperature measurements can provide an alternative to heat flux measurements, and can aid in realistic computational investigations by providing measured boundary conditions. The temperature of a wall can be important in industry in order to find hot spots and cool regions where damage or flame quenching may occur. Wall temperature measurements can also provide much information about flame wall interactions. Many researchers use thermocouples to measure the wall temperature in impinging flames [61, 66, 85, 87, 159, 204-206, 209, 220, 222, 227], and have thermocouples drilled into the

impingement surfaces at various positions to give spot readings. A thermal imaging camera can give a non-intrusive, 2D image of a temperature field of a flat surface, provided the emissivity is known. However, thermal imaging is not often used in impinging flame studies. The principles of thermal imaging cameras have been discussed in Section 2.3.2.1 along with applications and limitations. This section will discuss the use of thermal imaging cameras with particular regards to impinging flames and to the work in this thesis that deals with the limitations of thermal imaging cameras and the solutions to the problems.

Air Jets

Thermal imaging has been used to test the heat transfer from air jets to thin stainless steel foil sheets, using the thermal imaging camera on the back of the foil [149, 181-184]. Matt finish paint was used on the back surfaces in order to gain an emissivity of 0.99 for accurate temperature measurements. The foil sheets were thin enough (~ 0.05 mm thick) so that lateral conduction was negligible and so that a constant heat flux was assumed. The temperature difference across the plate was shown to be negligible so that the thermal images taken on the back of the plate were the same as on the impinged side [181]. The thermal images were used to calculate the local Nusselt numbers, with heat loss estimated experimentally. The uncertainties in the measurements of heat transfer coefficients were stated to be between 3.4 and 7% [181]. However, thermal imaging has not been extensively used in combustion systems or impinging jet flames where high heat transfer rates occur.

Impinging Flames

For impinging flames, high temperatures are attained, which also causes high radiation loss (Eq. 2.24, p. 30). Thermal imaging can be used to evaluate the radiation loss from a flame impinged plate, which has not been studied in depth. This thesis will look at the radiation loss from uncooled flame impinged plates. It will also deal with problems faced when measuring the temperature of surfaces whose emissivity depends on the temperature of that surface, which will vary across the surface when impinged upon by a flame.

Emissivity Problems

It has been discussed in Section 2.3.2.1 that thermal radiation detected by thermal imaging cameras depends on viewing angle, reflection, and the wavelength of emitted

radiation. The resolution of these factors will be discussed in more detail in Chapter 3. It has also been discussed that for accurate temperature measurements with thermal imaging cameras the emissivity must be known and the emissivity can depend on the temperature of the surface. Therefore, an iterative methodology has been developed to deal with this problem, using a quartz plate, whose emissivity depends on temperature. This will be discussed in more detail in Chapter 3.

Flame Emission

The wavelength of radiation to be detected is limited by the thermal imaging camera. Therefore, the flame temperature cannot be measured by the cameras used in this thesis due to the high spectral emissions from the flames, and so a 'flame switch off' method has been developed from [150], in which the flame is switched off after reaching a steady state. The image recorded by the thermal imaging camera represents a 'thermal footprint' of the flame impinged wall. The high thermal inertia of the impingement surfaces means that the wall temperature can be measured in this way to analyse the flame wall interaction and heat transfer to the plate. In addition, the thermal imaging camera can be used to monitor when a steady state is reached.

Thermal imaging can be used to measure the thermal footprints of flame impinged walls provided the surface emissivity is known, even if the emissivity depends on the temperature being measured. This can allow non-intrusive, 2D measurements of the wall temperatures, from which radiation losses can be calculated and flame wall interactions analysed, particularly when used with other techniques such as schlieren and direct imaging. These methods will be utilised and developed in this thesis.

2.4.9. Conclusions

Many aspects of combustion and flame wall interactions of impinging flames have been discussed. It has been shown that combustion, and in particular impinging flames, is a very complex and extensive topic.

Experimentally, measuring heat transfer to and from impingement surfaces requires known temperature gradients, which can be difficult to measure. Also, parameters such as emissivity, thermal conductivity and convection heat transfer coefficients must be known to calculate heat flux. However, temperature distributions across the plate combined with information regarding the flame structure and flow properties can give

insight into flame wall interactions, and how these interactions differ for different flame and flow properties. Simple burner geometry and controlled flow conditions can give bases for meaningful comparisons between different fuels in order to compare the effect of fuel and flow properties on flame-wall interactions. In addition, computational studies often approximate impingement surfaces as isothermal, whereas wall temperature distributions may provide more realistic boundary conditions for impinging flame studies. This thesis will deal with the flame wall interactions of impinging flames using wall temperature distributions obtained by thermal imaging, using a flame switch off technique, and flame structure measurements using schlieren and direct imaging.

In addition, an iterative methodology has been developed in order to deal with measuring the temperature of surfaces whose emissivity depends on that temperature with thermal imaging techniques. This will be discussed in Chapter 3. The radiation losses from the plates will also be calculated using the temperature profiles. The schlieren method will be utilised for quantitative analysis of the turbulent structures within impinging flames.

Many properties affect the flame wall interaction of impinging flames. The properties that will be compared in this thesis will be Reynolds number, equivalence ratio, nozzle-to-plate distance, thermal loading, fuel composition and ignition location. In addition, two plate materials, namely fused quartz and heavily oxidised steel, will be used in order to compare the effect of plate material on the flame wall interaction, and the effects of oxidisation and soot will be discussed.

An aspect of combustion that has not been widely studied in relation to impinging flames is the ignition and flame propagation characteristics in impinging jet flames. Ignition location in impinging flames can determine flame modes, and flame propagation characteristics can be very important in hydrogen mixtures due to the high laminar burning velocity. The ignition properties of hydrogen are very different to those of hydrocarbon fuels and an impinging flame configuration can allow simple geometry and optical access to ignition and flame propagation mechanisms and the effect of fuel and flow conditions on these phenomena. The next section deals with the literature pertaining to ignition and flame propagation phenomena.

2.5. Ignition and Flame Propagation

2.5.1. Introduction

This thesis will explore an interesting phenomenon noticed with hydrogen impinging flames; when ignited near the plate and propagating towards the nozzle, a non-linear acceleration was observed. This was not observed for methane flames. The properties of hydrogen differ greatly to those of methane and the effect will be looked at. This section deals with the literature pertaining to ignition and flame propagation characteristics in combustion studies and in impinging flames.

2.5.2. Flame Propagation Configurations

The principles of ignition and flame propagation have been discussed in Section 2.2.1.3. Various experimental configurations can be used to study flame propagation and these will be discussed in this section. Following that, flame propagation in jet flames and impinging flames will be discussed.

Spherical Bomb

The constant volume or constant pressure bomb method; where a flame is ignited at the centre of a spherical/cuboid chamber (see Fig. 2.7a, p. 20) and the flame propagation is recorded, is often used to experimentally find unstretched burning velocities. This is done by calculating the flame propagation speed with respect to burned gases and calculating the effects of stretch and Markstein lengths by extrapolating to zero stretch using the linear relationship between stretch and burning velocity (Eq. 2.19, p. 22) [22, 243-245]. It has been shown that the stretched burning velocity for hydrogen/methane mixtures increases exponentially with hydrogen content and can reach up to 18 m s^{-1} for hydrogen-air flames, and that the Markstein length increases with hydrogen content, increasing the diffusion-thermal instability of the flame front [244, 246].

Deflagration to Detonation

The flame front can also be considered to be a reaction wave propagating through a combustible mixture, and for premixed flames the reaction can be categorised into explosive reactions; where a combustion wave is not required and heat generation is extremely fast, deflagration reactions; where the combustion wave propagates at subsonic speed, and detonation reactions; where the combustion wave propagates at

supersonic speed [22]. A 1D stationary combustion wave (from the reference frame of the wave) can be visualised by Fig. 2.33, where the unburned and burned gases are represented by subscripts 1 and 2 respectively and u, p, T and ρ are the velocity, pressure, temperature and density of the gases respectively. A combustion wave in a duct may undergo a deflagration to detonation transition (DDT) if the turbulent burning velocity is high enough to cause a shock wave ahead of the flame, increasing the pressure and temperature and further increasing the maximum turbulent burning velocity and accelerating the flame [247]. For channels with non-slip walls, the DDT is determined by the flow ahead of the flame front [248]. Flame propagation and the propagation of shock waves are integral in studying the effects and causes of DDT.

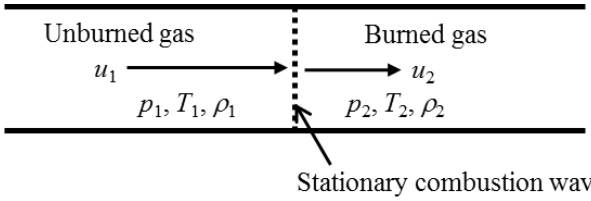

Figure 2.33: Stationary 1D combustion wave (adapted from [22]).

Triple Flames

Flame propagation has also been studied in triple (or tribrachial) flames; consisting of a lean premixed branch, a rich premixed branch and a diffusion tail trailing from the triple point, propagating along a stoichiometric contour (Fig. 2.34). In partially or non-premixed flames, triple flames are responsible for flame propagation and stabilisation [249], and are important in lifted flame jets, autoignition fronts and for flame propagation in mixing layers (commonly found in flame jets), boundary layers and opposed flame spread [250]. The effects of CO addition on the propagation of CH_4 triple flames after ignition has been studied [249], and it was found that the normalized global flame speed was (as theoretically predicted) proportional to the square root of the density ratio between the reactants and the products (Eq. 2.31 [251]) for flames with low CO content but not for the higher CO content as the flame was still in the developing stage.

$$\frac{\text{Maximum propagation speed}}{\text{Stoichiometric burning velocity}} = \sqrt{\rho_{\text{unburned}} / \rho_{\text{burned}}}. \qquad (2.31)$$

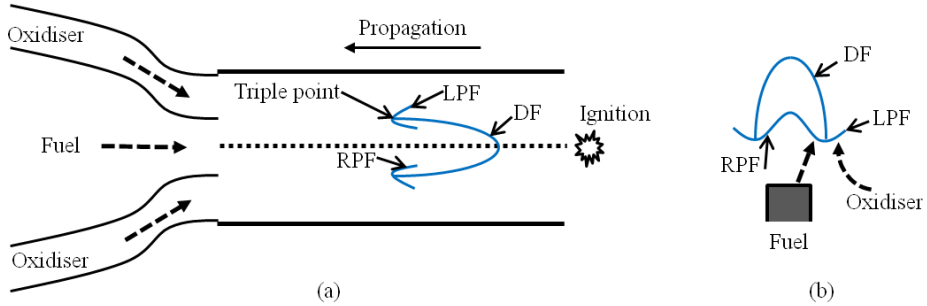

Figure 2.34: Triple flames; (a) In a tube configuration (adapted from [249]) and (b) Lifted jet flame (adapted from [250]). DF, LPF and RPF are diffusion flame, lean premixed flame and rich premixed flame respectively.

The propagation speed of triple edge flames with respect to the unburned gas depends strongly on the mixture concentration gradient in front of the edge, since the concentration gradient affects the local laminar burning velocity and the effective thickness of the flammable region [250]. The propagation of laminar propane jets ignited downstream and propagating towards the nozzle has been studied and it was found that the displacement speed varied non-linearly with axial distance due to the flow velocity being similar to the propagation speed of the triple flame, and significant buoyancy effects were observed when compared to the flame in microgravity [251]. Other propagation properties specific to jet flames will now be discussed.

2.5.3. Flame Propagation in Jet Flames

Lifted flames

Flame propagation in lifted flames is important for studies of lift-off height and flame stabilisation [252]. Changing the flow conditions can cause a change in lift-off height; the flame may propagate upstream/downstream, changing the lift-off height, and then stabilise. The interaction between large scale turbulent structures and a lifted flame are responsible for lift-off height fluctuations of the order of nozzle jet diameters. This is due to excessive stretch causing local flame extinction which allows vortices to carry the stabilisation point downstream, with turbulent flame propagation carrying the flame upstream again [252].

Turbulence can affect the flame propagation in lifted and non-lifted jet flames because of the interaction between the flame chemistry and the flow fields, due to local flame extinction and strain rates caused by the turbulence. The interaction of vortices and flame propagation will now be discussed.

Vortex Flame Interactions

The structure of premixed turbulent flames and the mechanisms controlling their propagation is important for accurate modelling, and the interaction between a laminar flame and turbulent flow can provide a better understanding of the turbulent flame propagation [77]. Straight flow disrupted by a vortex can produce mixtures that experience a range of strain rates [253]. The vortices can affect the flame propagation in three ways, depending on the values of the vortex maximum rotational velocity normalised by the laminar flame speed (U_θ/S_L) and the vortex core diameter normalised by the flame thickness (δ_V/δ_{L0}) [77]:

a) Small U_θ/S_L and δ_L/δ_{L0}: There is little or no effect from the vortex – the flame is faster than the vortex and propagates through it with only a small amount of wrinkling.
b) Intermediate U_θ/S_L and δ_L/δ_{L0}: The flame is significantly wrinkled – pockets of hot gases may be entrained into the burnt products.
c) High U_θ/S_L: Flame quenching may occur.

The vortices can also affect the regions of autoignition, depending on the scale of chemistry relative to the vortex [253]. The flame base of a lifted turbulent jet can be affected by vortex interactions which cause the flame base to move radially inward, subjecting it to larger gas velocities and moving the position of the flame base downstream [254].

Turbulence and vortex interactions in jet flames affect the turbulent flame propagation, depending on the size of the turbulent structures, owing to effects caused by strain due to the turbulence. This may also be affected by the fuel type used and the next section deals with the effects of hydrogen on flame propagation in jet flames.

Hydrogen

In turbulent jets, the mixture sensitivity can cause the turbulence in the jet to either promote flame propagation, leading to flame acceleration, or to cause flame quenching. In well-developed turbulence, this effect can be characterised by the expansion coefficient (the ratio of the density of the unburned to burned gases), which is more significant in hydrogen mixtures [55]. In turbulent hydrogen jets ignited at different locations from the nozzle, two regimes can be observed: fast combustion; where the

flame can propagate upstream and downstream even if the flow velocity is more than 100 m s^{-1}, and slow unstable combustion; where the flame can only propagate upstream [55]. For the fast regimes observed in [55] the upstream velocity reached 18 m s^{-1} and the downstream velocity reached up to 70 m s^{-1}, and this regime could only be observed for mixtures with > 11 % hydrogen. In addition, upstream propagation was more difficult when ignited further downstream [55].

For non-premixed lifted jets, where the lift is caused by coaxial air, the stabilisation is due to edge flame propagation [255]. However, the addition of nitrogen in non-premixed hydrogen lifted flames can cause the flame structure to become more premixed, due to the destruction of weak edge flames by turbulent structures, changing the stabilisation mechanism to premixed flame propagation [255]. Another non-premixed configuration using hydrogen to study edge flame propagation is the counter-flow regime, where local extinction causes thinning of the reaction zone, establishing an edge flame [256]. This edge flame interacts with an autoignition kernel, and the interaction is more significant with NO addition due to the catalytic effect, and the concentrations of H_2 and NO are significant to the sensitivity of ignition [256].

For ignition and flame propagation mechanisms, the concentration of hydrogen and the ignition location are significant, and fast propagation velocities can be observed. The next section deals with ignition and flame propagation in impinging flames.

2.5.4. Ignition and Flame Propagation in Impinging Flames

Flame propagation in impinging flames has not been widely studied. For flame propagation of jet flames near an impingement plate, the ignition location may affect the stable flame modes [34], including whether the flame is lifted or attached, and whether unburned fuel impinges on the plate at the stagnation region. Local re-ignition of areas extinguished due to a cold impingement plate may also occur due to the propagation from hot products, and the propagation of flames near solid surfaces is a very complex phenomenon [257].

Flame Stretch in Impinging Flames

Many studies focus on the effects of flame curvature and strain rate and it has been observed that flame curvature changes with respect to the location in the turbulent flame zone of an impinging methane air flame [258]. Also, transient flame propagation in

areas of high stretch rate, caused by impingement of a microjet on counterflow flames of H_2 and N_2, can exist (whereas the steady flame cannot), allowing reignition of the flame [201].

The ignition location is important in determining the combustion mode in impinging flames [34, 80]. The global stretch rate (the ratio of mean nozzle exit velocity to nozzle-to-plate distance) has been identified as a cause for preventing ignition in the centre of a blown ring flame (see Section 2.2.2.1), whereas a normal ring flame can be ignited in the stagnation region, causing transformation into a disc flame [34]. The global stretch rate, ignition location, equivalence ratio and turbulent structures all affect the final flame structure in impinging flame jets [34].

Propagation after Ignition

The propagation from ignition to combustion for methane and propane impinging jets has also been studied using digital flame colour discrimination (DFCD) and schlieren, focusing on the propagation of the flame from the point of ignition to a stable flame [212]. That work is similar in configuration to the work in this thesis; however different experimental techniques and fuels will be used. There is a lack of research concerning the propagation of hydrogen impinging jets, which will be a focus of this thesis. The propagation of hydrogen is very different to that of methane and propane and so the propagation of hydrogen flames after ignition in an impinging flame configuration will be compared to methane, and the effect of CO_2 addition to hydrogen will also be explored. Varying nozzle-to-plate distances and fuel exit velocities will also be explored.

2.5.5. Conclusions

Some important parameters, including flame stretch, and some common configurations concerned with ignition and flame propagation have been discussed. It has been identified that hydrogen content is significant in flame propagation studies due to the density difference between the burned and unburned gases, and that flame stretch is present in the stagnation region of impinging jet flames. However, there is a lack of research concerned with the ignition and flame propagation of hydrogen impinging jet flames, and this will be studied in this thesis.

2.6. Literature Review Conclusions

Advances in computational ability, theoretical understanding and optical techniques have allowed combustion to be studied in more depth. Cleaner fuels such as hydrogen and syngas have received much attention in recent decades. However, the properties of hydrogen are very different to the properties of other mainstream fuels such as methane and propane. Therefore, the differences between hydrogen and these hydrocarbons must be properly understood for the development of combustion devices.

An impinging flame configuration gives a simple geometry, good optical access and a controllable experimental environment, which is excellent for the study of flame-wall interactions of jet flames. Research in impinging flames has been reviewed, and most researchers study methane or butane flames impinging onto water cooled plates to look at the heat flux distribution. This thesis will use uncooled plates and will look at the temperature profiles of the flame impinged plates, rather than the heat flux, as the wall temperature can give information into the flame wall interaction and radiation losses from the plate. In addition, hydrogen and syngas will be the main fuels studied in this thesis as these fuels are becoming more widely used but their properties differ greatly from hydrocarbon fuels. The fuels will also be compared to propane and methane.

The schlieren technique is excellent for visualising convective plumes and density gradients in jet flames, and with high speed imaging, can allow high spatial and temporal resolution of the density structure of the jet flames. The mixing regions, convective motion and turbulent structures can be visualised, and these will be applied in an impinging flame configuration, which has been studied in less depth with the schlieren technique than for free jet flames. A method for quantifying the turbulent structures from the schlieren images will be developed and schlieren will also be used for observing the flame front propagation following ignition in an impinging flame configuration.

PIV can give quantitative information about flow fields and velocity distributions in impinging flames. PIV was attempted in this thesis but was unsuccessful due to various limiting conditions. These will be discussed in the next chapter.

Thermal imaging cameras are able to record 2D quantitative images of the temperature of the impingement plate. The experimental technique is non-intrusive and can give high spatial resolution when compared to thermocouples, which would give spot readings and require drilling. Thermal imaging can be a useful tool for monitoring combustion systems, for example spotting hot spots or low temperature regions where damage or flame quenching may occur. This thesis will develop the thermal imaging technique for use with impinging flames. A flame switch-off method will be developed in order to obtain thermal footprints of the flame impinged plate, and to give measurements of the high temperature, uncooled surface. The thermal footprints will also be used to calculate radiation losses from the plate, which so far have not been widely studied. An iterative emissivity correction method will be developed in order to deal with surfaces whose emissivity depends on the temperature being measured, using fused quartz as a basis. The effect of plate material will be studied by also using a heavily oxidised steel plate. The thermal footprints will be used with the schlieren technique to test the effects of flame-wall interactions of propane, hydrogen and syngas flames. The methodologies mentioned will be described in the next chapter.

The areas to be studied in this thesis will be in two parts; firstly, the effects of fuel and flow conditions on the flame wall interactions of hydrocarbon, hydrogen and syngas flames impinging normal to a flat, uncooled plate will be studied using two nozzle diameters and two plate materials. This will allow information to be gained regarding hydrogen and syngas impinging jets at a range of experimental conditions. The wall temperature measurements will give quantitative information about the wall temperature profiles, which can be compared to the schlieren and direct images. The results will also be compared to propane impinging jets, and the effects of nozzle-to-plate distance and plate material will be analysed. Secondly, the flame propagation of impinging hydrogen jets will be studied, focusing on the effect of ignition location and comparing to impinging methane jets, and hydrogen with carbon dioxide and air addition. This will add to the limited research concerning the ignition and flame propagation of hydrogen impinging jet flames.

Advanced optical techniques will be utilised and developed in order to study the flame wall interactions and flame propagation of impinging flames of hydrogen and syngas under various flow conditions. Comparisons will be made with flames of propane and

methane and with varying syngas compositions. CHEMKIN and Gaseq will be utilised to calculate the 1D laminar flame speeds and adiabatic temperatures of the compositions used, which will aid in the physical understanding of the results obtained.

The theory and application of various experimental techniques has been discussed, along with a review of impinging flame studies. The next chapter deals with the specifics of the experimentation used in this thesis, including the burner, piping and impingement plate configuration, the gas control system, and the schlieren, direct imaging and thermal imaging setup. The methodologies for the flame switch off technique, thermal profiling, steady state determination, temperature dependent emissivity, radiation loss calculations, flame front propagation, and turbulent structure quantification will be described in the next chapter. Details of the PIV setup will also be discussed along with the problems faced with this technique for the aforementioned configuration. The computations using CHEMKIN and Gaseq will be discussed in the chapter following that.

3. Experimental Setup and Methodologies

3.1. Introduction

The main principles of various experimental techniques have been given in Chapter 2. This chapter focuses on the experimental setup and apparatus used in the remainder of the thesis. The specifications will be given, including for the flow control methods and imaging tools. The methodologies developed will be described, including an accuracy evaluation of each methodology.

3.2. Rig Setup

This section gives details of the rig used in the experiments. The details of the burners, plate holder and plate materials will be given, followed by a description of the mixing system, ignition methods, fuels and flow control.

3.2.1. Burners

There were two burners, with different nozzle sizes, used for the gaseous fuels in this thesis. Both burners had circular nozzles with pipes long enough to obtain fully developed flow. The nozzles and burner housing were made from stainless steel.

Small Nozzle

The first 'small burner' (Figs. 3.1a and b) had a nozzle inner diameter of 4.6 mm which was surrounded by a honeycomb mesh (37.8 mm diameter) that could allow the flow of air (coflow) around the nozzle. This burner was designed and built at the University of Manchester. The nozzle size allowed a range of flow conditions depending on the flow rates achievable for each individual flow controller, which will be discussed in Section 3.2.3. It also helped to prevent flashback due to the small interior piping, which would take heat away from the flash back flame before it could travel to the main fuel pipes. However, flashback was still a risk with the hydrogen flames, and so the hydrogen compositions were diluted with 1.67×10^{-5} m^3 s^{-1} nitrogen in order to prevent flashback. However, the nozzle size was too small to admit PIV measurements due to seeding particle clogging. The coflow section allowed a straight flow of air or inert gas to surround the main flame. Coflow air helps to stabilise flames and suppress flickering [113, 160]. The coflow was fed into a separate section whereby the air was fed through glass beads, which aided mixing and gave a uniform flow, and exited the burner through

the honeycomb which straightened the flow (Fig. 3.1a). Coflow was used in some of the experiments but was mostly not used. The burner housing was painted black in order to reduce thermal reflections from the burner to the plate for the thermal imaging measurements.

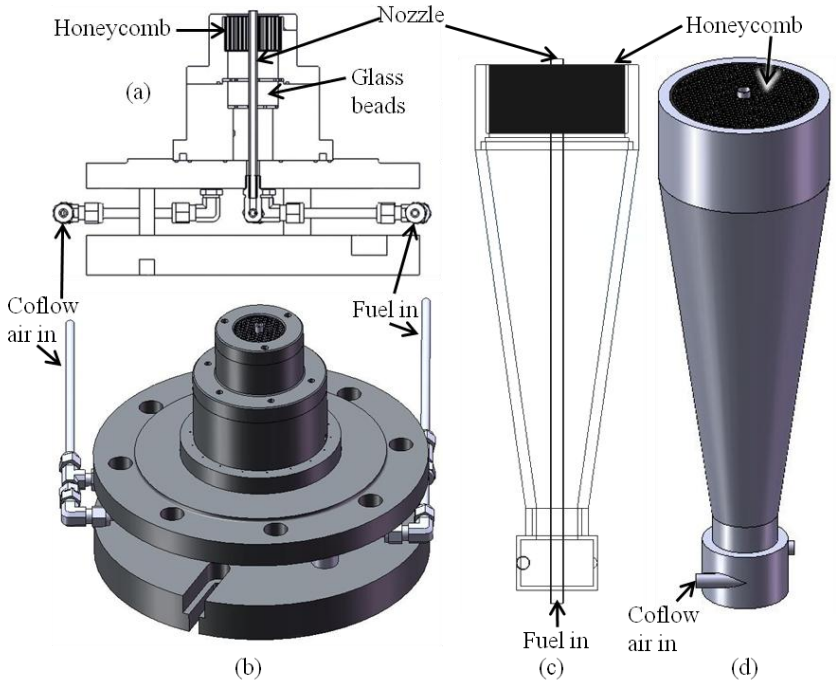

Figure 3.1: (a) Cross section and (b) Outward image of the 4.6 mm nozzle, straight coflow burner and (c) Cross section and (d) Outward image of the 8.0 mm nozzle, swirl coflow burner.

Large nozzle

The second burner (Figs. 3.1c and d) had a larger nozzle size of 8.0 mm (inner diameter). This allowed larger flow rates to be used without blow-out occurring. This meant that the thermal loading could be tested to higher values with lower nozzle exit velocities. The larger nozzle presented a greater risk of flashback, since the inner diameter of the nozzle was larger and so would take more time to quench the flame. Adding nitrogen reduces the laminar flame speed as will be discussed in Chapter 4, and increases the nozzle exit velocity so that the risk of flashback is reduced. The larger nozzle burner was designed to allow PIV measurements of the fuel stream to be taken, since the nozzle size and flow velocity could be large enough for the seeding particles to pass through without getting stuck and clogging up the pipes. However, many problems occurred with the PIV measurements as will be described in Section 3.7.

This burner was designed by the author at the University of Sheffield. It had a section for coflowing air to exit in a swirling motion. It did this by having the air enter a small chamber at the base of the burner, via two pipes that were tangential to the cylindrical surface. This caused a turning motion before the air was fed into a conical chamber where it slowed down and mixed via diffusion before exiting the burner in a swirling motion. However, coflow was not used on the second burner due to time restraints, and is reserved for the scope for future work.

3.2.2. Impingement Plates and Device

This section gives details of the device used for holding the plate above the flame, and of the specifications of the two plates used in the experiments.

Device

A schematic diagram for the device that held the plate is shown in Fig. 3.2. It consisted of a heavy stand, capable of holding the plate in place without wobbling. A vertical knife edge and a screw system with a turning knob were installed to move the plate up and down accurately to 1 mm. The plate was supported by an upper ring, 0.39 m in diameter, with three small, evenly spaced spindles to hold the plate at the edges without causing disturbances in the flow. The device allowed the plate to be held horizontally without wobbling and the plate could be moved up to 0.8 m in the vertical direction.

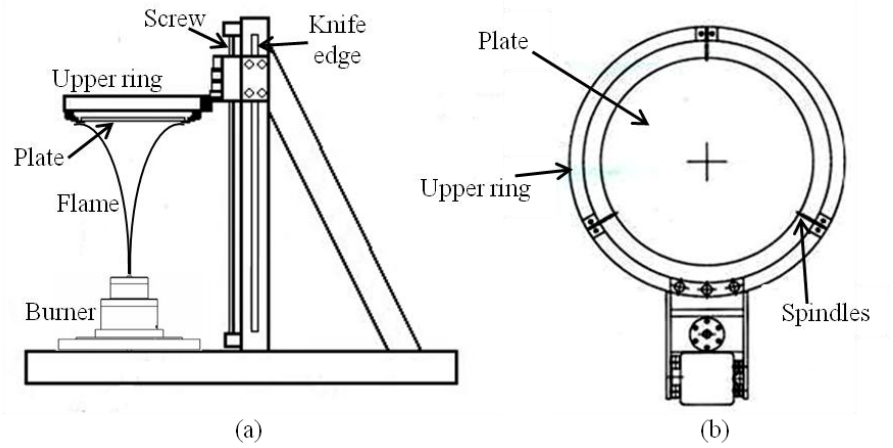

Figure 3.2: Device for holding the plate (a) Side view and (b) Top view.

In all cases in this thesis, the plate was held horizontally above a vertical impinging jet flame. The device allowed viewing horizontally from the side, used for the schlieren, direct imaging and PIV measurements, and from the bottom (at a minimum angle of 40°

to the plate normal) used for thermal imaging and direct imaging. The specific setups for these experimental techniques will be discussed in Sections 3.4 to 3.7.

Plate Materials

The experiments were performed using impinging flames of various fuels and flow conditions. In addition to this, two different impingement plates were used. The first was a heavily oxidised stainless steel plate, 0.3 m in diameter and 10 mm thick. The emissivity of oxidised steel is widely known to be insensitive to temperature, and its value was taken as 0.79 from [236] (between 473 K and 873 K) and [235] (between 293 K and 811 K). The temperature ranges in these sources are very close to the temperature range of the plate in the results and so a constant emissivity of 0.79 was assumed for all cases. This allowed the thermal imaging measurements to be made without emissivity corrections. However, for some of the experiments the plate had been polished, and became unevenly oxidised when heated. This allowed oxidisation effects to be explored and will be discussed in Section 5.2.5. In addition, for some cases the surface was coated with soot, and so a constant emissivity of 0.96 was assumed for these cases [237, 238].

The other plate was a fused quartz plate, 0.3 m in diameter and 6 mm thick. The emissivity of quartz varies with temperature, which allowed experiments to be performed regarding this emissivity-temperature dependence. This will be discussed in Section 3.6.4. Unfortunately, the quartz plate cracked when heated with the hydrogen flame, due to uneven thermal stresses, and so the results for the quartz plate are limited to propane flames.

3.2.3. Fuel and Flow Control

This section deals with the specifics of the fuel compositions, ignition methods, flow control and gas mixing systems.

3.2.3.1. Fuels

The fuels for both burners were supplied from gas cylinders, which were kept outside for safety reasons. The individual gases were propane (C_3H_8), methane (CH_4), hydrogen (H_2), carbon monoxide (CO), carbon dioxide (CO_2), nitrogen (N_2) and air. The air was supplied from an air compressor which was installed inside the lab. However, the air

from the compressor was more humid than from the cylinder, and so bottled air was substituted for the PIV experiments. This will be discussed in Section 3.7.

The propane and methane were not mixed with the other gases (except premixing air), but the gases for the syngas were mixed in order to achieve the required compositions. The mixing system will be described in Section 3.2.3.3. Compositions of syngas with the maximum values of H_2, CO, CO_2 and N_2 respectively were used based on data from various sources provided by Siemens, Lincoln (Table 3.1). In order for simpler experimentation at a laboratory scale, the compositions were changed by removing the minor constituents and keeping the H_2/CO volume ratio the same. In this way, syngas compositions named 'high H_2', 'high CO', 'high CO_2' and 'high N_2' were studied and the compositions are shown in Table 3.2.

	High H_2	**High CO**	**High CO_2**	**High N_2**
% H_2	61.9	31.8	34.4	10.7
% CO	26.2	63.5	35.1	29.2
% CH_4	6.9	0.4	0.3	0.01
% CO2	2.8	3.6	30.0	1.9
% N_2 + Argon	1.8	0.5	0.2	54.0
% H_2O		0.2		4.2
H_2/CO Ratio	2.36	0.5	0.98	0.37
Source	SVZ, Schwarze Pumpe	Opti, Nexen	Shell, Pernis	Puertellano, Spain
Gasifier	CoGen GSP	Unspecified	CoGen Shell	IGCC
Fuel Source	Coal/Waste	Unspecified	Oil	Coal/Pet Coke

Table 3.1: Syngas properties taken from real syngas data.

Composition	**H_2/CO**	**% H_2**	**% CO**	**% CO_2**	**% N_2**
High H_2	2.36	70.3	29.7		
High CO	0.50	33.4	66.6		
High CO_2	0.98	34.6	35.3	30.1	
High N_2	0.37	11.4	31.1		57.5

Table 3.2: Constituents by volume of the syngas compositions with minor constituents removed.

The propane and methane flames could become quite sooty and so an extraction system was put in place to remove the soot particles from the ar. It also meant that any fuel that was leaked into the air was quickly removed. The extraction caused a slight draught in the air and so the burner was placed directly underneath the extraction system in all cases to stop the flow being distorted. However, the extraction was not strong enough to change the flow fields and the effect of the extraction on the flame was minimal in all cases.

3.2.3.2. Ignition

For the wall temperature measurements (Chapter 5), where the ignition mechanism did not significantly affect the results, the flames were ignited with a pilot flame. This was produced by a single pulse spark Cricket Firepower Lighter, which used a piezoelectric mechanism to generate voltages over very short time intervals and LPG fuel. The flame was held above the burner nozzle until a flame was established and then removed.

For the ignition experiments (Chapter 6), the flames were ignited with the same device but without the gas, so that only a spark was produced, hereafter named the 'spark igniter'. In addition, for some of the results, an ignition device was designed in order that the ignition location could be fixed. This consisted of an electric spark generated between two steel electrodes with sharpened edges, hereafter named the 'electrode igniter'. The spark was generated from a Kawasaki ignition-coil (TEC-KP02) and powered by a sealed lead acid battery (12 volts, 1.2 amp-hours). It produced a consistent spark voltage of approximately 1 kV. The flames were ignited at various locations between the plate and nozzle, which will be discussed, along with the accuracy of these methods, in Section 3.4.4.

3.2.3.3. Mixing System

A mixing system was designed in order that the gases for the compositions with/without premixed air were well mixed before entering the burner nozzle. The system, shown in Fig. 3.3, consisted of separate pipes for each fuel, 6mm in diameter. The flow rates were controlled by flow controllers, which will be discussed in Section 3.2.3.4, and LabVIEW, which will be discussed in Section 3.3. The gas lines were connected to a series of 'tee' junctions placed after the flow controllers, connecting them to the main fuel line. This pipe then led to a mixing cylinder, 500 cm^3, where the fuels became well

mixed due to the diffusion of the gases from the small pipes into the large cylinder, and from vortices created in the corners of the cylinder. The mixed fuel then exited the cylinder into the second main fuel line, 6 mm in diameter, which was connected to the burner nozzle. The air for the premixing was fed into the mixing chamber in the same way as the other gases. However, the air for the coflow was separated from the premixing air before the flow controller, and fed into its own (larger) flow controller and directed to the coflow section of the burner (Fig. 3.3). The individual flow controllers will now be discussed.

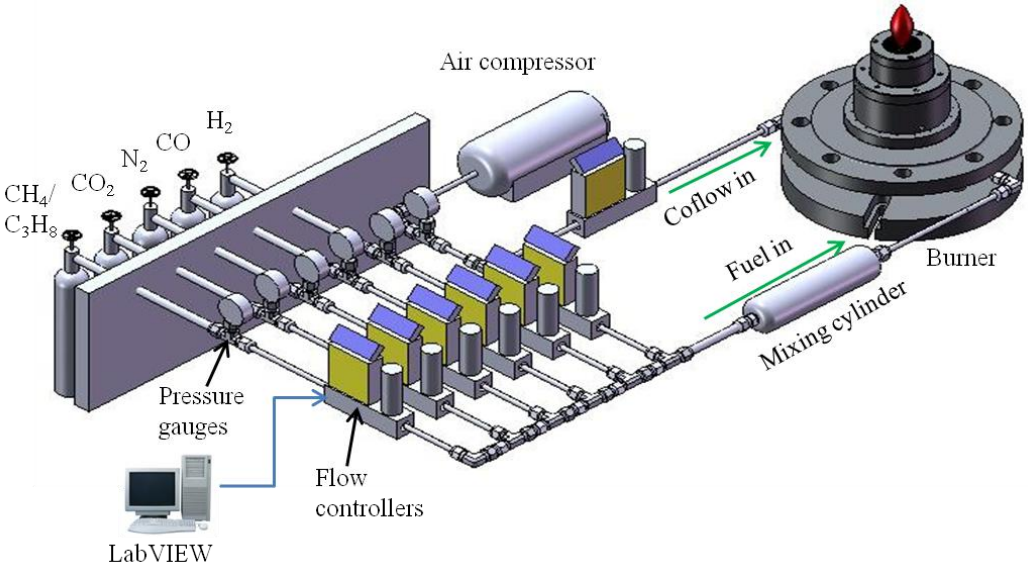

Figure 3.3: Sketch of the piping system for the mixing of the gases for the fuel and separate coflow junction (not to scale).

3.2.3.4. Flow Controllers

The flow rates of the fuels were individually controlled by digital Gas Flow Control (GFC) Aalborg flow controllers and LabVIEW. The LabVIEW system will be discussed in Section 3.3. The flow controllers had individual maximum flow rates to allow a range of nozzle exit velocities. The maximum nozzle exit velocities, for the individual gases and for the syngas compositions are shown in Table 3.3. However, due to factors causing blow-out, flames could not be stabilised at the maximum flow rates for all fuels, and so the values in Table 3.3 are based on the flow controller capabilities and not for stable flames. The equivalence ratio and Re dependence on the blow-out and impingement plate stabilisation, and hence the actual ranges of flow conditions will be discussed in Chapter 6.

Gas	Maximum Flow Rate ($m^3 s^{-1}$)	Maximum Nozzle Exit Velocity ($m s^{-1}$)	
		Small Nozzle	Large Nozzle
H_2	1.0×10^{-3}	60.2	19.9
CO	1.0×10^{-3}	60.2	19.9
CO_2	1.0×10^{-3}	60.2	19.9
High H_2	1.4×10^{-3}	84.2	27.9
High CO	1.5×10^{-3}	90.3	29.8
High CO_2	2.8×10^{-3}	168.5	55.7
High N_2	1.4×10^{-3}	84.2	27.9
C_3H_8	1.0×10^{-3}	60.2	19.9
CH_4	1.0×10^{-3}	60.2	19.9
N_2	8.3×10^{-4}	50.1	16.6
Premix Air	8.3×10^{-4}	50.1	16.6
Coflow Air	3.3×10^{-3}		

Table 3.3: Maximum flow rates and corresponding nozzle exit velocities for each gas and nozzle size.

The flow controllers use a primary flow conduit and a capillary sensor tube, both at laminar flow so that the ratio of the flow rates is constant [259]. Temperature sensing windings on the sensor tube are then heated and the gas flow transports heat from the upstream to the downstream positions. This causes a temperature differential that is proportional to the change in resistance of the windings, which is in turn linearly proportional to the instantaneous flow rate [259]. Output voltage signals are then generated, which correspond to the gas flow rate.

The gases flow through a proportionating electromagnetic valve with an appropriately selected orifice in order to maintain the flow rate at the selected value [259], which is controlled by the LabVIEW system. Due to this method of controlling the flow rates, slight fluctuations occur, but these do not significantly affect the results. Therefore, all flow rates quoted in this thesis are the averaged flow rates produced by the flow controllers. The next section describes the LabVIEW system used for controlling the flow rates of the individual gases, including using LabVIEW to calculate various properties of the fuels depending on the flow rates used.

3.3. LabVIEW

LabVIEW is a computer program that allows the calculation of equations and the control of devices via an image based programming language. In order to control the individual flow rates of the gases, a LabVIEW Virtual Instrument (VI) was used. This VI allowed the user to input the desired flow rate and would send the signal to the flow controllers using a data acquisition (DAQ) card system. This meant that the gases could be accurately mixed to the correct proportions.

Modifications were made to the VI so that values of Reynolds number (Re), equivalence ratio (ϕ), nozzle exit velocity (v), thermal loading, viscosity (μ), density (ρ), molecular weight, Wobbe number and total flow rate could be seen on the screen. It also gave values of mass and volume percentages of the individual fuel components. However, due to the small fluctuations in the voltage readings of the DAQ card these values also fluctuated. Therefore, a separate VI was designed to calculate these values using a manual input of the individual flow rate values. The front panel (i.e. the user interface) of this VI is shown in Fig. 3.4. When CH_4 was used, the values for C_3H_8 were changed to those for CH_4, as these controllers shared one data cable.

An example of the use of the block diagram (i.e. the programming space) of the VI is shown in Fig. 3.5. This example is for the nozzle exit velocity calculations. More details of the other calculations and the whole block diagram are given in Appendix A. The nozzle exit velocity was calculated from Eq. 3.1:

$$v = \left(F \middle/ \pi r^2\right)\left(0.001 \middle/ 60\right), \tag{3.1}$$

where v is the nozzle exit velocity (in m s^{-1}), r is the nozzle radius, F is the total flow rate (in litre/minute) and 0.001/60 is the conversion factor for changing litre/minute into m^3 s^{-1}.

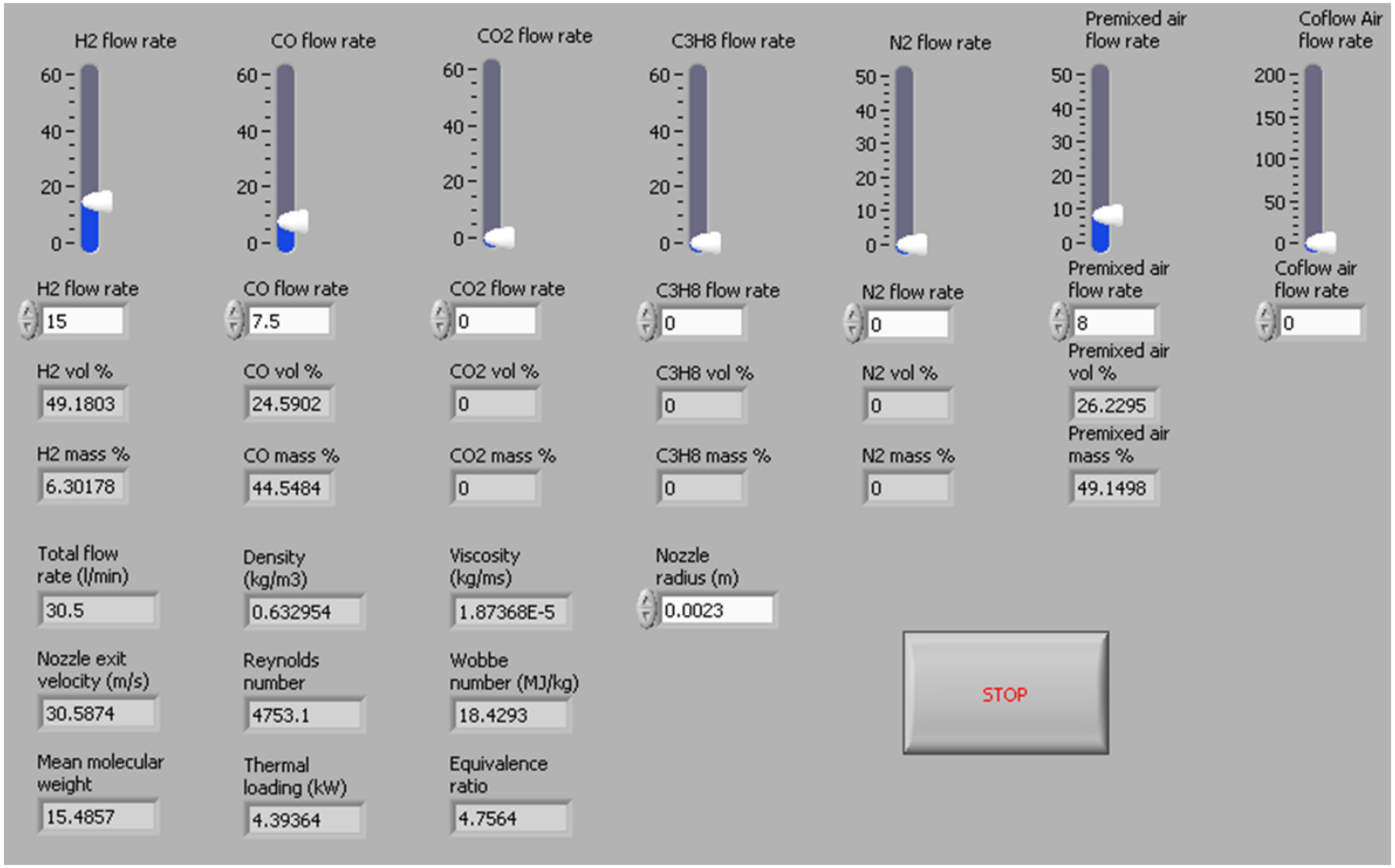

Figure 3.4: Front Panel of the LabVIEW VI at an example flow mixture.

In the VI (Fig. 3.5) the flow rate values were used as the input commands and summed to give the total flow rate. The nozzle radius was added as an input and this was squared (multiplied by itself in the bottom middle of Fig. 3.5) and multiplied by π to give the nozzle area. The total flow rate was then divided by the nozzle area and multiplied by 0.001/60 to give the fuel exit velocity as in Eq. 3.1. This small block diagram is a section taken from a larger block diagram (see Appendix A) which includes the other calculations shown in the front panel in Fig. 3.4.

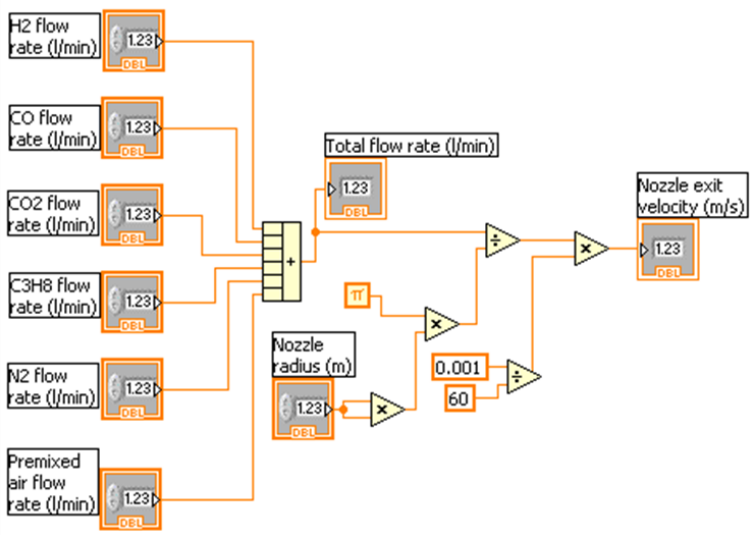

Figure 3.5: Nozzle exit velocity calculations using LabVIEW.

LabVIEW can be a very useful tool for quickly calculating the properties of given gas mixtures, and for electronically controlling the individual gas flow rates. It was used to find the flow rates of the mixtures at specified conditions, for example finding a mixture of a certain composition at a certain thermal loading and equivalence ratio. The VI (Fig. 3.4) was used prior to the experiments, adjusting the flow rates using a trial and error method until the desired conditions were met. The resulting flow rates were then inputted into the VI that was connected to the rig and was used to control the gas flow rates.

The experimental apparatus used for controlling the flow and igniting and mixing the fuel, and the rig have been described. The following sections deal with the specifications and methodologies for the various diagnostic techniques. Accuracy evaluations will also be given for each of the methodologies described.

3.4. Schlieren

3.4.1. Experimental Setup

Specifications and Configuration

The schlieren technique (described in Section 2.3.3.1) was used for visualising the density distributions within the flame and surrounding gases. The Z-type arrangement was used (Fig. 3.6) as this was easier to accommodate in the lab since it requires less space. A monochrome Photron SA 1 high speed camera was used to capture the results. λ/10 grade parabolic mirrors were used to ensure high quality results. The light source was a 500 W Xenon lamp, which gave a high enough intensity of light for the schlieren technique.

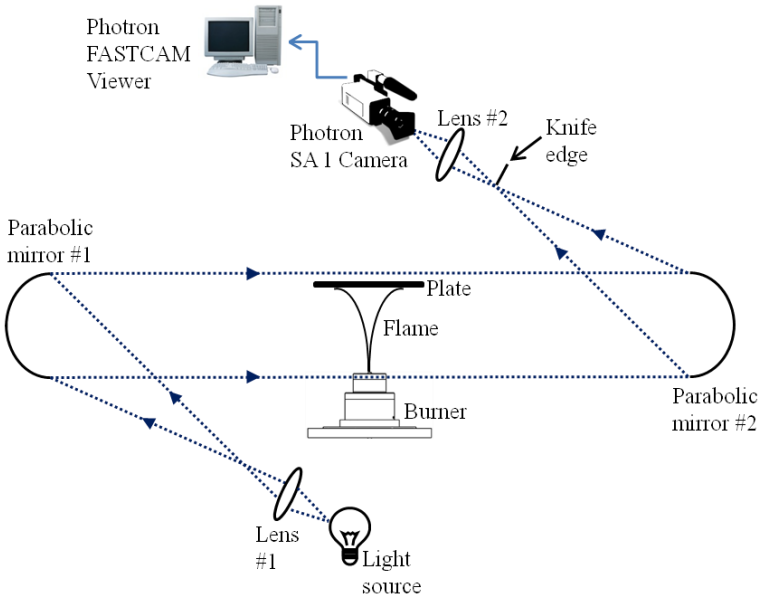

Figure 3.6: Z-type schlieren setup.

Procedure

The mirrors had a focal length of 3.048 m and a diameter of 0.3048 m. When setting up the schlieren, lens 1 (Fig. 3.6) was used to focus the light onto mirror 1 and then the angle of mirror 1 was adjusted so that the beam fully covered the area of mirror 2. A screw was then placed on top of the burner nozzle, and lens 2 was used to focus the image onto the camera, using the screw thread as a visual aid. The knife edge was then positioned at the focal point of the beam from mirror 2 and adjusted until the darkness of the image was correct. The camera was turned on and connected to the Photron

FASTCAM Viewer software during the setup to help with the focusing of the image and the adjustment of the knife edge.

The analysis procedures for the various schlieren diagnostics will now be given, along with accuracy evaluations for each methodology.

3.4.2. Impinging Flame Structure

Methodology

The schlieren images were used to visualise the flow structure and turbulence. Structures such as the flame boundaries between the products and the ambient air, and the products and reactants, unburned fuel, position of the hot gases and heat convection can easily be seen with the schlieren technique (Fig. 3.7). However, the schlieren imaging gives an integrated view of the changes in density throughout the flow field, and is not a '2D slice'. Therefore, some obscuring is seen by the hot gases towards the front and back edges of the plate (Fig. 3.7), which bend downwards, due to flame bulging in the outward radial direction [11]. This causes the hot gas region to appear thicker than it actually is in the stagnation region.

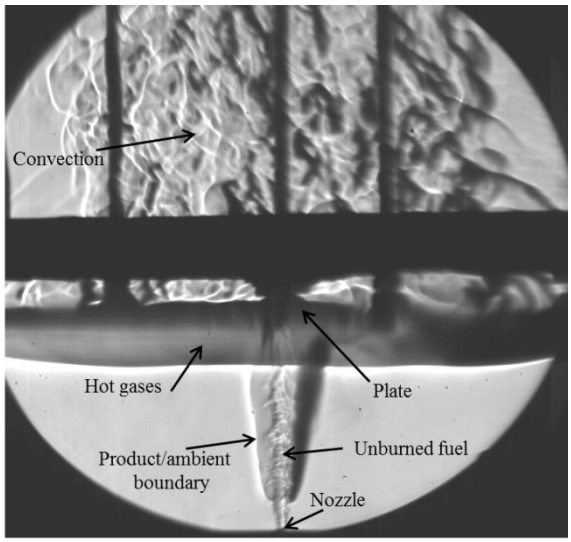

Figure 3.7: Example schlieren image of a lifted propane flame showing the positions of the nozzle and plate, flame edge, hot gases, unburned fuel and convection currents off the top of the plate.

In addition, the 3D qualities of the flame might make the flame appear differently on the image than in reality, for example if the flame is lifted on one side the schlieren might not pick up this information depending on the viewing angle. However, much

information can be gained by using schlieren imaging, particularly when used with other techniques, as will be shown in Chapter 5.

Accuracy

The images captured in this work were all taken using the maximum shutter speed of 1 μs and a frame rate of 1000 fps. The high shutter speed allowed good temporal resolution and ensured that there was no blurring of the image even when the velocity of the fluid was high. The frame rate allowed high speed analysis to be performed on the schlieren images. The camera resolution of 1 Megapixel (MP) was high enough to allow visualisation of small features in the flow such as the unburned gases and small scale turbulent structures. A quantitative methodology was also developed to analyse the turbulent structures visible in the density fields of the impinging flames and this will be discussed now.

3.4.3. Wrinkle Scale Methodology

Methodology

A typical schlieren image of an impinging flame can clearly show two distinctive regions: the fuel/air mixing region and the flame/hot gas/air region, as these regions are visually different from one another and can be picked out by eye. Each region has characteristic scales. The wrinkling scale in the fuel/air region is small in comparison with the flame/hot gas/air region due to the much lower density in the latter. It is reasonable to say that more ambient air mixing with the hot combustion gases would reduce the average size of the turbulent structures, especially when the Reynolds number (based on the nozzle diameter) is the same or very close, due to the added mixing in this region. In addition, the flame edge and unburned fuel streams can also be seen. Analysis of turbulence wrinkling scales was performed using the schlieren images in the following way.

The schlieren images give a visual distribution of the integrated density gradients in the flame, unburned fuel and hot gas/flame impingement regions (Figs. 3.8a (i) to (iii) respectively). A methodology has been developed to quantify the size of these turbulent structures, whereby the lines in the image were detected using the MATLAB line detection tool (Fig. 3.8b). The percentage of space occupied by boundaries (white pixels/total pixels) was defined as the ‘wrinkle scale’. This gives an estimate of the

average number of the turbulent structures in each area and so the smaller the value of the wrinkle scale, the larger the average size of the structures and vice versa.

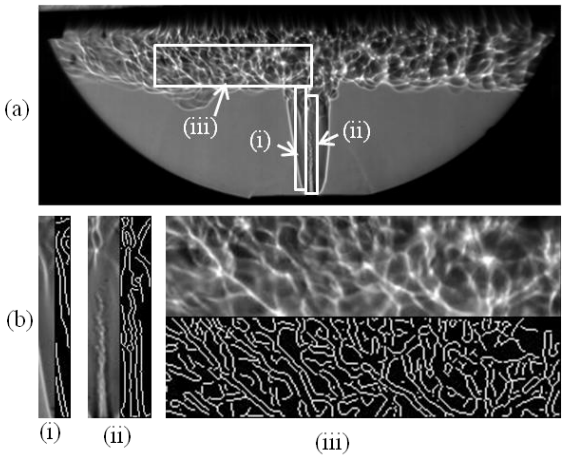

Figure 3.8: (a) Example schlieren image with (i) The flame region, (ii) The fuel region and (iii) The impinging region and (b) Corresponding line images.

Interrogation Areas

From the image (Fig. 3.8a), it is clear that there are distinctive small scale and large scale 'wrinkles' in the flame, unburned fuel/air and hot gas/air zones (Fig. 3.8a (i to iii) respectively). Three interrogation areas were assigned to these zones and they are defined as 'flame', 'fuel' and 'impinging' respectively as shown in Fig. 3.8. The flame area was defined as an area starting 5 mm left of and 4 mm up from the nozzle and spanning an area of 5 mm to the left and 64 mm upwards (Fig. 3.8a (i)). The fuel area was defined as an area enclosed by 5 mm to either side of the nozzle and spanning upwards by 25 mm for the pure hydrogen flames and 67 mm for the syngas flames (Fig. 3.8a (ii)), due to the larger height of the unburned fuel for the syngas cases (Section 5.5). The impinging area was defined as an area from the centre line, 4 mm down from the plate and spanning an area of 0.1 m to the left and 33 mm downwards (Fig. 3.8a (iii)). In this way, different regions of the flame and different flame conditions could be compared in terms of the size of the turbulence scales.

Accuracy

The areas were chosen to ensure that the interrogation zones were of equal size and position for the various cases and so that they did not go outside of the flame area, which would give a larger amount of empty space and so would reduce the wrinkle scale value. The resolution of each image was kept the same so that the wrinkle scales

could be comparable between cases. The methodology was developed in order to compare the flame wall interaction of different flow conditions in the same setup, and not as a general methodology for quantifying turbulence in flames.

The wrinkle scales for ensemble averages of sequences of 26 images at time intervals of 1 ms were calculated for the three flame interrogation areas. The analysis was only performed on the cases with notable turbulent structures visible in the schlieren images, which were the hydrogen premixed cases and the syngas cases (Sections 5.4.4.2 and 5.5 respectively).

3.4.4. Flame Front Propagation

Methodology

Schlieren was also utilised for the analysis of the ignition and flame propagation characteristics of impinging flames. The flame edge position can be seen due to the large density variations between the burned and unburned gases. The propagation of the boundary between the hot products and the reactants/ambient air mixture will be studied and the results will be presented in Chapter 6.

Images from the points of ignition to attachment were captured using high speed schlieren imaging. The images were then analysed in the following way: The pixel information was used to calibrate the height per pixel from the nozzle to the plate. A sequence of images, starting with the ignition and ending with the flame attachment to the nozzle or contact with the plate, was used for the analysis, in which the height of the flame boundary at the centre line was plotted. Five ignition locations were studied; ignition at the centre of the plate, at radial plate locations of 50 mm and 100 mm from the centre, and axial locations of half way between the nozzle and the plate and at the nozzle itself. Example sequences of images for the ignition process for the plate centre, between the nozzle and the plate and the nozzle locations are shown in Figs. 3.9a to c respectively. The analysis was done for the lower flame boundary in the cases where the flame was ignited at the plate and in the middle, named ‘Plate’, ‘Plate, 50 mm’, ‘Plate, 100 mm’ and ‘Middle, Down’ respectively. It was done for the upper flame boundary for the cases where the flame was ignited at the nozzle and the middle locations, named ‘Nozzle’ and ‘Middle, Up’ respectively, since the flame propagated upwards and downwards when ignited in the middle (as shown in Fig. 3.9b).

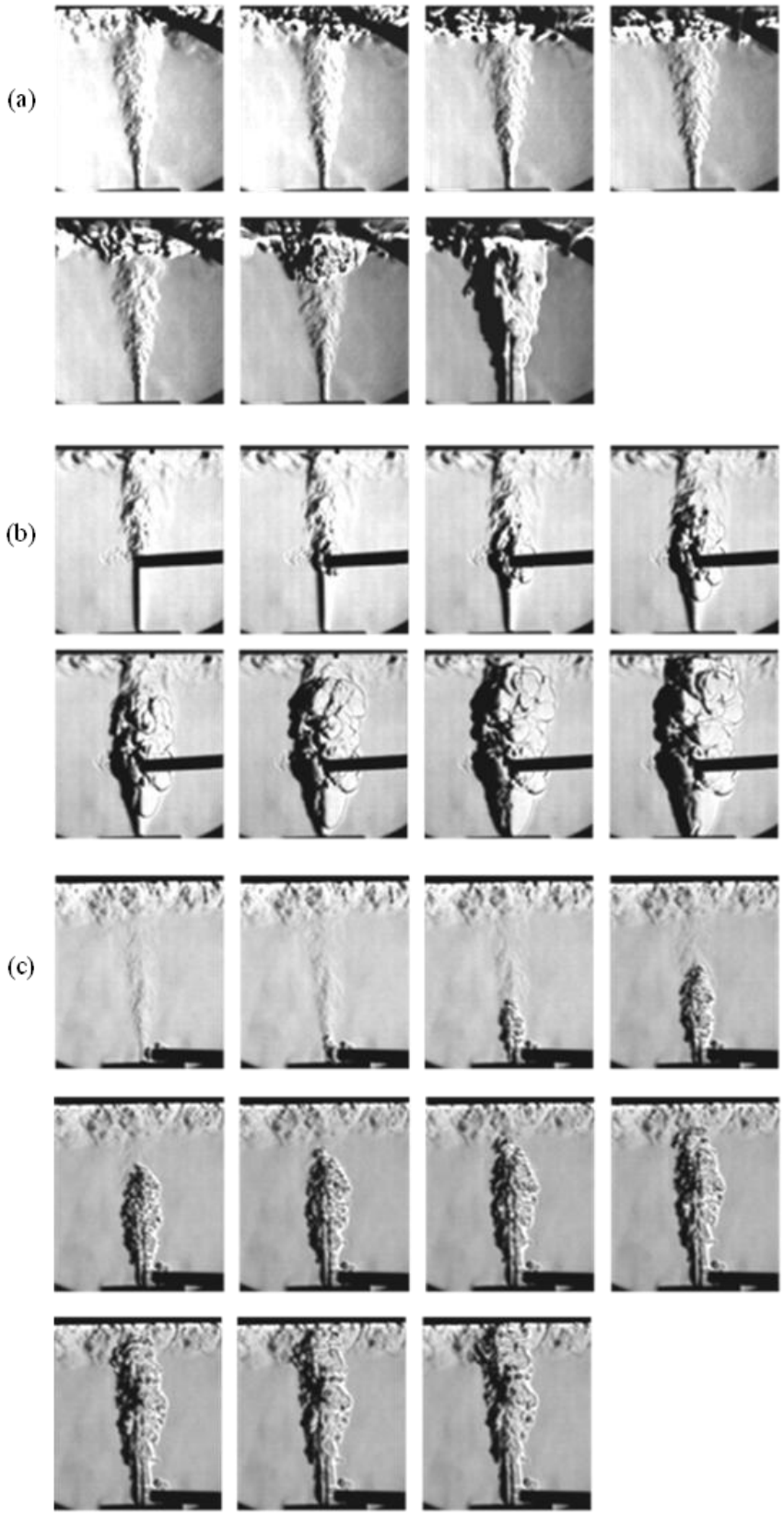

Figure 3.9: Example of ignition sequences for hydrogen diffusion flames at 10 ms^{-1} when ignited at (a) The plate, (b) The middle and (c) The nozzle, with 0.04, 0.001 and 0.002 s between images respectively.

The heights of the respective flame boundaries at the centre line were then plotted against time, with ignition at t = 0 s. In addition, for the cases ignited at 50 mm and 100 mm from the plate centre, the radial position of the flame was plotted as well. From these plots, best fit polynomials of the order of 3 to 6 were fitted to the data, and the derivatives were found and used to plot the velocity of the flame front at the centre line against time. Figures 3.10a and b show examples of the height and velocity plots respectively for hydrogen flames at 10 m s^{-1}. The data points in Fig. 3.10b are for the velocity calculations using $\Delta h/\Delta t = (h_2 - h_1)/(t_2 - t_1)$, whereas the lines are for the calculations using the gradients of the best fit polynomials as described above. It can be seen that the lines taken from the best fit polynomials fit the data quite well but they do not take into account the zero velocity condition at t = 0. However, these lines give much smoother curves and remove the disjointedness that arises from the data processing. In addition, the velocity at t = 0 will be equal to the fuel velocity rather than 0 m s^{-1}. However, the fuel velocity cannot be subtracted from the propagation velocity since it differs between the nozzle and the plate due to air entrainment.

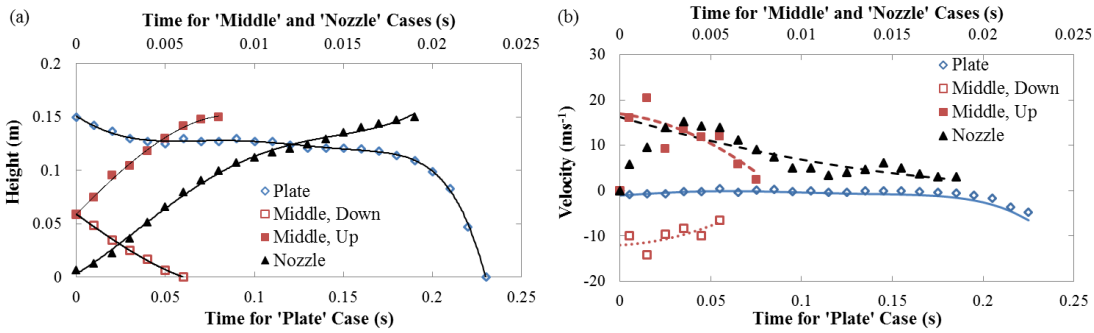

Figure 3.10: Example of (a) Height and (b) Velocity plots for a hydrogen diffusion flame at 10 m s^{-1}.

Pixel information was also used to calculate the spreading rates, θ, of the unburned fuel for each of the cases, as shown in Fig. 3.11. Pixel values from corner points of the 'triangle' of unburned fuel (before ignition) were used to calculate Eq. 3.2, where the symbols are demonstrated in Fig. 3.11, with the coordinate in the top left corner of the image at (0, 0). The spreading rate was used to qualitatively represent the amount of mixing with the ambient air in the shear layer.

$$\tan(\theta) = \frac{[(x_2 - x_1)/2] - [(x_{02} - x_{01})/2]}{y_0 - y_1}. \quad (3.2)$$

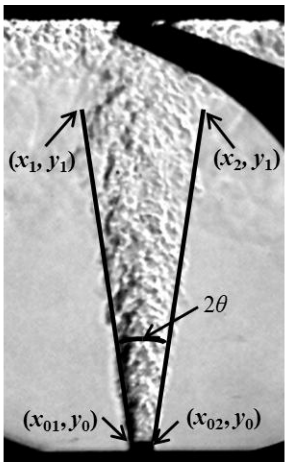

Figure 3.11: Example of the co-ordinate locations for calculating the spreading rate.

Accuracy

The flames in Sections 6.3.3 and 6.4 were ignited with the spark from the Cricket Firepower Lighter, judging the positions by hand. Each spark was produced by pressing the button manually. There were slight changes in the position of the igniter for each separate case, but this did not affect the results significantly compared to the larger changes in ignition location that were the subject of the study, and it was attempted to get as close to the plate centre, middle and nozzle as possible for the plate, middle and nozzle locations respectively. The spark generated hot gas pocket was approximately 20 mm in diameter before ignition took place, and so small changes in axial/lateral position of the igniter did not affect the results due to the large size of the spark in contact with the fuel/air mixture at the point of ignition.

Figure 3.12 shows the differences for two attempts with a small change in lateral position for the case of pure hydrogen diffusion flames at 28 ms^{-1}. Attempts 1 and 2 were with the igniter at 0.01 m and 0.002 m from the centre of the plate respectively. It can be seen that there is a difference in the height and velocity values, however, the trends are the same and of similar time scales (within 3 %). There are many uncontrollable factors that affect the repeatability of the results, such as fluctuations in the flow controllers that will affect the local flow velocity, fluctuations in ambient temperature and pressure, plate temperature and igniter power. In addition, the electrodes were not always a constant distance apart for the electrode igniter. The

differences in propagation time from the point of ignition to attachment were compared for two repetitions for most of the cases studied. On average, the difference between the propagation times, t_1 and t_2 (i.e. $|t_1-t_2|/((t_1+t_2)/2)$), for two repeated cases is 18.8 %, with the differences for turbulent, transitional and laminar flames at 19.0 %, 29.4 % and 15.2 % respectively. This is because of changes in axial position of the igniter, fluctuations in the flow velocity caused by the flow controllers, unreliability of the igniter kernel size and power and that the fuel must be ignited as soon as possible and so the fuel composition may not be perfectly steady when ignited. Therefore small changes in the igniter position do not significantly affect the results when compared to other factors.

The igniter was attempted to be in contact with the plate/nozzle for the 'Plate' and 'Nozzle' cases and so the axial position of the igniter did not significantly affect the results in these cases. The axial position for the 'Middle' cases can be seen by the height of the marker points at ignition (t = 0) on the graphs. Figure 3.9 shows that although the igniter was placed within the flow, and was quite large in size, the flow field is still symmetrical, indicating that the effect of the igniter to the flow field is minimal. The electrode igniter was used for the flames in Sections 6.2 and 6.3.2. This igniter was set to a fixed height using a screw thread and so was more accurate in terms of the ignition location, although could not be used as close to the plate or nozzle as the spark igniter. In addition, it had to be removed from the flame once ignited, causing small changes in location when replaced. No shock wave could be detected in the experiments. The sparks were relatively weak and may not have produced a shock wave and so in this study the shockwave did not play a role in the ignition process.

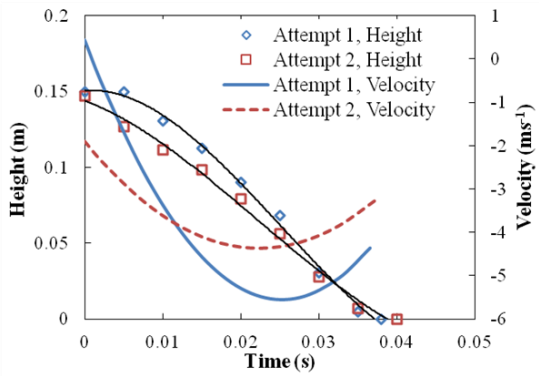

Figure 3.12: Graph of change in results with small change in ignition position for a hydrogen diffusion flame at 28 ms^{-1}, ignited at the plate centre.

The exposure time used in the high speed imaging was 1μs and the maximum velocity observed was less than 3 m s^{-1} for the methane flames, and 90 ms^{-1} for the hydrogen flames, which means that the flame front moved no more than 3 μm or 90 μm within 1 frame for the methane or hydrogen flames respectively. This means that the images were sharp enough to judge the height of the flame to an accuracy of 1 pixel. However, discrepancies occurred when judging the flame front position due to interferences from convection currents in the ambient air. These discrepancies were no more than 4 pixels. The largest distance per pixel observed was 0.46 mm and so the height measurements are accurate to 1.8 mm, and the error bars are too small to add to the graphs.

The accuracy of the curve fitting depends on the number of data points in the height/time graphs. For some of the cases, the velocity was so fast that only 5 data points were recorded. The curve fitting was performed in MATLAB and the lowest degree polynomial was used to give the best fit for the data and to avoid over-fitting. This method is accurate enough for the velocity trend approximations (Fig. 3.10), but not for calculating acceleration values, as this would require differentiating twice.

The propagation of the flame front is three dimensional and the schlieren images do not pick up on the 3D motion of the flame front. However, the analysis was done for the centre line of the flame front, which still gives insightful information into the propagation with or against the fuel stream flow. The main focus of the flame propagation studies is the trends of the instantaneous, time dependant propagation of the flame front at different conditions. Therefore, the results were not averaged over different cases as this would remove the instantaneous behaviour. The schlieren will be used for the aforementioned diagnostic techniques, and will be compared with the thermal imaging results and with the direct imaging. The next section deals with the use of the direct imaging camera for the impinging flames.

3.5. Direct Imaging

3.5.1. Experimental Setup

A Casio EX-F1 6 MP digital camera was used alongside the schlieren imaging so that visual images of the flames could be compared with the schlieren images. The camera has frame rate settings from 30 to 1200 fps for recording videos, with reduced image

size (336 x 96 Pixels) for the higher frame rate. It has International Standards Organisation (ISO) sensitivity settings ranging from 100 to 1600, and shutter speeds from 60 to 1/40000 s, with an ISO of 400 representing the slowest shutter speed and 1600 the fastest. The aperture size can be adjusted from f_{ap} = 2.7 to 7.5 [260]. The shutter speed and aperture size were varied when capturing images of the flames since the hydrogen flames have a much lower emission in the visible range and so a longer exposure time creates more visible images. The shutter speed for the propane flames was reduced due to the high emission from the yellow sooty flames. This was so that images could be captured showing the flame size and shape with the best temporal resolution and brightness for each flame. Since the images were only used for qualitative visualisation, the camera settings could be adjusted to suit the flame type without affecting the results. The camera was positioned horizontally to the plate so that the images could be compared to the schlieren images. In addition, for some cases, the camera was also positioned at an angle to the plate so that the flame distribution across the plate and the flame mode could be more easily visualised.

3.5.2. Comparison with Schlieren

The images showed vast differences in the position and size of the visual flame and the schlieren images; Fig. 3.13 shows an example of schlieren and direct images of the same flame. The position of the hot gas layer from the schlieren image (Fig. 3.13a) is represented by the white line in the direct image Fig. 3.13b). The flame also appears thicker in the schlieren images due to the mixing of the unburned and burned gases. This allows the flame wall interactions to be analysed in terms of the visual flame and of the density variations and hot gas layers.

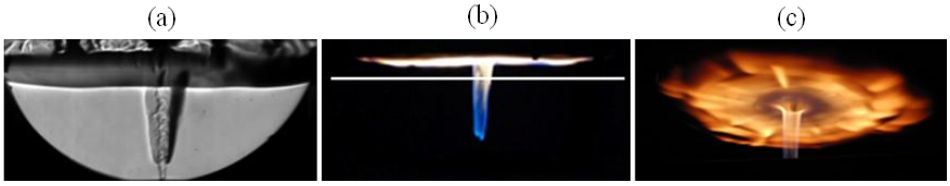

Figure 3.13: Examples of (a) A schlieren image, (b) A direct image from the side and (c) A direct image from below, for a lifted propane flame.

Figure 3.13c was taken at a different angle to Fig. 3.13b and shows the flame distribution across the plate but not the shape of the jet. Figure 3.13b and c also

illustrate the differences in camera shutter speed; for the higher shutter speed (Fig. 3.13c) the temporal details of the flame can be seen but the lower shutter speed (Fig. 3.13b) shows the flame colour and position. In addition to the flame visualisation, thermal imaging was used to measure the wall temperature. This will be discussed now.

3.6. Thermal Imaging

In addition to the flame structure visualisation techniques discussed, thermal imaging will be used to study the flame wall interaction in terms of the temperature distribution across the plate. Various methodologies have been developed in order to utilise thermal imaging as a tool for impinging flame analysis. These methods will be described in this section and the results will be presented in Chapter 5.

3.6.1. Experimental Setup

Camera Types

Two thermal imaging cameras were used; the FLIR SC3000 and the FLIR SC640. The mechanisms of these cameras have been described in Section 2.3.2.1.2. The SC3000 uses the self-cooling analysis system and the SC640 uses the uncooled microbolometer focal plane array. The specifications of each camera are outlined in Table 3.4.

The SC3000 was used for the experiments in this thesis due to the lower wait time and the higher frame rate. The SC640 has a higher spatial resolution and so was also used for some experiments. However, these results are not presented here as they were for comparison with the PIV measurements which were unsuccessful as will be discussed in Section 3.7. When balancing out the advantages of each camera, the SC3000 was more suited to the experiments, since portability and quick cool down times were not particularly required, whereas a high frame rate at a large picture size and a short wait time were very advantageous,. In addition, the resolution of the SC3000 was sufficient.

Feature	FLIR SC3000	FLIR SC640
Mechanism	Self-cooling analysis system.	Uncooled microbolometer focal plane array.
Frame rate	50 Hz with no reduction in viewing area, to 750 Hz with reduced viewing area size.	15 Hz with no reduction in viewing area, to 30 Hz with reduced viewing area size.
Cool down time	Approximately 6 minutes.	No cool down time.
Size/Portability	Large heavy camera and equipment not suitable for portable use with PC.	Smaller camera and equipment (weighing 1.7 kg) for portable use.
Wait time/availability	Needs to be booked 2-3 months in advance.	Needs to be booked > 5 months in advance.
Software	ThermaCAM Researcher.	ThermaCAM Researcher.
Temperature range	253 K to 2273 K.	233 K to 2273 K.
Accuracy	± 1 % for temperatures up to 423 K and ± 2% for temperatures over 423 K.	Unspecified.
Thermal sensitivity	20 mK at 303 K.	60 mK at 303 K.
Spectral range	8 to 9 μ.	7 to 13 μ.
Resolution	320 x 240 pixels.	640 x 480 pixels.

Table 3.4: Properties of the SC3000 and SC640 thermal imaging cameras.

Setup

Figure 3.14 shows the setup used for the thermal imaging. The thermal imaging camera was positioned at an angle of 45° to the plate normal for the quartz plate and 40° for the steel plate, which was the smallest angle achievable in the setup while being able to observe enough of the plate. This was acceptable since the directional emissivity for non-conductors is generally constant for angles less than the grazing angle of 40 ° for conductors and 70° for non-conductors [132]. Also, diffuse emissivity is nearly always an acceptable approximation, even though glassy materials may display strong secular peaks [130]. Since the angles were kept the same for the same plate material, the results could be quantitatively compared meaningfully. The methodologies developed for the thermal imaging analysis of impinging flames will now be discussed.

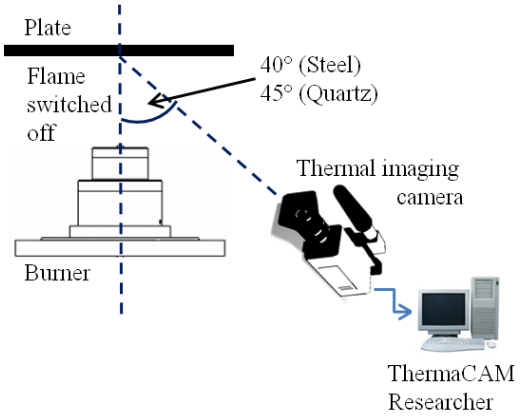

Figure 3.14: Schematic of the thermal imaging camera setup.

3.6.2. 'Flame Switch Off' Method

Methodology

The spectral ranges of both cameras were too small to measure the flame temperature due to the high range of emissions from the flame. Therefore the thermal imaging was used to measure the plate temperature by obtaining a 'thermal footprint' of the flame on the plate. This was done by heating up the plate at the set flow conditions and waiting until a steady state was reached. The steady state was determined by watching the temperature readings at particular 'spots' on the image (SP01, SP02 and SP03 in Fig. 3.15) and waiting until the temperature was no longer rising. This means that the temperature has reached a steady state since the amount of heat being put into the system from the flame is equal to the amount of heat lost to the atmosphere and to the plate. The large fluctuations seen in the first part of the graph in Fig. 3.15b are due to the flame emissions and movement. Three spots were chosen at different radial positions, and hence different temperature regions, for higher accuracy.

Once a steady state was achieved the camera was set to record at 50 Hz for the SC3000 and 15 Hz for the SC640, so that a high fame rate could be reached without loss of viewing area. The temperature could not be monitored while recording due to the slow buffering rate. The flame was then switched off suddenly at the valve and the 1st image without a flame was used for the analysis (for example the last image in Fig. 3.16). The plate was then left to cool before the next case (negative gradient curves in Fig. 3.15b)

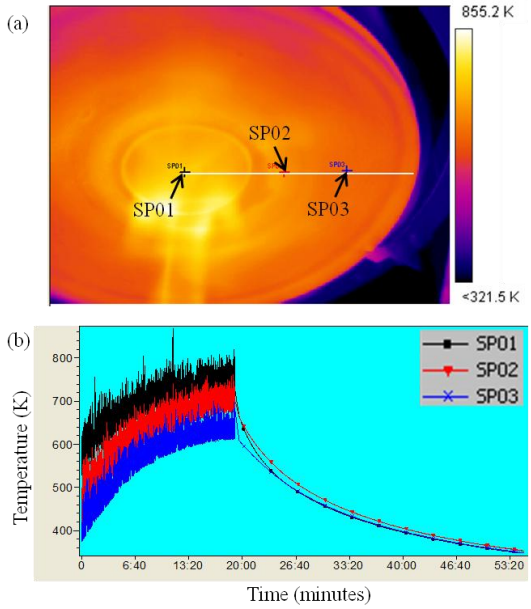

Figure 3.15: (a) Snap shot of thermal image with the flame impinging on it and three spot positions (b) Screen snap shot of the graph showing the temperatures of the spots against time, displaying the heating and cooling of the plate.

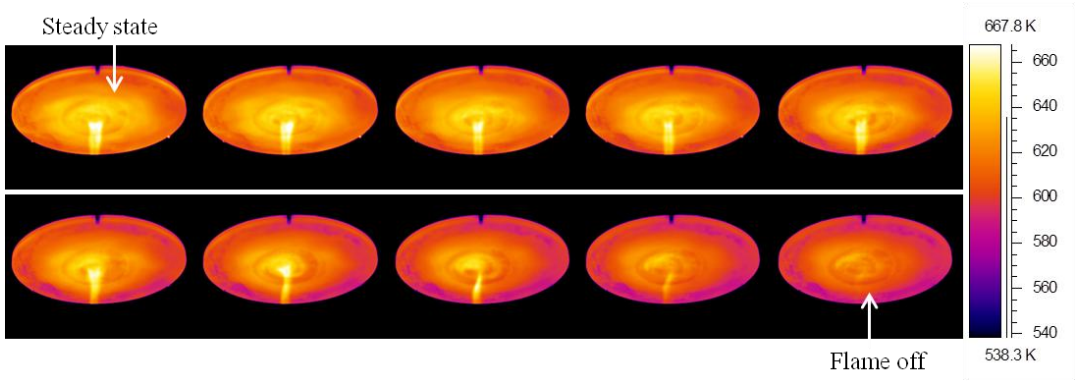

Figure 3.16: Example sequence of the flame switching off (each image is 0.02 s apart).

Accuracy

The SC3000 gave a greater accuracy in this method due to the higher frame rate of the camera. The maximum temperature variation for the quartz plate was less than 1 % within the first 0.2 s and for the steel plate was < 1 % in the first 1.5s, giving an accuracy of 1 % for the quartz plate and 0.13 % for the steel plate over 0.2 s between switching off and the flame becoming completely extinguished (Fig. 3.16). Due to the high thermal inertia of the plate, the temperature can be measured in this way to represent the temperature of the plate while the flame is impinging on it. Certain

analysis tools available in the software could then be applied to the image for image processing and analysis and these will be described now.

3.6.3. Thermal Profiling

Methodology

In order to profile the thermal footprint of the plate, the pixel information for the plate temperature values were extracted for a line taken across the centre of the plate (Fig. 3.17a) using the THERMACAM Researcher software. From this profile, the temperature along the centre line of the plate was plotted against radial distance and defined as the 'temperature profile' of the plate (Fig. 3.17b). Steep temperature gradients near the ends of the line demarcated the positions of the edges of the plate.

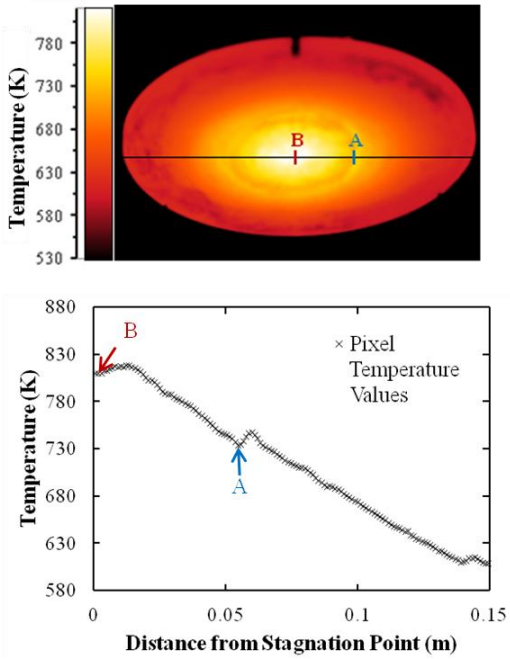

Figure 3.17: (a) Thermal image of the steel impingement plate heated by a premixed propane flame and (b) Corresponding thermal profile.

The heat transfer to the plate can occur via three different scenarios: heat transferred from the direct flame impingement (i.e. the combustion zone), hot gas impingement (i.e. the products) or the fuel and air mixture impingement (i.e. the reactants). The heat transferred from the flame will be higher than that of the products, which will in turn be higher than that of the cool reactants. The thermal footprints can be used to identify the most likely scenario at certain plate locations, and can aid the understanding of how the flame conditions can affect the heat transfer to the plate. A peak in the temperature

profile indicates that heat is flowing away from that location in both radial directions (Fig. 3.17b, point A), and so it is likely that the actual flame is impinging on the plate at this location. On the other hand, a dip near the stagnation region (Fig. 3.17b, point B) indicates that heat is flowing inwards towards the centre of the plate, showing that unburned fuel or fuel/air mixture reaches the plate at this region. The schlieren and direct images can help to verify this information.

In addition, radiation losses from the plate were calculated using a trapezoidal numerical integration of the radiation heat loss equation (Eq. 2.24, p. 30) in MATLAB. For the steel plate, the pixel temperature information was used for $T(r)$, and $\varepsilon(r)$ was set at 0.79, or 0.96 for the plates covered in soot. The method for the quartz plate will be discussed in Section 3.6.4.

Accuracy

The average distance per pixel was 150 mm per 150 pixels, giving a maximum error of 0.7 % in the radius distance measurements. The error in the temperature measurements as discussed in Section 3.6.2 is maximum 1 % for the quartz plate and 0.13 % for the steel plate, for the switch off method. However, differences in temperature will occur depending on the determination of steady state. Since the temperature increase when being heated is exponential, and due to the variations in temperature due to the flame, it can be difficult to assess when a steady state has been reached (Fig. 3.15). This will produce less repeatable results. Figure 3.18 shows two attempts for propane flames impinging on the steel plate at various equivalence ratios. It can be seen that there are quite large differences for the diffusion and $\phi = 15.8$ cases (around 10 %), but not much difference for the other premixed cases (around 1 %). The average change between two cases taken at positions of 0, 0.05, 0.1 and 0.15 m from the stagnation point is 5.1 %.

The emissivity must be inputted into the software and if the incorrect emissivity is entered then the error will be significant. Using a typical temperature value of 688 K from a thermogram of the steel impingement plate; when the emissivity was changed from 0.79 to 0.80 or 0.78 the temperature changed by 0.4 %. However, when the emissivity was changed to 0.7 or 0.9, the difference was 4 %, and for 0.6 it was 17 %. For a lower temperature reading of 457 K, the values are 0.3 %, 3 % and 6 % respectively. Therefore the error in the temperature reading with respect to the

emissivity for the steel plate is around 0.4 %, since the emissivity is accurate to 1 decimal place. The emissivity for the quartz plate will be discussed in Section 3.6.4. The temperature values were not compared to thermocouple readings due to the need for drilling and also since the thermocouples could not withstand the high temperatures produced by the direct flame impingement. This is reserved for the scope for future work.

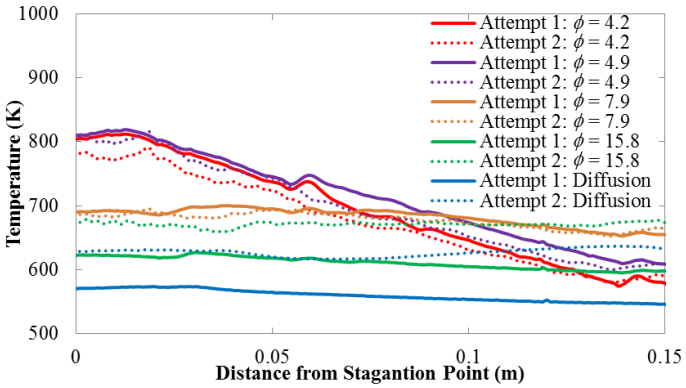

Figure 3.18: Differences between two attempts for propane premixed flames using the flame switch off method.

The angular dependence of emissivity and infrared radiation was tested for the plates by taking images of the plate at angles of 30°, 45°, 60° and 75° when heated by a premixed propane flame and plotting the change in viewed temperature. The 30° angle could not be used for the experiments as the whole radius of the plate could not be seen. The differences in temperature for various radial positions results are given in Table 3.5. For the quartz plate, there is a minimal difference of less than 2 % between the temperatures for angles between 30° and 60°. However, the temperatures changed dramatically for the 75° angle, agreeing with the theory regarding the angular dependence of emissivity. For the steel plate, the temperature difference was less than 8 % between angles of 30° and 75°, but reduced to 3 % between 30° and 45° (Table 3.5). This shows that the angular dependence of the thermal radiation plays no significant role in the temperature determination, but that the angular dependence of the emissivity of the materials used in this thesis matches the theory for conductors and non-conductors [130, 132]. The next section deals with the methodology to deal with the temperature dependent emissivity properties of the quartz plate.

Radial Position (m)	Quartz Plate - Maximum Difference Between 30° and 60° (%)	Steel Plate - Maximum Difference Between 30° and 45° (%)
0.05	0.97	1.36
0.075	1.86	3.01
0.1	0.37	2.04
0.125	1.69	2.74

Table 3.5: The maximum temperature changes at various radial positions with change in viewing angle for the quartz and steel plates heated by a premixed propane flame.

3.6.4. Temperature Dependent Emissivity

Some materials, for example fused quartz, have emissivities that depend on temperature. This can cause problems with thermal imaging cameras, as the emissivity determines the output temperature value. This section deals with an iterative methodology used with the thermal imaging software to resolve this issue.

Emissivity of Fused Quartz

The temperature-dependent values of emissivity for fused quartz were taken from [261] for 873 K < T < 1329 K and from [130] for T = 294 K (with emissivity equal to 0.93 for the room temperature value). These values are shown in Fig. 3.19 and lines of best fit for polynomial and exponential equations have been plotted, with the lines and equations shown on the graph. These best fit lines will be compared for various cases. It can be seen that the polynomial fits the data more closely. However, the turning point of the polynomial will cause problems for temperatures higher than those shown on the graphs. In addition, the two curves will grow further apart for higher temperatures. However, any temperatures higher than 1329 K calculated using this methodology should be discarded since the curve fitting only takes into account temperatures between 293 and 1329 K. In addition, since there is a large gap between 293 K and 873 K, care should also be taken for these temperatures values. However, most temperatures studied in this thesis are within the range of 873 to 1329 K.

The spectral diapasons used in [261] were 3.6 - 5.0 μm, although it is not specified whether the emissivity measurements were limited to this range or whether these were total emissivity values, and in [130] total emissivity was used. This thesis will assume that the emissivity-temperature curve will behave in the same way for the camera using

a spectral range of 8 - 9 μm, as most surfaces, except for highly conductive metals, can be approximated as grey bodies [262].

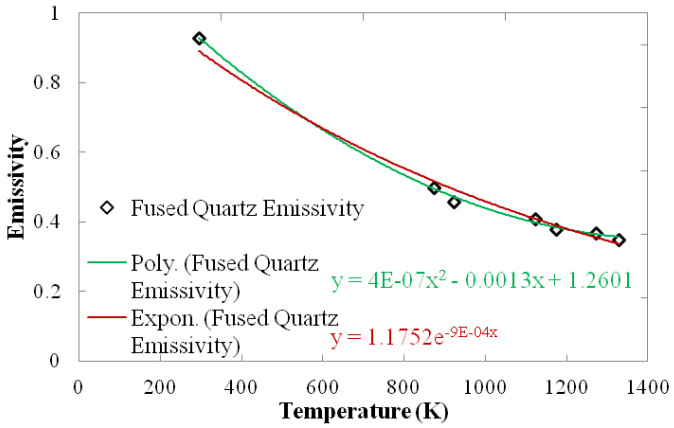

Figure 3.19: Emissivity values for various temperatures from sources [130, 261] with the best fit polynomial and exponential curves.

Methodology

For the thermal profiling, the emissivity along the line had to be inputted as a constant value, giving incorrect temperature profiles. To overcome this difficulty, a series of 'spots' were taken along each centre-line, 8 pixels apart (crosses on the line in Fig. 3.20), whereby the emissivity of each spot could be inputted individually. An iterative procedure was then performed on these series of spots for each case in question. In order to obtain an accurate approximation, the emissivity at each spot should be determined. Initially, the emissivity can be set to any value, and in this thesis it was set to the default value of 0.98. The initial temperatures at each spot were then extracted and the first iterations of the emissivities were calculated from Eqs. 3.3 and 3.4:

$$\varepsilon = 4\times10^{-7}T^2 - 0.0013T + 1.2601, \tag{3.3}$$

$$\varepsilon = 1.1752\ \mathrm{e}^{-9\times10^{-4}T}, \tag{3.4}$$

where ε is the emissivity of the plate at each point and T is the temperature of the plate (in K) at the corresponding point. The emissivities were then separately inputted into the spots in the image and the first iterations of the temperatures extracted. This procedure was repeated until the emissivities had converged to two decimal places, usually requiring four or five iterations.

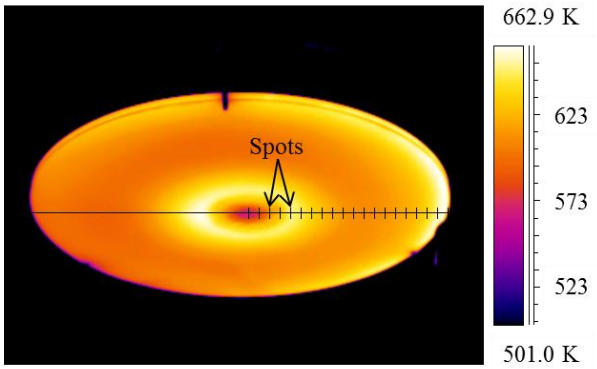

Figure 3.20: The spot analysis tool arrangement for an example thermal image.

An example of the iterations in the temperature profiles for the polynomial and exponential curves are given in Figs. 3.21a and b respectively. The initial temperatures were taken from the data extracted from the line and the iterations were performed on the spots (Fig. 3.20), giving fewer data points. This example is for the quartz plate having been heated by a propane premixed flame and with a normalized nozzle-to-plate distance (h/d) of 21.7 and an equivalence ratio of 7.9. It can be seen that the exponential and polynomial curves give different results, due to the differences in the curve fittings (Fig. 3.19). This will be discussed in more detail in Chapter 5. When the diffusion flames were used, the plate was covered in soot and so the methodology was not used for these cases. Instead the temperatures from the initial line were used with an emissivity of 0.96 as for the soot-covered steel plate.

The radiation losses for the plate were calculated in the same way as for the steel plates (Section 3.6.3), except that instead of using the pixel information from the line, the iterated spot values were used, along with the emissivities for each individual spot, giving values for $T(r)$ and $\varepsilon(r)$ for use in Eq. 2.24 (p. 30).

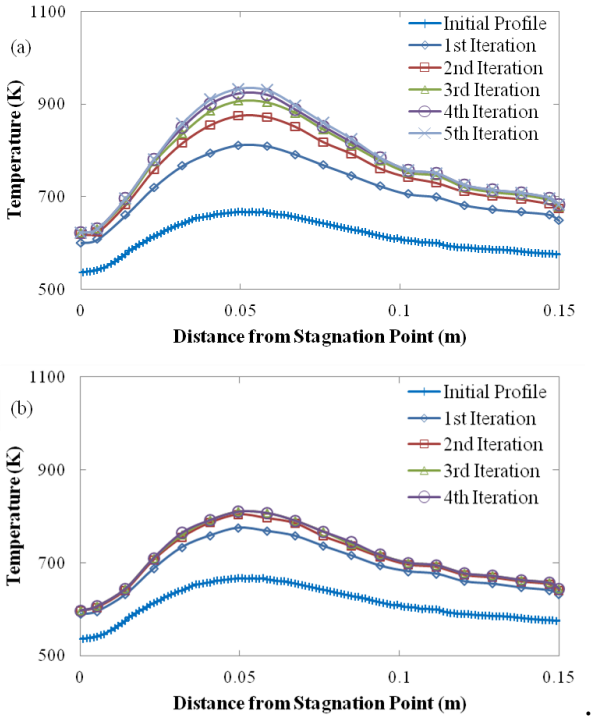

Figure 3.21: An example of the iterations for the emissivity correction method using (a) The polynomial and (b) The exponential fits.

Accuracy

The initial spot temperatures were matched with the temperatures from the points in the line (at each 8 pixel mark) to give distances accurate to 1 pixel, which was typically equal to 0.001 m in distance. The emissivity values are converged to 2 decimal places. Therefore, the main error from this technique is in the accuracy of the emissivity-temperature curves and of the emissivity values. The curve fittings will be discussed and compared in Chapter 5. The improvement of the accuracy of this technique is reserved for the scope for future work. For this thesis, the emissivity values from the sources and the curve fits in Fig. 3.19 will be used for the purposes of assessing the methodology and the effects of the temperature dependent emissivity of the quartz plate with respect to impinging flames. The use of PIV for the impinging flames will now be discussed.

3.7. Particle Image Velocimetry

In addition to the thermal imaging and visualisation techniques, Particle Image Velocimetry (PIV) was attempted in order to obtain quantitative measurements of the flow velocity near the wall. This will be discussed in this section.

3.7.1. Experimental Setup

Particle Image Velocimetry (PIV) was attempted for mapping velocity distributions within the flow as discussed in Chapter 2. Figure 3.22 shows the schematic of the PIV setup. A double pulsed Nd:YAG laser sheet with a 532 nm wavelength, 10 mJ per pulse and a 15 Hz pulse rate was used to illuminate a cross section of the flame through the centre. A TSI POWERVIEW Plus camera was positioned perpendicularly to the laser sheet in order to capture the cross sectional image. Aluminium oxide (Al_2O_3) particles were introduced into the flow using a Dantec Dynamics (model 10F01) solid particle, sonic jet seeder. The Al_2O_3 particles were 3 μm in diameter with a density of 4000 kg m^{-3}.

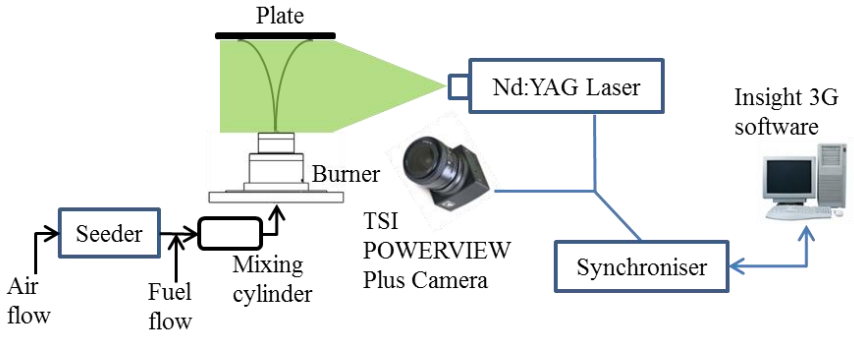

Figure 3.22: Schematic of PIV setup.

The seeding particles were introduced into the air flow, which was connected to an 8 mm pipe to the burner. The fuel line was connected to the seeded air via a tee junction placed after the seeder to avoid risk of a fuel leak, as the seeder was not 100 % leak proof. This meant that diffusion flames could not be studied using PIV. In addition a one-way valve was installed to avoid the hydrogen leaking into the seeder via backflow.

The camera and laser were connected to a TSI LASERPULSE Synchroniser (model 610035) in order that the laser pulse, camera shutter and data acquisition could be operated simultaneously, to a 1 ns resolution. The synchroniser was controlled by Insight 3G software which was also used for data processing.

PIV can be used in this way to gain 2D velocity distributions of the particles within the flame. Information such as vorticity and velocity magnitude can also be computed. However, in order for the results to be meaningful, the particles must follow the flow accurately and must also scatter sufficient light from the laser to be picked up by the

camera. Therefore the seeding density must be large enough to scatter enough light while the particle density must be low enough to follow the flow. The seeding density must also be consistent if ensemble averages of the results are to be performed.

3.7.2. Problems

Many challenges arose when using PIV for the impinging flames in this thesis. Various solutions were put in place to deal with these problems and these will be discussed now.

Seeding Particle Agglomeration

Many problems arose when seeding the flow. The main problem was inconsistent seeding density caused by blockages in the piping system. A main cause of the blockages was the humidity in the air flow. This caused the powder particles to agglomerate. The following measures were put in place to resolve this issue. Firstly, compressed bottled air was used rather than air from the compressor inside the lab. This reduced the humidity of the air flow. In addition, the seeding particles were baked in an oven at 473 K for 10 minutes prior to the experiments. This dried the particles out before introducing them into the air flow. Figures 3.23 and 3.24 show sequences of images taken for air flow at a nozzle exit velocity of 6.5 m s^{-1}, with and without baking the particles respectively, for bottled air. The nozzle is located in the bottom left of the images and the plate is seen by the line at the top of the images. It can be seen that baking the particles helps to appease the particle flow through the pipes, giving nearly consistent seeding density over the sequence of images (Fig. 3.23). Whereas not baking the particles causes clogging and inconsistent seeding density as well as blocking the flow (shown by the straight flow out of the nozzle in the latter images in Fig. 3.24). This was followed by bursts of high seeding density flow (shown by the pink areas in Fig. 3.24).

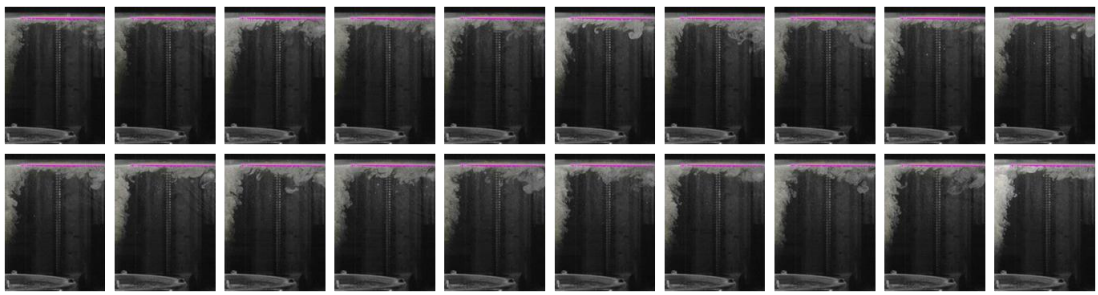

Figure 3.23: PIV sequence of air flow after baking the seeding particles.

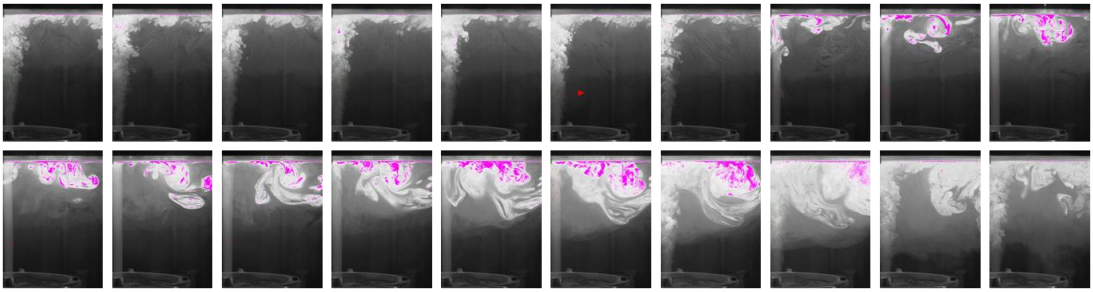

Figure 3.24: PIV sequence of air flow without baking the seeding particles.

However, these images are for the flow of air, and since it is impinging flames that are the subject of this thesis, it is the near wall flow of the flames that is important. The hydrocarbon fuels could not be used due to the low air flow rates required to sustain premixed flames, whereas the hydrogen flames could exist with much higher air flow velocities. However, other problems arose when using the hydrogen flames, which will be discussed now.

Hydrogen

When using hydrogen, a one-way valve had to be used in order to stop the backflow of hydrogen into the seeder. The valve contained small parts and became totally blocked after each case, so that it did not stop the backflow and hydrogen leaked into the air through the seeder. Cleaning the valve between each case solved this problem, but the valve still caused the seeding particles to become stuck, and to be released in short bursts of high seeding density powder. Figure 3.25 shows a burst of high density seeding particles followed by a decline in seeding density for a typical case.

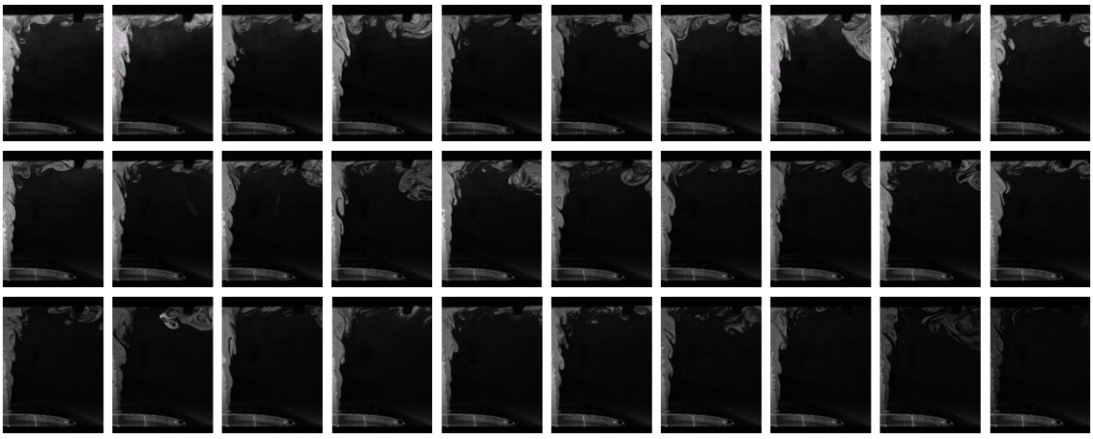

Figure 3.25: PIV sequence of hydrogen premixed flame.

In addition, when hydrogen was used, the seeding particles did not follow the flow along the plate. The drag force (Eq. 3.5) for the hydrogen premixed composition in Fig. 3.25 is 3.7 times larger than for the air composition in Fig. 3.23 (based on the nozzle exit velocities) due to the higher velocity of the former. Therefore, the high velocity change in the stagnation region caused the seeding particles to remain in the stagnation region when hydrogen was used. This was also observed by the seeding particles becoming stuck to the plate in the stagnation region in a cone shape after each case was completed.

$$F_D = 1/2\left(\rho v^2 C_D A_D\right), \tag{3.5}$$

where F_D is the drag force, ρ is the density, v is the fluid velocity, C_D is the drag coefficient, which depends on the geometry of the object, and A_D is a reference area.

Light Scattering from the Plate

If the seeding problems can be overcome, PIV can be a useful tool for obtaining local velocity information within the flow and can be combined with schlieren and thermal imaging to give a more complete description of the flame structure and heat transfer. However, information very close to the plate cannot be gained due to heavy scattering of light from the plate surface (shown by the pink lines at the plate location in Fig. 3.23). The height of the camera with respect to the plate can be adjusted so that the light does not scatter into the camera lens, but this reduces the amount of information regarding the flow near the wall. Lower laser intensity can also be used so that the laser does not damage the camera but this reduces the scattering intensity.

Unfortunately, the accumulation of the problems discussed and the combination of equipment and time constraints meant that PIV could not be used to analyse the flame wall interaction of impinging flames in this thesis. Therefore, the development of the PIV technique for use with the other techniques that are a main focus of the thesis is reserved for the scope for future work (Chapter 8).

3.8. Conclusions

Details of the experimental setup have been given, including the two burners, the plate holding device and the ignition and flow control methods. The fuels used in the remainder of the thesis have been discussed, including the syngas compositions, and the

plate materials, fuel control and mixing system have been described. LabVIEW has also been used to control the flow rates and to calculate various properties of the fuel compositions used. The setup is excellent for studying the flame wall interaction of various impinging flames due to the ability to visualise the flame and flow structures from various angles and to control the flow rates for adequate mixing of the individual fuels.

The imaging tools have been described, including direct imaging, high speed schlieren, thermal imaging and PIV. The setups of each diagnostic technique have been given in relation to the impinging flame setup. The methodologies that have been developed for these techniques have been discussed. These are the wrinkle scale technique and flame front propagation analysis for the schlieren technique, and the flame switch off method, thermal profiling and temperature dependent emissivity methodology for the thermal imaging. The comparison of the direct imaging with the schlieren imaging has also been discussed. An accuracy evaluation for each methodology has been given. It has also been discussed why PIV could not be used in the experiments in this thesis. The combined use of these experimental techniques and methodologies can allow meaningful comparison and discussion of the flame wall interaction of impinging flames.

The next chapter describes of the details of CHEMKIN and Gaseq for the computational analysis of the laminar flame speeds and adiabatic flame temperatures of the mixtures used in the thesis. Following that will be the experimental results using the techniques and methodologies discussed in this chapter.

4. Computations

4.1. Introduction

Thermodynamics and chemical kinetics have greatly increased the scientific knowledge regarding combustion and the mechanisms involved, which, along with advances in computational power, has allowed detailed simulations of complex combustion processes and a larger range of combustion phenomena to be investigated. The use of computational means allows processes to be simulated before experimentation which can save time and resources. Other uses of computation in combustion are seen in Computational Fluid Dynamics (CFD) with approaches such as LES and DNS [263]. Both methods are used for predicting unsteady features of flow fields, such as vortices, and for solving complex flow fields which can be used for turbulence and mixing modelling [264], and can be used alongside many experimental techniques, which have also developed greatly over the last few decades.

Chemical thermodynamics applies the laws of thermodynamics to non-equilibrium systems, in particular to systems which involve chemical reactions [22, 265], using thermochemical laws:

- *The heat change accompanying a chemical reaction in one direction is exactly equal in magnitude, but opposite in sign, to that associated with the same reaction in the reverse direction.*

- *The resultant heat change, at a constant pressure or constant volume, in a given chemical reaction is the same whether it takes place in one or in several stages* [22].

Chemical thermodynamics allows the prediction of the effects of a change in temperature, pressure or composition on an equilibrium reaction [265], which can be applied to programs such as the National Aeronautics and Space Administration (NASA) Chemical Equilibrium with Applications (CEA) and Gaseq to predict the adiabatic flame temperature and final equilibrium product species concentrations [22, 266]. Gaseq will be discussed in more detail in Section 4.2 and will be used to calculate the adiabatic flame temperature of the various compositions used in this Thesis.

Chemical kinetics, unlike chemical thermodynamics, is able to give information regarding the rates of the chemical processes involved [22]. Chemical kinetics is a study of the reaction rates and mechanisms in chemical reactions and of the factors that affect the reaction rates, including temperature, reactant concentration, pressure and radiative effects [13, 22]. Chemical kinetics has been applied to the computer program CHEMKIN, which can determine a wide range of thermodynamic properties and mechanisms, including adiabatic flame temperature, flame speed, autoignition time and detailed reaction mechanisms [267]. CHEMKIN will be discussed further in Section 4.3 and will be used to calculate the laminar flame speed and adiabatic temperature of the mixtures used in this thesis.

This chapter deals with the computations used to calculate the adiabatic flame temperature and laminar flame speeds of the fuels used in this thesis. The basics of Gaseq and CHEMKIN will be discussed along with the specific setups for the computations performed in this chapter. Graphs of adiabatic temperature and laminar flame speed against equivalence ratio will be given for the various fuel compositions.

4.2. Gaseq

4.2.1. Description

Gaseq is a chemical equilibrium program for Windows [266]. It can be used to calculate a variety of parameters for equilibrium processes. It uses chemical thermodynamics to calculate final product species, temperature, density and viscosity (among others) for equilibrium reactions. Figure 4.1 shows a screen shot of the calculations performed for a stoichiometric hydrogen-air flame. The initial reactant mole fractions, temperature and pressure can be specified, as can the product set (for example, $H_2/O_2/N_2$ or Hydrocarbon/N_2/O_2) and problem type (for example, adiabatic temperature at constant volume or pressure, or shock calculations). The product composition and final variables can then be calculated (Fig. 4.1).

Gaseq will be used in this chapter to calculate the adiabatic flame temperatures of the mixtures used for a range of equivalence ratios. The problem type will be set at adiabatic temperature at constant pressure, with initial temperature and pressure of 298 K and 1.0 atmosphere (atm) respectively. Gaseq can provide a larger range of

equivalence ratio results than CHEMKIN due to the constraints for CHEMKIN at lean and rich mixtures. In addition, Gaseq will be used to verify the CHEMKIN results.

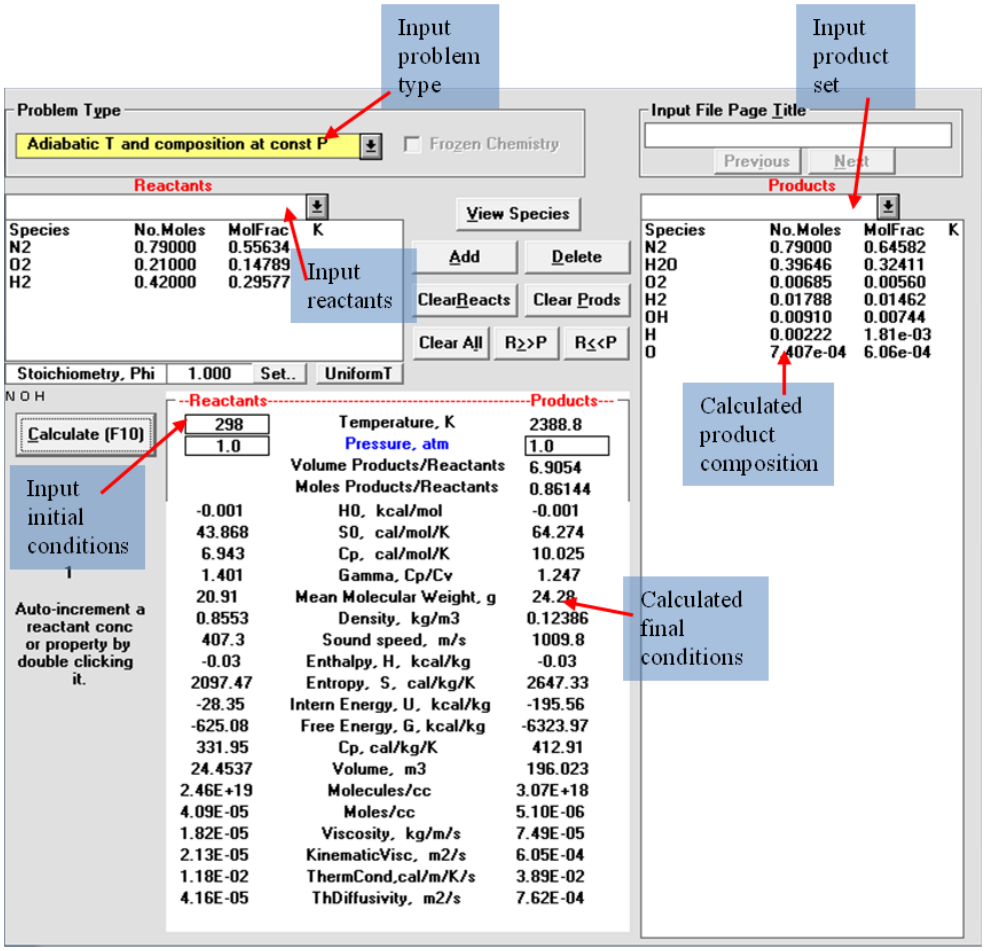

Figure 4.1: Screen shot of Gaseq calculations.

4.3. CHEMKIN

4.3.1. Description

CHEMKIN, as the name suggests, uses chemical kinetics rather than just chemical thermodynamics. It utilises detailed reaction mechanisms and reaction rates to give information about thermodynamic processes.

1D Laminar Flame Structure

For this thesis, CHEMKIN will be used with PREMIX, which uses the 1D laminar flame structure to calculate the adiabatic temperatures, product species concentrations and laminar flame speeds at various positions along the flame length. Figure 4.2 shows

an example of the 1D laminar flame structure for a stoichiometric hydrogen-air flame calculated using PREMIX.

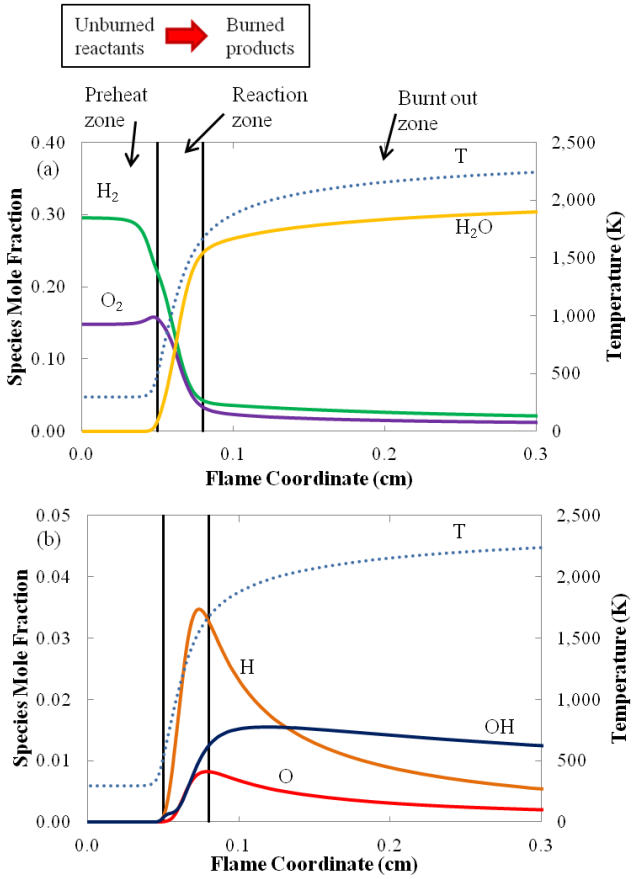

Figure 4.2: 1D laminar flame structure showing the temperature and (a) The major species and (b) The major radicals for a stoichiometric hydrogen-air flame, calculated using CHEMKIN with PREMIX.

The major species (H_2, O_2 and H_2O) are shown in Fig. 4.2a and the major radicals in Fig. 4.2b. It is assumed that the unburned gases are moving from left to right through the *reaction zone* where they combust into the burned gases and where high temperatures are released (Fig. 4.2a) and radicals are produced (Fig. 4.2b). Left of the reaction zone is the *preheat zone*, which is composed of only reactants (H_2 and O_2). This zone is diffusion dominated and consists of heat and mass diffusion into the reactants [268]. To the right of the reaction zone is the *final oxidation* (or *burnt out*) *zone*, where there is a slow approach to the final equilibrium state, which is composed of only products species (Fig. 4.2). The graphs in Fig. 4.2 have been cut at 0.3 cm so that the profiles in the reaction zone can more easily be seen. Further to the right, the

temperature continues to rise slowly and the radical species fractions approach zero. Most hydrocarbon and hydrogen flames follow this structure [268]. The adiabatic flame temperature is calculated in the far right (at ~ 10 cm); where all of the reactants have combusted into products and all of the available heat has been released. The laminar flame speed is calculated at the left where the unburned mixture propagates into the burned mixture (Fig. 4.2a).

Governing Equations and Boundary conditions

PREMIX computes the temperature and species profiles (Fig. 4.2) in steady-state, premixed laminar flames [269]. Two configurations can be used; burner stabilised or freely propagating adiabatic flames [269]. It uses the governing equations (Eqs. 4.1 to 4.4) along with transport properties relating to the diffusion coefficients and thermal conductivities for multi component formulas or for a mixture averaged diffusion model [269]. The transport and thermodynamic properties and subroutines are stored in the CHEMKIN and TRANSPORT databases. In addition, boundary conditions are imposed for the two configurations. For the burner stabilised flames, the temperature and mass flux fractions are specified at the cold boundary and have vanishing gradients at the hot boundary [269]. For the freely propagating flames, the flame location is fixed by specifying the temperature at one point so that the temperature and species gradients nearly vanish at the cold boundary [269].

Continuity: $$F_M = \rho u A_c, \tag{4.1}$$

Energy: $$F_M \frac{dT}{dx_f} - \frac{1}{c_{pg}} \frac{d}{dx_f} k A_c \frac{dT}{dx_f} + \frac{A_c}{c_{pg}} \sum_{i=1}^{N} \rho Y_i V_i c_{pgi} \frac{dT}{dx_f} + \frac{A_c}{c_{pgk}} \sum_{i=1}^{N} \omega_i h_i M_i = 0, \tag{4.2}$$

Species: $$F_M \frac{dY_i}{dx_f} + \frac{d}{dx_f}\left(\rho A_c Y_i V_i\right) - A_c \omega_i M_i = 0 \qquad (i = 1,..., N), \tag{4.3}$$

Equation of State: $$\rho = \frac{p\overline{M}}{RT}, \tag{4.4}$$

where x_f is the spatial coordinate, F_M is the mass flow rate (independent of x_f), ρ is the density, u is the velocity of the fluid mixture, A_c is the cross sectional area of the stream tube encompassing the flame, T is the temperature, c_{pg} is the constant pressure heat

capacity, k is the thermal conductivity, Y_i is the mass fraction of species i, V_i is the diffusion velocity of species i, N is the total number of species, ω_i is the molecular production rate of species i, h_i is the specific enthalpy of species i, M is the molecular weight, p is the pressure and R is the universal gas constant [269].

Newton Method

The PREMIX program uses the Newton iteration method to calculate the flame profiles for freely propagating flames, which will be the setup used for the computations in Section 4.4. The unreacted mole fractions are inputted into the program, and the initial estimated reactant, product and temperature profiles are specified in the reaction model, which will be discussed in Section 4.3.2. The Newton iteration is then implemented, which is followed by a time-step Newton iteration if this fails. These methods will be briefly described here. The initial estimate of the mole fractions takes the form of flat lines for the reactants in the preheat zone and for the products in the burnt zone, connected by straight lines through the reaction zone, as shown in Fig. 4.3. The intermediates, such as the radicals, take on a Gaussian peak at the centre of the reaction zone. The linear starting profiles do not affect the accuracy of the results due to the coarse starting mesh [269].

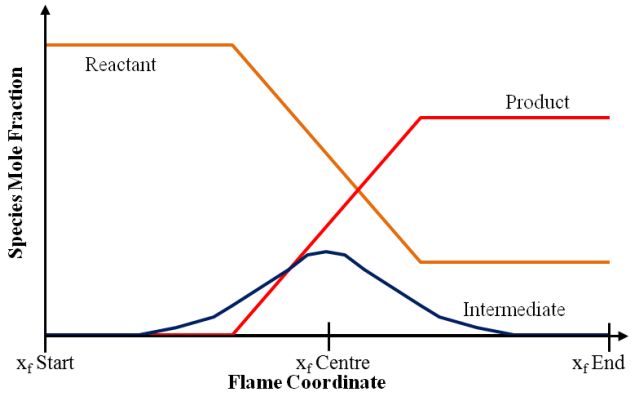

Figure 4.3: Example of initial guess profile shape for the numerical approximation (adapted from [269]).

The procedure begins by using finite difference approximations to reduce the boundary value problem (Eqs. 4.1 to 4.4) to a set of algebraic equations. A very coarse mesh is used to begin with which is then refined at the points where the solution or gradients change rapidly. This procedure is repeated until the solution is resolved to the degree

specified by the user [269]. For the Newton method, initially the governing equations are discretised. The boundary conditions are then implemented and the iterations begin from the starting estimate (Fig. 4.3). A fixed temperature profile is used to converge the species distributions and then the energy equation is implemented in order to converge the temperature profiles [269].

A damped Newton's method is used to solve the non-linear algebraic equations on each mesh, whereby a sequence of iterations are determined that approach the true solution to within the limits specified by the user. The user specifies the tolerance of the convergence, with a tolerance of 10^{-3} or 10^{-4} giving an accuracy of 3 - 4 significant figures respectively [269]. In order for an accurate solution, a fine mesh must be used. Therefore, the user begins the iterations on a coarse mesh and uses the solution as the starting point for the iterations on a finer mesh. This makes the starting guess more accurate for each finer mesh size used [269].

If a suitable convergence cannot be obtained, then the program proceeds to perform time steps. Time stepping takes a solution that is not in the convergence domain of the Newton method to one that is [269].Time derivatives are added to Eqs. 4.1 and 4.3 to give a set of parabolic partial differential equations, and are approximated by finite differences at time levels t and $t + 1$. The discretised transient problem is then a system of non-linear algebraic equations at time level $t + 1$ [269], which can be solved using the Newton method. If it fails to converge with the time steps then smaller time steps or a new starting estimate should be used [269]. The next section will look at the reaction mechanism that was used with the PREMIX program, which will be followed by the specifics of the setup for the computations performed in Section 4.4.

4.3.2. Reaction Mechanisms

Various reaction mechanisms are available to use with the CHEMKIN PREMIX program. For methane, the most common mechanism is the Gas Research Institute (GRI)-Mech, carried out at The University of California at Berkeley, Stanford University, The University of Texas at Austin, and SRI International [270]. However, this thesis deals with flames of methane, propane, hydrogen and syngas. Therefore, a mechanism was used that is able to cover all of these fuels. This is the University of Southern California (USC) Mechanism called the High-Temperature Combustion

Reaction Model of H_2/CO/C_1-C_4 Compounds [271]. It was developed from the GRI-Mech, with additional reaction models of H_2/CO, ethylene and acetylene and C_3 fuel combustion [271]. The mechanisms, transport data and thermochemical data can be found in the source [271]. It can be applied to a wide range of combustion set-ups and incorporates thermodynamic, kinetic, and species transport updates relevant to high-temperature oxidation of hydrogen, carbon monoxide, and C_1-C_4 hydrocarbons [271].

It has been validated against experimental data for laminar flame speeds (and other tests including ignition delay and burner stabilized flames). For hydrogen-air and hydrogen-air equivalent (with nitrogen replaced by argon or helium), and for hydrogen with CO, the results match very well with experimental data (Figs. 4.4a and b respectively). However, for the methane and propane, the results are slightly off. Nevertheless, it was deemed more appropriate to use the same mechanism for all of the fuels for consistency. This makes it a suitable choice for using with hydrogen, syngas, propane and methane fuels and means that all of the computations can be performed with the same reaction mechanism.

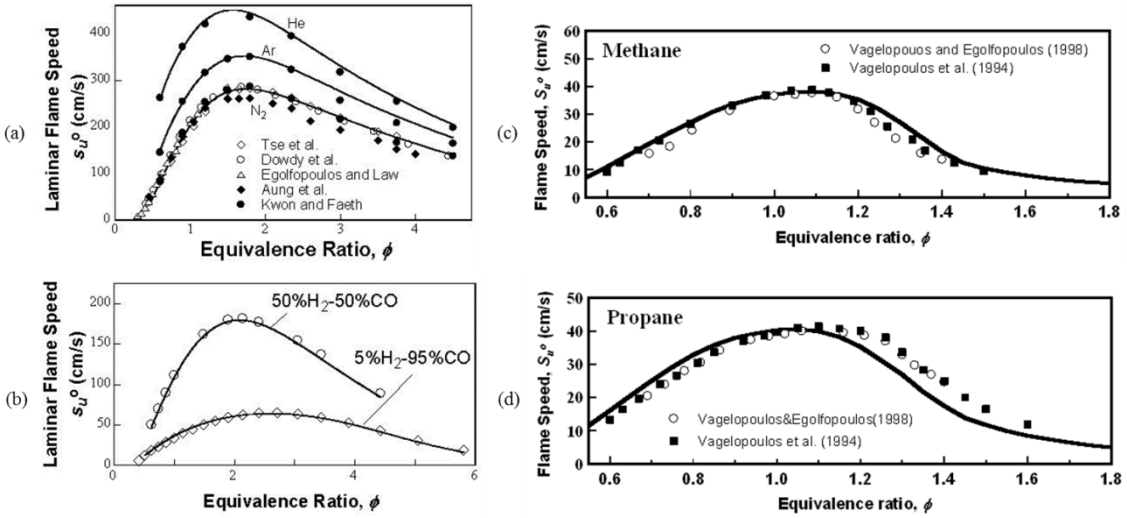

Figure 4.4: Validation of the USC Mechanism with experimental data for (a) H_2-air and H_2-air equivalent, (b) H_2 and CO, (c) CH_4 and (d) C_3H_8 fuels (sourced from [271] with references therein).

4.3.3. Setup and Method

The USC reaction mechanism was used with the PREMIX program for all of the fuels used in this thesis. The input values were kept the same for the different fuels and these

are outlined in Table 4.1. Where 'initial' is stated, the values were changed for the next iterations and those shown in the table are the initial values. Otherwise, the values were kept constant for all iterations. Following the first iteration, the values were changed in the order shown in Table 4.2. First the mesh size was refined by decreasing the GRAD and CURV values. Following this, the computational interval was increased to go beyond the reaction zone, so that the adiabatic flame temperature could be taken at x_f = 10 cm, and the laminar flame speed at x_f = -1 cm.

Code	Definition	Value
NPTS	Number of points to begin uniform mesh.	20
GRAD	Controls the number of points inserted in regions of high gradient.	1.0 (initial)
CURV	Controls the number of points inserted in regions of high curvature.	1.0 (initial)
XSTR	Defines the start position of the computational interval (cm).	0.0 (initial)
XEND	Defines the end position of the computational interval (cm).	0.3 (initial)
XCEN	Estimated value for the centre of the flame (cm).	0.2
WMIX	Estimate of the width of the flame zone (cm).	2.0
PRES	Pressure (atm).	1.0
TFIX	Temperature fixed for flame speed calculation.	350.0
FLRT	Initial estimate of mass flow rate (g cm^{-2} s^{-1}).	0.04
RTOL	Relative tolerance (defines accuracy).	1 x 10^{-4}
TIME	Number of time steps of specified time interval (s).	200 of 2 x 10^{-7}

Table 4.1: Values of the parameters used in the PREMIX program.

Iteration	Parameter Varied	Previous Value	New Value
1	GRAD and CURV	1.0	0.5
2	GRAD and CURV	0.5	0.2
3	GRAD and CURV	0.2	0.1
4	XEND	0.3	2.0
5	XSTR	0.0	-1
6	XEND	2.0	10.0

Table 4.2: Values of the parameters that were varied for the iterations in CHEMKIN.

An example of the results from this process is given in Fig. 4.5 for a hydrogen-air flame. Figure 4.5a shows that the adiabatic flame temperature still increases past the

reaction zone, slowly increasing towards the adiabatic flame temperature. Between x = 2 and 10 cm, the temperature no longer increases and so this temperature can be used as the adiabatic flame temperature. Figure 4.5b is zoomed in to a section of the reaction zone from Fig. 4.5a, so that the iterations can be seen more clearly. It can be seen that, for each iteration, more points are added to the areas of higher gradient and curvature and even the second iteration has many more points than the initial one.

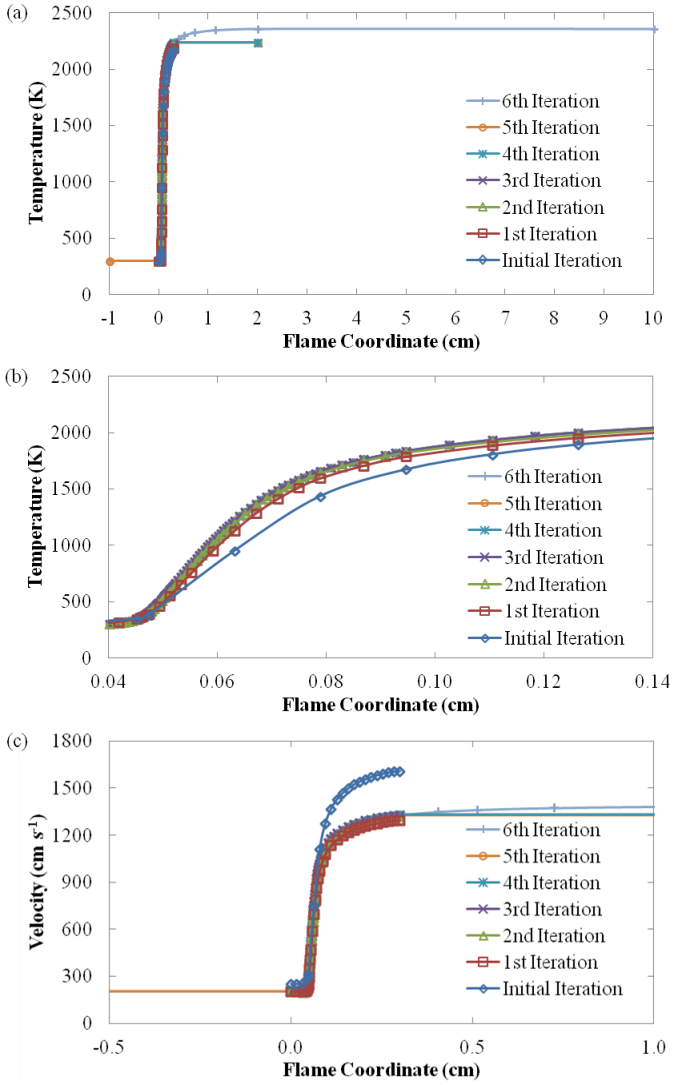

Figure 4.5: Graphs showing the iterations for a hydrogen-air flame for (a) Adiabatic flame temperature (with a zoomed in section shown in (b)) and (c) Laminar flame speed.

Figure 4.5c shows the flame speed profiles. Again this has been zoomed in so the iterations can be seen more clearly. It can be seen that the initial iteration is

overestimated on both sides of the flame zone. However, the 5th and 6th iterations show the same velocity to the left of the reaction zone, where the laminar flame speed is calculated, and so this value can be used for the laminar flame speed. The process was repeated for various values of equivalence ratio until the program could no longer compute the values due to the mixtures being too lean or too rich. This will be discussed for the individual fuels in Section 4.4.

4.4. Results

This section presents the results of the final iterations of adiabatic temperature and laminar flame speed against equivalence ratio, calculated using CHEMKIN, for the fuel compositions used in Chapters 5 and 6. The adiabatic temperatures will also be compared to the results from Gaseq, described in Section 4.2. All of the results presented in this section are for fuels combusting in air.

4.4.1. Hydrocarbons

Figures 4.6a and b show the adiabatic temperatures calculated for propane and methane respectively using Gaseq and CHEMKIN. The laminar flame speeds calculated using CHEMKIN are shown in Fig. 4.7. Gaseq is able to calculate a higher range of equivalence ratios than CHEMKIN; CHEMKIN could not compute the values for $\phi <$ 0.6 or $\phi >$ 1.3 for methane, or $\phi <$ 0.6 or $\phi >$ 1.4 for propane as the mixtures are too lean and rich respectively. The ϕ = 1.4 values could be computed from x = 0 to 2 (iteration 4, Fig. 4.5) for propane but not for lower values of x. Therefore the values shown in Figs. 4.6 and 4.7 are less accurate for ϕ = 1.4 than for the other equivalence ratios. It can be seen from Fig. 4.6a that for the lean mixtures, the Gaseq and CHEMKIN values correspond well for propane, but slightly less so for the richer/leaner mixtures (up to 2.4 % difference). For methane (Fig. 4.6b) the values correspond very well for all values of ϕ (within 0.5 %).

The adiabatic temperature for propane (Fig. 4.6a) peaks at an equivalence ratio of 1 and drops more steeply on the lean side than the rich side, giving a peak value of 2270 K, dropping to 583 K at ϕ = 0.1 and to 1068 K at ϕ = 3 (from Gaseq). The laminar flame speed peaks at 0.398 m s^{-1} at an equivalence ratio of 1.1 and drops at similar rates on either side of the peak to 0.163 and 0.183 m s^{-1} at ϕ = 0.6 and 1.4 respectively (Fig. 4.7).

For methane the adiabatic temperatures and laminar flame speeds both peak at $\phi = 1$. The peak value of the adiabatic temperature is 2225 K, dropping to 577 K at $\phi = 0.1$ and 1012 K at $\phi = 3$, being slightly lower than for propane at the same equivalence ratios (Fig. 4.6). The laminar flame speed peaks at stoichiometry at 0.361 m s^{-1}, dropping to 0.118 and 0.237 m s^{-1} at $\phi = 0.6$ and 1.3 respectively (Fig. 4.7). The laminar flame speed is consistently lower for methane than for propane.

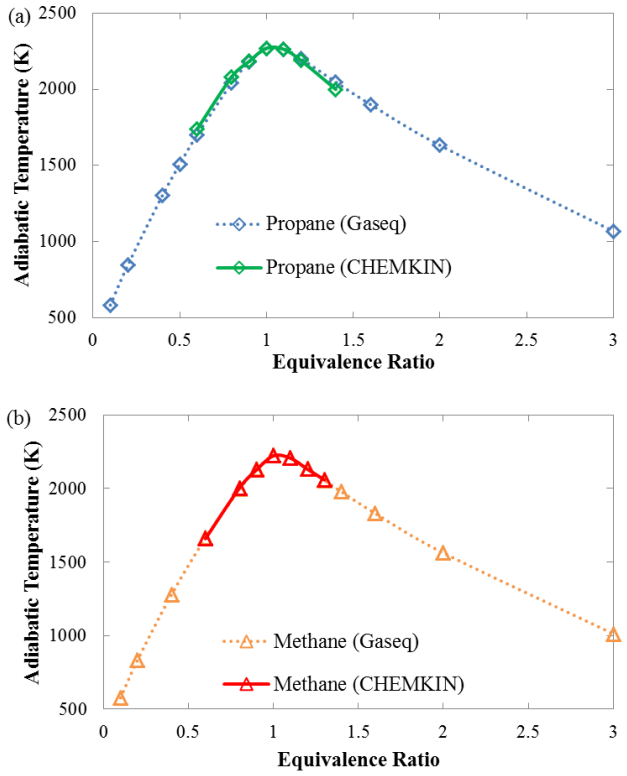

Figure 4.6: Adiabatic temperatures calculated using CHEMKIN and Gaseq for (a) Propane and (b) Methane against equivalence ratio.

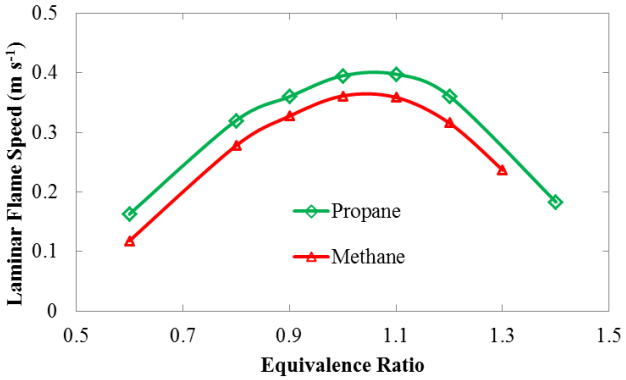

Figure 4.7: Laminar flames speeds against equivalence ratio for methane and propane calculated using CHEMKIN.

Propane and methane have very similar laminar flame speeds and adiabatic flame temperatures, with the laminar flame speed and adiabatic flame temperature of methane at stoichiometry being 9 and 2 % lower respectively than propane. However, it is well known that the laminar flame speed of hydrogen is much faster than that of hydrocarbon fuels. The next section will look at the results of the CHEMKIN and Gaseq calculations for hydrogen, and for the hydrogen compositions with small amounts of nitrogen and CO_2 corresponding to the fuels used in this thesis.

4.4.2. Hydrogen with Additions

Figure 4.8 shows the laminar flame speeds calculated for hydrogen, hydrogen with 10 % nitrogen (which is the highest percentage of nitrogen used for the dilution of the hydrogen to prevent flashback in this thesis), and hydrogen with 18 % carbon dioxide, which is the percentage of hydrogen used for the H_2 + CO_2 compositions in Chapter 6. The hydrogen and H_2 + N_2 compositions could be calculated between ϕ = 0.6 and 4, and the H_2 + CO_2 between 0.6 and 3.

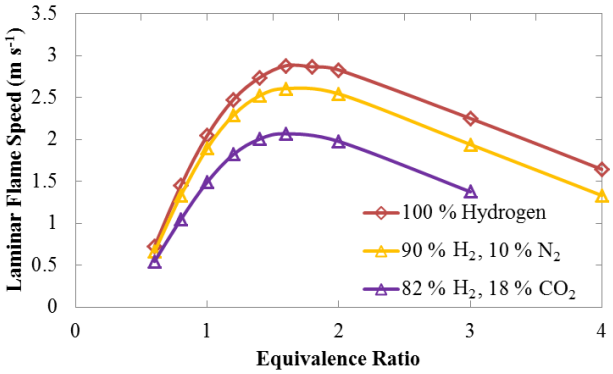

Figure 4.8: Laminar flame speeds of hydrogen, hydrogen plus nitrogen and hydrogen plus CO_2 calculated using CHEMKIN.

The laminar flame speed of hydrogen (red line in Fig. 4.8) is much higher than that of methane and propane, being 5.7 and 5.2 times that of methane and propane respectively at stoichiometry. In addition, the laminar flame speed peaks at a richer mixture composition of ϕ = 1.6 compared to methane and propane which peak at ϕ = 1 and 1.1 respectively. The laminar flame speed of hydrogen is 8.0 and 7.2 times that of methane and propane respectively at the peak values. The laminar flame speed of hydrogen reduces less steeply on the rich side than on the lean side of the peak value, in contrast to methane and propane.

When Nitrogen or CO_2 are added to the hydrogen, the laminar flame speed reduces significantly (yellow and purple lines in Fig. 4.8 respectively). The change is very small for the lean mixtures, and increases as the mixture gets richer. Following the peak value, the reduction in laminar flame speed remains at approximately 0.3 m s^{-1} for hydrogen with 10 % N_2 (9 - 19 % reduction between ϕ = 1.6 and 4), and 0.85 m s^{-1} for H_2 + 18 % CO_2 (28 to 39 % reduction between ϕ = 1.6 and 3). The reduction in laminar flame speed is more significant for the H_2/CO_2 composition, partly due to the increased concentration of the diluent.

Figure 4.9 shows the adiabatic temperatures of the H_2, H_2/N_2 and H_2/CO_2 compositions calculated using CHEMKIN. It also shows the temperatures for hydrogen calculated using Gaseq (blue data points). The discrepancies between the Gaseq and CHEMKIN calculations for hydrogen are similar to the hydrocarbons at the rich mixtures (within 0.5 %), but move further apart for the lean mixtures, with a difference of 3.2 % at ϕ = 0.6.

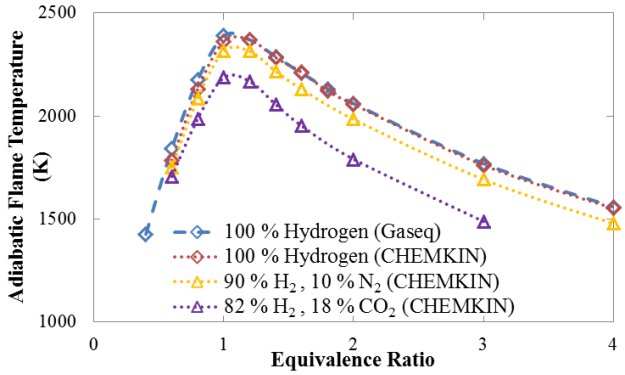

Figure 4.9: Adiabatic flame temperatures of hydrogen, hydrogen plus nitrogen and hydrogen plus CO_2, calculated using CHEMKIN, and of hydrogen calculated using Gaseq.

Similar to the hydrocarbon flames, the adiabatic temperature of hydrogen peaks at stoichiometry. The peak hydrogen flame temperature is 7.3 and 5.2 % higher than that of methane and propane respectively (Fig. 4.6). When N_2 or CO_2 are added to the hydrogen, the adiabatic flame temperature reduces. For the H_2 + 10 % N_2 flame, the peak temperature reduces by 2.2 %, and for the H_2 + 18 % CO_2 flame, the temperature reduces by 8.2 %.

Hydrogen has a much higher laminar flame speed than the hydrocarbon fuels (approximately 10 times higher), and also has a larger adiabatic flame temperature. This will cause higher heat transfer rates due the higher flame temperature and faster propagation speeds due to the faster laminar flame speed. The effect of changing the fuel on the wall temperature will be studied in Chapter 5. Propane will be compared to hydrogen, which has a higher adiabatic flame temperature, and so higher expected wall temperatures. In addition, the propagation for hydrogen will be compared to that of methane, which has a much lower laminar flame speed and so a slower expected propagation of the flame front.

The effect of adding nitrogen or carbon dioxide to hydrogen flames is a significant reduction in adiabatic temperature and laminar flame speed. This effect is larger for the richer compositions. The effect of CO_2 addition on the propagation of hydrogen flames will be studied in Chapter 6. These will be compared to flames of hydrogen and nitrogen, which will be used throughout the thesis. The H_2 + CO_2 flames have lower adiabatic flame temperatures and laminar flame speeds than the H_2 + N_2 compositions used in the thesis. In addition, syngas compositions will be looked at. The laminar flame speeds and adiabatic temperatures of the syngas compositions will be discussed in the next section.

4.4.3. Syngas Compositions

The laminar flame speeds and adiabatic temperatures were calculated for the four compositions of syngas, namely, high H_2, high CO, high CO_2 and high N_2, and for pure hydrogen. Figures 4.10a and b show the adiabatic temperatures calculated using Gaseq and CHEMKIN respectively. It can be seen that the results agree well between the two computational methods. The adiabatic temperature of H_2, high H_2 and high CO are all very similar at stoichiometry, with differences of maximum 0.7 %. However, as the compositions become richer or leaner, the adiabatic temperature of high CO becomes higher than that of H_2, with the high H_2 composition lying in between. Even so, the differences between H_2 and high CO are 1.6 and 5.2 % at ϕ = 4 and 0.04 respectively (using Gaseq). For the high CO_2 and high N_2 compositions, the changes are a lot more drastic, with differences in adiabatic temperature of 11.1 and 18.4 % respectively from pure H_2 at stoichiometry. However, the trends still remain the same for all

compositions, with a sharp peak at stoichiometry and reducing more slowly on the rich side than the lean side.

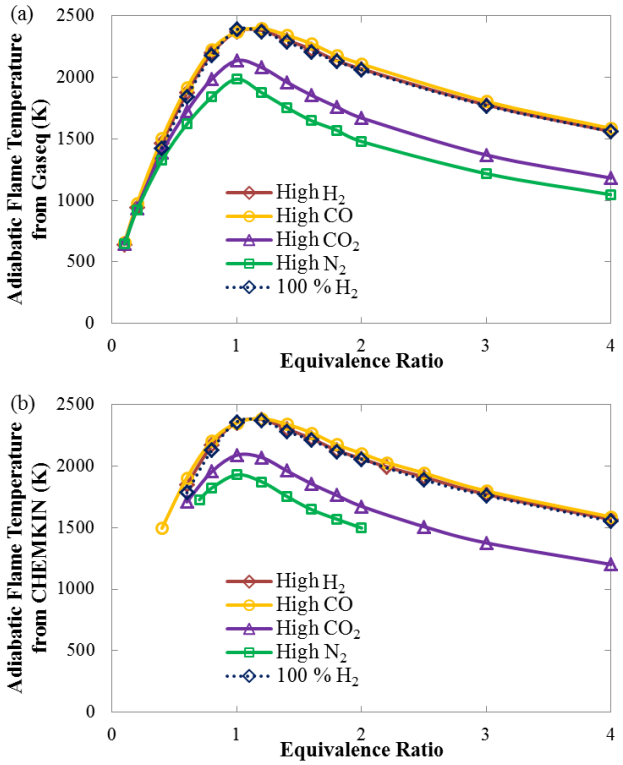

Figure 4.10: Adiabatic temperatures of pure hydrogen and the syngas compositions using (a) Gaseq and (b) CHEMKIN.

For the laminar flame speed (Fig. 4.11) the trends are different for the different compositions, due to the differences between hydrogen and carbon monoxide. It can be seen from Fig. 4.11 that as more CO is added to the hydrogen (blue dotted line, red line and yellow line represent CO/H_2 ratios of 0, 0.4, and 2.0 respectively), the laminar flame speed reduces drastically, particularly at stoichiometry. In addition, the peak moves into a richer part of the mixture, causing richer mixtures to have a higher laminar flame speed than the lean or stoichiometric mixtures. As more CO is added, the peak moves further and further to the rich side.

When CO_2 is added (purple line in Fig. 4.11, $CO/H_2 = 1.0$), the peak only moves a little away from stoichiometry although the CO/H_2 content is higher than for the High H_2 flame ($CO/H_2 = 0.4$). From Fig. 4.8, Section 4.4.2 it was shown that the addition of CO_2 to pure hydrogen causes the laminar flame speed to reduce but does not affect the position of the peak. However, for the syngas compositions, the addition of CO_2 seems

to move the peak closer to stoichiometry. The addition of CO_2 causes the laminar flame speed to be lower than that of the High CO flame, even though it has a higher H_2/CO ratio. Again, the addition of nitrogen in the High N_2 composition causes a larger reduction in laminar flame speed and adiabatic flame temperature than for the High CO_2 flame.

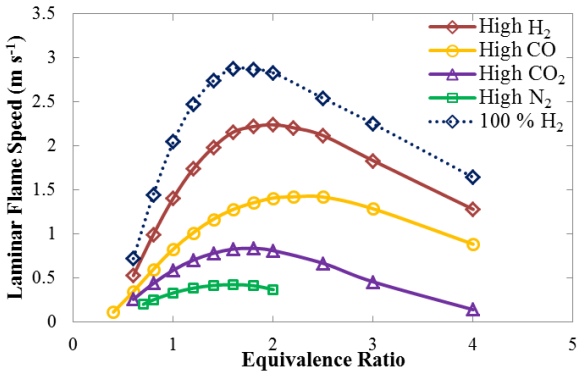

Figure 4.11: Laminar flame speeds of pure hydrogen and the syngas compositions.

4.5. Conclusions

Gaseq and CHEMKIN have been used to calculate the laminar flame speeds and adiabatic temperatures of propane, methane, hydrogen, hydrogen with nitrogen and CO_2 addition and the four syngas compositions against equivalence ratio. The adiabatic flame temperature results agree well for Gaseq and CHEMKIN, although Gaseq is able to calculate a larger range of equivalence ratios.

The adiabatic temperatures peak at stoichiometry for all of the cases studied, since at this value, more heat is available as all of the reactants will combust into products. The adiabatic temperature is slightly lower for methane than for propane. The adiabatic temperature is higher for hydrogen, and remains quite similar for the high H_2 and high CO compositions. The temperature significantly reduces when CO_2 or N_2 are added to the hydrogen or syngas compositions.

Again the laminar flame speeds are lower for methane than propane, but significantly higher for hydrogen. In addition the laminar flame speed trends are different for the hydrocarbon fuels, hydrogen with additions compositions and again for the syngas compositions. There is a sharper decline on the lean side for the hydrogen compositions and a more distinct peak. When CO is added, the peak shifts towards the rich side, but

the addition of CO_2 causes the peak to move back towards stoichiometry. Again, the CO_2 or N_2 additions cause the laminar flame speed to reduce significantly.

The results for the computations can help to aid the understanding of the flame wall interaction and how it differs for different fuels. This will be explored alongside the experimental results in Chapters 5 and 6, which will explore the flame wall interactions for the wall temperature and flame propagation respectively.

5. Results Part 1: Wall Temperature

5.1. Introduction

This chapter presents the results of the thermal profiling techniques. The thermal profiles will be compared to direct and schlieren images in order to assess the flame wall interaction of impinging flames at various fuel and flow conditions. The results of the temperature dependent emissivity methodology will be discussed. The differences between hydrogen and propane will be looked into, and the syngas fuel compositions will be explored. The relative effects of Reynolds number and thermal loading on the wall temperature profiles will be compared first.

The experimental conditions studied were limited by the constraints of the burner: that is the Reynolds number and thermal loading values were determined by the lift-off and blow out of the propane flames.

5.2. Effect of Reynolds Number and Thermal Loading

5.2.1. Introduction

Due to the complex properties of impinging flames, such as Reynolds number, thermal loading and equivalence ratio, it is impossible to compare the effects of one parameter while keeping the others the same. Therefore this section deals with the significance of Reynolds number and thermal loading by using two nozzle diameters with hydrogen diffusion and premixed flames. This allows one parameter to be kept the same while changing the other. In this way the importance of the thermal loading, Reynolds number and *h/d* were compared. As discussed in Chapter 3, 1.67 x 10^{-5} m^3 s^{-1} N_2 was added to all compositions. These experiments were performed on a polished steel plate, which became oxidised during the experiments. Therefore the effects of the oxidisation will also be discussed.

5.2.2. Experimental Conditions

The experimental conditions are outlined in Table 5.1. Since the plate became slightly oxidised after the first experiment, an emissivity of 0.79 (for oxidised steel) was used for the thermal images, although this does not represent the actual emissivity. The specific effects of the plate oxidation will be discussed in Section 5.2.5. Base test cases

were chosen for the small nozzle burner for the diffusion and premixed flames. These were at typical values of thermal loading and Reynolds number for the hydrogen flames used in this thesis. For the diffusion flames, the base case was then compared to cases with the same thermal loadings, but different Reynolds numbers, using the second nozzle size. Following that, the same Reynolds numbers but different loadings were tested. In addition, for each case two nozzle-to-plate distances were used; the first corresponding to the same *h* and the other to the same *h/d* as the base case (Table 5.1).

Case	**Loading (kW)**	**Reynolds Number**	***ϕ***	**Nozzle Diameter (m)**	***h/d***
Base (Diffusion)	1.8	403	Diffusion	0.0046	21.7
Same loading and *h*	1.8	232	Diffusion	0.008	12.5
Same loading and *h/d*	1.8	232	Diffusion	0.008	21.8
Same Re and *h*	4.3	403	Diffusion	0.008	12.5
Same Re and *h/d*	4.3	403	Diffusion	0.008	21.8
Base (Premixed)	1.8	2401	2.8	0.0046	21.7
Same Re and *h*	3.2	2405	2.8	0.008	12.5
Same Re and *h/d*	3.2	2405	2.8	0.008	21.7

Table 5.1: Experimental conditions for the Reynolds number and thermal loading comparisons.

A premixed flame at $\phi = 2.8$ was used for the premixed base case. This represents the richest premixed mixture used in the rest of this chapter. Unfortunately, this equivalence ratio could not be sustained at the thermal loading of 1.8 kW for the larger nozzle due to flashback associated with the low nozzle exit velocity. Therefore, only comparisons using the same Reynolds number but a different loading were performed.

5.2.3. Diffusion Flames

Figure 5.1 shows the temperature profiles for the diffusion cases outlined in Table 5.1. The trends were affected by the plate oxidation, which will be discussed in Section 5.2.5. It can be seen that when the thermal loading is kept the same but the Reynolds number is changed (red lines), the temperature profiles remain fairly similar to the base case (black line). The average deviations from the base case were 9 % and 2 % for the

same *h* and *h/d* values respectively. In contrast, when the Reynolds number was kept the same but the thermal loading changed, the plate temperatures were significantly increased (blue lines). The average deviations from the base case were 32 % and 34 % for the same *h/d* and *h* respectively, which is considerably larger than the Reynolds number effect. Therefore, changing the thermal loading has a much more significant effect on the diffusion flame temperature profiles than changing the Reynolds number or nozzle-to-plate distance. This is due to the higher thermal output of the case with the higher thermal loading. The effect on the premixed case will now be discussed.

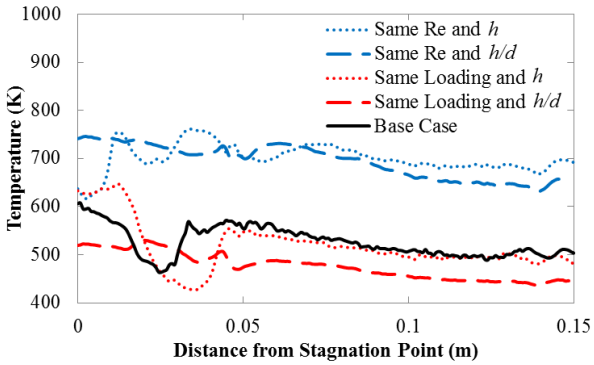

Figure 5.1: Plate temperature profiles comparing the effects of Reynolds number and thermal loading for hydrogen diffusion flames.

5.2.4. Premixed Flames

Figure 5.2 shows the temperature profiles for the premixed cases shown in Table 5.1. Again, a large discrepancy can be seen between the base case (black line) and the cases with the same Reynolds number but different thermal loading (blue lines). It should be noted that the two blue lines have the same Re and loading but different *h/d*, showing that *h/d* has only a small effect on the temperature profiles. The deviations from the base case are very comparable to the diffusion flames, with average deviations of 31 % and 39 % from the base case for the same *h/d* and *h* cases respectively.

Therefore, the effect on the wall temperature of changing the thermal loading at the same Reynolds number is similar to the diffusion flames. However, changing the Reynolds number has a larger effect on the flashback of the hydrogen flames, due to the lower nozzle exit velocity at the same thermal loading and larger nozzle diameter. The focus of this chapter is the effect of fuel and flow variations on the wall temperature profiles. For this reason, the comparisons made in the remainder of this chapter will be

made at a constant thermal loading and *h/d* unless the aforementioned parameters are the subject of comparison. The effects of fuel composition and equivalence ratio can then be compared at selected values of thermal loading and nozzle-to-plate distance. However, it should be noted that other factors such as the Reynolds number and flow velocity will have a large effect on the temperature profiles, and care should be taken when making comparisons.

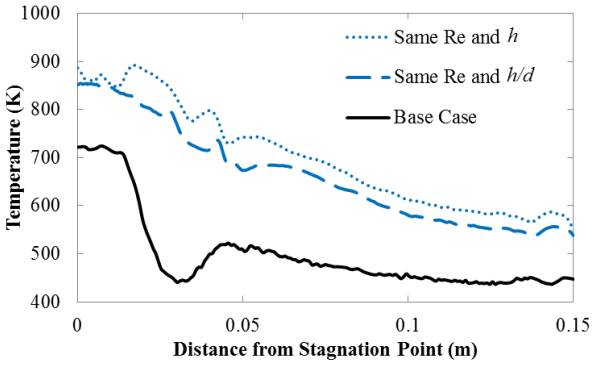

Figure 5.2: Plate temperature profiles comparing the effects of Reynolds number and thermal loading for hydrogen premixed flames.

5.2.5. Plate Oxidisation

The effects of the plate oxidation can be seen in Figs. 5.1 and 5.2. The base case for the diffusion case was performed with minimal oxidisation on the plate. When the plate becomes slightly oxidised, its emissivity increases until it becomes oxidised enough that an emissivity of 0.79 could be used. Following the first test, the plate had become slightly oxidised over the whole area, with a larger amount of oxidation in the ring around the stagnation point, shown by the dip in the curve (black line in Fig. 5.1). This pattern was carried over to the premixed base case and the diffusion case at the same thermal loading and *h* (black line in Fig. 5.2 and red dotted line in Fig. 5.1 respectively). This dip in the temperature profile was caused by the larger amount of oxidisation around the stagnation region causing a higher actual emissivity and so a lower temperature output value. Following that were the blue dotted lines in Figs. 5.1 and 5.2, which had uneven oxidation around the stagnation region, shown by the bumpy profiles. After those cases, the plate became quite evenly oxidised, which is shown by the dashed lines in Figs. 5.1 and 5.2, which have smoother temperature profiles.

The emissivity of the lightly oxidised steel was unknown, but for heavily oxidised steel it is 0.79 (Section 3.2.2). Therefore, the rest of the cases for the steel plate were performed on the plate having been heavily oxidised by repeated testing. This allowed a constant emissivity of 0.79 to be used with the thermal imaging software.

5.2.6. Conclusions

It has been shown that the thermal loading has a large effect on the impingement plate temperature, and so it will be used as a control variable in the rest of the wall temperature results in this chapter. This will allow comparisons to be made with regards to equivalence ratio, fuel composition, nozzle-to-plate distance and thermal loading. However, it should be noted that the Reynolds number has a significant effect on the heat transfer and should be carefully considered in the wall temperature analysis.

The steel impingement plate becomes oxidised after each test, and so a heavily oxidised steel plate will be used for the rest of the results in order to facilitate the thermal imaging measurements. Heavily oxidised steel has a constant emissivity, however many materials have emissivities that depend on temperature. The next section deals with the methodology dealing with this type of temperature dependence.

5.3. Quartz Plate

5.3.1. Introduction

This section looks at the wall temperature profiles of the quartz plate heated by propane flames at various conditions. It presents the results of the methodology described in Section 3.6.4. The method overcomes the issues faced when using thermal imaging to calculate temperatures of materials with temperature dependent emissivity. The heat transfer to quartz materials is important in industries such as the lighting industry [58], solar applications [272] and glass production [273], and quartz was used in this section as its emissivity is highly temperature dependent, making it a suitable choice for study. The methodology could be applied to other materials whose emissivity is a function of temperature, as long as the dependence is known.

Thermal radiation heat transfer is highly dependent on temperature and so the temperature profiles were used to calculate the radiation heat loss from the plate using

Eq. 2.24 (p. 30). It will be shown that even a slight change in the temperature distribution can result in large variations in the radiation heat loss, and that complete temperature distributions should be considered in computational boundary conditions, for example, or instead of using isothermal approximations.

5.3.2. Experimental Conditions

The experimental conditions for this section are given in Table 5.2. Propane was used for each case, with a thermal loading of 1.6 kW, which corresponds to a fuel flow rate of 1.67×10^{-5} m^3 s^{-1}.

Section	*h*/*d*	ϕ	*v* (m s^{-1})	Re	Coflow (m^3 s^{-1})	Coflow (m s^{-1})
5.3.3	10.9	Diffusion	1.0	1039	None	None
	21.7	Diffusion	1.0	1039	None	None
	32.6	Diffusion	1.0	1039	None	None
	43.5	Diffusion	1.0	1039	None	None
5.3.4	21.7	Diffusion	1.0	1039	None	None
	21.7	Diffusion	1.0	1039	1.67×10^{-4}	0.15
	21.7	Diffusion	1.0	1039	3.33×10^{-4}	0.30
	21.7	4.2	6.7	2539	None	None
	21.7	4.2	6.7	2539	2.50×10^{-4}	0.22
	21.7	7.9	4.0	1758	1.67×10^{-4}	0.15
	21.7	7.9	4.0	1758	5.00×10^{-4}	0.45
5.3.5	10.9	Diffusion	1.0	1039	None	None
	10.9	15.8	2.5	1346	None	None
	10.9	7.9	4.0	1758	None	None
	10.9	4.9	5.8	2276	None	None
	10.9	4.2	6.7	2539	None	None
	21.7	Diffusion	1.0	1039	None	None
	21.7	15.8	2.5	1346	None	None
	21.7	7.9	4.0	1758	None	None
	21.7	4.9	5.8	2276	None	None
	21.7	4.2	6.7	2539	None	None

Table 5.2: Experimental conditions for the quartz plate results.

The equivalence ratios, velocities and Reynolds numbers were calculated using LabVIEW as described in Appendix A. The temperature profiles were determined using the SC3000 thermal imaging camera. The emissivity was set to 0.96 for the soot covered surfaces for the diffusion flames and ϕ = 15.8. The temperature dependent emissivity methodology was used for the other premixed cases, using the default emissivity of 0.98 for the initial iterations.

5.3.3. Nozzle-to-Plate Distance

Figure 5.3a shows the temperature profiles of the impingement plate at various values of *h/d* for propane diffusion flames. For *h/d* = 10.9 (Fig. 5.3a, black dotted line), the temperature increases towards the edge of the plate due to the flame spreading out more and coming around the edges, increasing the heat transfer to the outer region. As *h/d* is increased, the temperatures towards the edges of the plate decrease. Figure 5.3b shows the maximum and stagnation point temperatures with increasing *h/d*. For *h/d* > 10.9, the maximum temperatures occur just away from the stagnation region, due to the intense combustion zones at these locations. The position of this temperature peak moves radially outward with decreasing *h/d* (Fig. 5.3a). For *h/d* = 10.9, the maximum temperature occurs at the edge of the plate due to the flame curving around the plate edge (Fig. 5.3a).

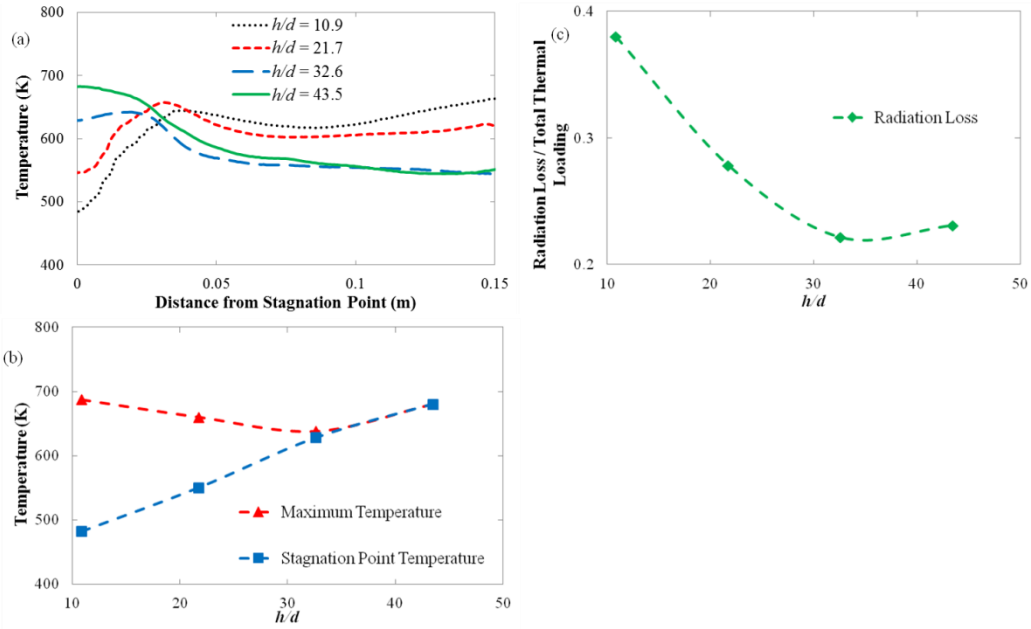

Figure 5.3: (a) Temperature profiles of the quartz impingement plate, (b) Maximum and stagnation point temperatures and (c) Radiation losses for various *h/d*.

At *h/d* = 43.5 the stagnation point temperature is equal to the maximum temperature, due to the lack of unburned fuel impinging on it, shown by the schlieren images in Fig. 5.4. As *h/d* decreases (Figs. 5.4d to a respectively) the schlieren images show that amount of unburned fuel impinging on the stagnation region increases, causing the temperature to decrease and the cool region at the stagnation zone to be wider (Fig. 5.3a). This also causes the difference between the maximum and stagnation point temperatures to become larger (Fig. 5.3b).

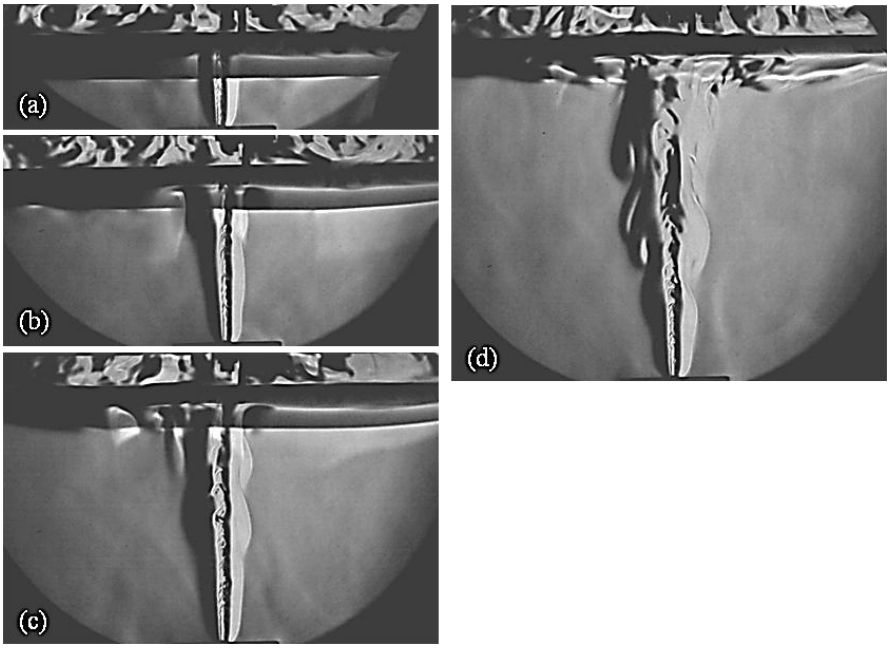

Figure 5.4: Schlieren images of the propane diffusion flames at *h/d* = (a) 10.9, (b) 21.7, (c) 32.6 and (d) 43.5.

Figure 5.3c shows the radiation heat loss from the plate as a function of *h/d*. The radiation losses have been normalised by the thermal loading. It shows that as *h/d* increases between 10.9 and 32.6, the radiation loss from the plate decreases. This is due to more heat being lost to the atmosphere caused by the greater distance between the nozzle and the plate. In addition, the schlieren images (Fig. 5.4) show that as the plate height is increased, there is more turbulence in the flame and so more mixing occurs with the cool ambient air, which increases the heat loss to the surroundings. For the lower plate heights, the higher temperatures towards the edge of the plate with decreasing *h/d* (Fig. 5.3a) (caused by the larger area of flame impingement) seem to have more of an effect on the radiation loss than the increased unburned fuel impingement, since the radiation losses increase with lower plate heights (Fig. 5.3c).

However, when the cool central core no longer impinges on the plate, the radiation loss starts to increase slightly, which is due to the extra heat that is added to the plate due to the combustion at the stagnation region.

The nozzle-to-plate distance significantly affects the plate temperature profiles for propane diffusion flames. This is due to the amount of unburned fuel impinging on the plate, the amount of mixing with the cool ambient air, and the width of the flame across the plate. When the cool central core of unburned fuel impinges on the plate, the radiation losses are affected more by the higher temperatures towards the edges of the plate, caused by the large flame area. However, when *h/d* is just higher than the inner reaction zone, the radiation losses are larger due to the lack of unburned fuel impingement. The changes in temperature profiles that are due to the section of the flame that impinges on the plate significantly affect the radiation losses from the plate. The next section presents the effect of coflow on diffusion and premixed propane flames at a constant *h/d*.

5.3.4. Coflow

The results in this section will be performed at a constant *h/d* of 21.7, varying instead the amount of coflow and the equivalence ratio. The emissivity methodology will be used to look at the effects of using coflowing air with the premixed propane flames but not with the diffusion flames, again due to the soot deposition.

5.3.4.1. Diffusion Flames

Figure 5.5a shows the effect of coflow air on the plate temperature profiles for impinging diffusion flames of propane. Figures 5.5b and c show the maximum and stagnation point temperatures and the radiation heat losses respectively. The coflow air has a high impact on the plate temperature profiles for diffusion flames; decreasing the temperatures towards the edges of the plate and decreasing the width of the low temperature stagnation region, while the temperature of the high temperature ring around the stagnation point remained relatively the same (Fig. 5.5a). In addition, the maximum temperature and the radiation loss decreased rapidly for 0.3 m s^{-1} of coflow air. This could be due to the coflow air impinging on the parts of the flame towards the outer edges of the plate, taking heat away in the form of conductive and convective heat transfer.

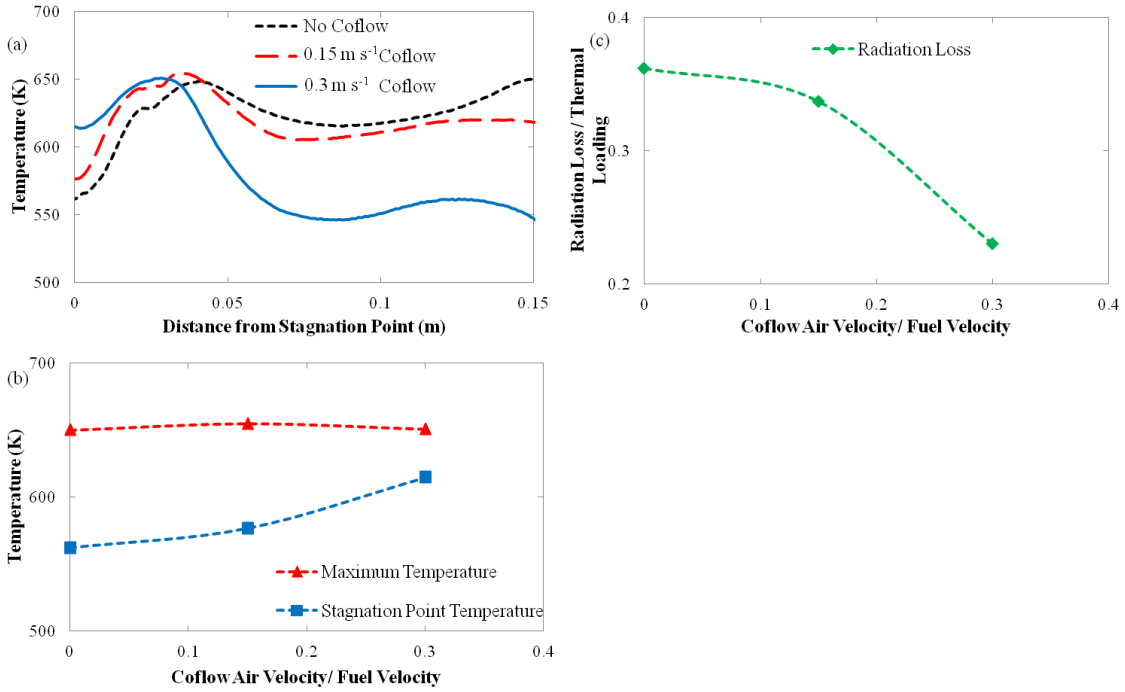

Figure 5.5: (a) Temperature profiles for propane diffusion flames with varying coflow, (b) Maximum and stagnation point temperatures and (c) Radiation losses from the plate.

On the other hand, the stagnation point temperature increased rapidly for the higher coflow amount (Fig. 5.5b). This could be due to more air entrainment for the higher coflow velocities, causing more efficient combustion and higher temperatures within the reaction zone, due to the added mixing of air increasing the adiabatic flame temperature and laminar flame speed (see Chapter 4). Figures 5.6a and b show the schlieren and direct images respectively for the cases with varying coflow. It can be seen that the case without coflow has slightly more unburned fuel impinging on the stagnation region, due to the coflowing air aiding the mixing process and causing the fuel to be burnt more quickly. This can also be visualised by the larger amount of turbulence in the fuel stream near to the plate for the higher coflow amounts. However, not much difference can be seen between the images other than that.

The coflow amount has a large effect on the temperature profiles of propane diffusion flames. The coflowing air causes more air entrainment, causing higher temperatures within the reaction zone, while also removing heat from the wall jet region and the burned gases through convective heat transfer. The coflow air tends to increase the temperature of the stagnation region by facilitating combustion due to the added mixing

with the coflow air. However, it reduces the temperature of the plate at the wall jet region due to the cooling of the burned gases by the coflow impingement.

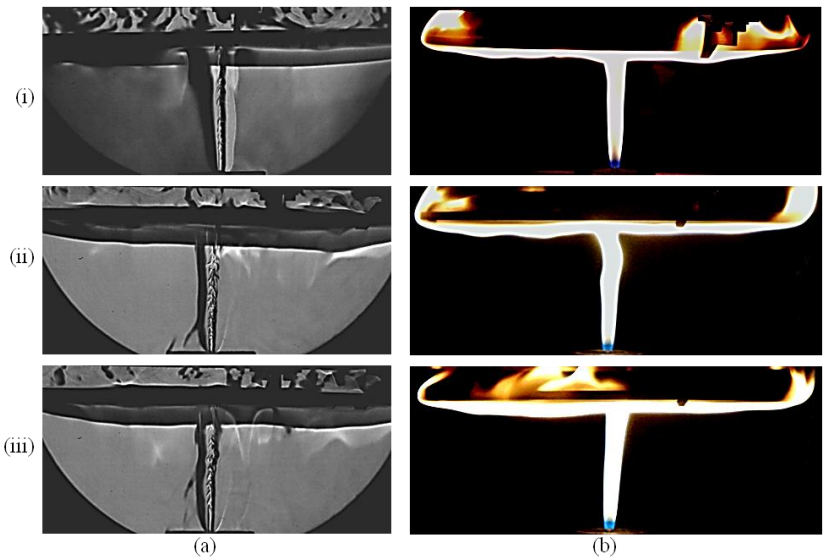

Figure 5.6: (a) Schlieren and (b) Direct images of propane diffusion flames with (i) No coflow, (ii) 0.15 m s^{-1} coflow and (iii) 0.3 m s^{-1} coflow.

5.3.4.2. Premixed Flames

This section deals with the effect of coflow on propane premixed flames, using the temperature dependent emissivity methodology. Figures 5.7a to c show the temperature profiles of the plate before and after the corrections using the polynomial and exponential curve fits respectively for varying coflow amounts. The analysis was done for two equivalence ratios; 4.2 and 7.9. Figure 5.7a shows that there is minimal difference in the temperature profiles when coflow air is increased, but that the equivalence ratio has a much more distinct effect; with more premixed air increasing the temperature at the stagnation region while reducing it in the wall jet region.

Figures 5.7b and c show that the temperatures increase when the emissivity corrections are performed. For the ϕ = 7.9 cases, it can be seen that when the corrections are performed, the temperature profiles become more defined, that is the higher temperatures increase further than the lower temperatures. This is the case for both curve fits, although the polynomial fitting (Fig. 5.7b) causes a much larger increase in the temperature values than the exponential fitting (Fig. 5.7c). The difference in scale of the two graphs (Fig. 5.7a compared to b and c) should be noted.

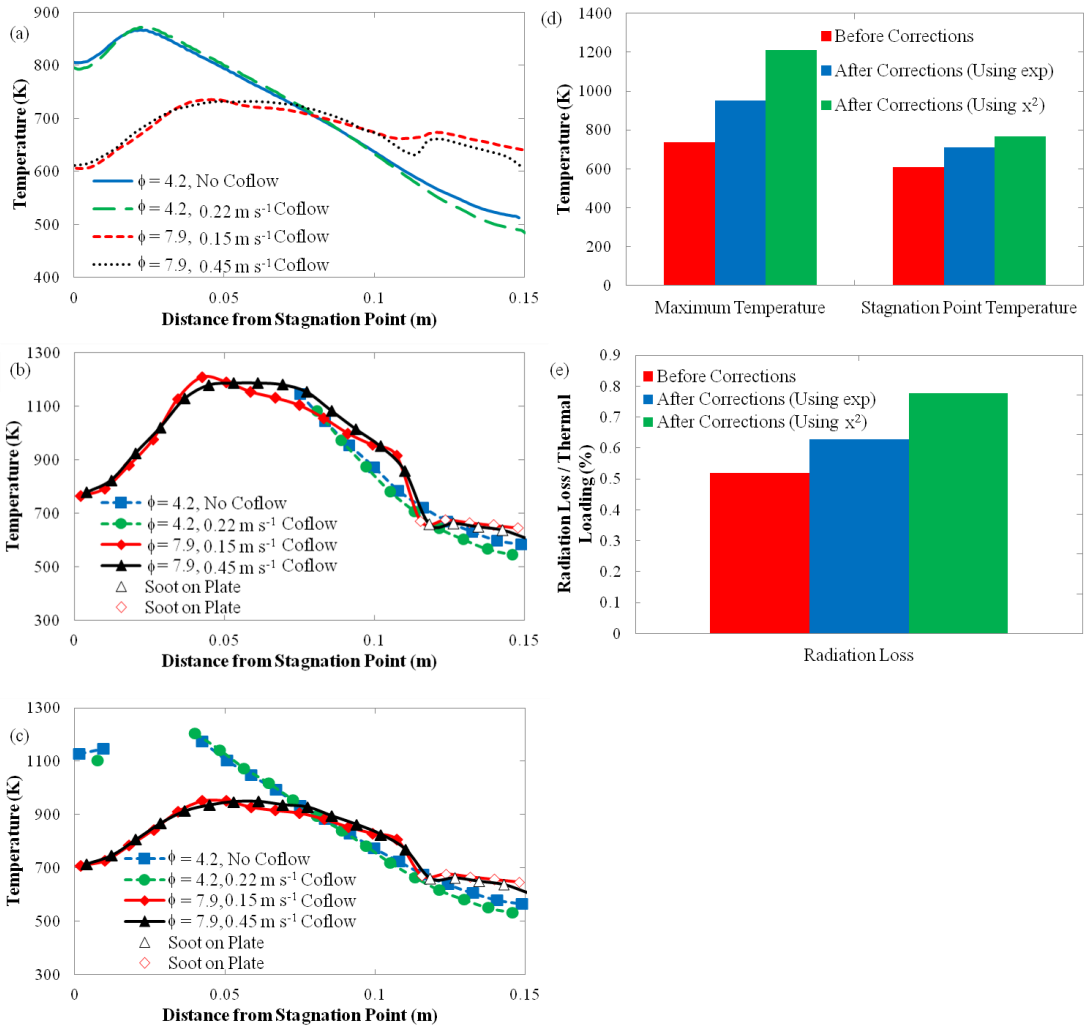

Figure 5.7: Temperature profiles for propane premixed flames with varying coflow and equivalence ratios (a) Before corrections, (b) and (c) After the corrections using the polynomial and exponential curve fits respectively, and (c) Maximum and stagnation point temperatures and (d) Radiation losses for ϕ = 7.9, 0.15 m s^{-1} coflow.

A limitation in the software meant that when the temperatures were above 1213K, the temperature could no longer be determined, and so for ϕ = 4.2, part of the temperature profile is missing after the iterations had converged (Figs. 5.7b and c). This was due to the settings used for the camera which can only record between certain temperature values. A higher temperature setting could be used, but this would mean that the lower temperatures could not be recorded. This will be discussed in Section 5.3.5.2. However, the initial temperature profiles can still provide qualitative information into these cases. For the ϕ = 7.9 cases (Fig. 5.7, black and red lines), a dip followed by a slight temperature rise can be seen at around 0.12 m. This is because there was soot on the

plate for these cases, which was burnt off in the centre. The white data points in Figs. 5.7b and c are for the soot on the plate and were performed with an emissivity of 0.96. The first white point is located at the intersection between the parts of the plate with and without soot, and so the emissivity at this point is undetermined, causing the disjointedness of the curve.

Figures 5.8 and 5.9 show the schlieren and direct images for the premixed cases at ϕ = 7.9 and 4.2 respectively. It can be seen that for the ϕ = 7.9, lifted flame, case (Fig. 5.8), the coflow air causes a higher lift-off height and a wider flame width. This slightly affects the temperature profiles, causing a higher temperature in the wall jet region for the higher coflow amount (black lines in Fig. 5.7). For the ϕ = 4.2, ring flame, case (Fig. 5.9) the coflow air causes the wall jet region to be more turbulent, due to the coflow air impingement. This could be the cause for the slight differences in the temperature profiles (blue and green lines in Fig. 5.7).

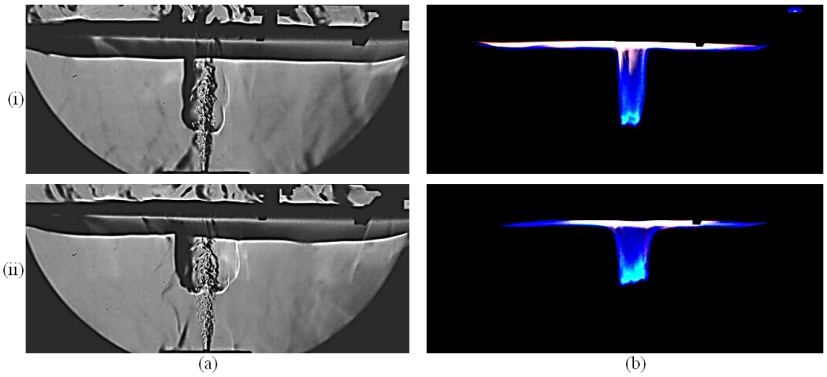

Figure 5.8: (a) Schlieren and (b) Direct images for propane flames at ϕ = 7.9 with (i) 0.15 m s^{-1} and (ii) 0.45 m s^{-1} coflow.

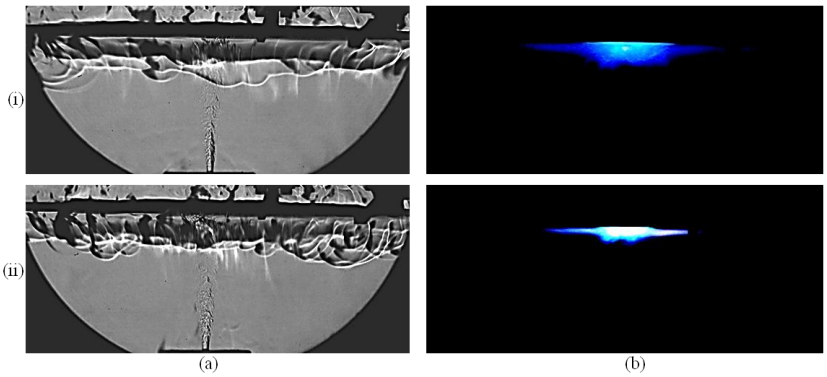

Figure 5.9: Schlieren images for propane flames at ϕ = 4.2 with (a) No coflow and (b) 0.22 m s^{-1} coflow.

The maximum and stagnation point temperatures were only plotted for the ϕ = 7.9 cases since the ϕ = 4.2 cases could not be plotted in the stagnation or maximum temperature regions due to the reasons discussed above. Figure 5.7d shows these values for the 0.15 m s^{-1} coflow amount for the two corrections and for the default emissivity of 0.98. The behaviour of the 0.45 m s^{-1} coflow is very similar; the maximum and stagnation point temperatures do not change significantly for the different values of coflow and, in addition, the maximum temperatures occur at a similar distance from the stagnation point for both cases (Figs. 5.7a to c). Therefore, the coflow effect on the temperature profiles for the premixed flames is much less than on the diffusion flames, although the effect on the flame shape is more significant (Section 5.3.4.1).

It can be seen that the emissivity corrections have a much larger effect on the maximum temperatures than the stagnation point temperatures, and that the effect of using the polynomial is twice that of using the exponential curve. In addition, Fig. 5.7d shows the radiation losses from the plate before and after the corrections for the same case. The corrections have a significant effect on the radiation losses, increasing from 52 % to 63 % and 78 % of the input thermal loading for the exponential and polynomial fits respectively. Therefore, the emissivity and curve fits are significant in determining the temperature profiles, and the subsequent radiation losses from the plate. More detailed analysis of the emissivity of quartz with respect to temperature would help to determine the plate temperatures more accurately and this is reserved for the scope for future work. The effects of the equivalence ratio on the radiation losses could not be discussed due to the software limitations discussed above. However, a more detailed account of the equivalence ratio effects without coflow will be given in the next section.

5.3.5. Equivalence Ratio

The equivalence ratio comparisons were made at two nozzle-to-plate distances and 5 equivalence ratios. The results will be discussed separately for each nozzle-to-plate distance.

5.3.5.1. Lower Nozzle-to-Plate Distance (*h/d* = 10.9)

Figures 5.10a to c show the temperature profiles of the quartz plate heated by propane flames of various equivalence ratios before and after the corrections for the polynomial and exponential fits respectively. These cases are for *h/d* = 10.9. For the diffusion flame

and ϕ = 15.8, the plate was covered in soot and so a constant emissivity of 0.96 was used and the corrections were not performed on these cases (yellow and green lines respectively). The limitation in the software that affected the ϕ = 4.2 cases in Section 5.3.4.2 also affected the ϕ = 4.2 case here for the polynomial fit (Fig. 5.10b). Again, the exponential fit produced lower final temperatures due to the different curve fitting (Chapter 3), and so the limitation did not affect the ϕ = 4.2 case here.

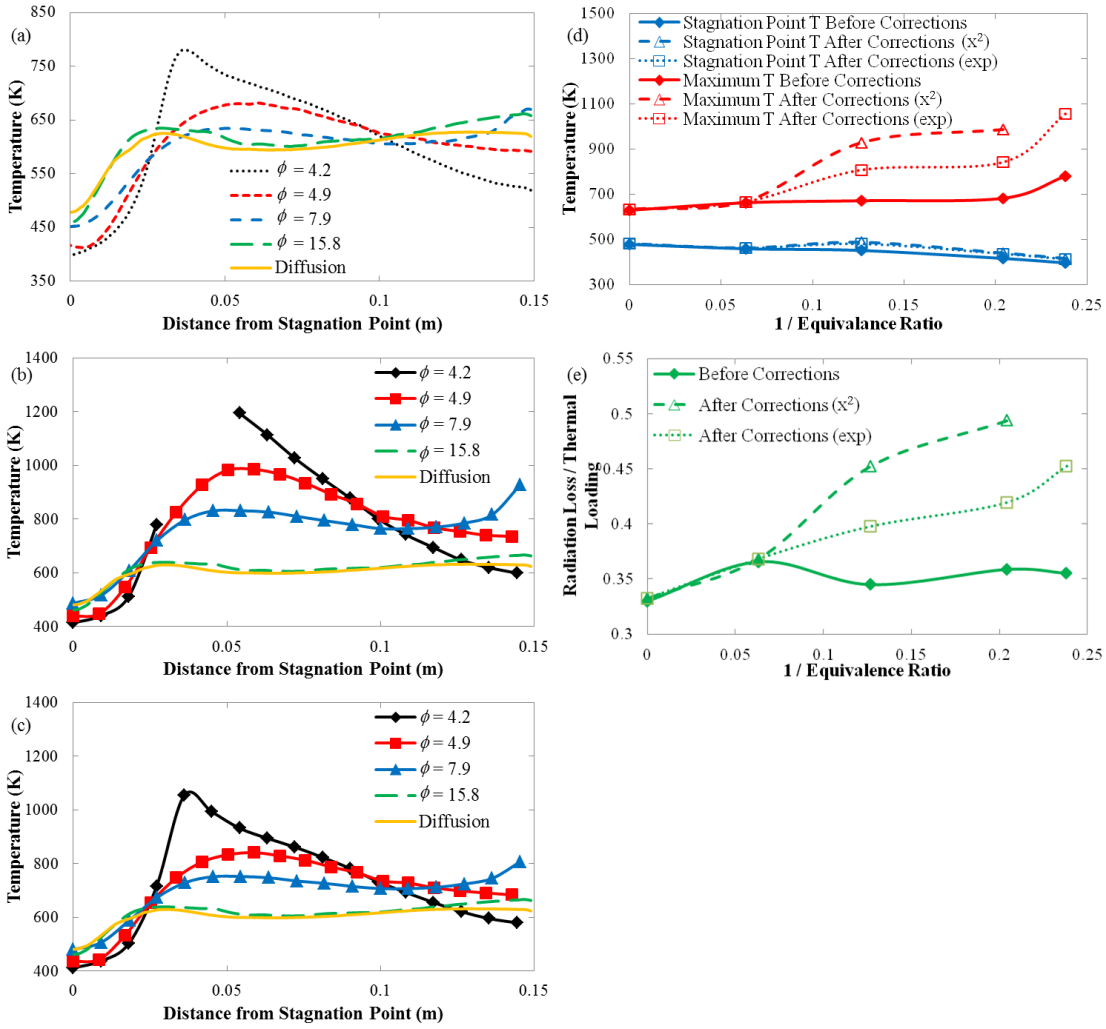

Figure 5.10: Temperature profiles of the quartz plate heated by propane flames of various equivalence ratios at *h/d* = 10.9 (a) Before and (b) and (c) After the corrections for the polynomial and exponential fits respectively, and (d) Maximum and stagnation point temperatures and (e) Radiation losses from the plate before and after the corrections.

The temperature corrections effectively 'stretch out' the temperature profiles so that the lower temperatures towards the edges and the stagnation region remain fairly similar but the higher temperatures slightly away from the stagnation region become much higher. The high temperatures also needed additional iterations to converge; requiring up to seven iterations, while the lower values required only four. In addition, fewer iterations were required for the exponential curve fit.

The temperature profiles (Figs. 5.10b and c) show that as the equivalence ratio is decreased, the stagnation region becomes cooler while the temperatures in the wall jet region become higher. Figure 5.11 shows that as the equivalence ratio changes, so does the flame mode. The flame first becomes lifted (Fig. 5.11 iii) and then becomes a ring flame, with unburned fuel impinging on the stagnation region (Figs. 5.11 iv and v). As the flame mode changes, the plate edge temperature first becomes higher, due to the added heat from the more premixed flame, and then lower due to the smaller flame area across the plate. However, for $\phi = 4.2$, the flame has a higher adiabatic temperature (Chapter 4) and also more turbulence in the stagnation region. This accounts for the high peak at 0.04 m (Fig. 5.10c). The premixed lifted flames are bluer in colour, rather than yellow, and so less soot is produced. Therefore, the effect of the luminous radiation heat transfer from the flame to the plate will be reduced. However, the effect is not significant as the plate temperatures still increase with added premixed air.

Figure 5.10d shows the maximum and stagnation point temperatures before and after the corrections, against $1/\phi$. The maximum temperatures are all higher than the stagnation point temperatures due to the large amount of unburned fuel impinging on the stagnation region at this height; Fig. 5.11a shows that all of the flames exhibit unburned fuel in the stagnation region, due to the low *h/d*, and so the cool stagnation region is quite similar for all flames (Figs. 5.10b and c). The maximum and stagnation point temperatures move further away from each other as the equivalence ratio is decreased, due to the premix air causing higher flame temperatures away from the stagnation region. For $\phi > 7.9$, the maximum temperatures occur at the edges of the plate, due to the flames extending beyond this point and heating the plate from the edge as well as from the bottom (Figs. 5.11b (i to iii)). This causes the increase in maximum temperature at $\phi = 7.9$ (Fig. 5.10d). The larger difference in maximum temperature

between the uncorrected and corrected cases for $\phi < 15.8$ is due to the larger difference in emissivity (from $\varepsilon = 0.98$) for the cases without soot on the plate. Again, the polynomial fitting caused higher final temperatures than the exponential fitting.

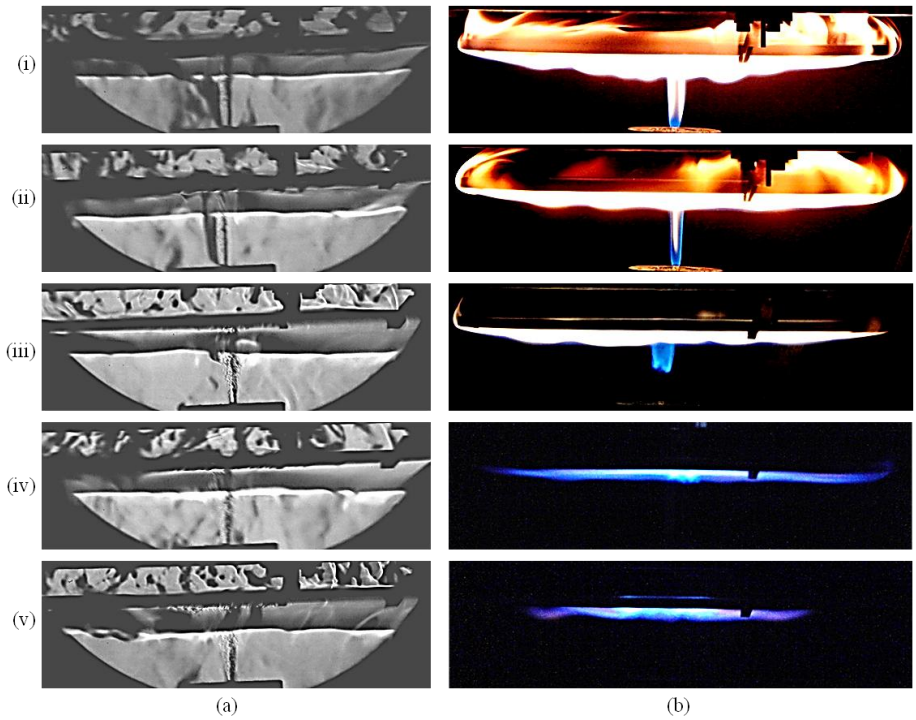

Figure 5.11: (a) Schlieren and (b) Direct images of the propane flames at h/d = 10.9 and for (i) Diffusion flames and premixed flames at ϕ = (ii) 15.8, (iii) 7.9, (iv) 4.9 and (v) 4.2.

Figure 5.10e shows the radiation losses before and after the corrections for the various equivalence ratios. The radiation loss for $\phi = 4.2$ polynomial corrections could not be calculated due to the missing data points in the curve as discussed above. The adiabatic flame temperature peaks at a value of $\phi = 1$ (Chapter 4), and so the radiation loss would be expected to peak at this value also. However, for fuel rich flames, due to the air entrainment in the shear layer, air is added to the fuel between the nozzle and the plate, and so the local equivalence ratio at the plate is decreased. This means that the radiation loss from the plate would be expected to peak at a nozzle exit value higher than $\phi = 1$. However, for this case, a lean enough mixture was not achieved and so the radiation loss continues to increase with a decrease in ϕ. This will be discussed in more detail in Section 5.4.3. For the exponential fitting, there is an almost linear increase in radiation loss with increases in $1/\phi$. Whereas for the uncorrected cases, the radiation loss

decreases after ϕ = 15.8, but increases after this point for the polynomial fitting. Again, this shows the importance of the curve fitting in determining the temperature profiles and the radiation losses, which depend heavily upon the temperature values and the emissivity values.

The higher nozzle-to-plate distance will now be discussed, using the same cases, which will produce less unburned fuel at the stagnation region. These cases will be compared to this section.

5.3.5.2. Higher Nozzle-to-Plate Distance (*h/d* = 21.8)

The same values of equivalence ratio were studied for the higher nozzle-to-plate distance of 21.8. Figures 5.12a to c show the temperature profiles before and after the corrections respectively. Again, the corrections were not performed on the diffusion and ϕ = 15.8 cases due to the soot on the plate. For ϕ = 4.9, the camera limitations discussed in Sections 5.3.4.2 and 5.3.5.1 applied, and so a complete profile was not possible due to the temperatures reaching above the camera setting temperatures. However, for ϕ = 4.2, a different setting was used when filming, which meant that higher temperatures could be recorded, but lower temperatures could not. This affected the initial temperature profiles (Fig. 5.12a); for T < 492K the temperature could not be calculated and is shown as T = 492K on the initial temperature profile graph. However, when the iterations were performed, and a lower emissivity entered, the temperature could be calculated by the software. This then presented another problem. Firstly for the polynomial fitting; for T > 1625 K, the emissivity values did not converge but started to oscillate. This was due to Eq. 3.3 (Section 3.6.4) only being valid for values of T up to the turning point of the 2nd power polynomial (T = 1625 K). Beyond this point the extrapolated emissivity increased again, which caused oscillations in the calculations. This meant that temperatures above 1625 K could not be calculated and so information was lost for part of the temperature profile. Secondly, for the exponential fitting, the iterated temperatures became very high and again reached beyond the limits of the software. In fact, any value beyond 1329 K is based on extrapolation and care should be taken in analysing these extrapolated data. Figure 5.12b again shows that the temperatures calculated after the emissivity corrections were much higher than the initial temperatures, particularly for the polynomial fitting.

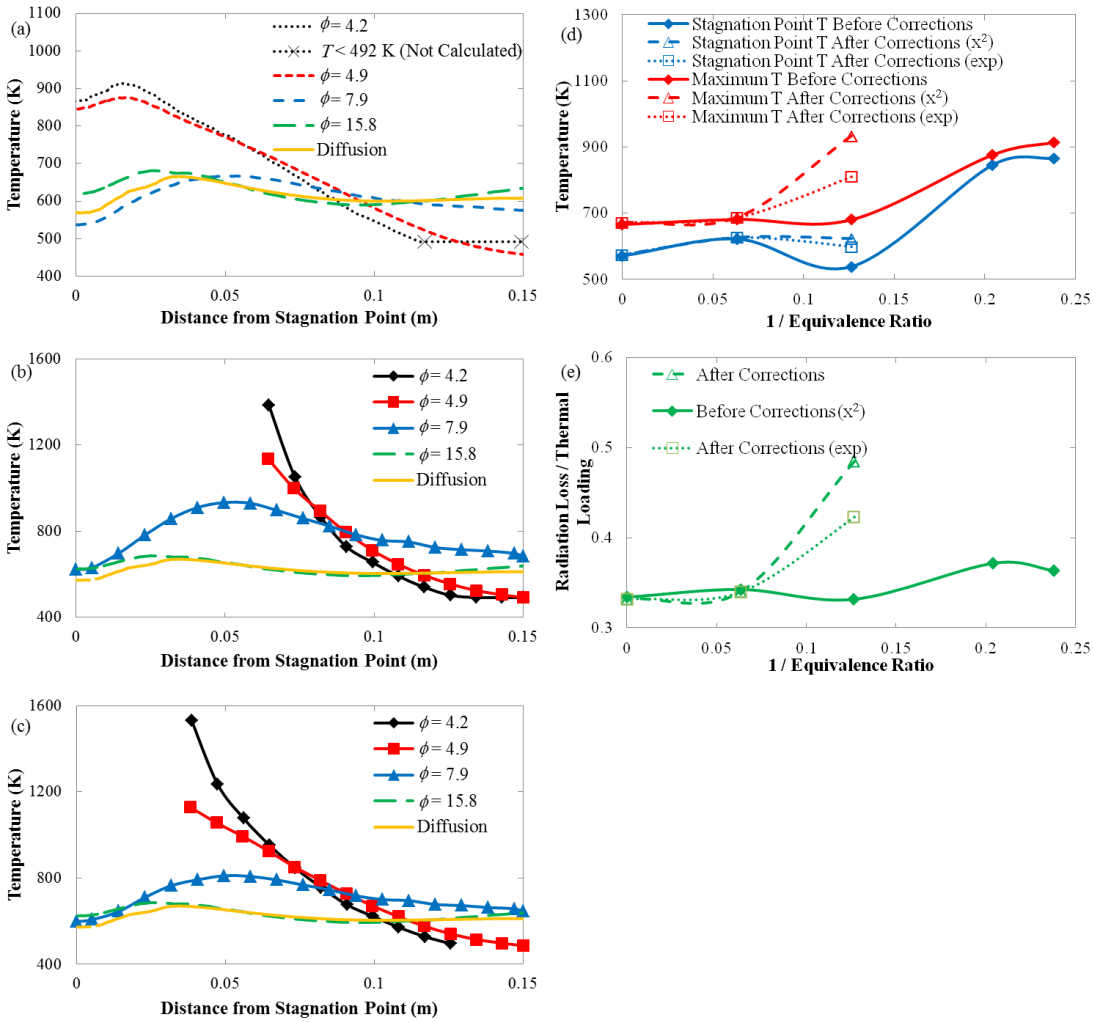

Figure 5.12: Temperature profiles of the quartz plate heated by propane flames of various equivalence ratios at *h/d* = 21.7 (a) Before and (b) and (c) After the corrections for the polynomial and exponential fits respectively, and (c) Maximum and stagnation point temperatures and (d) Radiation losses from the plate before and after the corrections.

Figure 5.12a shows a qualitative view of the temperature profiles and shows that equivalence ratio has a large effect; higher equivalence ratios gave steeper curves, showing that the heat was concentrated towards the centre of the flames, which was expected [224]. The results are quite different to the *h/d* = 10.9 case, due to the section of flame that impinges onto the plate. Figures 5.13a and b show the schlieren and direct images of the flames respectively. Similar trends to *h/d* = 10.9 can be seen when the equivalence ratio is varied, but the flame spread across the plate is much smaller for the higher *h/d*, accounting for the steeper curves in the temperature profiles. Unburned fuel

can still be observed at the stagnation region for all equivalence ratios. The temperature profiles (Figs. 5.12b and c) for ϕ = 4.2 and 4.9 (ring flames) are quite similar to each other, as are those for ϕ = 15.8 and the diffusion flames (attached flames). However, the difference in flame mode causes the temperature profiles to be quite different for the ring flames than for the attached and lifted flames (Fig. 5.13).

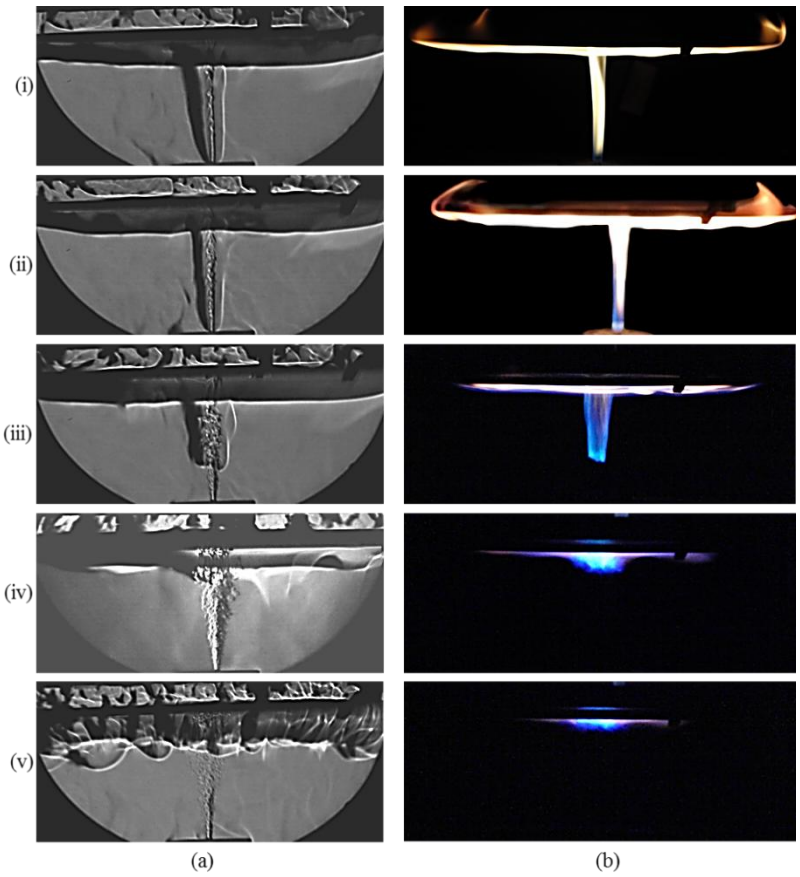

Figure 5.13: (a) Schlieren and (b) Direct images of the propane flames at *h/d* = 21.7 and for (i) Diffusion flames and premixed flames at ϕ = (ii) 15.8, (iii) 7.9, (iv) 4.9 and (v) 4.2.

Figure 5.12d shows the maximum and stagnation point temperatures for the quartz plate at *h/d* = 21.7 before and after the corrections. The temperature for ϕ = 4.2 and 4.9 could not be shown due to the reasons described above for the high temperatures attained. For the other cases, the maximum temperature is always higher than the stagnation point temperature due to the unburned fuel impingement. In addition, the position of the maximum temperature first moves radially inward (for the diffusion flame to ϕ = 15.8), but then moves outward as more air is added and as the flame lifts off (Fig. 5.12a, blue

line). This is due to the change in flame mode. For the ring flames, the maximum temperature is quite close to the stagnation region.

Figure 5.12d shows the radiation loss from the plate for the various equivalence ratios. Again, the ϕ = 4.2 and 4.9 cases after the corrections were not calculated due to the incomplete temperature profiles. In contrast to the stagnation point temperatures, the radiation loss curves before the corrections for *h/d* = 21.7 are very similar in shape to those for *h/d* = 10.9, in that there is a dip in the curve for the lifted flame, but a higher radiation loss for the ring and attached flames. However, when the corrections are performed, the radiation loss curve increases with a decrease in equivalence ratio. Again, no peak in the radiation loss curve was observed. In addition, the radiation losses from the plate are slightly higher for *h/d* = 21.7 than for *h/d* = 10.9, since for the lower *h/d*, more heat is lost to the exhaust gases escaping round the edges of the plate.

5.3.6. Conclusions

This section has used an iterative methodology to calculate temperature profiles of a quartz impingement plate using the temperature dependence emissivity methodology and an SC3000 thermal imaging camera. Each emissivity correction converged within 4-7 iterations, showing that this is a very useful method of using the temperature dependence emissivity for a quartz plate. The lower values of temperature seemed to converge more quickly than for the higher temperatures, but for these the values of emissivity did not need to be re-entered into the software, and so the later iterations took less time.

The problems discussed relating to the non-convergence of the emissivity could be overcome by obtaining emissivity information for higher temperatures and applying this to the emissivity-temperature equation. Unfortunately, time and experimental constraints prevented this from being performed and this is reserved for the scope for future work. The results could be made more accurate by obtaining more detailed emissivity data and making a more accurate approximation of the emissivity-temperature curve. However, the results shown are accurate enough for the intended use.

The temperature profiles and plate radiation losses for the quartz plate were calculated for various flow conditions for propane impinging flames. The profiles were also compared to schlieren and direct images. It was found that:

- The emissivity corrections increased the calculated temperatures and produced more defined temperature profiles. The corrections also made the maximum and stagnation point temperatures and the radiation loss from the plate higher than for the initial temperatures taken from the software. However the radiation curve shapes changed due to the emissivities being different for the soot covered plates.

- The flame modes produced by different equivalence ratios significantly affected the temperature profiles; for similar flame modes at different Re and ϕ, the temperature profiles were very similar but for different flame modes, the temperature profiles were very different.

- The nozzle-to-plate distance had a large effect on the temperature profiles due to the amount of unburned fuel impinging on the stagnation region and to the size of the flame spread across the plate and around the edges.

- Coflowing air had a large effect on plate heated by diffusion flames but minimal effect on that of premixed flames, although the effect of the flame shape was larger for the premixed flames than the diffusion flames. For the diffusion flames, the coflowing air caused more air entrainment, causing higher temperatures within the reaction zone, while also removing heat from the wall jet region and the burned gases through convective heat transfer.

For the quartz plate, the corrected temperature values were higher than when using the default emissivity of 0.98 in the software due to the lower emissivity values. The methodology in this paper could very easily be applied to other materials and thermal imaging cameras provided that the temperature dependence of the emissivity is known or can be found out, and that software allows the user to input emissivities into particular points of the thermogram.

Unfortunately, the quartz plate could not be used for the hydrogen flames due to the high temperatures of these flames. Therefore, in order for the effects of hydrogen and

syngas to be studied, the oxidised steel plate was used. This plate has an emissivity of 0.79 and so the initial profiles from the line could be used rather than the spots. The next section will compare impinging flames of propane and hydrogen with the steel plate, which will be followed by an analysis of the syngas compositions. In addition the propane cases will be compared to the cases in Section 5.3.5 for the quartz plate at the same conditions.

5.4. Propane and Hydrogen Comparisons

5.4.1. Introduction

Hydrogen is currently considered the 'fuel of the future' with many companies investing in the production and utilisation of hydrogen and hydrogen mixtures such as syngas. Therefore, the burning and heat transfer characteristics need to be investigated in order that it may be properly utilised in the future. Hydrogen has very different combustion properties, for example a higher burning velocity, diffusivity and adiabatic flame temperature, to other mainstream fuels such as propane. Therefore, it is important to compare these fuels to see what impact this might have in a confined combustion environment. However, since the properties of hydrogen and propane are very different, it makes it difficult to make meaningful comparisons. Therefore, propane and hydrogen will be studied separately in this section, at three thermal loadings and at various equivalence ratios. Much information can be gained in this way to compare aspects such as wall temperature, radiation losses from the plate and blow-out/flashback limits.

5.4.2. Experimental conditions

The experimental conditions for the pure propane and hydrogen flames are given in Table 5.3. Three thermal loading values were chosen for each fuel to compare the effect of diffusion and premixed flames at the various loadings. All comparisons were done at h/d = 21.7. The equivalence ratios were decreased to the leanest possible mixtures without blow-out or flashback occurring.

.

Fuel	Thermal Loading (kW)	ϕ	Re
Propane	1.6	Diffusion	1039
	1.6	15.8	1346
	1.6	7.9	1758
	1.6	4.9	2276
	1.6	4.2	2539
	3.2	Diffusion	2079
	3.2	15.8	2691
	3.2	7.9	3516
	3.2	6.1	4031
	4.7	Diffusion	3118
	4.7	15.8	4037
	4.7	7.9	5274
Hydrogen	1.8	Diffusion	403
	3.5	Diffusion	603
	5.3	Diffusion	828
	1.8	2.8	2401
	1.8	1.1	5717
	3.5	2.8	4522
	3.5	1.5	8521

Table 5.3: Experimental conditions for the propane and hydrogen comparisons.

5.4.3. Propane

Propane was studied at three values of thermal loading and at various equivalence ratios. The results for the first thermal loading (1.6 kW) will be compared to the quartz plate (Section 5.3.5.2). However, the equivalence ratio values are not exactly comparable since there was a slight leak in the air flow controller for the quartz plate measurements. This was rectified for these measurements. Therefore, the flame shapes differ slightly, although the results are still relatively comparable. The results will also be compared to hydrogen flames at three thermal loading values. However, the values of equivalence ratio are not the same for the hydrogen and propane flames, due to experimental constraints, which will be discussed in the next section. The achievable equivalence ratios can also give insight into the differences between the hydrogen and propane flames, particularly when the schlieren images are used.

Figures 5.14a to c show the effect of equivalence ratio on the temperature profiles for the propane flames at 1.6, 3.2 and 4.7 kW respectively. At each thermal loading, the equivalence ratio was lowered until the flame blew out. It can be seen that the equivalence ratio has a large effect of the temperature profiles for each thermal loading. This is due to the change in flame mode, as was described in Section 5.3.5.2.

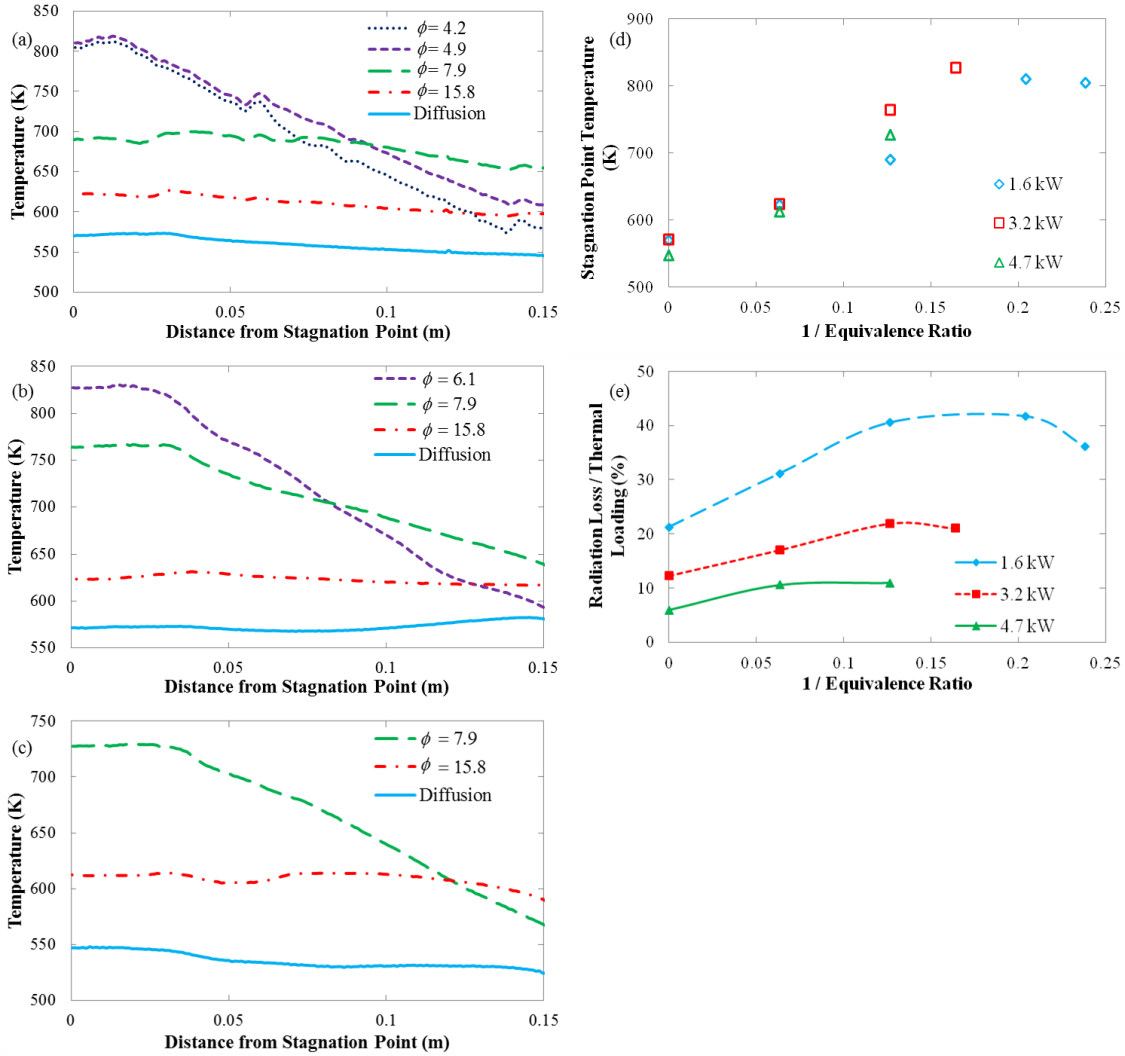

Figure 5.14: Temperature profiles for the steel plate heated by propane flames at (a) 1.6 kW, (b) 3.2 kW and (c) 4.7 kW, (d) Stagnation point temperatures and (e) Radiation losses from the plate.

Figure 5.15 shows the schlieren images for the propane flames. It can be seen that as the thermal loading is increased (b to d respectively), the change in flame mode occurs more rapidly, and so the flame blows out at higher equivalence ratios for higher thermal loadings. For 1.6 kW, the flame blew out a minimum achievable ϕ of 4.0. Even though

this is still quite fuel rich at the nozzle, the blue colour of the flame at the plate (Fig. 5.15a (v)) indicated that the flame was relatively leaner, due to enhanced local fuel/air mixing with the entrainment of air upstream. This air entrainment can be seen by the widening of the unburned fuel section observed in the schlieren images (Fig. 5.15b (i to v) respectively). As ϕ was decreased, the flame changed from the initial yellow diffusion flame to the blue premixed flame. Correspondingly, the flame spread across the plate became smaller because the fuel was burnt up more quickly due to the added air and turbulence. This can be seen by the steeper temperature curves in Figs. 5.14a to c; as the equivalence ratio is decreased the heat becomes more concentrated towards the stagnation region. The same sequence was observed for the 3.2 and 4.7 kW flames (Figs. 5.15c and d respectively) but the change in flame mode happened more quickly with changes in ϕ due to the higher Reynolds numbers (Table 5.3).

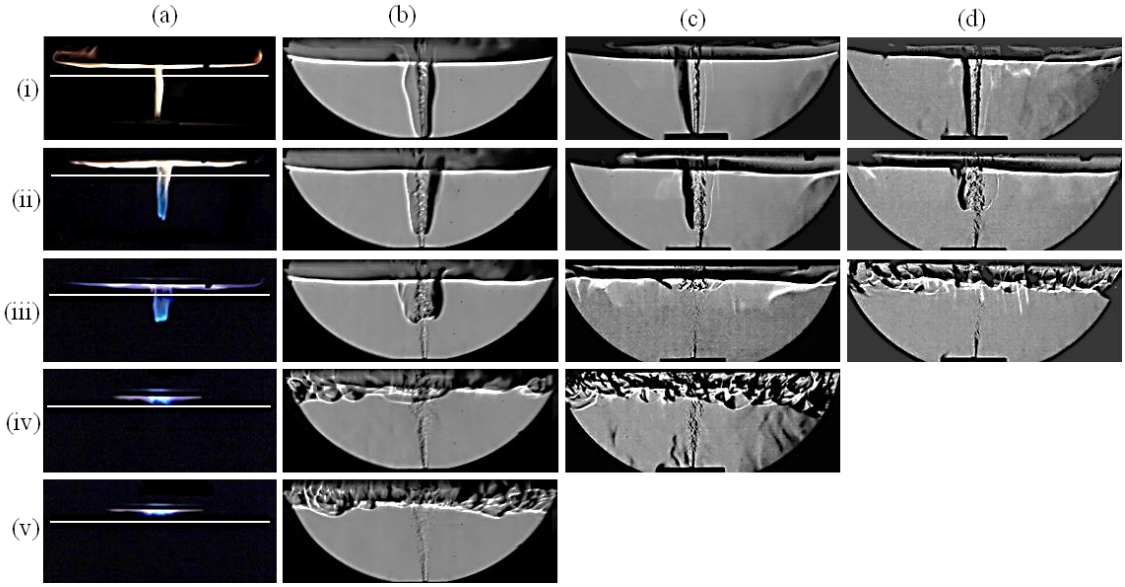

Figure 5.15: (a) Direct images and (b) Schlieren images for (i) propane diffusion flames and propane flames at ϕ = (ii) 16.3, (iii) 8.2, (iv) 5.1 and (v) 4.3 respectively at 1.6 kW, and Schlieren images at (c) 3.2 kW and (d) 4.7 kW for (i) diffusion flames and for ϕ = (ii) 16.3, (iii) 8.2 and (iv) 6.3, with the invisible gas layer positions sketched onto the direct images.

Slight peaks in the temperature profiles can be seen for the propane flames. For the 1.6 kW cases (Fig. 5.14a) these are observed at 0.03 m for the diffusion flame, moving outwards to 0.06 m for ϕ = 4.2 and 4.9, which were both blown ring flames with similar

flame diameters impinging on the plate (Fig. 5.15a (iv and v)). The positions of the peaks indicate the intense combustion zones located away from the stagnation points. There are slight dips in the temperature profiles at the stagnation region for all cases (Figs. 5.14a to c); the heat on the plate surface is flowing radially inwards due to the unburned fuel impinging on the plate which is verified by the schlieren images (Fig. 5.15). This also decreases the total heat that could be transferred to the plate for the propane flames as the probabilities of the flame or hot gases impinging on the plate are reduced. It is interesting to note that the plate temperature for $\phi = 4.2$ is lower than that of $\phi = 4.9$ for the thermal loading of 1.6 kW (Fig. 5.14a). This would imply that as the equivalence ratio is decreased past a certain point, the total heat transfer to the plate also decreases. This is due to the increase in wrinkles in the flame (Fig. 5.15b (v)). As a result more ambient air was mixed with the hot gases, cooling them down.

It can be seen that for the 1.6 kW propane flames the thickness of the invisible gas layer is approximately constant for the richer flames (Fig. 5.15a (i to iii)). However, as the flame becomes more turbulent, the layer of hot gases increases in thickness in parts of the wall jet region (Fig. 5.15a (iv and v)). For the blown ring flames, the non-uniform thicknesses in the gas layers are caused by turbulent structures which appear to move radially outwards with the convection currents. These structures are more prominent for the $\phi = 4.2$ flame than the $\phi = 4.9$ flame due to the higher Reynolds number.

When the 1.6 kW flames (Fig. 5.14a) are compared to the quartz plate (Section 5.3.5.2), it can be seen that the temperatures for the steel plate are lower than for the quartz plate. In addition, the heat is more evenly distributed across the steel plate. This is due to the higher thermal conductivity of steel; at a steady state, the heat conducted radially through the plate is much higher, smoothing out the temperature profiles. The heat conducted through the plate is also higher, causing a higher temperature on the top side of the plate; radiating and convecting more heat to the surroundings and lowering the overall plate temperature.

Figure 5.14d shows the stagnation point temperatures against $1/\phi$. It can be seen that for the diffusion flames and $\phi = 15.8$, the stagnation point temperatures are quite similar for the three thermal loadings. However, as ϕ is decreased, the stagnation point temperatures move further apart for each thermal loading. Again, this is due to the

larger change in flame mode at the different thermal loadings; for a particular equivalence ratio, the flame mode is different for different thermal loadings. This is also due to the fuel being burnt up more quickly for the flames with higher Reynolds numbers (Table 5.3).

Figure 5.14e shows the radiation losses from the plate, normalised by the thermal loading. It can be seen that for the 1.6 kW flames, there is a peak in the curve at around $\phi = 6$. At this equivalence ratio, there is a maximum amount of heat transferred to the plate. For the impinging flame experiments, the fuel has time to mix with air before combusting in the plate region, particularly for the lifted flames, and so the local equivalence ratio at the plate will be lower than that at the nozzle. The peak indicates that the flame has entrained enough air to reach local stoichiometric conditions by the time the flame hits the plate, causing a maximum heat transfer. For the 3.2 kW case, the peak is at around $\phi = 8$, and for the 4.7 kW case it is around $\phi = 10$. This means that as the thermal loading is increased, the amount of premixed air required to obtain stoichiometric conditions at the plate is reduced. This is due to the increase in Reynolds number with the increase in thermal loading at the specified equivalence ratios (Table 5.3). The radiation losses from the plate as percentages of the thermal loading decrease with thermal loading. This is due to more heat being lost to the atmosphere via mixing with the cool ambient air, and also to the increased convective heat loss from the top of the plate with increasing plate temperature. It shows that as the thermal loading is increased, the configuration becomes less efficient at heating the plate, even though the plate temperature is increased.

It has been shown that for propane flames impinging onto an oxidised steel plate, the thermal loading and equivalence ratio have significant effects on the plate temperature profiles. When ϕ is decreased the flame modes change from attached diffusion flames to lifted partially premixed flames and finally to blown ring flames. As this happens, the plate temperatures become hotter near the stagnation region and cooler towards the plate edges. In addition, the radiation losses initially increase due to the added heat from the leaner flames. This is followed by a decrease in radiation loss due to the entrainment of air causing local lean conditions at the plate. It is also caused by a reduction in temperature of the hot gases due to mixing with the cool ambient air caused by the

greater turbulence in the flames. The change in flame mode happens more quickly for the higher thermal loadings due to the higher Reynolds numbers of these flames. This also causes the temperature profiles to change more quickly with changes in ϕ.

The next section will look at hydrogen flames at similar thermal loadings as the propane flames. However, it was possible to sustain much leaner conditions with the hydrogen flames, and so the equivalence ratios will not be identical to the propane flames. Therefore, the diffusion flames at the three thermal loadings will be looked into first, and compared to the propane flames. This will be followed by an examination of the equivalence ratio effects of the hydrogen flames on the wall temperature profiles.

5.4.4. Hydrogen

Firstly hydrogen diffusion flames will be looked at for the values in Table 5.3. These will be compared to the propane diffusion flames at similar thermal loadings. Following this, flames at fuel rich and near stoichiometric conditions will be compared for two values of thermal loading.

5.4.4.1. Diffusion Flames

Hydrogen and propane diffusion flames differ in many properties. The propane flames were quite luminous, producing a lot of soot. This increases the radiation heat transfer from the flame to the plate. The hydrogen flames produced a lot of water, which condensed on the cool plate but evaporated after a couple of minutes of heating. In addition, the flame temperature (Chapter 4) and calorific value of hydrogen flames are much higher than of propane flames. It will be shown that the flame shapes are also quite different at similar thermal loadings.

Hydrogen diffusion flames were studied at three thermal loadings (Table 5.3) and the temperature profiles are shown in Fig. 5.16a. An emissivity value of 0.79 was used for the temperature calculations, corresponding to heavily oxidised steel with no soot deposition. The propane profiles from Section 5.4.3 have been repeated in Fig. 5.16a for comparative purposes. The profiles for the hydrogen flames are less smooth near the stagnation region than near the edges of the plate because of the high temperature induced oxidisation of the plate. This is not observed in the temperature profiles for the propane flames as the plates were covered in soot, which gives a more even surface

along the plate. The general trends for the hydrogen flames were not affected by the uneven surface caused by the heavily oxidised plate and so the plate was not replaced. Also, a new plate would be oxidised again after a few tests causing inconsistency between the different cases, as discussed in Section 5.2.5. The temperature profiles of the hydrogen flames (Fig. 5.16a) show a bumpy region followed by a small peak at approximately 0.03 m and a smoother decline towards the edge of the plate. At the peak, the heat is flowing away from the hot region both radially inwards and outwards. These peaks indicate the intense combustion zones usually found in impinging flame jets due to good fuel/air mixing just away from the stagnation region [11]. Smaller peaks can be observed in the propane cases (Fig. 5.16a) at approximately the same radial distance, however these peaks are not as distinguished due to the lower adiabatic flame temperature of propane (Chapter 4).

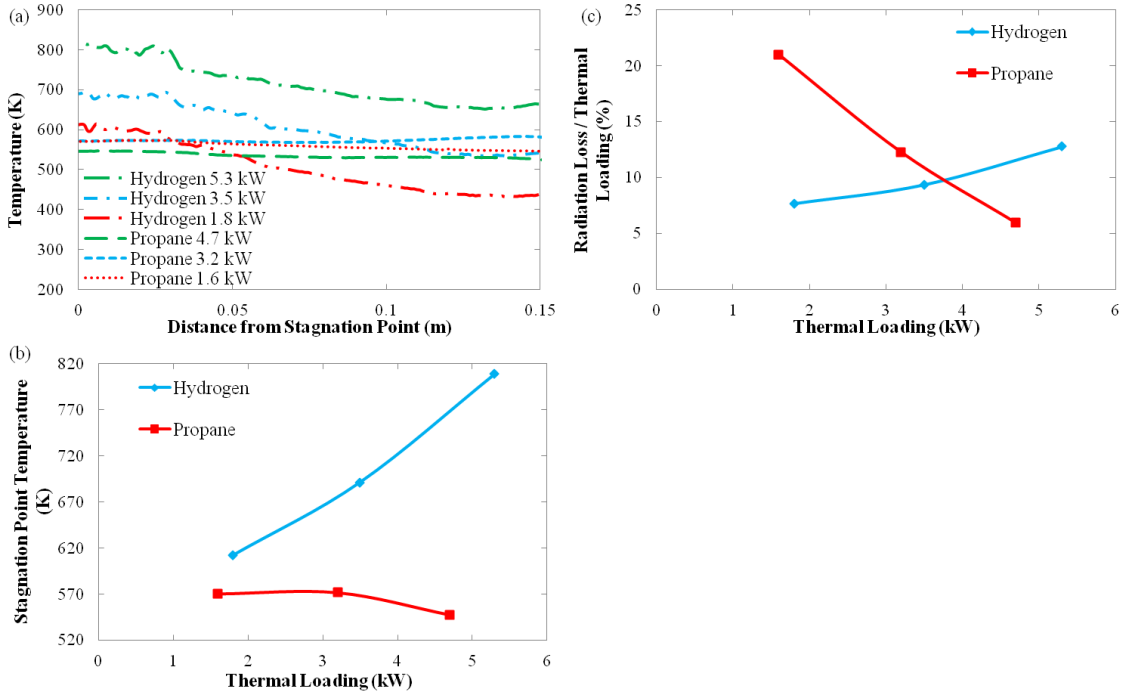

Figure 5.16: (a) Plate temperature profiles for hydrogen and propane diffusion flames at various thermal loadings, (b) Stagnation point temperatures and (c) Radiation losses from the plate.

The plate temperatures (Fig. 5.16a) were observed to be higher for the hydrogen flames than for the propane flames at the higher thermal loading settings, even though a similar range of thermal loading conditions was applied to both cases. This may be due to a couple of factors. Firstly, from Chapter 4 it was shown that hydrogen plus nitrogen

composition has a much faster laminar burning velocity (4.8 times faster at stoichiometry) and a higher adiabatic flame temperature (4.6 % higher at stoichiometry) than propane. The higher flame temperature of the hydrogen flames causes elevated local heat transfer and the faster laminar burning velocity increases the pressure and temperature within the flame. Also, the higher molecular diffusivity of the hydrogen allows easier mixing with the surrounding air which corresponds to a more elevated convective heat transfer. Secondly, it could also be caused by the larger amount of exhaust gases going over the edge of the plate for the propane flames, due to the larger flame size (shown by the direct images in Fig. 5.17), lowering the plate temperatures. The temperature profiles for the hydrogen flames increase quite steadily and quickly across the whole plate surface with increasing thermal loading (Fig. 5.16a). However, for the propane flames, the temperature only rose slightly as the thermal loading was initially increased, and in fact decreased for the 4.7 kW propane flame (Fig. 5.16a) due to more heat being lost to exhaust (Fig. 5.17a (iii)). This did not occur for the hydrogen flames as the entire flame areas were contained within the plate area (Fig. 5.17b).

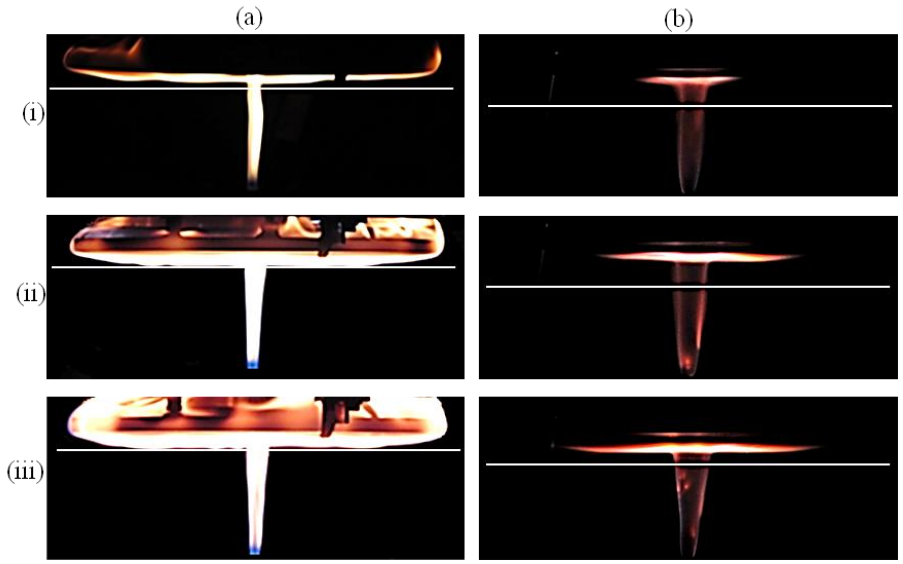

Figure 5.17: Direct images for (a) Propane flames at (i) 1.6 kW, (ii) 3.2 kW and (iii) 4.7 kW and for (b) Hydrogen flames at (i) 1.8 kW, (ii) 3.5 kW and (iii) 5.3 kW, with invisible gas layer positions shown by the white lines.

The profiles for the hydrogen cases all show higher temperatures as the stagnation region is approached, whereas the profiles of the propane flames illustrate a slight reduction towards the stagnation region (Fig. 5.16a) due to the unburned fuel impinging

on the plate. This can be seen in the schlieren images in Fig. 5.18a for all three propane cases. The stagnation point temperatures for the propane and hydrogen diffusion flames are shown in Fig. 5.16b. It can be seen that the temperatures increase quite steadily with thermal loading for the hydrogen flames. This is due to the decrease in unburned fuel with thermal loading, shown by the schlieren images in Fig. 5.18b. Only a very small amount of unburned fuel impinging on the plate is found for the hydrogen cases at the lower thermal loadings, and for the thermal loading of 5.3 kW, the jet fuel core starts to become wrinkled and burns out before reaching the plate surface (Fig. 5.18b (iii)). However, for the propane flames the stagnation region temperature decreases with increasing thermal loading, due to the increase in unburned fuel caused by the higher flow rate for the higher thermal loading cases. The density difference between the propane unburned fuel and the ambient air is quite similar, whereas the hydrogen flames have a much higher density difference and a higher molecular diffusivity, causing faster diffusion between the unburned fuel and ambient air. This causes the fuel to be burnt up more quickly for the hydrogen flames.

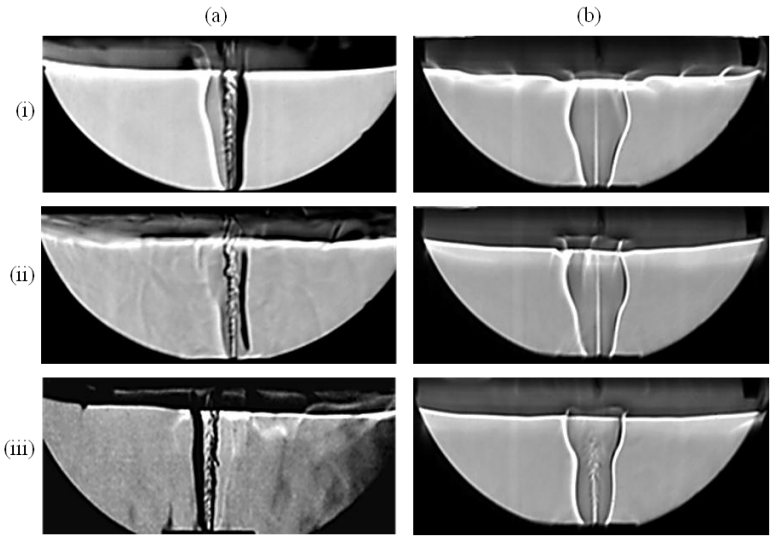

Figure 5.18: Schlieren images for (a) Propane flames at (i) 1.6 kW, (ii) 3.2 kW and (iii) 4.7 kW and for (b) Hydrogen flames at (i) 1.8 kW, (ii) 3.5 kW and (iii) 5.3 kW.

The invisible gas layers that can be seen in the schlieren images in Fig. 5.18 have been sketched onto the direct images (Fig. 5.17) using scaling of the schlieren images to mark the approximate average position. The invisible gas layers have very similar thicknesses for all thermal loadings for the propane diffusion flames (Fig. 5.17a), and

for the hydrogen flames (Fig. 5.17b). However, the thickness for the hydrogen flames is larger than for the propane flames in all cases. This is due to the higher molecular and thermal diffusivity for the hydrogen flames, increasing the diffusion between the flames and the ambient air. This also causes a thicker flame width, as can be seen in Fig. 5.18.

The radiation losses from the plate as percentages of thermal loading (shown in Fig. 5.16c) decrease for increasing thermal loadings for the propane flames. This is due to a higher percentage of the heat being lost to the surroundings, exhaust and unburned fuel at higher thermal loadings. In contrast, the radiation losses for the hydrogen flames increase quite steeply with thermal loading, due to the fact that the entire hydrogen flame impinges on the plate surface (Fig. 5.17b) with minimal heat lost to the exhaust gases. The percentage of radiation loss from the plate for the 3.2 kW propane flame is comparable to that of the 5.3 kW hydrogen flame. This is due to the fact that the hydrogen flame is concentrated towards the centre of the plate and so the cooler edges of the plate reduce the overall radiation loss from the plate for the hydrogen flame. Therefore, there is a balance between the exhaust gases reducing the radiation losses for the propane flames, and the cool areas of the plate reducing them for the hydrogen flames. If a larger plate was used, then the radiation losses would be lower for the hydrogen flames. If a smaller plate was used then the radiation losses would be lower for the propane flames, due to the larger amount of exhaust gases. In addition, the emissivity of the plate heated by the hydrogen flames (ε = 0.79) reduces the radiation loss for each temperature value when compared to that of the propane flames (ε = 0.96), and reduces the radiation heat absorption from the flame to the plate.

Since steel is a very good conductor of heat, the radiation losses shown for the underside of the plate will be very similar to the radiation losses from the top of the plate. Therefore, the total radiation loss from the plate as a whole will be approximately twice that of the radiation lost from the underside of the plate. This means that twice the value of the radiation loss from the underside of the plate can be used to approximate a minimum amount of heat transferred to the plate from the flame. However, since heat will also be lost due to convection from the top side of the plate the actual heat transferred to the plate will be higher than this value, and so it is only the minimum approximated value of heat transferred. Using this method, Fig. 5.16c shows that for the

propane flame at 1.6 kW at least 40 % of the heat from the flame reached the plate and was lost due to radiation. However, it is only at least 12 % for the 4.7 kW propane flame due to the large amount of heat lost from the flame going over the edges of the plate. The high percentage of radiation loss from the plate indicates that radiation loss from the plate should be considered in impinging flame configurations. The radiation loss from the plate reduces the overall plate temperature when heated in the steady state condition, and when using high conductivity materials this heat loss is almost doubled. However, even if the wall has thermal insulation or water cooling, the radiation loss from the underside will still be significant.

It has been shown that the fuel and thermal loading have significant effects on the plate temperature profiles for propane and hydrogen diffusion flames. The flame shape, including the flame spread across the plate, and the flame temperature and diffusivity affect the heat transfer to the plate. For the hydrogen flames, the temperatures are concentrated towards the plate centres, with steep gradients towards the edges of the plate. This is due to the small flame area on the plate and to the high temperatures and diffusivity of the hydrogen flames. The temperatures of the plates heated by the propane flames are more evenly distributed and are much lower than for the hydrogen flames. In addition, the large flame area across the plate causes the plate temperatures to be reduced for higher thermal loadings due to heat lost via exhaust gases. The next section looks at the plate temperature for hydrogen premixed flames.

5.4.4.2. Premixed Flames

The analysis for the hydrogen premixed flames was performed at two values of equivalence ratio for two thermal loadings as outlined in Table 5.3. Much lower equivalence ratios were achieved for the hydrogen premixed flames than for the propane premixed flames due to the higher burning velocity and reactivity, and lift-off and blow-out/blow-off were not observed. This is in agreement with [274] where lift-off was not achieved until an exit velocity of 730 ms^{-1} was reached in pure H_2 flames (from a 2 mm diameter nozzle). The maximum velocity was 34 ms^{-1} in these experiments. The equivalence ratio was lowered until the flame became unstable at the base, which was at ϕ = 1.1 for the 1.7 kW case and at ϕ = 1.5 for the 3.5 kW case. This is similar to the

propane flames, which experienced blow-out at higher equivalence ratios for higher thermal loadings.

Figure 5.19a shows the temperature profiles for the hydrogen premixed cases. The results show that, for both thermal loadings, as ϕ was decreased the plate temperatures decreased dramatically. This is in contrast to the premixed propane flames at equivalent thermal loading conditions (Section 5.4.3), which increase in temperature with ϕ for each of the propane cases. The only similarity between the propane and hydrogen premixed cases is the slight temperature decrease at ϕ = 4.3 (minimum ϕ achieved) for the propane premixed flames at 1.7 kW (Fig. 5.14a).

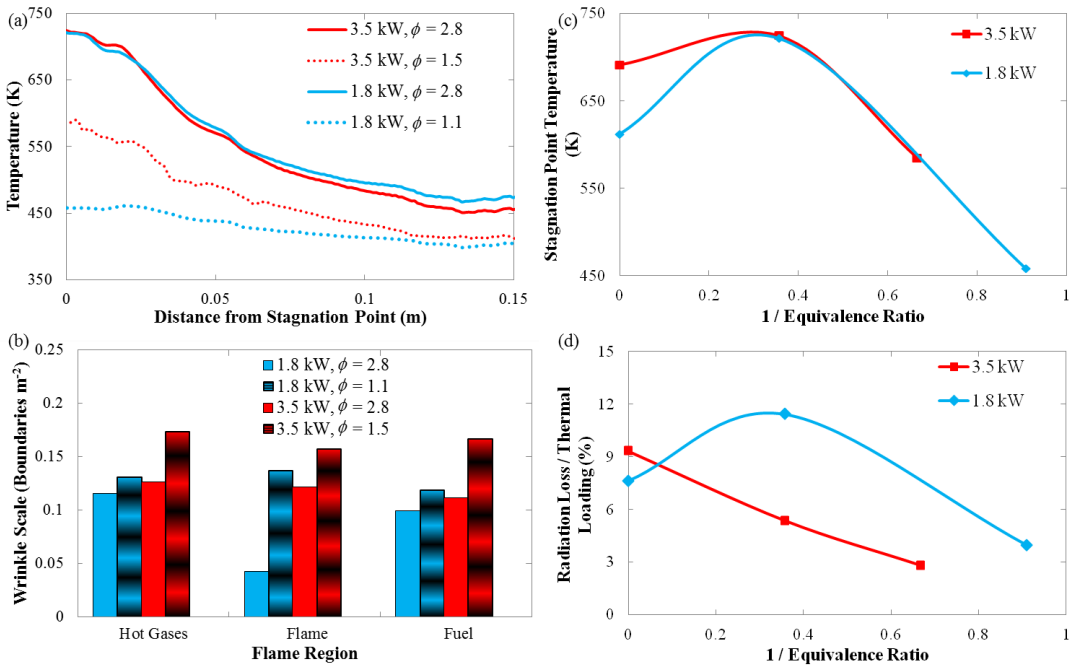

Figure 5.19: (a) Plate temperature profiles, (b) Wrinkle scale analysis, (c) Stagnation point temperatures and (d) Radiation losses from the plate for hydrogen premixed flames at various equivalence ratios and thermal loadings.

Figures 5.20a and b show the direct and schlieren images respectively. When more air was added, the flame became smaller and more turbulent, until the flame was no longer impinging on the plate at the minimum equivalence ratios of 1.1 and 1.5 (for the 1.7 and 3.5 kW cases respectively) (Figs. 5.20 (ii) and (iv)). This is in contrast to the propane flames, which lifted off as more air was added. This is due to the differences in laminar flame speed for the two fuels (Chapter 4). The hydrogen with nitrogen laminar flame

speed was calculated to be 4.8 times faster than propane at stoichiometry. Therefore, when the nozzle exit velocity was increased for the propane flames, the laminar flame speed was not fast enough to counteract this, and the flames lifted off. However, for the hydrogen flames, the laminar flame speed was so fast that the flame could propagate against the upwards flow and the flame reduced in size rather than lifted off. This is the cause for the dramatic decrease in temperature at the minimum ϕ; it meant that the higher rate of heat transfer caused by the high thermal diffusivity of hydrogen no longer affected the plate, since only combustion products were in contact with it.

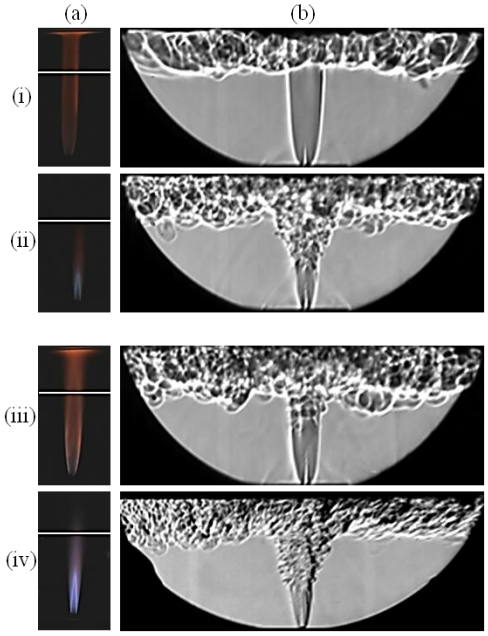

Figure 5.20: (a) Schlieren and (b) Direct images of hydrogen premixed flames at (i) 1.8 kW, ϕ = 2.8, (ii) 1.8 kW, ϕ = 1.1, (iii) 3.5 kW, ϕ = 2.8 and (iv) 3.5 kW, ϕ = 1.5, with approximate positions of the jot gas layers sketched onto the direct images.

Furthermore, the schlieren images (Fig. 5.20b) show that more mixing occurred with a reduction in equivalence ratio, depicting huge differences in the schlieren wrinkling structures in the hot gas layers. The wrinkling structures became much smaller with decreasing ϕ (Figs. 5.20b (i to ii) respectively), which is an indication that strong mixing between the fuel and the surrounding air takes place as more air is added. Figure 5.20b shows a large amount of small scale wrinkling of the hot gases, which increased with the reduction of ϕ. This was due to the very high Re for the hydrogen premixed cases, which contrasted strongly with the low Re for the hydrogen diffusion cases (Table 5.3).

This large range of Re for the hydrogen flames accounts for the differences in trend with ϕ, and for the differences from the propane cases which had a much smaller range of Re over the equivalence ratios studied. The corresponding illustration in Fig. 5.19b shows that the 'wrinkle scale' increases quite evenly across the three regions as ϕ changes from 2.8 to 1.5 for the 3.5 kW flame (3rd and 4th columns respectively). It also increases with a decrease in ϕ for the 1.8 kW flame (1st and 2nd columns respectively), particularly in the 'flame' region. This means that the average size of the turbulent structures in the flame section decreased dramatically for ϕ = 1.1 at 1.8 kW, and so more heat was transferred to the surrounding air which lowered the plate temperature. This wrinkling was caused by the enhanced mixing between the burnt hot gases and the air surrounding the impinging jet.

For the thermal loading of 3.5 kW, and ϕ = 2.8, the radial plate temperature profile is very similar to, and in fact slightly lower than, that of the thermal loading of 1.8 kW (Fig. 5.19a). Again, this is due to the small scale wrinkles appearing in the top of the flame section of the 3.5 kW case which were not observed in the 1.8 kW case (Figs. 5.20b (iii and i) respectively). It can be seen from Fig. 5.19b that the wrinkle scale values are the lowest for the 1.8 kW, ϕ = 2.8 flame (1st columns), which shows that this flame has the least amount of small scale wrinkles. This causes less heat to be lost to the mixing with ambient air before the flame reaches the plate, and thus raises the plate temperature when compared to the 3.5 kW case. In contrast, for the lower equivalence ratio the temperature is elevated for the higher thermal loading. This is due to the more similar sizes of wrinkle scales, and the slightly higher ϕ (Fig. 5.19b); there is only a slight increase in the quantity of wrinkles from the 1.8 kW to the 3.5 kW cases (2nd and 4th columns respectively) for all three interrogated areas, even though Re is almost doubled (Table 5.3). This can also be visualised in the schlieren images (Figs. 5.20 (i and iii) for ϕ = 2.8 at 1.8 kW and 3.5 kW respectively, and (ii and iv) for ϕ = 1.1 and 1.5 at 1.8 kW and 3.5 kW respectively). This shows that more wrinkles in the flame causes the plate temperature to become lower due to enhanced mixing with the cool ambient air.

For ϕ = 2.8 and for both thermal loadings, there is a slight peak in the temperature profiles at around 0.02 m. As described for the hydrogen diffusion flames and the

propane premixed flames (Sections 5.4.4.1 and 5.4.3 respectively), these peaks indicate the intense combustion zones in the impinging flames. However, for ϕ = 1.1 and 1.5, there seems to be a peak at about 0.03 m for both thermal loadings. Since the flame is not impinging on the plate, this cannot be attributed to the intense combustion zones as observed previously. However, the schlieren images (Figs. 5.20b (ii and iv)) show that this location is approximately where the boundary of the cone of hot gases meets the layer of hot gases spread across the plate. This means that at this cone edge location, more heat is being transferred to the plate, indicating that the burned gases are hotter in this region. The radial heat then flows very rapidly away to the edge of the plate (indicated by the step gradients (Fig. 5.19a)) for the ϕ = 2.8 cases and less rapidly for the ϕ = 1.1 and 1.5 cases. This implies that there is a much larger temperature difference between the centre and the edge of the plate for ϕ = 2.8, which is due to the direct flame impingement.

For the hydrogen flames, the colours of the hydrogen flames changed from transparent to a bright blue at the base as ϕ was decreased (Figs. 5.17b and 5.20a respectively). It is worth noting here that the images have been enhanced in order to show the hydrogen flame shape, as the transparent nature of the hydrogen flames means that it would be difficult to show them without enhancement. The transition to a blue colour is similar to the propane flames, which, as mentioned, changed to a bluer colour and reduced in size as the flames became leaner. The invisible gas layer (Fig. 5.20a) increases slightly in thickness with a decrease in ϕ for each case. This is due to the added turbulence from the increase in Re.

Figure 5.19c shows the stagnation point temperatures against $1/\phi$ for each thermal loading. For the hydrogen premixed cases, the maximum temperatures occur at the stagnation point, due to the lack of unburned fuel impinging on this region. For both thermal loadings, the stagnation point temperatures initially increase with added premixed air and then decrease after ϕ = 2.8. The increase is due to the reduction in unburned fuel impinging on the stagnation region, and the increase in flame temperature, as premixed air is added. The temperatures then decrease due to the lack of direct flame impingement and also due to the small scale wrinkles that are present in the flames for the lower equivalence ratios. For ϕ < 2.8, the stagnation point temperatures

are the same for both thermal loadings, since it is only hot gases impinging on the plate. This implies that the hot gases are the same temperature for the same equivalence ratios at the different thermal loadings.

Figure 5.19d shows the radiation losses from the plate. The radiation losses for the premixed hydrogen flames are much lower than for the propane flames. This is because as the equivalence ratio was decreased the amount of direct flame impingement also decreased. Also, since there was no unburned fuel impinging on the plate for all of the premixed hydrogen cases (Fig. 5.20b), this means that all of the heat transferred to the plate comes from the hot gas impingement for all plate locations at $\phi = 1.1$ and 1.5. This decreases the total heat available and so reduces the overall plate temperatures and hence the radiation losses from the plate. A peak in the curve for the radiation losses from the plate, shown in Fig. 5.19d, occurs at $\phi \approx 3$ for the 1.8 kW case. This indicates that at 1.8 kW, stoichiometry at the plate was achieved at approximately this nozzle exit equivalence ratio, as it has the highest heat loss from the plate, as discussed in Section 5.4.3. In addition, at $\phi = 1.1$ and 1.5, all of the reactants were burnt up before the plate was reached. There was no peak in the radiation loss curve for the 3.5 kW case. The radiation loss percentages were lower for the higher thermal loading, similar to the propane flames. However, the reasons for this are different. For the propane flames this was partly caused by the increased convective heat loss from the plate with increasing plate temperature. However, for the hydrogen flames, it is due to the increased turbulence in the flame with increased thermal loading, causing the plate temperatures to be lower for the higher loading values.

It has been shown that the equivalence ratio, Reynolds number and thermal loading significantly the plate temperatures for premixed hydrogen flames. As the equivalence ratio is increased to near stoichiometric conditions, the flame height reduces significantly, so that only hot gases are impinging on the plate. The wrinkle scale analysis helps to explain why plate temperatures are similar, and even lower, for the flames at the same equivalence ratio but higher thermal loading values. The effect of equivalence ratio is quite different for hydrogen flames than for propane flames, due to the differences in flame mode and Reynolds number, and hydrogen flames could be sustained at much leaner mixtures.

5.4.5. Conclusions

The plate temperatures for propane and hydrogen flames have been analysed at three values of thermal loading and at various equivalence ratios. It has been shown that the effect of equivalence ratio is very different for hydrogen and propane flames. In addition, the thermal loading and wrinkling observed in the schlieren images have significant effects of the premixed flames. The following observations were made:

- For the propane flames, adding premixed air causes the flame mode to change from attached, to lifted, to blown ring flames. This has a large effect on the plate temperature profiles. However, for the hydrogen flames, premixed air causes the flame length to become shorter so that, at near stoichiometric conditions, only hot gases were impinging on the plate. In addition, the propane flame blew out at much richer concentrations, whereas the hydrogen flames could withstand much lower equivalence ratios.
- For the diffusion flames, increasing the thermal loading caused the flame width on the plate to become larger. In addition, the propane flames had much larger flame spread across the plate than the hydrogen flames at the same thermal loadings. This caused a large amount of heat to escape around the edges of the plate, reducing the plate temperatures. It also caused the temperature profiles for the hydrogen diffusion flames to be much more concentrated towards the centre than for the propane flames.
- The plate temperatures were much higher for the hydrogen flames due to the higher flame temperature and thermal diffusivity. In addition, the molecular diffusivity and density ratio between the burned and unburned gases caused a thicker flame width for the hydrogen flames and a thicker layer of hot gases underneath the plate.
- The wrinkle scale methodology was utilised for the hydrogen premixed flames due to their notable turbulence. It helped to explain the similarities in plate temperature profiles; the plate temperatures were similar for flames with similar wrinkle scales at specific sections of the flame and hot gas regions, even at very different Reynolds numbers.
- The stagnation point temperatures were analysed for the different compositions and it was shown that the unburned fuel has a large effect on the stagnation point

temperature as expected. In addition, for the near stoichiometric hydrogen flames, the stagnation point temperatures were similar for the two values of thermal loading, due to the lack of flame or fuel impingement in this region. This implied that the hot gas impingement temperatures were comparable for the same equivalence ratios at different thermal loadings.

- The radiation losses from the plate were analysed and it was found that the radiation losses as percentages of the thermal loading decreased with increasing thermal loading. This is partly due to the lower efficiency of the flame to heat the plate at higher thermal loadings (due to higher mixing with the cool ambient air and to heat being lost to exhaust gases), and partly to the increase in heat loss by convection from the top of the plate with increasing plate temperature.

It has been shown that using plate temperature profiles obtained by thermal imaging can be a useful method for comparing the effects of various fuel and flow properties, particularly when used with direct and schlieren imaging. The effects of flame shape and fuel properties have been analysed and impinging flames of propane and hydrogen have been compared in terms of the thermal footprint left on the flame impinged steel plate. The next section will look into the effects of syngas fuel composition on the plate temperatures, comparing syngas compositions from real data in terms of the flame shapes and thermal footprints.

5.5. Syngas

5.5.1. Introduction

The effects of syngas on wall temperature and flame structure when compared to hydrogen and hydrocarbon flames are of practical importance because combustor walls or other combustor components may be damaged by burning high hydrogen content syngas. In addition, the compositions of syngas vary widely from source to source. Therefore, the effects of changing the syngas content should also be explored. There has been much focus on fundamental hydrogen-enriched syngas research in recent years, however syngas has not yet been extensively studied in impinging flame configurations and heat transfer studies. This section looks at various syngas compositions and their effect on the wall temperature of the flame impinged steel plate.

5.5.2. Experimental conditions

As for the hydrogen flames, the syngas compositions were studied for diffusion flames and for the leanest achievable mixtures before the base became unstable and the flame started to lift. It was not deemed safe to work with lifted syngas flames due to the danger of blow-out and potential release of CO into the air. Unfortunately, due to the wide range of mixture compositions for the syngas flames, and to experimental constraints, the premixed compositions could not be sustained at similar equivalence ratios. In addition, the high N_2 composition could not be achieved at all, even for the diffusion flame, due to the high volume of nitrogen in the composition. Therefore, only the high H_2, high CO and high CO_2 compositions were studied, the compositions of which have been discussed in Section 3.2.3.1. The tests were done at a thermal loading of 3.6 kW, so that the results could also be compared to the hydrogen cases at 3.5 kW. The experimental conditions are shown in Table 5.4. It should be noted that the Reynolds numbers are quite different for the different compositions at similar thermal loadings, and this will have an effect on the flame wall interaction, which will be discussed in the next section. An emissivity of 0.79 was used to calculate the temperature profiles as no soot was deposited on the plate. The high H_2 composition could be studied at the lowest equivalence ratio due to the high reactivity and laminar flame speed of hydrogen. In contrast, the high CO_2 composition could only be studied at very rich mixtures due to the dilution of the CO_2. Chapter 4 showed that the addition of CO and CO_2 to the syngas compositions caused the laminar flame speed to reduce. Therefore, lift-off was more likely for the high CO and high CO_2 compositions respectively, which was observed in the experimentation since these flames became unstable at the base for lower amounts of added premixed air.

Composition	ϕ	Re
High H_2	Diffusion	2334
	1.1	9260
High CO	Diffusion	5006
	5.5	6398
High CO_2	Diffusion	8504
	18.2	8455

Table 5.4: Experimental conditions for the syngas compositions.

5.5.3. Results

Diffusion and premixed flames of three syngas compositions; denoted 'high H_2', 'high CO' and 'high CO_2' (Tables 3.2 and 5.4) have been studied. Figures 5.21a and b show the plate temperature profiles for the syngas diffusion and premixed flames respectively. The plate temperatures for the premixed cases are much more concentrated towards the centre than for the diffusion cases. This is due to the flames reducing in size and covering a smaller area of the plate for the premixed cases, as can be seen from the direct images in Fig. 5.22a.

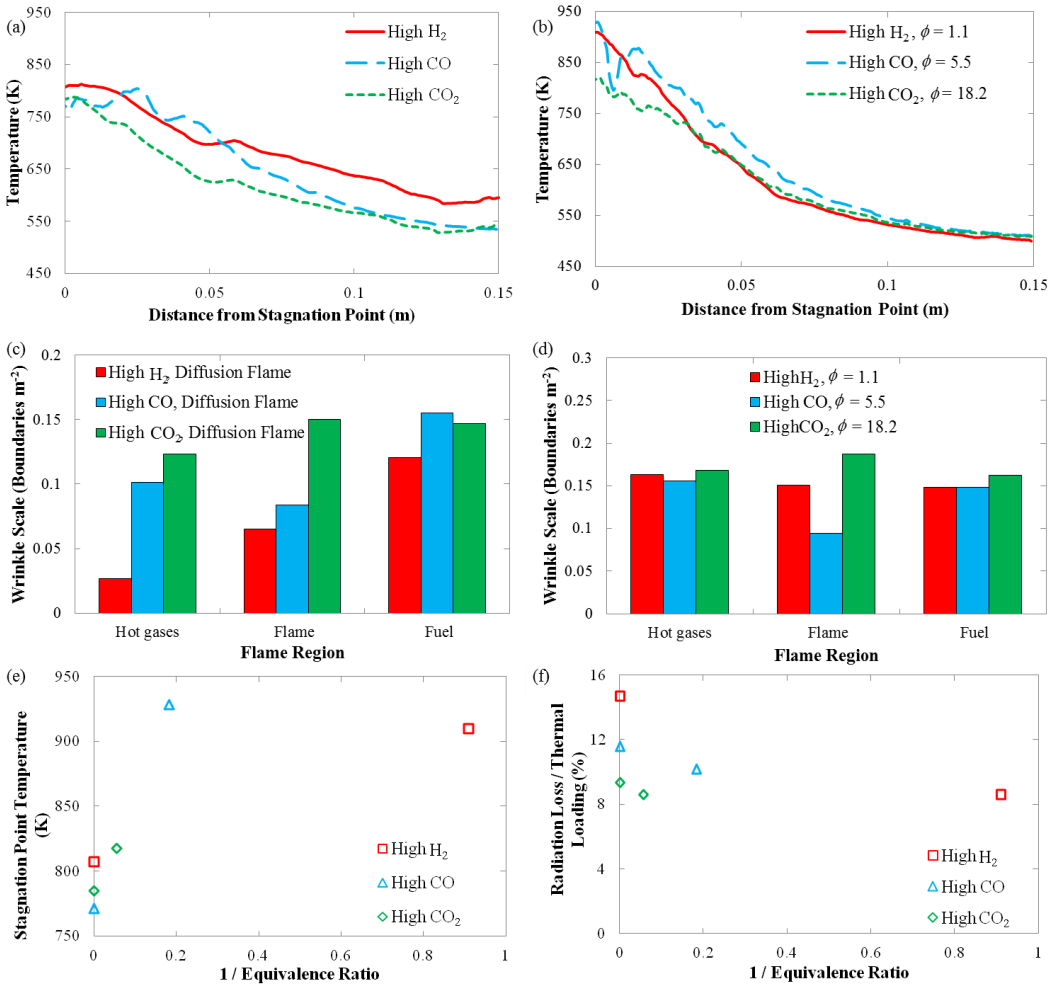

Figure 5.21: Temperature profiles for (a) Diffusion flames and (b) Premixed flames at equivalence ratios of 1.1, 5.5 and 18.2 for the high H_2, high CO and high CO_2 compositions respectively, (c) and (d) Turbulence scale analysis for the diffusion and premixed cases respectively, (e) Maximum temperatures, and (f) Radiation losses from the plate.

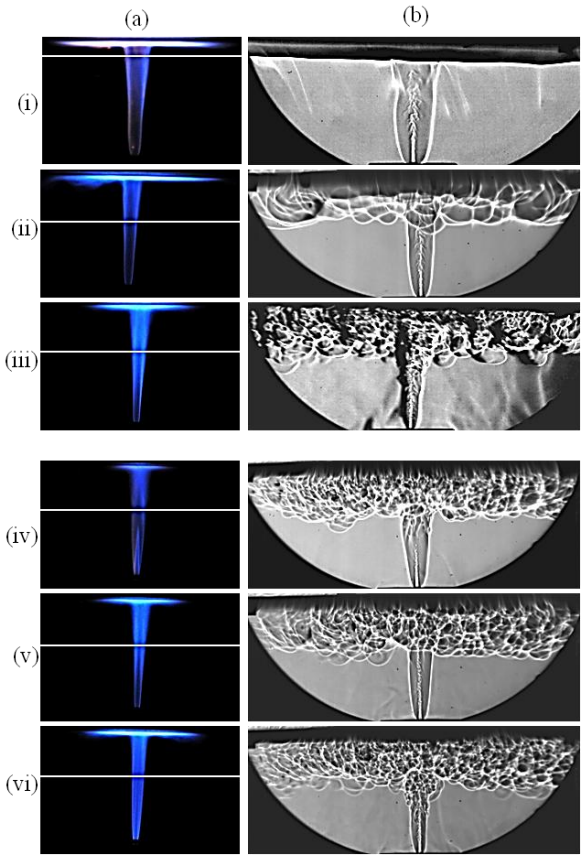

Figure 5.22: (a) Direct and (b) Schlieren images for diffusion flames for (i) High H_2, (ii) High CO and (iii) High CO_2 compositions, and for premixed flames for compositions of (iv) High H_2, (v) High CO and (vi) High CO_2 at ϕ = 1.1, 5.5 and 18.2 respectively, with approximate positions of the invisible hot gas regions sketched onto the direct images.

Figure 5.22a also shows that the flames are much more transparent for the high H_2 cases and much brighter for the high CO_2 cases, indicating that the extra CO and CO_2 cause the flame to be brighter and bluer. It can also be seen that the premixed cases have smaller transparent zones at the base of the flames and that a second conical shape is present in the central core for the high H_2 premixed case. Figure 5.22b shows that the unburned fuel zones are thinner for the premixed cases due to the premixed air aiding combustion in these areas. The invisible hot gas positions for the diffusion flames are dissimilar for the different compositions; becoming much thicker with an increase in CO or CO_2 concentration (Figs. 5.22a (i to iii) respectively). In addition, the schlieren images (Fig. 5.22b) show that for the diffusion flames, as the wrinkling quantity increases, the thickness of the gas layer also increases. However, for the premixed

cases, the thicknesses remain quite constant for each composition, even though the equivalence ratios and Reynolds numbers are very different.

In addition, Figs. 5.21a and b show that the plate temperatures towards the edge of the plate are all a very similar temperature for the premixed flames. From the wrinkle scale chart, shown in Fig. 5.21d, it can be seen that for the premixed cases, the wrinkle scales are very similar in all regions except for the high CO case in the flame region, where the wrinkle scale is much lower than for the other two flames. This is due to the absence of wrinkling in the flame region, just below the hot gas region, in the high CO case. This could account for the difference in trend in the thermal footprint for the high CO premixed case, which has a very steep dip near to the stagnation region at approximately 5 mm (Fig. 5.21b). The lower wrinkle scale for the high CO flame in the 'flame' region is also apparent in the diffusion case but is less noticeable on the wrinkle scale graph due to the comparison with the unwrinkled hydrogen flame (Fig. 5.21c). This shows that, although the nozzle exit Reynolds number and equivalence ratio are quite different, the wrinkle structures and wall temperature profiles in the wall jet region are quite similar near the lift-off limit for the three premixed compositions, and the temperature profiles are also quite similar.

The profile for the high H_2 diffusion flames is generally higher than for the high CO and high CO_2 diffusion cases. This is due to the higher thermal diffusivity and molecular diffusion rates for the syngas with higher hydrogen content. This can also be attributed to the variation in flame wrinkle structure; large scale wrinkles are observed in the diffusion case for the high CO flame whereas small scale wrinkles are seen in the high CO_2 diffusion case and in all of the premixed cases (Fig. 5.22b), causing more mixing with the cool ambient air. Figure 5.21a shows that the plate temperature is consistently higher for the high H_2 diffusion flames than for the high CO_2 diffusion flames, indicating that an even amount of heat is lost across the plate area due to the CO_2 dilution reducing the flame temperature (Chapter 4), and due to the extra wrinkles present in the high CO_2 flames which can be seen in Fig. 5.22b (iii). However, the plate temperature for the high CO diffusion flame shows a very different trend, with a dip near to the stagnation region and then two peaks at approximately 0.03 m and 0.04 m from the stagnation region. The temperatures at the peaks increase beyond those of the high H_2 case at these positions. The adiabatic flame temperature of the high CO

composition is slightly higher than that of the high H_2 composition for the fuel rich mixtures, which helps to explain why the plate can reach higher temperatures. The dip at the stagnation region is due to unburned fuel impinging on the plate (Fig. 5.22b (ii)) and the peaks occur at approximately the position of the flame/air boundary of the non-impinging section of the flame, as for the hydrogen premixed cases (Section 5.4.4.2). The plate temperatures for the syngas diffusion flames are all slightly higher than for the pure hydrogen at the similar thermal loading (Fig. 5.16a). This is due to the slight nitrogen dilution of the hydrogen cases, reducing the adiabatic flame temperature.

The stagnation point temperatures, shown in Fig. 5.21e, increase with a decrease in equivalence ratio for all three cases. This is in contrast to the pure hydrogen flames which decrease after a point, as discussed in Section 5.4.4. However, an equivalence ratio of 1.1 was not achieved for the high CO and high CO_2 flames at the nozzle size used due to the lower laminar flame speeds causing lift-off. At ϕ = 1.1, the laminar flame speed of the hydrogen plus nitrogen flame was approximately 30 % higher than for the high H_2 flame at the same equivalence ratio (Chapter 4). Therefore, the flame size, and consequently the plate temperature, did not reduce as significantly for the high H_2 case when premixed air was added. This caused the plate temperature to increase rather than decrease with added premixed air, in contrast to the hydrogen flame. The fact that the equivalence ratios achieved for the high H_2, high CO and high CO_2 compositions were 1.1, 5.5 and 18.2 respectively indicates that the addition of CO, and the consequential increase in Re and decrease in laminar flame speed, causes the flame to lift off and blow out more easily at the same thermal loading, and even more so for CO_2 addition. Since the addition of these gases reduces the percentage of hydrogen in the flame, it therefore also decreases the molecular diffusivity and flammability limits, making it more susceptible to flame blow-out.

The radiation losses, shown in Fig. 5.21f, decrease with an increase in equivalence ratio for all syngas cases. As there were only two equivalence ratios for each case studied, it is not known which exit equivalence ratio would be required to achieve stoichiometric conditions at the plate. The radiation losses from the plate are higher for compositions with higher H_2 concentrations, due to the higher flame temperature and the higher thermal diffusivity of hydrogen allowing for more efficient heat transfer. However, the radiation losses for the syngas compositions are all higher than those of the hydrogen

cases (Fig. 5.19d). This is likely to be due to the nitrogen dilution reducing the temperature of the hydrogen flames. The radiation losses from the plate decrease as the flame changes from diffusion to premixed for all three compositions. This is due to the flames reducing in size on the plate, which causes cool regions towards the edges of the plate and so reduces the overall temperature, as discussed in Section 5.4.3 for the hydrogen diffusion flames.

5.5.4. Conclusions

The effects of changing the syngas composition and premixing conditions on the wall temperature profiles have been studied. The radiation losses from the plate, stagnation point temperatures, wrinkle scales and invisible gas layers have been analysed. It has been found that:

- Premixing caused a reduction in flame size, similar to the hydrogen flames, which led to temperature profiles that were more concentrated towards the plate centre. In addition, this caused a reduction in the radiation losses from the plate.
- The premixed flames became unstable/lifted at very different equivalence ratios (and consequential Re) for the three compositions studied, due to the decrease in hydrogen concentration. In addition, the high N_2 composition could not be studied at all due to the very high percentage of nitrogen in the fuel.
- However, for the three compositions at the leanest concentrations, the wrinkle scales, temperature profiles and invisible gas layer thicknesses were quite similar, in contrast to the diffusion flames.
- For the diffusion flames, CO and CO_2 addition caused higher wrinkles in the flames, consistent with the increase in Reynolds number.
- The compositions with higher hydrogen content have higher thermal and molecular diffusivity, laminar flame speed and adiabatic flame temperature. In addition, the turbulence degree was lower, causing less mixing with the cool ambient air. These factors caused higher wall temperature profiles and in addition, higher radiation losses from the plate.

It has been shown that the wall temperature profiles are significantly altered by changing the syngas composition, due to the differences in diffusivity, flame speed and flame temperature. However, for the premixed flames at the leanest achievable

mixtures, the wall temperature profiles were similar. The wrinkle scale method and invisible gas layers taken from the schlieren images help to explain this. When used with schlieren and direct imaging, the wall temperature profiles along the plate can give insightful information into the flame wall interaction when the fuel composition and flow variables are changed. However, more insight could be gained by exploring a larger range of equivalence ratios for the syngas compositions. This is reserved for the scope for future work.

5.6. Wall Temperature Conclusions

Thermal imaging has been used alongside direct and schlieren imaging in order to evaluate the flame wall interactions of impinging flames of various compositions and flow conditions. The schlieren images were used to evaluate the turbulence within the flames, and to look at the flame thicknesses and invisible hot gas layers. The direct images were used to look at the flame colour and size along the plate. The thermal profiles were used to evaluate the plate temperature and radiation losses from the plate. When used together, these methods can provide significant information into the flame wall interaction and can allow comparison of flames of different fuel and flow conditions.

The significance of Reynolds number and thermal loading were looked into first and it was shown that for hydrogen flames, the thermal loading has a much more significant effect on the wall temperature profiles than the Reynolds number. Therefore, thermal loading was used as a control variable in this chapter, although the effect of the Reynolds number was also considered.

The temperature dependent emissivity methodology was utilised for the quartz impingement plate. It was shown that the emissivity corrections have a large effect on the temperature profile, especially for the higher temperature values. Consequently, it was shown that emissivity is a significant parameter when determining the temperature using a thermal imaging camera. Various compositions of propane were studied with the quartz plate and it was found that h/d, ϕ, and coflow amount significantly affect the wall temperature profiles. In addition, some of the results were compared to the steel plate. It was found that the steel plate exhibited less defined temperature profiles due to the higher thermal conductivity of steel compared to quartz.

The thermal profiling method was also used to compare hydrogen and propane flames. For the diffusion flames, it was shown that the propane flames were much more spread out across the plate, causing heat to be lost to exhaust around the edges of the plate. In contrast, the hydrogen flames were contained towards the centre of the plate, causing cooler regions at the edges of the plate and consequently lowering the overall plate temperature and radiation losses, although the maximum temperatures were higher. This caused the effect of increasing the thermal loading to be different for the different fuel types.

For the premixed flames, the hydrogen flames could be sustained at much leaner concentrations, due to the higher reactivity of hydrogen. In addition, adding premixed air had a very different effect on the hydrogen and propane flames. For the propane flames, it caused a change in flame mode from attached to lifted to blown ring flames. This change in flame mode significantly affected the wall temperature profiles. For the hydrogen flames, adding premixed air caused the flame to become shorter, so that at near stoichiometric conditions, the flame was no longer impinging on the plate. This is due to the fuel being burnt up very quickly for the leaner flames, and caused the wall temperature profiles to become lower.

A similar effect was seen for the syngas compositions; premixing caused smaller flame areas on the plate, causing the profiles to become more concentrated towards the centre. The syngas flames became unstable at the base at very different equivalence ratios (and Re) for the different compositions. However, the wall temperature profiles and wrinkle scale values were very similar for these flames. For the syngas flames with higher hydrogen content the wall temperatures and radiation losses were higher due to the higher flame temperature and diffusivity of these flames.

Wall temperature measurements can be useful for assessing the flame wall interactions of impinging flames. The heat transfer process of flame impingement to a surface is important in many process industries, for example the glass and metal industries, where impinging flames are used to generate high heat transfer rates. In addition, the effect of heating by different fuels is of importance in order to prevent flame quenching and/or hotspots on flame impinged surfaces.

It has been shown that thermal imaging is a useful tool for measuring the wall temperature using a 2D, non-intrusive measurement technique. Flames of varying fuel and flow conditions were compared in this way, and radiation losses from the plate were assessed, even for non-constant emissivities and temperatures. When combined with direct and schlieren imaging, features such as flame width across the plate, turbulence and mixing characteristics and flame colour were used to explain the wall temperature profiles. Under the same thermal loading and fuel composition, the fuel/air arrangement at the nozzle was found to have significant effect on the wall temperature. These methods have been successfully implemented to compare the flame wall interactions of propane, hydrogen and syngas flames at various flow conditions. In addition the steady state heating of the impingement plates was monitored using the thermal imaging camera. These methods can be applied to configurations in order to monitor uneven heating of flame impinged plates and to compare a wide range of flow properties. The next chapter deals with instantaneous measurements of flame propagation following ignition, as these properties also vary widely for various fuel and flow conditions. The flame wall interaction will be analysed by testing the effect of the impingement plate on the flame propagation.

6. Results Part 2: Flame Front Propagation

6.1. Introduction

An impingement configuration provides an inhomogeneous fuel/air scalar field in a variable velocity field, which is excellent for the investigation of flame propagation under complex conditions while still having good optical access. By igniting the impinging jet at different locations, the sensitivity of ignition location on the flame propagation dynamics can be studied. Ignition location is an important factor when determining the optimum design for some combustion devices. For example, in IC engines, the igniter or flow pattern may be changed in order to make the combustion process complete more quickly, and ignition occurs in the rich part of the inhomogeneous mixture [275], and so the location of the igniter with respect to the fuel mixture is an important topic. Also, gas turbine combustors may need to easily establish steady state flames or re-ignite, for example at high altitude, and the ignition process will need to finish as soon as possible. For this reason, it is important to study methods that may reduce or increase ignition time. Ignition time is related to the propagation of the flame boundary from the point of ignition to a stable state, and so, the effect of ignition location on the upwards and downwards propagation of hydrogen and methane impinging flames will be studied in this chapter.

The pure fuel will exit the nozzle and start to mix with ambient air to form a thin fuel/air mixture layer suitable for flame propagation. When a flame is initiated upstream, its propagation downstream will be enhanced by both the jet velocity and the buoyancy force. On the other hand the flame propagation has to overcome the two factors in order to propagate upstream. Also, higher jet velocity will enhance the fuel/air mixing and provide a more suitable mixture for ignition and propagation. These competing factors will result in complex flame propagation patterns if the flame is initiated at different spatial locations. In addition, the presence of the plate will affect the flow field, which will have an effect on the flame propagation.

As such, this chapter reports an interesting phenomenon regarding hydrogen impinging flames, which show a non-linear flame propagation pattern when the flame is ignited at different locations. Different ignition locations will be investigated in order to study the effect of ignition location on this phenomenon and to compare it to the upwards and

downwards propagation of the flame. The effects will be studied for hydrogen diffusion and premixed flames and also for H_2/CO_2 flames to see how the addition of air or CO_2 affects the non-linear propagation towards the nozzle. The results will also be compared to methane diffusion flames. In addition, two nozzle diameters will be used. The effect of the plate height will also be discussed. The experimental method has been described in Chapter 3.

6.2. Hydrogen and Methane Diffusion Flames

6.2.1. Introduction

The ignition and flame propagation properties for hydrogen and methane are vastly different. This is due to the differences in laminar flame speed, adiabatic flame temperature, flame stretch, density of burned/unburned fuels and flammability limits. As such, the flame propagation after ignition will be very different for the two fuels. This section will compare the propagation of the flame front (the boundary between the hot products and the cold reactant/ambient air mixture) of hydrogen and methane diffusion flames at three values of thermal loading. The height of the flame front will be plotted with respect to time and the fitted polynomials will be used to give the velocity curves of the flame front at the centre line. In addition, the radial velocity for the cases ignited away from the centre of the plate will also be compared.

6.2.2. Experimental conditions

The flame propagation after ignition was plotted for methane and hydrogen diffusion flames. The fuels were compared at three values of thermal loading and for ignition locations in the lateral direction (‘Plate’, ‘Middle’ and ‘Nozzle’ locations) and at radial distances along the plate (‘Plate, 50 mm’ and ‘Plate, 100 mm’ locations). The plate locations have been described in Chapter 3. The experimental conditions are shown in Table 6.1. Although the cases are compared by thermal loading, the 1.8 kW methane flame has a comparable Reynolds number to the 3.5 kW hydrogen flame, and so these cases can also be compared to see the effect of the Reynolds number compared to the effect of the thermal loading. In addition, the 5.3 kW methane flame has a similar nozzle exit velocity to the 1.8 kW hydrogen flame, and so the fuel effect at similar nozzle exit velocities will also be compared in this way. Unfortunately, the methane

could not be tested at higher nozzle exit velocities due to the flame becoming a lifted flame. The hydrogen flames could not be tested at lower nozzle exit velocities due to the risk of flash back. The hydrogen flames all have 1.67 x 10^{-5} m^3 s^{-1} of nitrogen as for the other hydrogen compositions presented in this thesis. The electrode igniter was used for these cases. A constant *h/d* of 32.6 was used for all of the cases shown in Table 6.1, and the small nozzle (4.6 mm diameter) was used.

Fuel	Loading (kW)	Re	Nozzle Exit Velocity (m s^{-1})
Methane	1.8	652	2.8
	3.5	1280	5.5
	5.3	1931	8.3
Hydrogen	1.8	403	10
	3.5	603	19
	5.3	828	28

Table 6.1: Experimental conditions for the methane and hydrogen diffusion flames.

6.2.3. Axial Ignition Locations

Hydrogen and methane flames were studied at three values of thermal loading for the axial ignition locations. Firstly the methane flame propagation will be discussed.

6.2.3.1. Methane

Figure 6.1 shows the height and velocity of the vertical component of the flame front at the centre line for the methane flames ignited at the 'Plate', 'Middle' and 'Nozzle' locations. It can be seen that the upwardly propagating flames (closed data points) exhibit parabolic height profiles, causing a linear increase in velocity (red and black dashed lines). The velocities increase with an increase in nozzle exit velocity, although the velocities reached are smaller than this exit velocity, since the fuel slows down when it mixes with the ambient air. The velocities for the cases ignited in the middle are higher than when ignited at the nozzle. This is because the fuel has mixed more with the ambient air at this location and so the laminar flame speed is increased.

For the downwardly propagating flames (open data points), the velocities exhibit parabolic profiles (red dotted lines and blue lines), whereby the velocity first decreases and then increases again near to the nozzle. When ignited at the plate, there is a large surface area of the fuel for the flame to propagate and so the propagation is fast.

However, when the flame moves closer to the nozzle, the fuel stream becomes thinner and the opposing velocity become higher. This causes the propagation to slow down. However, for the 2.8 m s^{-1} flame ignited in the middle (Fig. 6.1b (i)), the flame edge exhibits a constant downwards velocity. Since the fuel velocity and Re are quite low for this case, the change in the axial profile of the fuel stream velocity when mixed with the ambient air is lower, due to the lower turbulence and lower mixing in the shear layer. This means that the fuel velocity profile has a lower effect on the flame propagation.

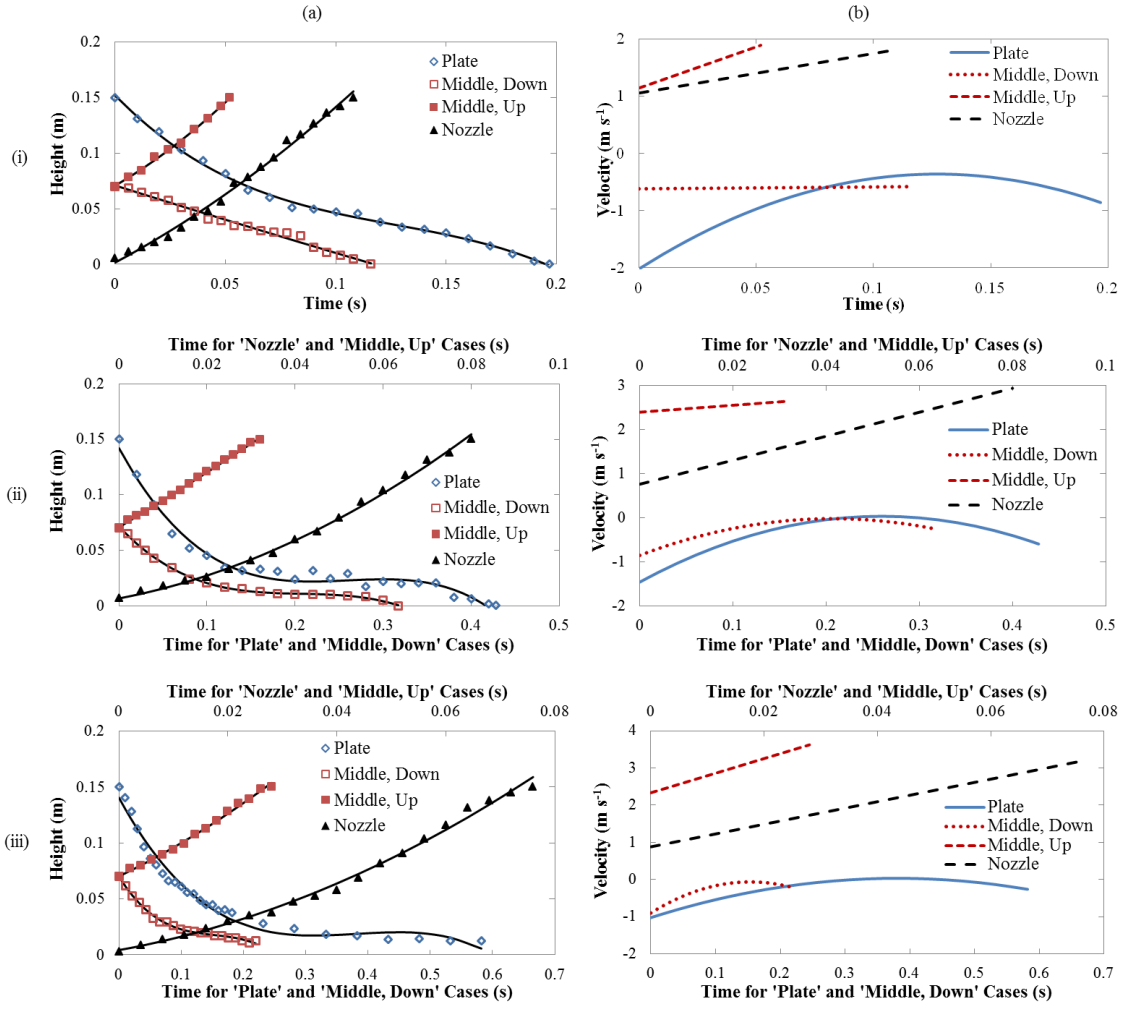

Figure 6.1: Plots of (a) Height and (b) Vertical velocity of the centre of the flame front for the axial ignition locations for methane flames at (i) 2.8, (ii) 5.5 and (iii) 8.3 m s^{-1}.

For the 5.5 m s^{-1} flame ignited at the plate (Fig. 6.1a (ii)), the flame boundary remains 20 mm above the nozzle for 0.1 s before suddenly accelerating again. The opposing flow becomes too strong for the downwards propagation, but after 0.1 s the unburned fuel has mixed with the hot products enough to allow downwards propagation. This is

also seen for the 'Middle, Down' case, where the flame remains 10 mm above the nozzle for 0.1 s before finally attaching. For the 8.3 m s^{-1} flame (Fig. 6.1a (iii)), the flame remains lifted at 12 mm above the nozzle as the nozzle exit velocity is too high for the opposing propagation. For the 2.8 m s^{-1} flame (Fig. 6.1a (i)), this effect is reduced due to the low opposing velocity.

The velocity profiles for the methane flames are quite consistent across the three cases, with the upwardly propagating flames having constant accelerations, and the downwardly propagating flames first slowing down due to the increased opposing flow, and then accelerating due to the mixing of the cool reactants and hot products. Hydrogen flames will now be looked at for the same values of thermal loading. As discussed in Section 6.2.2, one case with the similar Re and one with similar fuel velocity to the methane flames will be compared.

6.2.3.2. Hydrogen

Figures 6.2a and b show the height and velocity respectively for the three hydrogen flames ignited at the axial locations. The nozzle exit velocities for the hydrogen flames at the same thermal loadings are much faster than for the methane flames. This causes the upwards propagation velocities to be much higher. In addition, the laminar flame speed of the hydrogen plus nitrogen composition is much faster (5.2 times faster at stoichiometric conditions (Chapter 4)), which also causes faster propagation of the flame front. The propagation velocities for the hydrogen upwardly propagating flames are higher than the fuel exit velocities, unlike for the methane, due to the fast laminar flame speed and added effects of buoyancy when compared to the methane flames. Care should be taken to note the x-axis values.

However, in contrast to the methane flames, for the upwardly propagating hydrogen flames the flame front decelerates rather than accelerates. This is due to the more significant effect of the mixing with the ambient air. The higher fuel exit velocities and molecular diffusivity of the hydrogen flames cause the fuel to mix more with the ambient air in the shear layer. This causes the fuel to slow down, and so the overall propagation decelerates. In addition, when the fuel reaches the plate, the stagnation flow causes the vertical velocity to be zero, which prevents further upwards propagation, and slows the propagation down before the flame front reaches the plate. Flame stretch is

present in the stagnation region of impinging flames (as discussed in Chapter 2), which also reduces the flame speed and burning velocity, causing further deceleration of the flame front. The effect of flame stretch is more significant in the hydrogen flames due to the larger density difference between the burned and unburned gases. This in turn causes the velocity of the unburned fuel to slow down much more significantly than for the lower velocity methane flames. The decelerations are much more significant for the cases ignited at the nozzle than in the middle, due to the higher velocities in the further upstream locations. Similar trends are seen for the 'Middle, Down' cases at 19 and 28 m s^{-1} (Figs. 6.2b (ii) and (iii) respectively), where the flame front decelerates due to the increased velocity of the opposing flow.

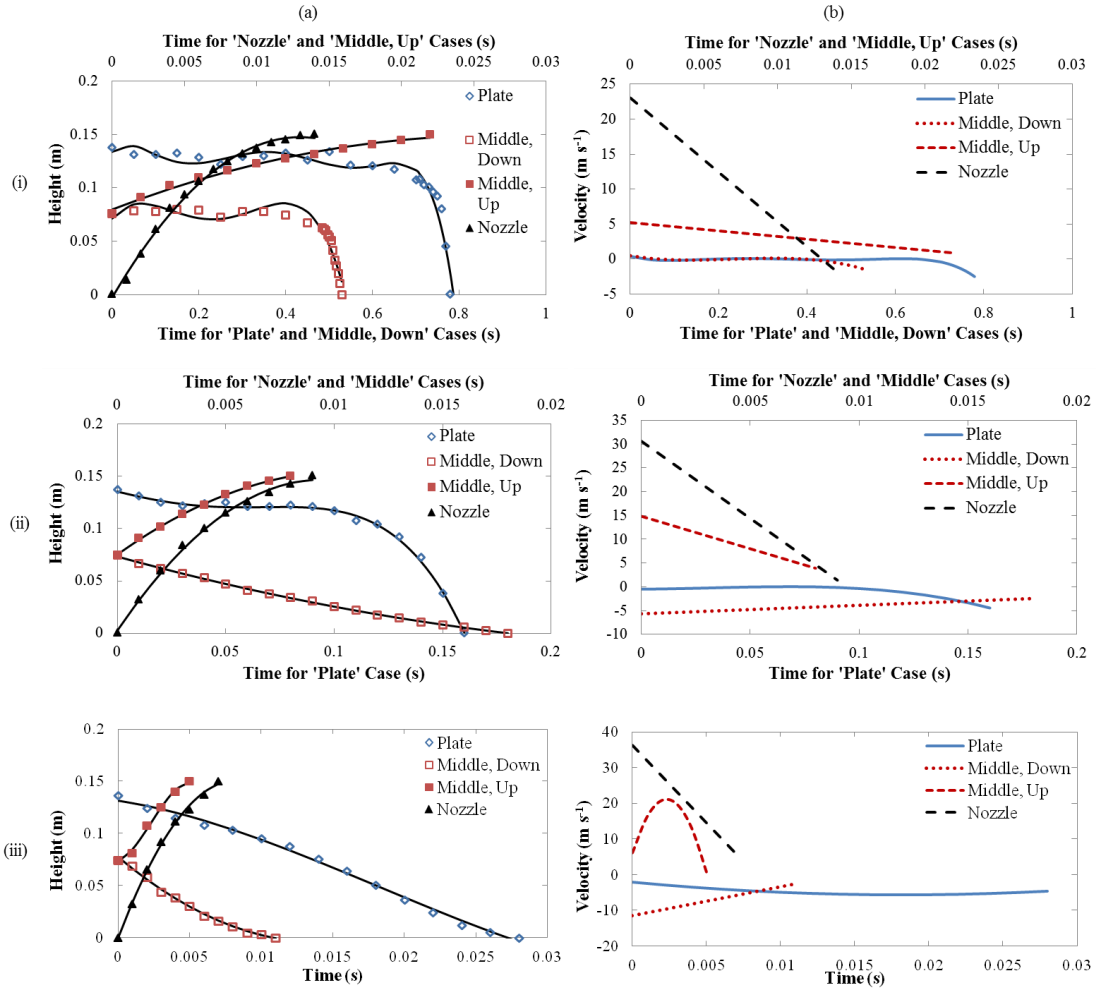

Figure 6.2: Plots of (a) Height and (b) Vertical velocity of the centre of the flame front for the axial ignition locations for hydrogen flames at (i) 10, (ii) 19 and (iii) 28 m s^{-1}.

For the 'Middle, Up' and 'Plate' cases at 28 m s^{-1} (Fig. 6.2b (iii)), the velocities exhibit parabolic profiles, starting off slow and then accelerating, before decelerating near the nozzle or plate respectively. The initial propagation is slow due to the increased mixing with the air causing more difficult ignition conditions. The deceleration is due to resistance from the burner or plate and from the increasing velocity of the opposing flow as the fuel stream becomes less wide, as discussed above. The 'Plate' velocity is smaller than those reached by the upward propagating cases due to the resistance from the opposing flow. Unfortunately the local flow velocity could not be calculated and so the flame front propagation velocities could not be normalised in this way.

However, there is an interesting trend for the downwards propagating flames ignited at the plate location for the 10 and 19 m s^{-1} cases. The flames exhibit a non-linear acceleration, first accelerating slightly then decelerating or maintaining an almost constant speed (with some oscillation) before accelerating suddenly towards the nozzle. This trend can be visualised in Fig. 3.9a (p115) (for the spark igniter). The first four images show that the flame does not propagate downwards but spreads across the plate. The fifth image shows the start of the downwards propagation, followed by a very suddenly acceleration towards the nozzle. This is represented on the graphs by an almost zero downwards velocity followed by a sudden downwards propagation.

This also happens for the 'Middle, Down' location for the 10 m s^{-1} flame. The sudden acceleration towards the nozzle for the 'Plate' cases can be explained by the flame spreading out across the plate before suddenly overcoming the upwards flow and propagating towards the nozzle. This is because the ignition is in a fuel rich part of the flame and so the initial flame spread is slow as it is difficult for the flame to propagate. As the flame spreads across the plate the flame boundary becomes hotter, and as the time increases the fuel mixes more with the air and the hot flame boundary, causing the flame to suddenly propagate downwards towards the nozzle. It can be seen from Fig. 6.2a (i) that for the 10 m s^{-1} flame, when ignited at the plate, there was a delay of about 0.74 s before the flame started to propagate quickly downwards. This was observed for the 19 m s^{-1} flame (Fig. 6.2a (ii)) with a much shorter delay of 0.11 s, but not for the 28 m s^{-1} case (Fig. 6.2a (iii)), which started to propagate downwards immediately, due to the enhanced mixing with the air caused by the higher Reynolds number of the fuel. This is also the case for the 'Middle, Down' cases at 19 and 28 m s^{-1}. The reduced delay

times indicate that the increased velocity aids the ignition of the fuel stream, due to the enhanced fuel/air mixing and higher turbulence of the fuel. This causes the unburned fuel to mix more quickly with the hot combustion products, giving faster propagation at the higher jet velocities. The increased velocity aids the combustion much more than overcoming the opposing flow hinders the propagation. Also, the increasing thermal loading allows the plate and also the product/reactant boundary to heat up more quickly, aiding the combustion near the plate and decreasing the delay times.

Both the upward and downwardly propagating flames behave differently for the hydrogen than for the methane flames at the same thermal loadings. This is due to the increased fuel exit velocity, diffusivity and laminar flame speed of the hydrogen flames. The effect of fuel exit velocity can be further examined by comparing the 8.3 m s^{-1} methane flame and the 10 m s^{-1} hydrogen flame (Figs. 6.1 (iii) and 6.2(i) respectively). It can be seen that the velocities for the upwardly propagating hydrogen flames are still significantly higher than for the methane flames at the similar velocity. In addition, the propagation accelerates for the methane flame while it decelerates for the hydrogen flame, due to the larger effect of the mixing with the ambient air caused by the higher diffusivity of hydrogen. For the downwardly propagating flames, the hydrogen flame has a delay at the plate before propagating downwards, whereas the methane flame propagates immediately and then remains above the nozzle, unable to overcome the opposing flow. It seems that for both fuels, when propagating downwards there is a certain inability to overcome the opposing flow which, as the heat is transferred to the reactants, can be overcome with a sudden acceleration towards the nozzle. This occurs at further downstream locations for the hydrogen flames. However, for the hydrogen flames, as the fuel velocity is increased, the ability to overcome the opposing flow is also increased, due to the increased thermal loading. For the methane flames, as the velocity is increased, it becomes more difficult to propagate against the opposing flow.

In addition to comparing by thermal loading and velocity, the 19 m s^{-1} hydrogen flames and the 2.8 m s^{-1} methane flames have similar Reynolds numbers (Figs. 6.2 (ii) and 6.1 (i) respectively). Again it can be seen that the upwardly propagating hydrogen flame has a much larger velocity than the methane flame at a similar Re. In addition, the downwardly propagating flames again show very different trends for the different fuels. Therefore, since the hydrogen and methane have such different properties, the

propagation characteristics of the flames ignited at various axial locations are very different even at similar Re, *v* and thermal loading.

6.2.3.3. Axial Location Conclusions

Hydrogen and methane diffusion flames have been compared at three values of thermal loading for axial ignition locations at the nozzle, plate and between the two. It has been shown that the propagation of hydrogen after ignition is very different to that of methane. This is due to the increased diffusivity, laminar flame speed and buoyancy of hydrogen when compared to methane. It has been found that:

- For the upwardly propagating methane flames, there is a linear acceleration. However, for the hydrogen flames, a deceleration of the flame front was observed. This is because the increased nozzle exit velocity and molecular diffusivity of the hydrogen causes more mixing with the ambient air. This in turn causes the axial velocity of the fuel stream to reduce. In addition, at the stagnation point, the vertical velocity becomes zero, and with the addition of flame stretch, which is more significant in the hydrogen flames, the overall propagation speed is reduced.
- The upwardly propagating hydrogen flames have much faster velocities than the methane flames due to the faster nozzle exit velocity and laminar flame speed, and buoyancy effects.
- For the downwardly propagating methane flames, parabolic velocities were observed, whereby the flame initially decelerates due to the increasing opposing fuel velocity. This was followed by an acceleration of the flame front, when the opposing flow velocity was overcome. This effect was minimalised for the lower velocity methane flame, due to the reduced opposing flow velocity. The parabolic velocity profiles were also observed in the higher velocity hydrogen flame for the ‘Plate’ and ‘Middle, Up’ locations.
- In addition, a non-linear acceleration of the flame front was observed for some downwardly propagating hydrogen flames. This was caused by an initial inability to overcome the opposing flow followed by a sudden acceleration towards the nozzle. This delay in initial propagation was shorter for higher

nozzle exit velocities since the increased velocity and thermal loading aid the combustion.

- The inability to overcome the opposing flow (shown by the delay in the hydrogen flames and by the deceleration in the methane flames) was reduced with increasing velocities for the hydrogen but increased for the methane flames, with the higher velocity methane flame remaining lifted from the nozzle. In addition, the inability to overcome the flow occurred at downstream location at the start of the ignition process for the hydrogen flames, but was a gradual deceleration near the nozzle for the methane flames.

The axial locations have been compared for hydrogen and methane diffusion flames. The next section will look into the effect of igniting at various radial positions along the plate for the same compositions.

6.2.4. Radial Ignition Locations

For the radial ignition locations, the flame was ignited in the plate centre (the same cases as in Section 6.2.3, repeated here for clarity), and at 50 mm and 100 mm away from the plate centre, in line with the schlieren view. The vertical propagation from the point of the flame reaching the plate centre to the nozzle attachment was recorded for each case. In addition, the horizontal propagation of the product/ambient boundary along the plate was analysed.

6.2.4.1. Methane

Figures 6.3a and b show the height and vertical velocity respectively for the methane flames at the three values of thermal loading (i to iii respectively). It can be seen that, for the vertical propagation, as the igniter is moved further from the plate centre, the initiation of the downwards propagation is delayed, as expected, due to the increased time taken for the flame front to reach the stagnation region. Similar trends for the downwards propagation are seen for the cases ignited at the three radial positions for the 2.8 m s^{-1} flame (Fig. 6.3 (i)), whereby the flame initially decelerates and then accelerates again towards the nozzle. However, for the 100 mm case (yellow line), the deceleration and final acceleration are reduced. For the 5.5 m s^{-1} flame (Fig. 6.3b (ii)), the final acceleration is not present, and the flames have constant decelerations for the 50 and 100 mm cases. This could be because, when the flame is ignited further from the

centre of the plate, the heat produced from the products is enough to overcome the opposing flow by the time the flame reaches the region of high opposing velocity, and the flame can reach the nozzle before the final acceleration occurs. However, for the higher velocity flame (Fig. 6.3b (iii)), the opposing flow becomes more significant and the flame decelerates and then accelerates near to the nozzle, where it remains lifted, as for the case ignited at the plate centre.

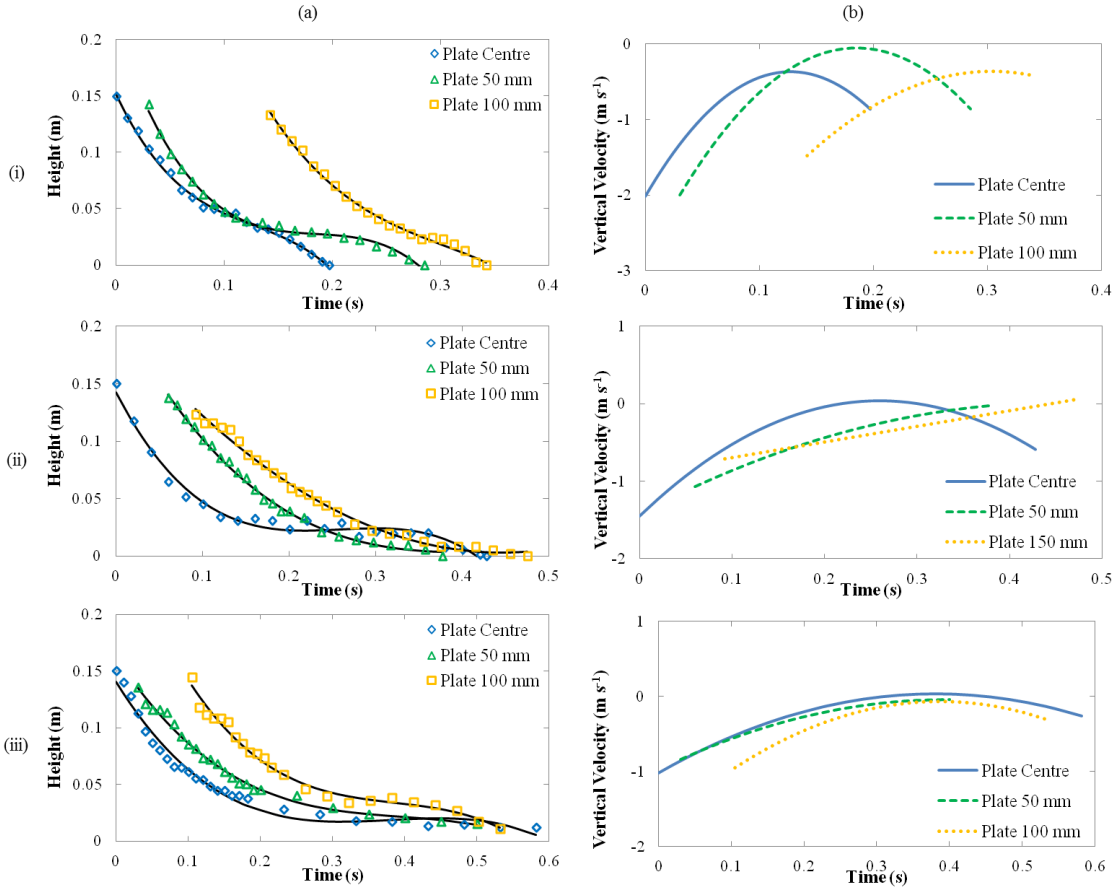

Figure 6.3: Plots of (a) Height and (b) Vertical velocity of the centre of the flame front for the radial ignition locations for methane flames at (i) 2.8, (ii) 5.5 and (iii) 8.3 m s^{-1}.

Figures 6.4a and b show the radial distances and velocities respectively for the three methane cases. The coordinate system is defined by r = 0 at the stagnation region, with positive r in the direction towards the igniter. Therefore, the 'Plate Centre Right' cases in Fig. 6.4a are flowing towards the position of the igniter for the other cases. These cases have been included in the plots for completeness. For the other cases, where the points are above the line at r = 0, the flame front is propagating against the flow, and below the line, with the flow. For the velocity curves, a negative velocity indicates that

the flame is propagating away from the igniter, across the stagnation region to the opposite plate edge.

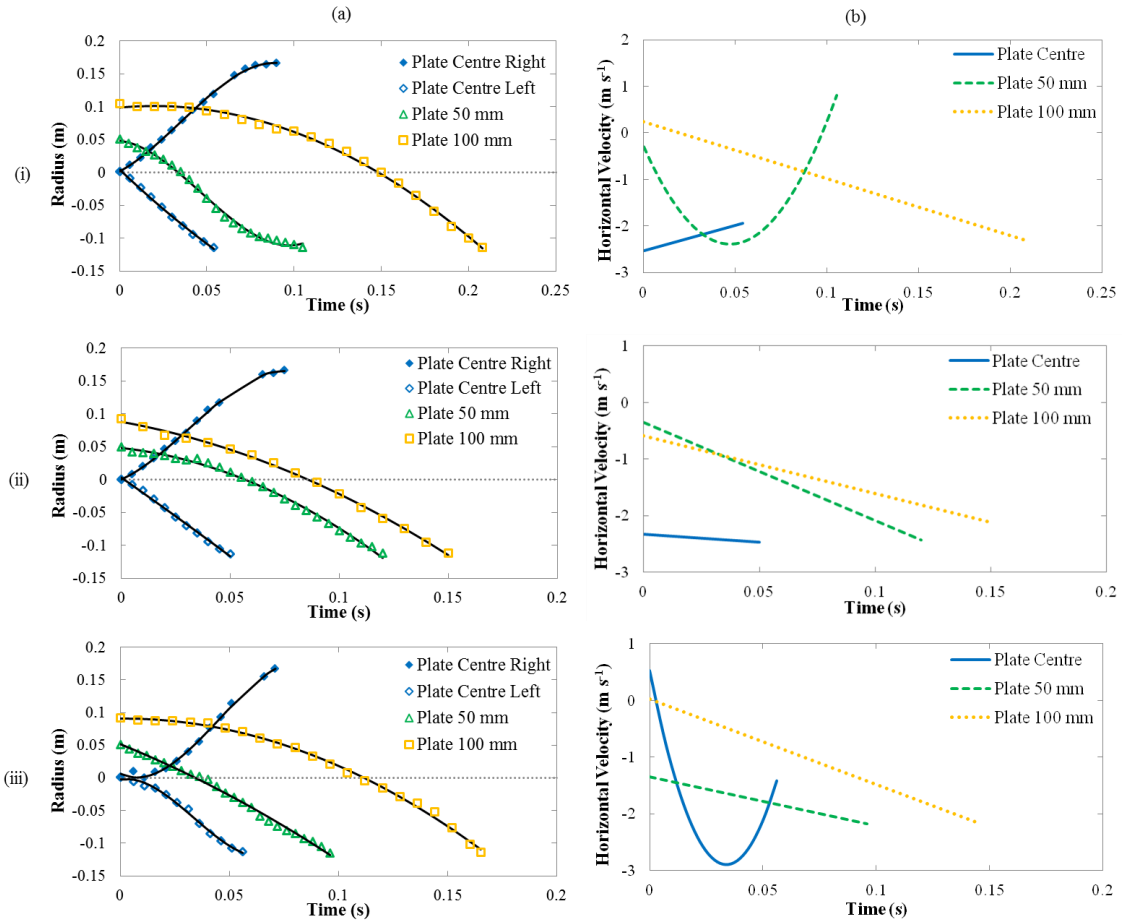

Figure 6.4: Plots of (a) Radius and (b) Horizontal velocity of the flame front for the radial ignition locations for methane flames at (i) 2.8, (ii) 5.5 and (iii) 8.3 m s^{-1}.

It can be seen for the 'Plate Centre Right' and 'Plate Centre Left' cases (blue data points in Fig. 6.4a) that the propagation is relatively symmetrical. The 'Plate Centre Right' cases have a larger distance plotted due to the setup of the schlieren images. It can be seen that the product/ambient boundary propagates past the edge of the plate before the horizontal propagation slows down due to the buoyancy and convection causing the rising of the hot gases around the edges of the plate.

For most of the cases in Fig. 6.4b, the velocity increases at a constant rate as the flame propagates from the point of ignition against the flow and past the stagnation region with the flow. However, for the 2.8 m s^{-1} flame at 50 mm and the 8.3 m s^{-1} flame ignited at the plate centre (Figs. 6.4b (i and iii respectively)), the flame edge then decelerates as

it approaches the plate edge. This could be due to the flow velocity also decreasing. However, this would need further investigation and is reserved for the scope for future work. The propagation of the hydrogen flames ignited at the radial positions will now be discussed.

6.2.4.2. Hydrogen

Figures 6.5a and b show the height and vertical velocity respectively for the hydrogen flames at the three values of thermal loading (i to iii respectively). It can be seen that, unlike for the methane flames, igniting further from the centre for the 10 m s^{-1} flame (Fig. 6.5a (i)) causes the downwards propagation to initiate sooner. This is also the case for the 19 m s^{-1} flame ignited at 50 mm from the centre (Fig. 6.5a (ii)). However, for the other cases (Fig. 6.5 (iii) and Fig. 6.5 (ii) – 100mm), igniting further from the centre causes the delay in downwards propagation to be longer, due to the further distance that the flame has to travel before reaching the fuel stream to propagate downwards. For the 28 m s^{-1} case, this is expected, since there is no delay in the downwards propagation of the flame ignited at the centre. However, for the 10 and 19 m s^{-1} cases, the delays that were observed in the 'Plate Centre' cases did not occur when ignited away from the centre. This is due to two reasons. Firstly, when ignited away from the centre, the plate has time to heat up before the initiation of the downwards propagation, which aids the propagation. Secondly, the heat produced from the horizontally propagating flame causes the cool reactants to heat up more quickly and so the flame can propagate against the fuel stream straight away. Therefore, the delay in downwards propagation can be reduced by igniting further away from the stagnation region. However, for the higher fuel velocity (Fig. 6.5 (iii)), where there was no delay when ignited at the plate, igniting further from the centre caused the total propagation time to be longer, and igniting at 100 mm for the 19 m s^{-1} flame was too far to overcome the extra distance and reduce the delay.

When igniting at 50 and 100 mm from the stagnation point, the downwards propagation velocities increased significantly when compared to the ignition at the centre, regardless of the delay times. This is in contrast to the methane flames, and could be due to the higher diffusivity of the hydrogen flames, causing faster mixing between the hot

products and cool reactants. This diffusion causes faster propagation when ignited further from the plate centre as more heat will be transferred to the reactants.

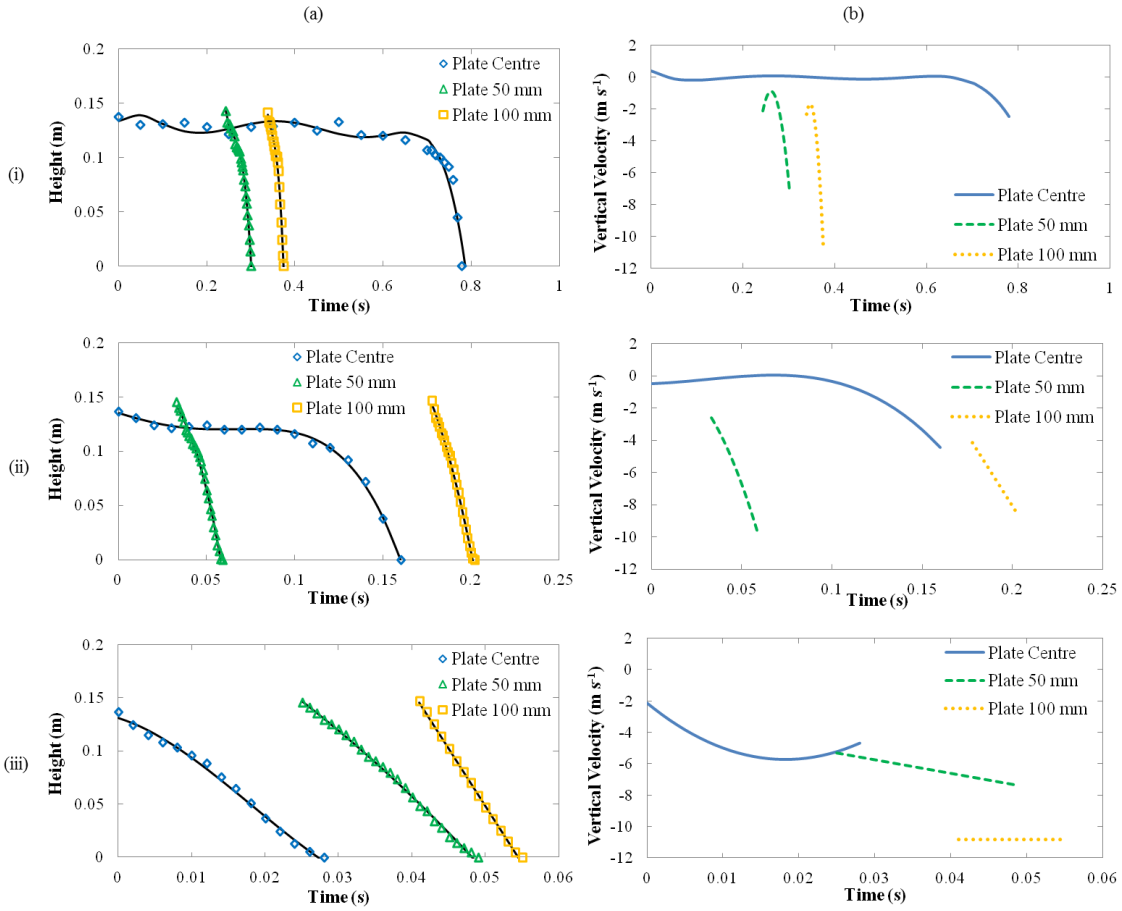

Figure 6.5: Plots of (a) Height and (b) Vertical velocity of the centre of the flame front for the radial ignition locations for hydrogen flames at (i) 10, (ii) 19 and (iii) 28 m s^{-1}.

Figures 6.6a and b show the radial distance and velocities for the hydrogen cases. The trends are quite different than for the methane cases. The flames ignited at 100 mm from the stagnation point exhibit similar profiles for all three fuel velocities; initially decelerating (or maintaining an almost zero velocity) before accelerating across the stagnation region. This is similar to the downwards propagation when ignited at the plate centre, where there was initially an inability to overcome the opposing flow before a sudden acceleration against the fuel stream. For the cases ignited at 50 mm, there is initially a positive velocity, whereby the flame moves away from the ignition source towards the plate edge, again before overcoming the opposing flow. For the 10 and 19 m s^{-1} flames ignited at 50 mm, the flame front then decelerates before reaching the opposite edge of the plate, as for some of the methane cases (Section 6.2.4.1). For the

flames ignited at the plate centre, the propagation decreases, due to the decrease of the flow velocity. Again, the analysis of the local flow velocity would be useful for further examination of this, and is reserved for the scope for future work. The initial inability to overcome the opposing flow at the plate edge has been seen for many of the hydrogen cases but not for the methane cases. Therefore, it will be studied in more detail in Section 6.4, with the addition of air and CO_2 to the flow.

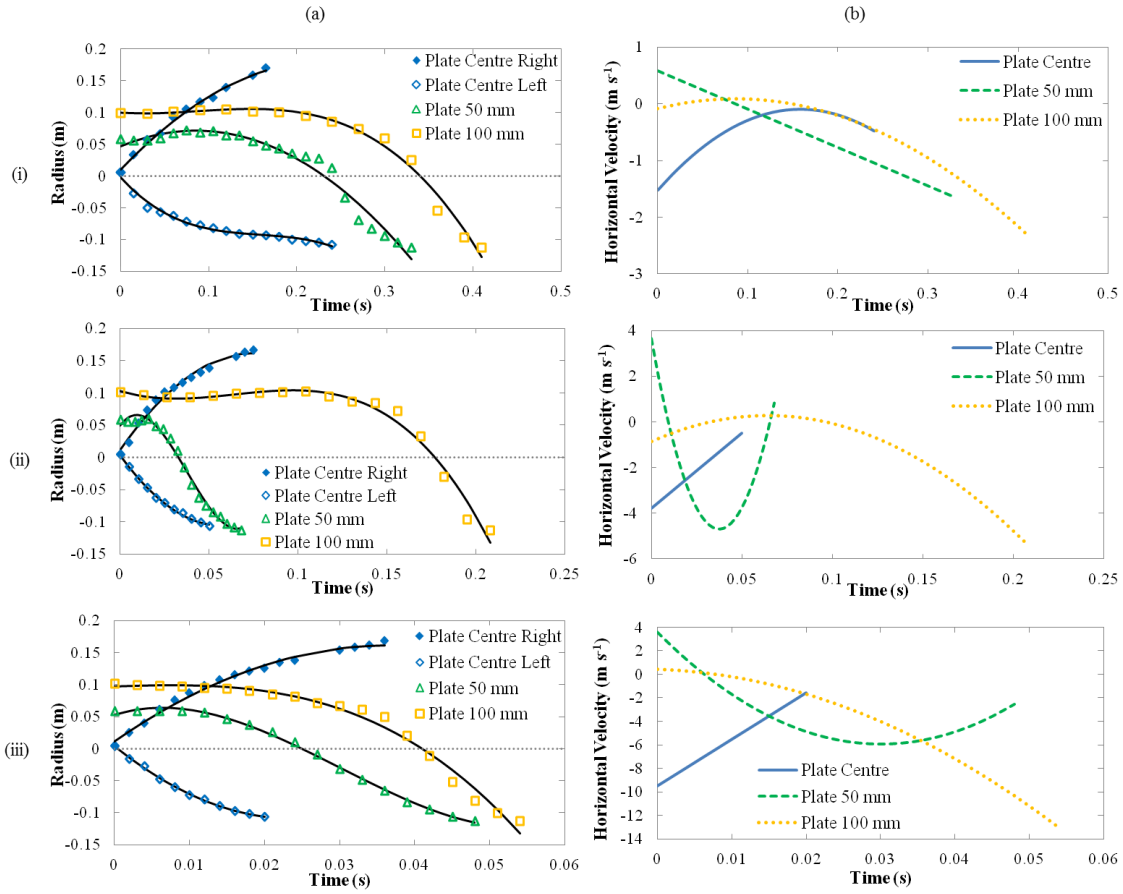

Figure 6.6: Plots of (a) Radius and (b) Horizontal velocity of the flame front for the radial ignition locations for hydrogen flames at (i) 10, (ii) 19 and (iii) 28 m s^{-1}.

6.2.4.3. Radial Location Conclusions

The vertical and horizontal propagation of the flame front when ignited at radial positions along the plate have been discussed. It has been found that:

- For methane, when the igniter was moved further away from the stagnation point, the initial downwards propagation occurred later, due to the time taken for the flame to reach the stagnation region. However, for the hydrogen flames,

moving the igniter away caused the downwards propagation to happen sooner for the lower velocity cases. This is because the initial inability to overcome the upwards flow was reduced due to the added heat from the plate and the hot gas/reactant boundary, and the lower initial opposing flow velocity at further radial distances.

- For the higher velocity hydrogen flames, where there was no delay when ignited at the plate centre, igniting further away caused a longer time before the initiation of the downwards propagation, as for the methane flames.
- For the methane flames at 5.5 m s^{-1}, ignited away from the stagnation point, no final acceleration was observed due to the extra heat produced being sufficient to immediately overcome the opposing higher velocity flow near the nozzle. For the 8.3 m s^{-1} flame, the opposing flow became more significant and caused the flame to decelerate significantly so that a final acceleration was observed when enough heat had been released into the reactants near the nozzle.
- For the methane flames, the radial velocity along the plate exhibited a constant acceleration. However, for the hydrogen flames, a non-linear velocity was observed, again due to the initial inability to overcome the opposing flow.

It has been shown that igniting the fuel away from the stagnation region can have significant effects on the downwards propagation of the flame, particularly for the hydrogen flames. Initial inability to overcome the opposing flow was also observed for the hydrogen radial velocities, although the delay in the downwards propagation was reduced when compared to igniting in the plate centre.

6.2.5. Hydrogen and Methane Comparison Conclusions

Hydrogen and methane diffusion flames have been compared in terms of the propagation of the flame front immediately after ignition in an impinging flame configuration. It has been shown that the hydrogen and methane flames behave very differently. This is mainly due to the differences in laminar flame speed, diffusivity and buoyancy. Changing the velocity has a more significant effect on the hydrogen flames due to the larger variations in nozzle exit velocity at the same thermal loadings, but also due to the increased mixing in the shear layer caused by the higher diffusivity and fuel velocity.

A common phenomenon noticed was the initial inability of the hydrogen flames to overcome the opposing flow. The propagation was aided by the increased thermal loading due to the higher plate temperature, and by igniting along the plate further from the stagnation region. For the methane flames, an inability to overcome the flow at the nozzle was observed. However, this effect was increased with increasing fuel velocity, unlike for the hydrogen flames.

This effect of the delay in initial propagation will be studied further in Section 6.4, along with the effects of air and CO_2 addition on the hydrogen flames. Since these flames are more similar to the pure hydrogen flames, the results should be more comparable than comparing methane and hydrogen. In addition, the effects of the nozzle-to-plate distance for hydrogen and methane flames will be studied separately in the next section.

6.3. Nozzle-to-Plate Distance comparisons

6.3.1. Introduction

Nozzle-to-plate distance comparisons on hydrogen and methane diffusion flames will be studied in this chapter. The aim is not to compare the two fuels as in Section 6.2, but to test the effect of different nozzle-to-plate heights. The analysis will be done separately for the two fuels.

6.3.2. Methane

6.3.2.1. Experimental Conditions

Comparisons of nozzle-to-plate distance were done for laminar methane diffusion flames at the heights and ignition locations shown in Table 6.2, ignited using the electrode igniter. The nozzle diameter was 4.6 mm, the Reynolds number, thermal loading and nozzle exit velocity were 512, 1.4 kW and 2.2 m s^{-1} respectively. The fuel was not ignited in the middle location for h/d = 10.8 due to the low nozzle-to-plate height. The low nozzle exit velocity ensured laminar, attached flames.

h/d	Ignition Location
10.8	Nozzle
10.8	Plate
21.7	Nozzle
21.7	Middle
21.7	Plate
32.6	Nozzle
32.6	Middle
32.6	Plate

Table 6.2: Experimental conditions for the nozzle-to-plate height comparisons for methane diffusion flames.

6.3.2.2. Results and Discussion

Figures 6.7a and b show the height and velocity for the methane flames in Table 6.2, ignited at the plate, middle and nozzle locations (i to iii respectively). The continuous and dashed lines in Fig. 6.7b are the velocities for the downwardly and upwardly propagating flames respectively. For the plate locations (Fig. 6.7 (i)), it can be seen that the flame front decelerates for all three cases. However, for the higher *h/d*, the velocity then increases again after it reaches a minimum at 0.1 s. This is similar to the trends observed for the higher velocity flames in Section 6.2, where the flame slows down due to the increasing opposing fuel velocity, and then speeds up again due to the increased heat from the flame. For these cases however, the fuel velocity is low enough that the flame can reach the nozzle before the velocity reaches this minimum value, except for the higher *h/d* case, which has a larger distance for propagation, and so experiences a larger effect from the flow field. The initial velocity of the flame front increases with increasing *h/d*, due to the reduced velocity of the opposing flame front at the further downstream locations.

For the flame ignited at the nozzle at *h/d* = 21.7 (Fig. 6.7 (iii), green data points), a constant velocity of 1.45 m s^{-1} was observed. This initial velocity is lower for both the higher and lower *h/d* cases. For the *h/d* = 32.6 case, the velocity increases as the flame propagates upwards. Again, this is similar to the higher velocity methane cases from Section 6.2; as the flame propagates, the hot combustion products mix with the cool reactants, causing the flame front to accelerate. For the lower *h/d*, the flame front

initially accelerates, but then decelerates due to the interaction between the flame and the plate, causing the flame front propagation to slow down as the flame approaches the plate. The larger change in velocity at the stagnation region due to the lower *h/d* also causes more flame stretch, decreasing the laminar flame speed and further reducing the propagation velocity.

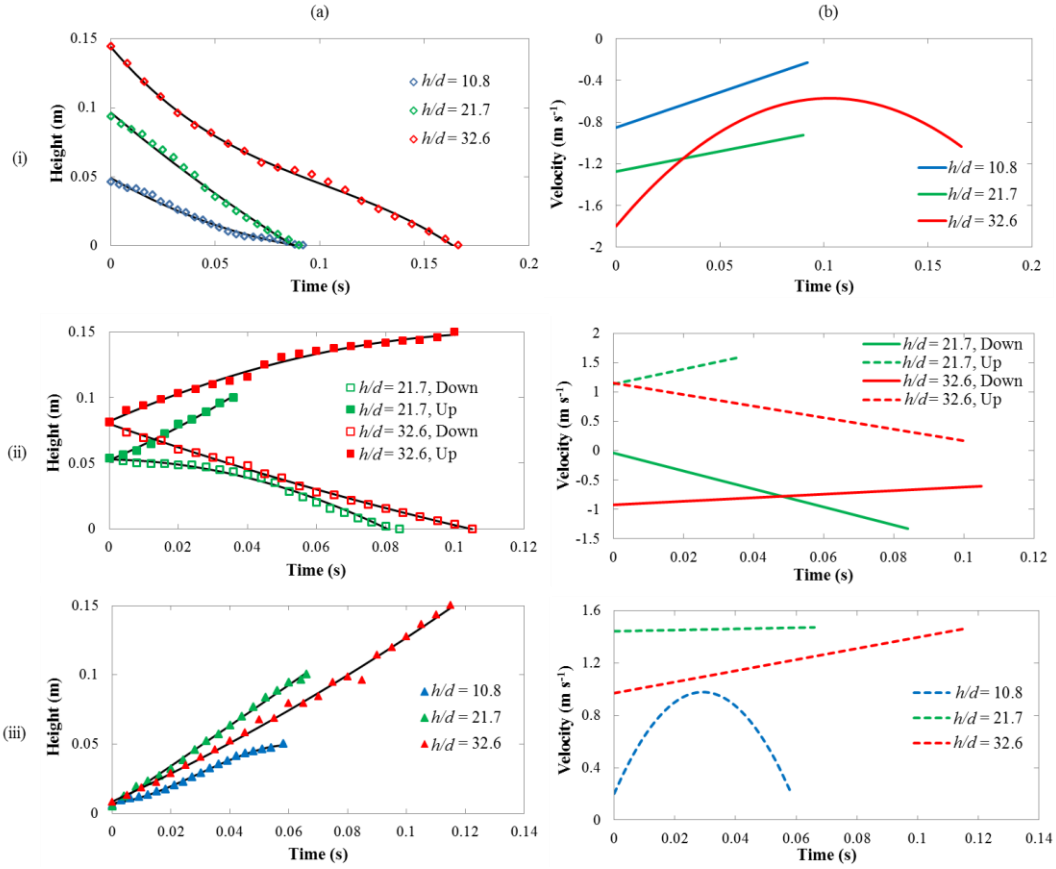

Figure 6.7: Plots of (a) Height and (b) Velocity of the flame front for methane flames ignited at (i) The plate, (ii) The middle and (iii) The nozzle, for various *h/d*.

The flames ignited in the middle behave differently for the two *h/d* studied (Fig. 6.7 (ii)). For *h/d* = 21.7 (green lines), the upwardly and downwardly propagating flames both accelerate after ignition, whereas the *h/d* = 32.6 flames both decelerate (red lines). The *h/d* = 21.7 downwardly propagating flame accelerates due to a slight initial inability to propagate downwards. This was not seen in the higher *h/d* cases, even for the higher velocity flames in Section 6.2. However, the delay was not seen for the plate case ignited at the same height above the nozzle (Fig. 6.7 (i) blue data points). More ignition locations for more nozzle-to-plate heights should be studied to further examine this phenomenon. This is reserved for the scope for future work.

The deceleration for the *h/d* = 32.6 case is due to the slowing down of the fuel stream velocity for the further downstream locations. The significance of the effect of the slowing down due to the fuel stream velocity profile and the acceleration of the flame front seems to be sensitive to ignition location and plate location. Again, more cases should be studied to further examine this effect. In addition, PIV could be used in order to evaluate the effect of the local fuel stream velocity. Again, this is beyond the scope of the work in this thesis and is reserved for future work.

6.3.2.3. Conclusions

The nozzle-to-plate height has a significant effect on the flame front propagation for the laminar methane diffusion flames. For the downwardly propagating flames, the velocities are higher for larger *h/d* and for further downstream ignition locations due to the reduced velocity of the opposing flow for these locations. For the upwardly propagating flames, the local fuel velocity profile causes a deceleration of the flame front. More cases should be studied in order to test the significance of the opposing effects for different *h/d*. The next section looks at the effect of nozzle-to-plate height on laminar hydrogen diffusion flames.

6.3.3. Hydrogen

6.3.3.1. Experimental Conditions

Comparisons of nozzle-to-plate distance were also done for laminar hydrogen diffusion flames at the heights and ignition locations shown in Table 6.3. The nozzle diameter was 8.0 mm, the Reynolds number, thermal loading and nozzle exit velocity were 459, 3.4 kW and 6.5 m s^{-1} respectively. 3.34 x 10^{-5} m^3 s^{-1} of nitrogen was added to the hydrogen to keep the compositions the same as in the rest of this chapter. Again, the fuel was not ignited in the middle location for *h/d* = 9.5 due to the low nozzle-to-plate height. The Reynolds numbers and *h/d* values are similar to the methane cases studied in Section 6.3.2, however, the nozzle diameter is larger and the spark igniter was used rather than the electrode igniter. Therefore, these cases will not be compared with the methane cases.

h/d	Ignition Location
9.5	Nozzle
9.5	Plate
18.8	Nozzle
18.8	Middle
18.8	Plate
36.8	Nozzle
36.8	Middle
36.8	Plate

Table 6.3: Experimental conditions for the nozzle-to-plate height comparisons for hydrogen diffusion flames.

6.3.3.2. Results and Discussion

Figures 6.8a and b show the height and velocity for the hydrogen flames ignited at the plate, middle and nozzle (i to iii respectively). The propagation times for the *h/d* = 36.8 cases were much longer than the other cases for all ignition locations. Therefore, a separate x-axis was used for these flames (top axes point to the red lines and data points).

For the plate location at *h/d* = 36.8 (Fig. 6.8 (i)), there is a very long delay of 0.55 s before the flame has produced enough heat to propagate downwards. This is because at this location, the fuel has mixed so much with the surrounding air that the ignition is in a fuel lean part of the mixture. This makes the initial ignition more difficult. However, when enough heat has been produced, the flame can then propagate into the reactant mixture. For the *h/d* = 18.8 case, the flame propagation is much faster, although there is still some initial inability to overcome the flow, with the velocity decreasing to 4.5 m s^{-1} before the flame propagates downwards very quickly. For *h/d* = 9.5, the flame again takes a longer amount of time to propagate. This is because the flame is ignited in a further upstream location, where the opposing velocity is higher, and so the initial propagation is slower. In this case, the *h/d* = 18.8 allows faster propagation when ignited at the plate due to the lower opposing flow velocity when compared to *h/d* = 9.5, and to the better mixture concentration when compared to *h/d* = 36.8.

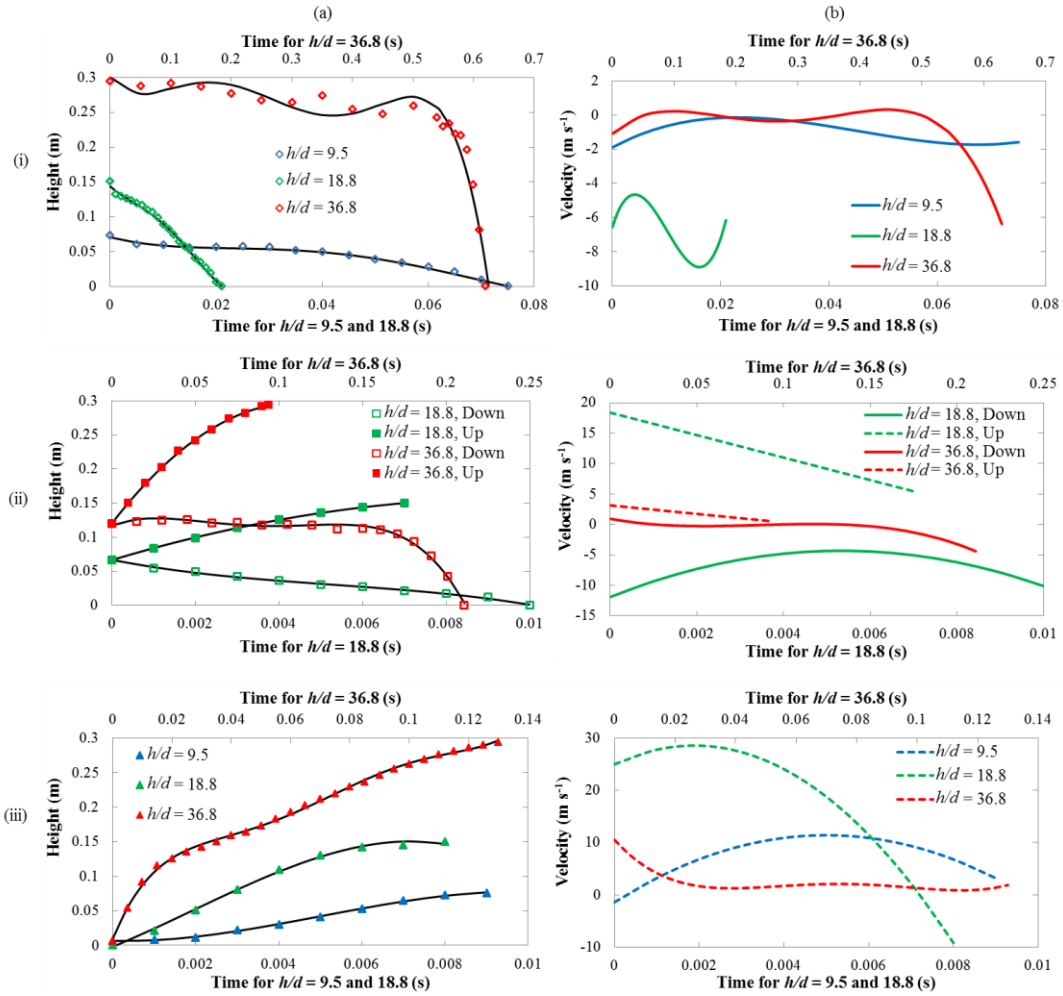

Figure 6.8: Plots of (a) Height and (b) Velocity of the flame front for hydrogen flames ignited at (i) The plate, (ii) The middle and (iii) The nozzle, for various *h/d*.

When ignited in the middle location (Fig. 6.8 (ii)), there is still a considerable delay of 0.16 s for the downwardly propagating flame at *h/d* = 36.8. This ignition location is at a similar height to the plate location for *h/d* = 18.8, which has a much faster propagation (Fig. 6.8 (i)). In contrast, the downwardly propagation flame ignited in the middle of the *h/d* = 18.8 location propagates much faster than the *h/d* = 9.5 flame ignited at the plate, which was ignited at a similar height. Again, PIV measurements of the local flow velocity would be useful in determining the reasons for this, which is reserved for future work. In addition, cases could also be studied for freely propagating flames to further determine the effect of the impingement plate.

For the upwardly propagating flames ignited in the middle (Fig. 6.8 (ii)), the propagation decelerates for both values of *h/d*. Again, this is due to the reduction in

local flow velocity further downstream. The initial velocity for the *h/d* = 18.8 case is much higher than for *h/d* = 36.8, due to the higher fuel velocity at the further upstream location. In addition, the deceleration is much larger for the lower *h/d*, due to the interaction between the flow and the plate, causing the flame to slow down more significantly.

For the *h/d* = 36.8 flame ignited at the nozzle, there is initially a very fast propagation of 10 m s^{-1}, which then reduces to around 1.5 m s^{-1} where it remains at that constant velocity until it reaches the plate. For the lower nozzle-to-plate heights, the velocity first increases, and then decreases near to the plate. The reduction in velocity for all cases is due to the reduction in fuel velocity as the flame moves downstream (which is more significant for the higher *h/d*), and to the interaction with the plate (which is more significant for the lower *h/d*). Similar to the plate and middle locations, the *h/d* = 36.8 flame ignited at the nozzle took a much longer time to propagate, due to the reduced velocity of the fuel near to the plate and to the larger propagation distance.

6.3.3.3. Conclusions

The propagation of the flame front for the laminar hydrogen flames behave differently for different *h/d*. For *h/d* = 36.8, there is a more significant difference due to the very large *h/d* causing a much slower fuel velocity near the plate, increasing the upwards propagation times, and also causing less favourable ignition conditions near the plate, creating a long delay between ignition and downward propagation.

Flames ignited at similar heights but with different plate placements behave very differently. PIV measurements of local flow velocity and measurements of ignition without an impingement plate would help to explain this. This is reserved for future work.

6.3.4. Nozzle-to-Plate Distance Conclusions

For both the hydrogen and methane laminar diffusion flames ignited at various locations for various *h/d*, certain phenomena were noticed. Firstly, when the flames were ignited in the middle location, and again at the same height above the nozzle but at the plate location, the propagation was very different. Therefore, the effect of the impingement

plate on the flame propagation should be studied further by testing more nozzle-to-plate distances and also by testing with no impingement plate.

The flame may either accelerate or decelerate depending on various parameters. On the one hand, the fuel stream slowing down further downstream causes a deceleration of the flame front for upwardly or downwardly propagating flames. On the other hand, as the hot combustion products mix with the cool reactants, the flame front accelerates. The balance between these two effects could be further studied by using PIV to evaluate the local flow velocity. This is reserved for the scope for future work. The next section will look into the effect of air and CO_2 addition on the propagation of hydrogen flames ignited at a constant nozzle-to-plate height.

6.4. Hydrogen with Air/Carbon Dioxide Addition

6.4.1. Introduction

This section looks at the effect of air and CO_2 addition on the propagation of hydrogen flames. The H_2/air and H_2/CO_2 ratio will be kept the same for each composition and the results will be studied for three values of thermal loading. Air and CO_2 addition affect the reactivity of hydrogen as well as the stretch effects, due to the change in laminar flame speed (Chapter 4) and the density ratio between the burned and unburned gases respectively. In addition, as the thermal loading is changed so is the Reynolds number, and so the effects of changing these parameters will also be explored. Two nozzle diameters will be used in order to compare the effects of Reynolds number on the flame propagation.

6.4.2. Experimental Conditions

The experimental conditions are shown in Table 6.4. The spark igniter was used for these results. A constant nozzle-to-plate distance of h = 150 mm was used for all results. This is because (as it will be shown) the results for the nozzle-to-plate height of 150 mm for the small nozzle results in this section (h/d = 32.6) are more similar to the results for the 150 mm nozzle-to-plate height (h/d = 18.75), than for the 294 mm (similar h/d) results of the larger nozzle at the same flow conditions in Section 6.3.3. Again, 1.67 x 10^{-5} m^3 s^{-1} of nitrogen was added for the 4.6 mm nozzle cases and 3.34 x 10^{-5} m^3 s^{-1} for the 8 mm cases so that the compositions were the same for both nozzle sizes. The flow

conditions for the hydrogen flames for the small nozzle are the same as in Section 6.2.3.2, but using the spark igniter instead of the electrode igniter, and will be compared to test the relative effect of the two igniters.

Nozzle Diameter (mm)	*h/d*	Fuel	Loading (kW)	Velocity (m s^{-1})	Re
4.6	**32.6**	H_2	1.8	10.0	403
			3.5	19.0	603
			5.3	28.0	828
		H_2 + air	1.8	12.0	904
			3.5	23.0	1559
			5.3	34.0	2218
		H_2 + CO_2	1.8	12.0	2076
			3.5	23.0	4232
			5.3	34.0	6471
8.0	**18.8**	H_2	3.4	6.5	459
			6.9	12.3	683
			10.3	18.1	934
		H_2 + air	3.4	7.8	1021
			6.9	14.9	1756
			10.3	22.0	2495
		H_2 + CO_2	3.4	7.8	2329
			6.9	14.9	4742
			10.3	22.0	7251

Table 6.4: Experimental conditions for hydrogen with air or CO_2 addition.

The effects of changes in axial position of the igniter were studied for three heights, named ‘Nozzle’, ‘Middle’ and ‘Plate’. These were ignited at the centre of the gas stream for all gases. The H_2/air and the H_2/CO_2 volume ratios were kept at 4.5 for all cases, giving volume percentages of air or CO_2 of 18 %. The Reynolds numbers range from laminar to the turbulent transitional regime (1000 < Re < 3000) to fully turbulent flames. Three thermal loadings were studied for the small nozzle and these were kept at 1.8, 3.5 and 5.3 kW for each composition. This allows for comparison between the compositions based on thermal loading. In addition, the large nozzle burner was used so that comparisons could be made at the same Reynolds number as the small nozzle (within a 13 % margin). In addition, for the hydrogen flames, the 3.5 kW flame for the

4.6 mm nozzle will be compared to the 3.4 kW flame for the 8 mm nozzle, to test the relative effects of Re and loading, and the 19 m s^{-1} flame for the small nozzle will be compared to the 18.1 m s^{-1} flames for the large nozzle to test the relative effects of the nozzle exit velocity for the different nozzle diameters.

6.4.3. Small Nozzle

6.4.3.1. Introduction

The following results were performed for the small nozzle (4.6 mm diameter). The effects of air and CO_2 addition to hydrogen flames on the flame front propagation will be analysed. The flame height with respect to time, and the velocities calculated from differentiating the best fit polynomials will be discussed. The effect of ignition location between the nozzle and plate will be explored for the three thermal loading values. In addition, the results will be compared to Section 6.2.3.2 for the electrode igniter

The flame could not be ignited with a spark at the 'Nozzle' location for the hydrogen premixed flames (Fig. 6.11) because the flames were too lean, and lighting with a pilot flame disturbed the schlieren image so that the flame front could not easily be seen. There was a small probability of failed ignition, and for these cases if the flame was not ignited within three tries, with approximately 1 s between each try, the fuel was turned off for safety reasons and the case was attempted again. This did not happen for the diffusion flames but happened occasionally for the premixed cases.

Also, the 3rd to 6th order polynomials did not fit the curves well for some of the downward propagating cases (the 'Plate' cases in Fig. 6.11 (i) and Fig. 6.12 (i) and the 'Middle, Down' case in Fig. 6.9 (iii)) and so it was seen fitting to use two separate polynomials for these cases. The x-axes for each polynomial overlap one another so that the transition is as smooth as possible. This is justified as the processes occurring in this ignition sequence are the initial spreading of the flame across the plate, followed by the sudden acceleration towards the nozzle, and the disjointed part of the curves occur at this change in process.

It should be pointed out that the ignition processes at the various locations have very different time scales, and so two separate x-axes scales were used in all of the graphs. The top axes point to the upwards propagating cases in all instances (Figs. 6.9, 6.11 and

6.12) and also the 'Middle, Down' cases for Figs. 6.9 (i) and (ii) and 6.11 (iii), and the 'Plate' cases in Fig. 6.9 (iii). The bottom axes point to the 'Middle, Down' and 'Plate' cases for all other instances. This is because the upward propagation is much faster than the downward propagation due to the added momentum from the jet velocity and buoyancy effects, and due to the delays in the downwards propagation that will be discussed in the following sections.

6.4.3.2. Hydrogen

Firstly, the effect of the ignition location on the hydrogen diffusion flames shown in Table 6.4 will be discussed. The cases shown in Fig. 6.9 are for the hydrogen diffusion flames of the same velocities and concentrations from Fig. 6.2 but using the spark igniter instead of the electrode igniter. It can be seen that the two igniters produce different results for the hydrogen flame propagation. This is for a few reasons. Firstly, the spark igniter and electrode igniter use different mechanisms to produce the sparks. Therefore the power produced by the igniters was different. From the schlieren images it was observed that the electrode igniter produced a much smaller flame kernel than the spark igniter, which evolved more slowly into the propagating flame. Secondly, the spark igniter was held by hand, and so the positioning of it was less reliable than the electrode igniter. However, for the electrode igniter, the points of the electrodes were not fixed distances apart, which also caused some unreliability. In addition, the electrode igniter axial positions were slightly different to the spark igniter, with the plate and nozzle locations being slightly away from the plate or nozzle respectively for the electrode igniter.

The non-linear velocity of the flame towards the plate or nozzle can be seen by the curved velocity profiles in Fig. 6.9b. This was observed as an increase in velocity followed by a decrease before the flame reaches the plate or nozzle. However, for most cases, as for the electrode igniter, a constant decrease in velocity is observed. The 10 and 19 m s^{-1} flames ignited at the middle location and propagating downwards (Figs. 6.9 (i) and (ii) respectively) show similar trends to the upwardly propagating flames, initially accelerating against the fuel stream and slowing down before reaching the nozzle. The time taken for propagation to the plate when ignited at the nozzle decreases with increasing velocity (with times of 0.019, 0.011 and 0.009 s for the 10, 19 and 28 m

s^{-1} flames (Figs. 6.9a (i) to (iii) respectively)), actually being slightly slower than the cases ignited by the electrode igniter (with times of 0.014, 0.009 and 0.007 s respectively). This could be due to the higher position of the electrode igniter.

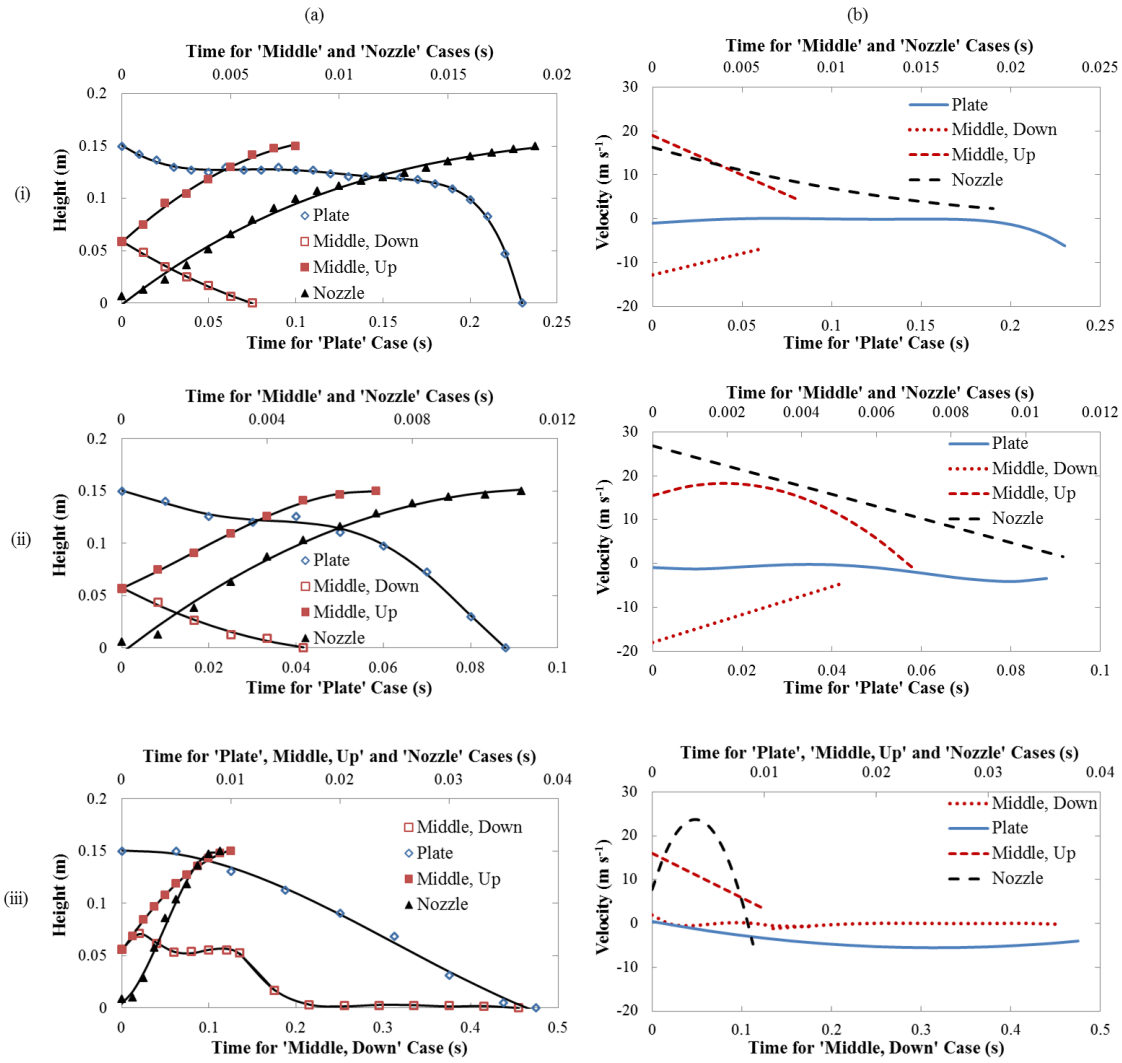

Figure 6.9: Plots of (a) Height and (b) Velocity of the centre of the flame front for hydrogen flames at (i) 10 m s^{-1}, (ii) 19 m s^{-1} and (iii) 28 m s^{-1}.

For the 'Plate' cases, the delays in initial propagation are again observed, with a decrease in delay time with increasing fuel velocity (Figs. 6.9a (i to iii respectively)). However, the delay times are different to the electrode igniter case. It can be seen from Fig. 6.9a (i) that for the 10 m s^{-1} flame, when ignited at the plate, there was a delay of about 0.18 s, and for the 19 m s^{-1} flame (Fig. 6.9a (ii)) a much shorter delay of 0.05 s, and no delay for the 28 m s^{-1} case (Fig. 6.9a (iii)). Compared to the much longer delays for the electrode igniter of 0.74 and 0.11 s for the 10 and 19 m s^{-1} flames respectively, it

seems that using the spark igniter causes the flame to propagate downwards more easily. This could be due to the larger flame kernel produced by the spark igniter. However, the change in trend with increasing fuel velocity are comparable for the two igniters; the increased fuel velocity aids the combustion much more than overcoming the opposing flow hinders the downwards propagation when the flame is ignited at the plate.

Contrary to the electrode igniter, when the flame was ignited in the middle location, there were no delays in the downwards propagation for the 10 and 19 m s^{-1} flames but a delay of approximately 0.13 s for the 28 m s^{-1} case, again causing non-linear acceleration of the flame. However, the electrode cases were ignited a little higher up than the spark igniter cases (as the spark cases were judged by hand), and so the ignition took place further downstream. It has been shown that a delay is more likely to occur at lower velocities when ignited at the plate. In addition, as shown in Section 6.2.3 for the electrode igniter cases, when ignited in the middle, a delay was observed for the lower velocity case but not for the higher two velocities, whereas delays were observed at the plate locations. Therefore, as the igniter is moved upstream, a delay becomes less likely. This could be the reason for the lack of delay in the spark ignited cases where there were delays in the electrode ignited case which were ignited slightly downstream.

For the higher velocity case ignited in the middle using the spark igniter, a delay was observed, but there was no delay for the 'Plate' case. This could be due to the difference in spreading rate with fuel exit velocity, defined as the angle that the unburned fuel makes as it exits the nozzle. It can be seen from Fig. 6.10 that for the hydrogen diffusion cases (orange lines) the spreading rate remains quite constant for the velocities of 10 and 19 m s^{-1} and then increases for 28 m s^{-1}. This helps to explain why the behaviour changes for the 28 m s^{-1} case ignited at the plate. The fuel will have mixed with more air by the time it has started to impinge on the plate, so that igniting at the plate (or in a further downstream location) will allow faster combustion due to the increased fuel-air mixing, reduced fuel velocity and higher flame surface area that this will cause. The mixing also causes more flame wrinkling which also increases the surface area of the flame and allows for easier combustion. However, when ignited at the further upstream middle location (spark igniter), the fuel has not mixed enough with the surrounding air, compared to the mixing at the plate or at the downstream 'Middle'

location (electrode igniter), and has a lower surface area. In addition, the local fuel velocity is higher further upstream. Therefore, the velocity of the fuel becomes a more important parameter than the spreading rate, with the nozzle exit velocity of the 28 m s^{-1} flame being too high to initiate an immediate downwards propagation of the flame. More investigation should be carried out to test varying ignition locations between the nozzle and the plate to find which locations would cause a delay. This is reserved for the scope for future work.

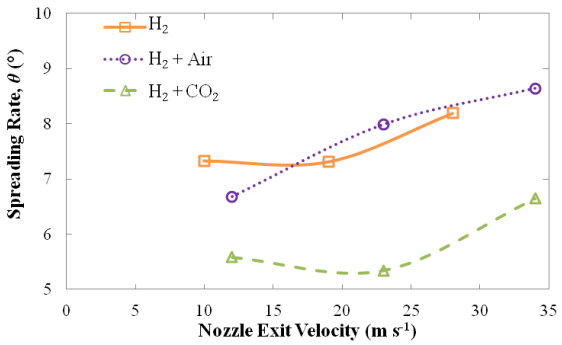

Figure 6.10: Spreading rates for the compositions shown in Table 6.4.

The results will be compared to the *h/d* comparisons in Section 6.3.3 with the large nozzle (Fig. 6.8). At similar thermal loadings (Figs. 6.9 (ii) and 6.8), the propagation times for the large nozzle ((Figs. 6.8 (i) and (ii))) are 4 times faster at *h/d* = 18.8 for the downwardly propagating flames (Fig. 6.9 (ii)), but 6 times slower/faster for the 'Plate' and 'Middle, Down' cases respectively at *h/d* = 36.8 (Figs. 6.8 (i) and (ii) respectively). For the upwardly propagating flames, the propagation times are less than 1.4 times faster for *h/d* = 18.8, but 14 and 11 times slower for the 'Middle, up' and 'Nozzle' cases respectively for *h/d* = 36.8 (Figs. 6.8 (ii) and (iii)). This means that at similar thermal loadings, the *h/d* = 18.8 results for the large nozzle are more similar to the small nozzle results at *h/d* = 32.6 (both have heights of 150 mm). At similar Re, the larger nozzle results are 11 and 7 times faster for the 'Plate' and 'Middle, Down' cases at *h/d* = 18.8, but 2.6 and 10 times slower/faster respectively for *h/d* = 36.8. For the upwardly propagating flames, the larger nozzle results are less than 2.4 times faster for *h/d* = 18.8, but 14 and 6.5 times slower for the middle up and nozzle cases respectively at *h/d* = 36.8. This means that at similar Re, the results are more similar for the upwardly propagating flames at the same height, but more similar for the downwardly propagating flames at the same *h/d*. However, the results are not wholly comparable due

to differences in nozzle size, flow profile and nozzle exit velocity, which will be discussed in Section 6.4.4. The results for the large nozzle in Section 6.4.4 will be compared at the same nozzle-to-plate height rather than at the same *h/d*, since overall the results are more similar.

6.4.3.3. Hydrogen and Air

Secondly, the analysis was done for hydrogen premixed flames (Fig. 6.11) with an H_2/air volume ratio of 4.5, which corresponds to an equivalence ratio of 10.5. The hydrogen velocity was kept the same as for the diffusion flames so that the thermal loadings could be kept the same (Table 6.4). As mentioned, there are no 'Nozzle' results for the premixed hydrogen cases as the flames could not be ignited with a spark at the nozzle location. Again, this agrees with the analysis in Section 6.4.3.2, which shows that at lower ignition locations the flame is more difficult to ignite due to the higher velocity and lower flame surface area. In this case the premixed air also hinders the ignition process. The disjointed polynomials affect the 12 m s^{-1} 'Plate' case here (Fig. 6.11 (i)). In addition, for the 34 m s^{-1} 'Plate' case (Fig. 6.11 (iii)), when the flame reached 4 mm up from the nozzle, it ceased propagating downwards and remained above the nozzle for 0.08 s before attaching to it. For this reason, the last 0.08 s was not included in the velocity curve approximation as the sudden deceleration caused problems with the curve fitting. The deceleration was due to the high opposing velocity at the nozzle location.

The premixed flames exhibit the linear decrease in velocity for the 'Middle, Up' ignition locations (Figs. 6.11 (i) to (iii)) and a parabolic velocity profile for the 'Middle, Down' location for the 34 m s^{-1} flame (Fig. 6.11 (iii)). The delay in downwards propagation occurred for all of the 'Plate' locations, and for the 'Middle, Down' locations at 12 and 23 m s^{-1}.

The 12 and 23 m s^{-1} flames ignited at the plate (Figs. 6.11 (i) and (ii)) behave very similarly to the diffusion cases, first spreading out slowly across the plate before suddenly accelerating towards the nozzle to complete the ignition process, as discussed in Sections 6.2 and 6.4.3.2. However, the process occurs much more slowly, with total ignition times of 1.55 and 0.17 s for the 12 and 23 m s^{-1} flames respectively, being 7 and 2 times slower than the diffusion cases at 10 and 19 m s^{-1} (and at the same thermal

loadings as the diffusion cases) respectively. However, the maximum velocity observed was almost twice as high for the 12 m s^{-1} premixed case than for the 10 m s^{-1} diffusion case due to the additional laminar flame speed with decreasing equivalence ratio (Chapter 4) and the higher Re (Table 6.4). The premixed flames have Reynolds numbers over twice as high as the diffusion cases at the same thermal loadings and they enter the turbulent transitional regime for the velocity of 23 m s^{-1}. This explains why the flame front propagation velocities are higher for the premixed cases, as the turbulence will aid the combustion, along with the additional laminar flame speed.

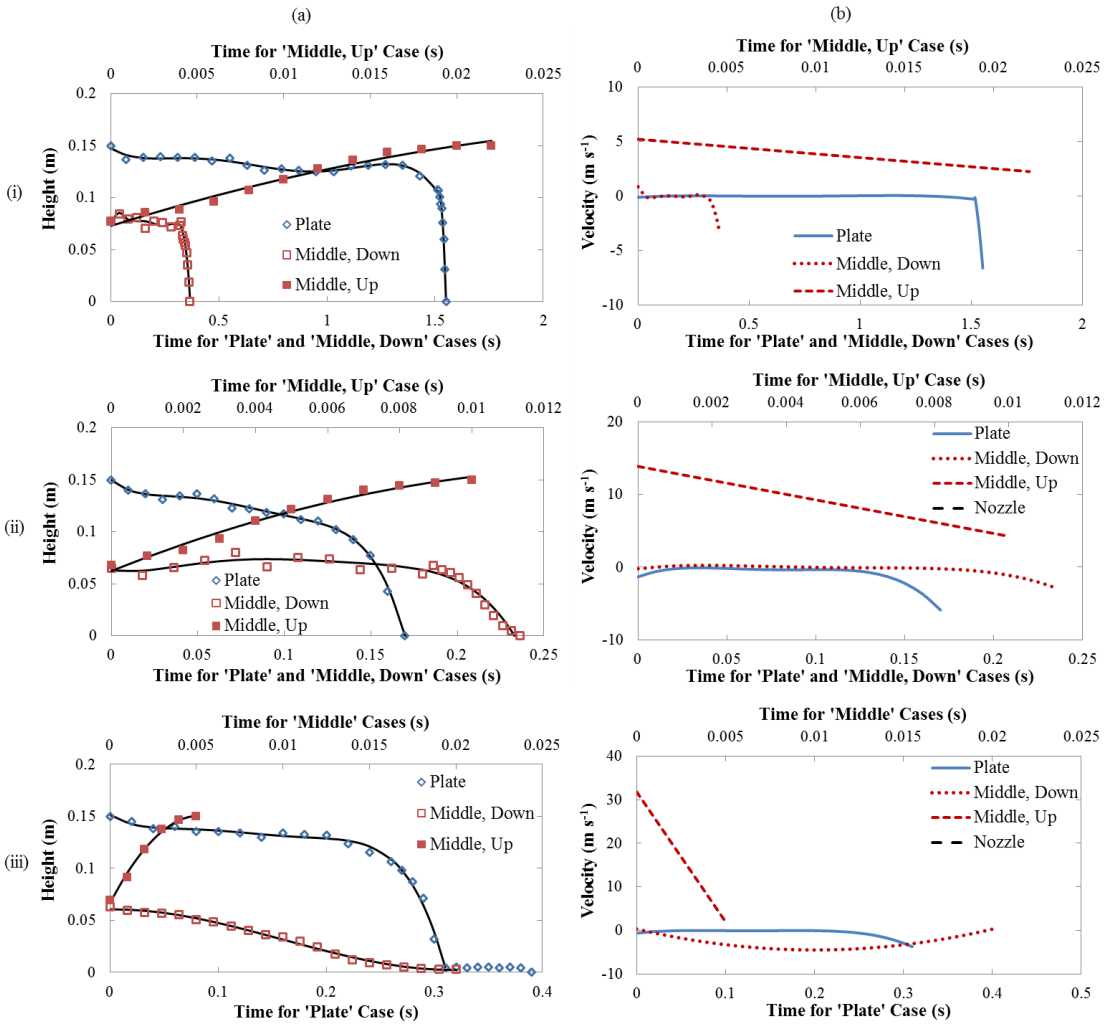

Figure 6.11: Plots of (a) Height and (b) Velocity of the centre of the flame front for hydrogen and air flames at (i) 12 m s^{-1}, (ii) 23 m s^{-1} and (iii) 34 m s^{-1}.

However, the delay times are still longer. The sudden acceleration towards the nozzle could also be accounted for by the fact that the plate heats up after the flame is stabilised on it, and so increases the flame speed due to the increase in temperature. (For

the diffusion flames, the flame mixes with the air at the plate and becomes better mixed, and so the plate temperature could increase the premixed flame propagation speed in this case as well). Also, for the 34 m s^{-1} case there is a delay (due to the flame spread) of approximately 0.25 s that is not seen in the 28 m s^{-1} diffusion case. This shows that the premix air hinders the ability of the flame to start to propagate downwards, even at the same thermal loadings and higher Reynolds numbers, but not necessarily the ability to propagate once initiated, as the downwards velocities are larger.

For the 'Middle, Down' cases the delay that was observed in the 28 m s^{-1} diffusion case was not present in the 34 m s^{-1} premixed case, but appeared in the 12 and 23 m s^{-1} premixed cases, with delay times of 0.4 to 0.18 for the 12 and 23 m s^{-1} flames respectively. This supports the notion that the premix air hinders the ability of the flame to begin propagating downwards, although increasing the thermal loading of the premixed flames seems to aid the initial downward propagation; the delay being shorter for the higher thermal loadings, rather than hinder it as for the diffusion flames ignited in the middle. This could be due to the steeper increase in spreading rate with velocity for the premixed flames (purple line in Fig. 6.10), causing the widening of the surface area that assists the downwards propagation to be more significant than the higher velocity of the opposing flow.

For the 'Middle, Up' cases, the maximum velocities for the diffusion flames were around 18 m s^{-1} for all three jet velocities (Fig. 6.9b). However, for the 'Middle, Up' premixed flames the maximum velocities increased quite steeply with jet velocity, with values of 5, 14 and 31 m s^{-1} for the 12, 23 and 34 m s^{-1} jet velocities respectively (Fig. 6.11b). This is a much larger change than for the hydrogen diffusion flames which indicates that the jet velocity is a much more significant parameter in increasing the upward propagation velocity for the premixed flames than for the diffusion flames, in contrast to the downwardly propagating flames.

6.4.3.4. Hydrogen and Carbon Dioxide

Thirdly, H_2/CO_2 flames were studied with H_2/CO_2 = 4.5 and at 12, 23 and 34 m s^{-1} (Fig. 6.12), corresponding to the same amount of hydrogen flow as the hydrogen diffusion and premixed cases (Table 6.4). Again, decelerations were observed for all upwardly propagating flames, and non-linear acceleration for the flames ignited at the 'Plate' and

'Middle, Down' locations. The 34 m s^{-1} H_2/CO_2 flame behaved in the same way as the premixed flame of the same velocity in that it stopped propagating downwards at 5 mm from the nozzle, where it remained for 0.07 s before attaching to the nozzle. Again, the last 0.07 s were not included in the curve fitting for the reasons described in Section 6.4.3.2.

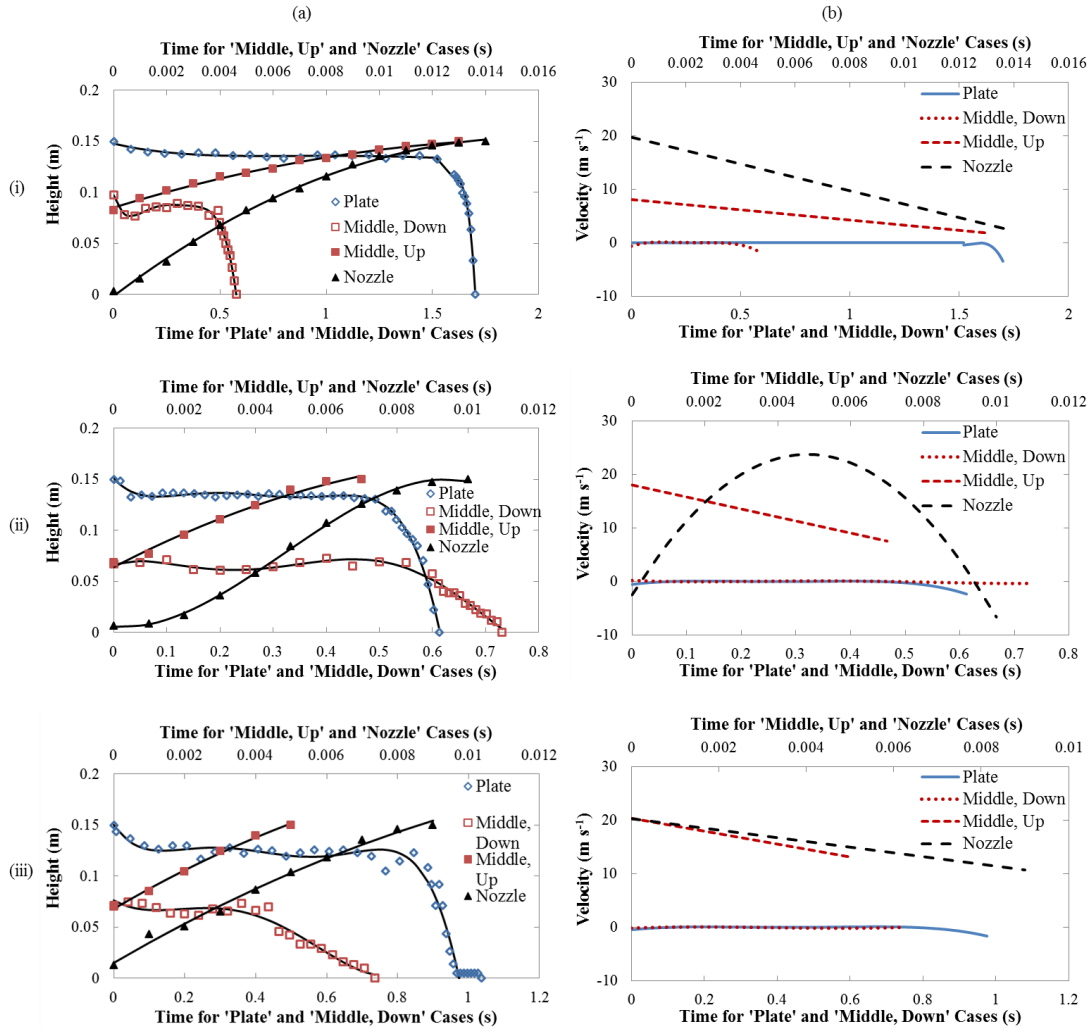

Figure 6.12: Plots of (a) Height and (b) Velocity of the centre of the flame front for hydrogen and CO_2 flames at (i) 12 m s^{-1}, (ii) 23 m s^{-1} and (iii) 34 m s^{-1}.

The propagation times for the 12, 23 and 34 m s^{-1} H_2/CO_2 flames ignited at the nozzle location were all slightly shorter than for the hydrogen diffusion flames at 10, 19 and 28 m s^{-1}, which can be accounted to the extra velocity of the added CO_2. However, for the 'Middle, Up' cases, as for the premixed flames, the maximum velocities increased quite steeply with jet velocity, with values of 8, 18 and 20 m s^{-1} for the 12, 23 and 34 m s^{-1} jet velocities respectively. Again, this indicates that the jet velocity is a much more

significant parameter in increasing the upward propagation velocity for the H_2/CO_2 flames than for the diffusion flames ignited in the middle. This could also be due to the increased buoyancy of the hydrogen diffusion flames, causing more similar upwards propagation for the three values of fuel velocity.

The downward propagation time for the 12 m s^{-1} flame ignited at the plate was slightly longer for the CO_2 case than for the premixed case. However, for the higher velocity cases, the delays were much longer, with total propagation times 4 and 3 times slower for the 23 and 34 m s^{-1} 'Plate' cases respectively. In addition, the 'Middle, Down' flames took 1.6 and 3 times longer for the 12 and 23 m s^{-1} H_2/CO_2 flames respectively than the premixed flames of the same velocities. A delay was also observed for the 34 m s^{-1} 'Middle, Down' case, which not seen in the premixed cases. This indicates that the CO_2 hinders the initial downwards propagation of the flame more than the premix air, since although the Reynolds numbers were higher for the H_2/CO_2 flames at the same thermal loadings, and the H_2/CO_2 flames were fully turbulent, the delay times were still longer. This could be due to the lower spreading rate for the H_2/CO_2 cases (green line in Fig. 6.10), which causes the local upwards velocity to be higher and causes more resistance to the downwards propagation. In contrast to the premixed flames, the downwards velocities ignited in the middle for the H_2/CO_2 flames are much lower than for the diffusion cases. This is because the CO_2 reduces the laminar flame speed and the adiabatic flame temperature of the fuel mixture significantly (Chapter 4).

Since the delay times were increased when air or CO_2 was added, and since the premix air aids combustion but the CO_2 dilutes the hydrogen, this implies that the reduced molecular diffusivity of the hydrogen when mixed with air or CO_2 is largely responsible for reducing the ability of the flame to begin the downwards propagation stage of the ignition process when ignited at the plate. This is because it hinders the hot mixture from mixing with the cold unburned fuel nearer to the nozzle, even though the turbulence degree is higher.

6.4.3.5. Conclusions

The effects of the igniter type and the addition of air or CO_2 on the propagation of hydrogen flames have been studied in this section. Igniter type, ignition location, fuel composition and jet velocity have been shown to affect the ability of hydrogen diffusion

and premixed flames and H_2/CO_2 diffusion flames to propagate with and against the fuel flow, in the following ways:

- Using the spark or electrode igniter produce different results, in particular, different delay times for the downwardly propagating flames. This is due to the different sizes of the flame kernel produced by the igniters and due to the differences in axial position of the igniters.

- For the hydrogen diffusion flames, the maximum upwards velocity for the middle locations increased a very small amount with jet velocity. However, for the premixed and H_2/CO_2 flames, the maximum velocity increased steadily with jet velocity, indicating that the jet velocity was a more significant parameter in increasing the propagation velocity for these cases than for the diffusion cases. This could also be due to the reduced effect of buoyancy for the H_2/air and H_2/CO_2 cases.

- A non-linear velocity or a decreasing velocity was observed when the flame propagated upwards or downwards when ignited in the middle or nozzle locations. This was caused by the widening of the fuel stream, decreasing the fuel velocity near the plate and so decreasing the propagation velocity, or increasing the velocity near the nozzle, causing more resistance to the downwards propagation. In addition, the flame stretch present in the stagnation region caused a reduction in flame speed and burning velocity and so caused the propagation of the flame front to slow down.

- A non-linear acceleration was observed for some of the 'Plate' cases, due to the delay caused by the flame spreading across the plate and also by the initial inability to overcome the opposing flow. A delay was also observed in some cases when ignited in the middle location, because the ignition was in the fuel rich zone, causing the initial flame spread to be difficult and slow. Various factors, including spreading rate, jet velocity and ignition location, affected the delay time for the different fuel compositions.

- The flame velocity and surface area at certain locations were affected by the spreading rate, and for the diffusion cases, the increase in spreading rate with

velocity allowed more mixing near the plate for the higher velocity flame, aiding combustion and causing the delay at the plate to be shorter. However, at the middle location, the high velocity becomes more significant in delaying the downwards propagation than the increased mixing does in aiding it, causing the delay to be longer.

- Conversely, for the premixed cases ignited in the middle, increasing the velocity caused the delay to be shorter. This could be due to the much steeper increase in spreading rate with fuel velocity, causing the higher velocity of the fuel that hinders the downward propagation of the flame to be less significant than the widening of the flame surface area that aids combustion.

- The premix air and added CO_2 also hinder the initiation of the downwards propagation of the flame when ignited at the plate and middle locations, even though the Reynolds numbers were much higher, due to the reduced molecular and thermal diffusivity of the fuel mixture hindering the spread of the heat produced by the combustion to the cold fuel flow.

The flame propagation after ignition is very complex and is affected by many factors, including fuel composition, igniter type and flow conditions. Flames at the same Reynolds numbers, but different thermal loadings and nozzle size will be studied in the next section in order to test the effect of Re, loading and nozzle size on the flame front propagation phenomena observed in this section.

6.4.4. Large Nozzle – Same Reynolds Number

6.4.4.1. Introduction

This section compares the effect of changing the nozzle size but keeping the Reynolds number the same for the cases studied in Section 6.4.3. This means that the nozzle exit velocities are lower but the thermal loadings are higher (Table 6.4). It causes the fuel to be easier to ignite due to the larger surface area of the fuel stream, and causes the plate to heat up more quickly due to the higher thermal loadings. The specific effects will be discussed for the three fuel compositions at three values of thermal loading.

The propagation times for the different cases for this nozzle size are more comparable for the various ignition locations. This means that only one axes scale needed to be used

for many of the cases, unlike for the small nozzle. These are for the diffusion cases (Fig. 6.13) and the premixed case at the higher velocity (Fig. 6.14 (iii)). For the other cases, care should be taken to note the axes scales for the different nozzle locations, as in Section 6.4.3.

6.4.4.2. Hydrogen

Figures 6.13a and b show the graphs of height and velocity against time respectively for the 6.5, 12.3 and 18.1 m s^{-1} hydrogen diffusion flames ((i), (ii) and (iii) respectively). For the downwardly propagating diffusion cases ignited at the plate, no delay was observed, unlike for the smaller nozzle. The propagation times for the 'Plate' cases decreased from 0.021 to 0.01 back to 0.012 s for the 6.5, 12.3 and 18.1 m s^{-1} flames respectively. For the 'Middle, Down' cases, the propagation times were 0.01, 0.006 and 0.004 s respectively. Due to the increased surface area and thermal loading, and the reduced opposing fuel velocity, the propagation times and velocities are much faster than for the smaller nozzle. This also increases the ability of the flame to initiate the downwards propagation, and so the flame can propagate downwards immediately.

The thermal loading of the 6.5 m s^{-1} large nozzle case is comparable to the 19 m s^{-1} case for the small nozzle, but the propagation time is still 10 times faster, even at a reduced Reynolds number. In addition, the highest velocity for the large nozzle (18.1 m s^{-1}) is comparable to the 19 m s^{-1} flame for the small nozzle, but with a much larger Reynolds number. However, the propagation time is still 7 times faster for the larger nozzle size. This is mainly due to the lack of delay for the flame spread, but the velocities reached are still somewhat higher for the larger nozzle cases. Therefore, the effect of the wider fuel stream is more significant on the propagation times than the effect of the thermal loading, Reynolds number and nozzle exit velocity.

The upwardly propagating flames all exhibit parabolic velocity profiles, except for the 'Middle, Up' flame at 6.5 m s^{-1}. This is in contrast to the smaller nozzle cases where most of the flames had a constant deceleration of the flame front. The spreading rates for these flames Fig. 6.14 (orange lines)) are wider than for the smaller nozzle size, causing a larger difference in the velocity along the axial direction of the fuel stream between the nozzle and the plate. This causes a higher deceleration of the flame front with the fuel stream. However, the flames first accelerate before this deceleration

occurs, to velocities much faster than the fuel velocity and much faster than for the smaller nozzle size. The increased fuel air mixing, caused by the wider surface area and nozzle size (at the same Reynolds number) causes the flames to propagate much faster, before being met by resistance from the plate, and slowing down due to the added flame stretch in the stagnation region.

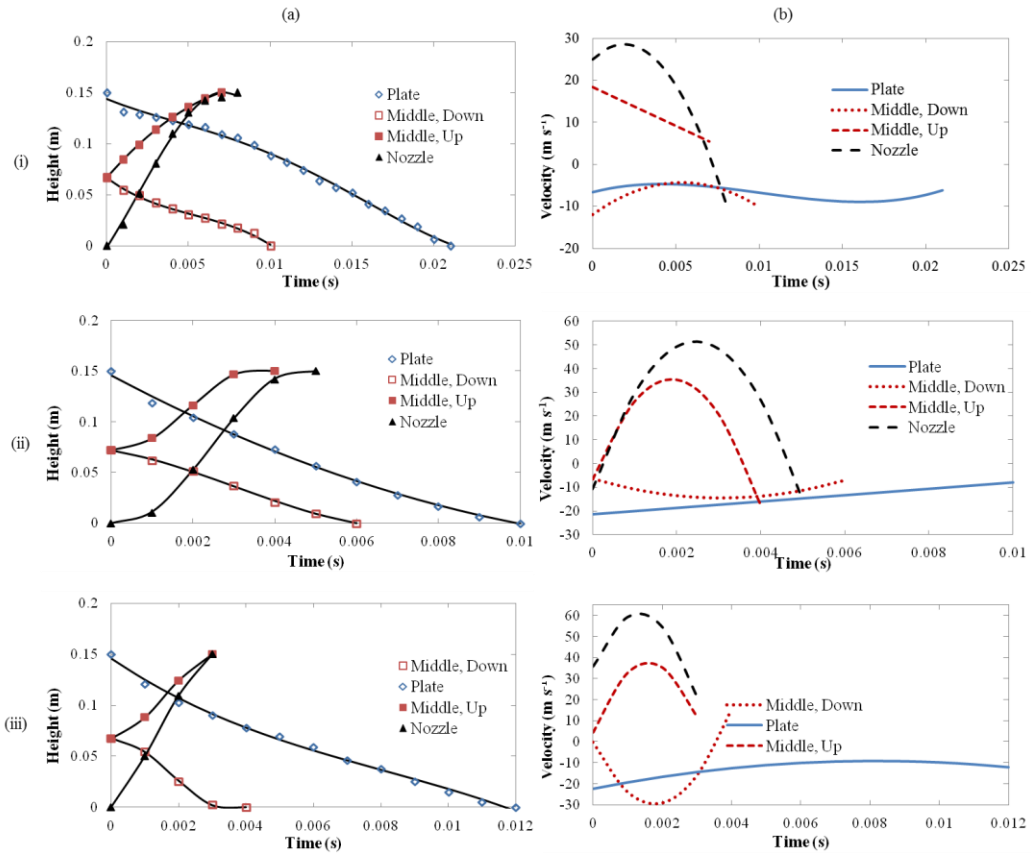

Figure 6.13: Plots of (a) Height and (b) Velocity of the centre of the flame front for hydrogen flames with large nozzle at (i) 6.5 m s^{-1}, (ii) 12.3 m s^{-1} and (iii) 18.1 m s^{-1}.

The propagation times for the ‘Middle, up’ and ‘Nozzle’ cases are within 0.001 s of each other for all of the nozzle exit velocities, even though the ‘Nozzle’ cases have twice the distance to go. This means that the velocities are higher for the nozzle cases. Again, this is in contrast to the small nozzle at the same Reynolds number, where the velocities for the ‘Middle, Up’ and ‘Nozzle’ cases were quite similar. More investigation of varying nozzle sizes should be performed to further examine this effect. The next section looks at the effects of air addition and will again be compared to the results for the smaller nozzle.

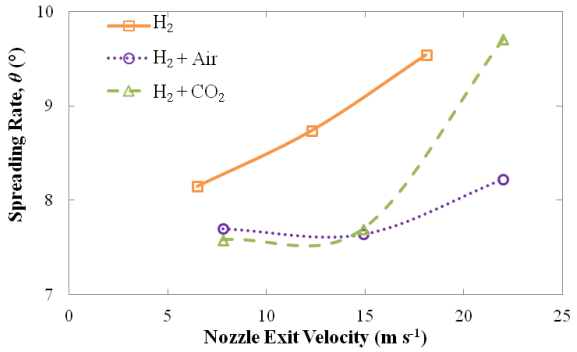

Figure 6.14: Spreading rates for the hydrogen flames with/without air and CO_2 addition for the large nozzle.

6.4.4.3. Hydrogen and Air

Figures 6.15a and b show the graphs of height and velocity respectively against time for the 7.8, 14.9 and 22 m s^{-1} flames ((i), (ii) and (iii) respectively). For the smaller nozzle, no ignition could be achieved at the nozzle locations. This was not the case for the larger nozzle, due to the increased area of the fuel stream aiding the initiation of the combustion. This is a similar effect to igniting downstream for the smaller nozzle size.

For the 'Plate' cases, delays of 0.12 and 0.02 s were observed for the 7.8 and 14.9 m s^{-1} flames respectively. A slight delay of 0.007 s was observed for the 'Middle, Down' case for the 7.8 m s^{-1} flame as well. This is in agreement with the results for the smaller nozzle in that the addition of air hinders the initial downwards propagation. Again, the propagation times and velocities are much faster than for the small nozzle results at the same Reynolds numbers, due to the increased mixing caused by the larger nozzle size. This causes a higher surface area for the flame to propagate, and increase the burning rate of the fuel.

For the upwardly propagating flames, the velocities reached are somewhat larger than for the diffusion flames, and for the flames at the smaller nozzle size. The addition of premixed air causes a faster laminar flame speed, and the wider surface area of the fuel stream and higher thermal loading assist the propagation of the flame. Similar to the diffusion flames, the 'Middle, Up' and 'Nozzle' flames take the same amount of time to propagate. However, for the higher velocity flame (22 m s^{-1}), the propagation of the 'Nozzle' flame takes longer (0.005 s compared to 0.002 s for the 'Middle, Up' location (Fig. 6.15a (iii))). These results cannot be compared to the smaller nozzle results at the

same Reynolds number due to the lack of ignition for the smaller nozzle. However, for the 'Middle, Up' flames, the propagation times were 4.4, 3.3 and 2.5 times faster for the larger nozzle results at 7.8, 14.9 and 22 m s^{-1} respectively. This means that increasing the fuel velocity has a smaller effect for the larger nozzle size. This could be due to the smaller change in spreading rate for the larger nozzle size; for the larger nozzle, the spreading rates are within 1°, whereas for the smaller nozzle, the spreading rate increases by 2° between the 3 cases (Figs. 6.14 and 6.10 respectively (purple lines)). A larger change in spreading rate causes a larger change in the fuel stream area, and so causes faster propagation for the higher velocity flames (when compared to the lower velocity flames) for the smaller nozzle, due to the increased mixing between the hot products and cool reactants. The next section looks at the effect of CO_2 addition, and will again be compared to the smaller nozzle.

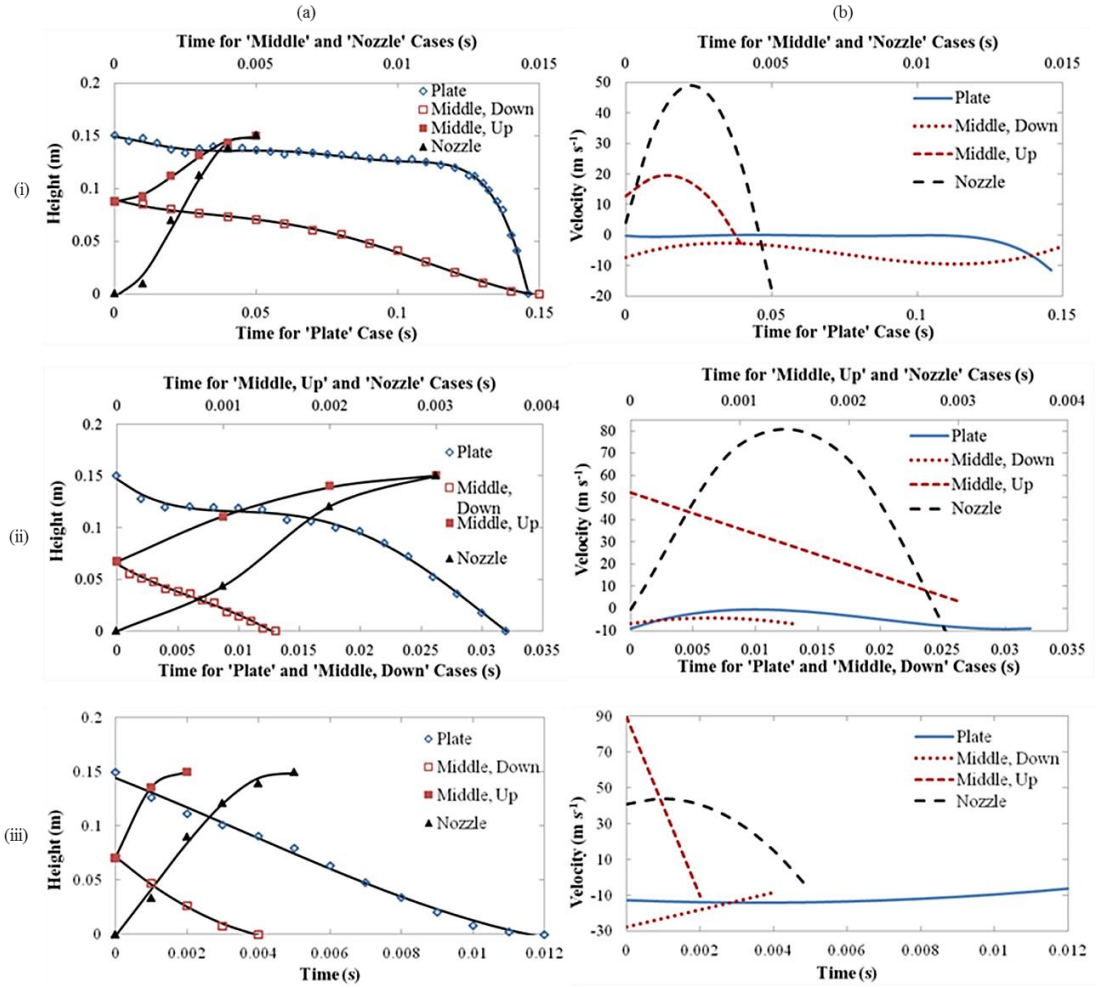

Figure 6.15: Plots of (a) Height and (b) Velocity of the centre of the flame front for hydrogen premixed flames at (i) 7.8 m s^{-1}, (ii) 14.9 m s^{-1} and (iii) 22 m s^{-1}.

6.4.4.4. Hydrogen and Carbon Dioxide

The effect of adding CO_2 is shown in Fig. 6.16. The propagation times for the 'Nozzle' location were 1.6, 1.7 and 2.3 times faster for the larger nozzle (for the 7.8, 14.9 and 22 m s^{-1} flames respectively). This is in contrast to the premixed flames, for which the propagation increased by smaller degrees with increasing fuel velocity. Again, this could be due to the spreading rate. Figure 6.14 shows that for the H_2/CO_2 flame (green line), the spreading rate increases quite steeply for the higher velocity flame. Again, this increase in spreading rate causes faster propagation for the higher velocity flame, and so causes a larger difference in propagation time for the 22 m s^{-1} H_2/CO_2 flame when compared to the small nozzle.

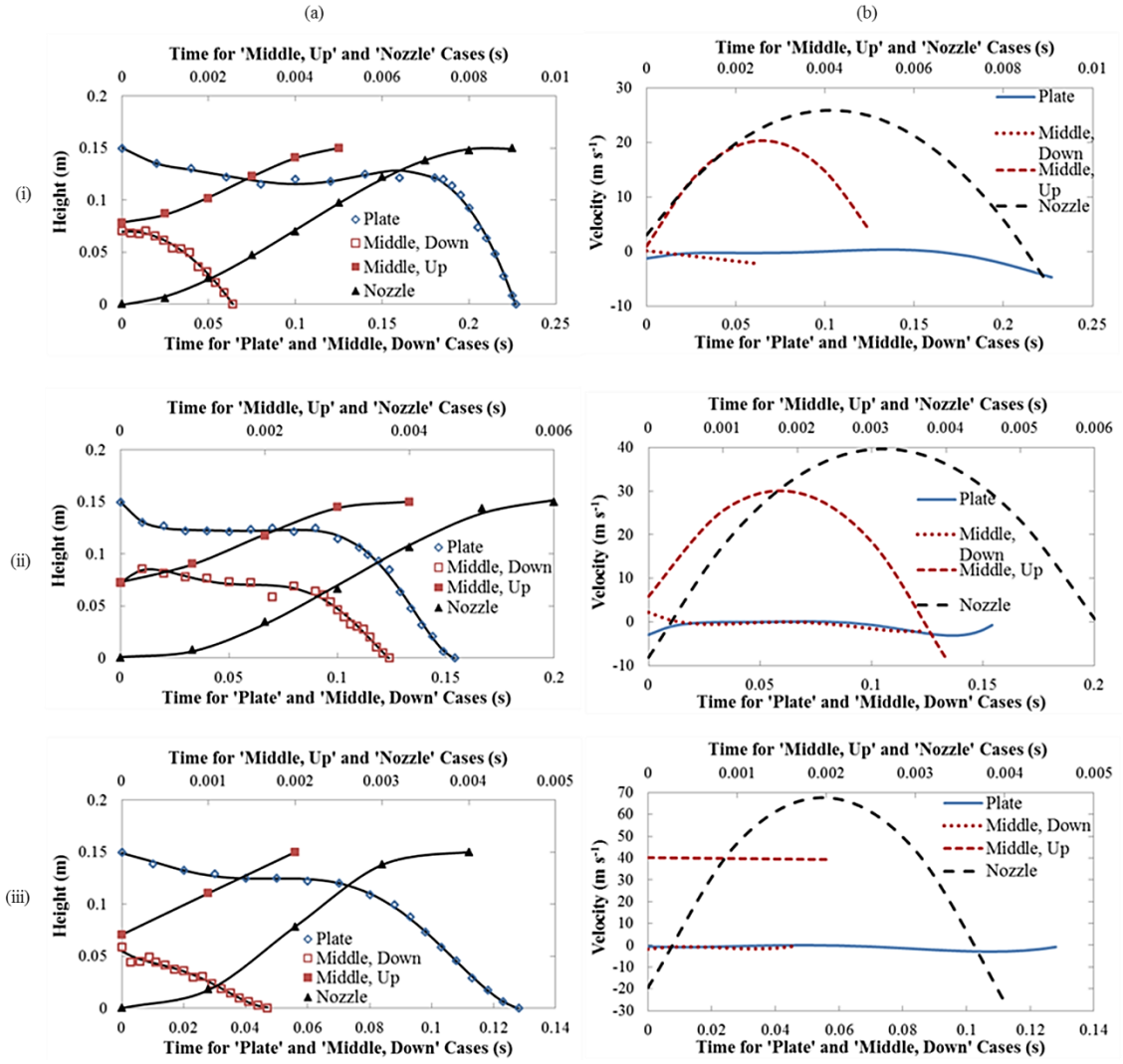

Figure 6.16: Plots of (a) Height and (b) Velocity of the centre of the flame front for H_2/CO_2 flames at (i) 7.8 m s^{-1}, (ii) 14.9 m s^{-1} and (iii) 22 m s^{-1}.

For the downwardly propagating flames, delays were observed for the 'Plate' cases, reducing in delay time with increasing thermal loading. This is similar to the smaller nozzle case. In addition, a delay was observed for the middle location for the 14.9 m s^{-1} flame. For the smaller nozzle, a larger delay was also observed for the flame with the corresponding Reynolds number. Similar velocities were also observed for both nozzle sizes. The propagation times for the 'Plate' cases were 7.5, 4 and 8 times faster (for the 7.8, 14.9 and 22 m s^{-1} flames) than the corresponding cases at the small nozzle. For the middle down cases, the flames propagated 9, 5.9 and 15.6 times faster respectively. For the premixed cases, the differences in propagation times were much larger, and for the diffusion cases, no delays were observed at all for the larger nozzle size. This shows that the nozzle size has a smaller effect on the H_2/CO_2 flames than for the diffusion or premixed downwardly propagating flames.

6.4.4.5. Conclusions

The results of Section 6.4.3 were repeated with the same Reynolds number but a larger nozzle size. This meant that the nozzle exit velocity was reduced but the thermal loading was increased. These results were compared to the results at the smaller nozzle. It was found that:

- The larger nozzle size widened the fuel stream and allowed more mixing with the air by the time the fuel reached the plate. This caused the downwards propagation to initiate without delays when ignited at the plate for the hydrogen diffusion flames. In turn, this caused faster downwards propagation times even for cases with the same thermal loading and lower Re, and for the cases with the same velocity but higher Re. This means that the widening of the fuel stream was more significant for initiating the downwards propagation than the thermal loading or fuel velocity for the hydrogen diffusion flames.
- The addition of premixed air and CO_2 hindered the initial downwards propagation of the flames ignited at the plate and in the middle, similar to the smaller nozzle, although the propagation times were much faster for the larger nozzle.
- The effect of increasing the nozzle size was smaller for the H_2/CO_2 downwardly propagating flames than for the diffusion and premixed flames.

- The widening of the fuel stream also caused faster upwards propagation for all fuel compositions due to the higher surface area increasing the burning rate of the fuel. Adding premixed air also increased the propagation speed of the flame front due to the higher laminar flame speed and flame temperature.
- The change in spreading rate with increasing fuel velocity was different for the small and large nozzles, and caused the upwards propagation to change by different degrees for the different fuels when the nozzle size was increased.
- Increasing the nozzle size allowed ignition at the nozzle location for the premixed flames, unlike the smaller nozzle, due to the larger surface area of the fuel stream.

The main effects caused by increasing the nozzle size but keeping the Reynolds number the same were increased ability for the fuel to initiate its downwards propagation (and to ignite the fuel at the nozzle), although delays were still observed when ignited at the plate and the middle for some cases. In addition, the propagation times were much faster for the larger nozzle size for all compositions.

6.5. Flame Front Propagation Conclusions

In this chapter high speed schlieren imaging and digital image analysis have been applied to evaluate the flame front propagation after ignition at specified locations. The technique is able to provide a temporal resolution down to 1 μs. Therefore the image blurring caused by flame propagation is very small. This allows the behaviour of the flame front to be studied for various cases, and changing various factors such as fuel composition, fuel velocity and ignition location has significant effects on the flame propagation trends. The propagation of the flame after ignition is very complex and can be affected by many factors.

It has been shown that changes in ignition location can affect the process of flame propagation after ignition. The total attachment times when ignited away from the nozzle can be greatly affected by changing the ignition location, geometry or flow conditions. This will be helpful for further investigations into optimising igniter conditions for devices where combustion processes are required to finish as soon as possible or where flames need to be established very quickly. An impingement configuration is convenient for the investigation of ignition and flame propagation in

inhomogeneous mixing and flow fields. The stagnation point has an area of low flame stretch, which slows down the laminar flame speed and consequently slows down the propagation of the flame. This causes a deceleration of the flame front when propagating towards the plate. This was seen more in the hydrogen cases than the methane cases, where the effects of flame stretch are more significant. In addition, the hydrogen has much stronger mixing with the ambient air, due to the higher molecular and thermal diffusivity, and due to the higher velocities of the flames used. This causes deceleration of the flame front, since, as the fuel entrains the ambient air, the local velocity is reduced. For the upwardly propagating flames, the flame front slows down as it propagates with a slower fuel velocity further downstream. For the downwardly propagating flames, as the flame propagates upstream, the opposing local fuel velocity is increased, which again slows down the flame front propagation. On the other hand, once the flame has been initiated, the flame front accelerates. The competing factors cause the flame in some cases to accelerate, and in others to decelerate. For some cases, a parabolic velocity is observed, whereby the flame front initially accelerates, and then slows down due to these factors.

In addition, for the downwardly propagating flames, a phenomenon was observed whereby there was an inability to overcome the opposing flow. For the hydrogen flames, this was observed as an almost zero velocity followed by a sudden acceleration when the flame was able to overcome the opposing flow. This occurred at the plate location and the middle location for some of the cases. For the plate location, the flame boundary was observed to spread out across the plate for a short amount of time. Following this, the flame would suddenly propagate downwards against the flow. This occurred when enough heat had been produced and mixed with the vertical flow stream, and when the plate was hot enough that downwards propagation was possible. Factors that affected the delay times were igniter type, nozzle-to-plate height, fuel composition and thermal loading.

Increasing the fuel exit velocity for the hydrogen flames ignited at the plate tended to cause a shorter delay time, due to the increased mixing between the fuel and hot products, and due to the higher thermal loading increasing the heat production rate and plate temperature. However, at the middle location, the increase of the opposing

velocity became more significant and caused longer delay times for the higher velocity fuels.

On the contrary for the methane flames, the inability to propagate against the flow was observed as a deceleration to an almost stop, quite close to the nozzle where the opposing velocity became too high, before again suddenly accelerating downwards when enough heat was transferred to the unburned gases. However, the velocity of the methane flames was much lower than the hydrogen flames at the same thermal loading, and so downwards propagation was easier at similar locations. For the methane flames, increasing the fuel velocity caused a longer delay, and for the highest velocity flame studied, the flame did not propagate to the nozzle, but remained slightly lifted above the nozzle, since the opposing velocity was too strong at this location.

The behaviour of hydrogen and methane flames was very different, due to the vast differences between the two fuels. However, large differences were also observed when air or CO_2 were added to the hydrogen. Both additions caused the delay in downwards propagation to be longer, although adding air still caused faster propagation. This is due to the reduced mixing of the hot products and cool reactants because of the lower molecular and thermal diffusivity. For the premixed flames, the delay was shorter for the higher velocity fuels ignited in the middle, in contrast to the hydrogen diffusion flames. This was also due to the spreading rate, and for the premixed flames, the increase in the surface area of the flame with increasing fuel velocity became more significant and aided the initial downwards propagation, rather than inhibit it.

The nozzle-to-plate distance, ignition location (radial or axial), fuel type and fuel properties and conditions all have significant effects of the propagation of the flame front immediately after ignition. Competing factors such as propagation with or against flow, accelerations and deceleration caused by various factors, mixing and velocity profiles caused complex propagation trends to be observed. Further examination of the effect of local flow velocity and mixing should be performed, for example by using PIV to calculate the fuel velocity. This is reserved for the scope for future work.

Using the high speed schlieren imaging, interesting trends have been observed and various flow conditions compared. Delays of downwards propagation can be avoided or induced by changing the flow conditions or igniting at different locations in the

impinging flame setup. It has been shown that the propagation of the flame front is quite complex, with competing factors causing faster or slower propagation of the flame front with or against the flow. The flame front propagation changes with respect to the location in the impingement configuration, being affected by the flow velocity, flow profile, impingement plate, heat production and mixing between cool reactants and hot products and products and the ambient air.

Some brief general conclusions regarding the flame wall interaction of various fuel and flow conditions using schlieren and thermal imaging will be given in the next chapter. This will be followed by the scope for future work and how these techniques could be improved or added to for further examination of the phenomena discussed.

7. Conclusions

This chapter presents the general conclusions regarding the development of the experimental techniques and their application to the heat transfer and flow diagnostic studies. A summary of the research in this thesis will be given with regards to the main points of interest and successfulness of the work carried out. The following chapter will present the scope for future work.

Various experimental techniques have been utilised and further developed in order to evaluate the flame wall interaction of impinging flames for a range of fuel and flow conditions. A vertical impingement configuration has allowed optical access so that flow properties, density variations and wall temperature could be studied. This configuration has been used widely in the literature for many hydrocarbon fuels but less widely for hydrogen and syngas fuels, which were the focus of this thesis. The study of heat transfer for hydrogen and syngas fuels is integral for their development for use in combustion devices, where flames may directly impinge onto combustor surfaces creating regions of high or low temperature which may damage the combustor or affect the combustion of the fuel. Syngas and hydrogen combustion is significant in the objective to steer away from fossil fuels and into cleaner combustion uses.

Since the properties of hydrogen are vastly different to those of hydrocarbon fuels, and since the composition of syngas varies widely across sources, systematic evaluations of the effects of various properties such as thermal loading, Re, equivalence ratio and fuel velocity have been performed in order to test their effects on the interaction between the impinging flame and the wall. It has been shown that the relative effects of these properties are different for the different fuels, and a slight change in nozzle exit conditions can significantly affect the wall temperature and flame propagation characteristics.

Thermal imaging is a useful tool for heat transfer studies, allowing non-intrusive, 2D measurements. However, it has not been widely used in the literature. Problems with the emissivity of some materials and with the wide range of spectral emissions from flames cause issues when using thermal imaging for impinging flame studies. Methodologies have been utilised and developed in order to try and address these issues. A flame switch off method was utilised so that the thermal footprint of the plate at a steady state

condition could be analysed. This allowed radiation losses from the plate to be evaluated and compared for different conditions, so that the relative overall effects of high or low temperature regions of the plate could be evaluated and compared. In addition, an iterative methodology was developed so that the thermal imaging could be used for the quartz plate, whose emissivity depends on the temperature being measured. This technique was useful for comparing conditions for various cases, and for comparing premixed and diffusion flames, where there was no soot and soot deposition on the plate respectively. However, it was shown that this methodology depended heavily upon the curve fits for the temperature dependent emissivity values and suggestions for improving this methodology will be discussed in the next chapter.

The combination of schlieren, direct and thermal imaging has allowed insight into the flame wall interactions. Features on the schlieren images were used to explain features in the thermal footprints, such as regions of low temperature in the stagnation region caused by unburned fuel impingement. In addition, turbulent structures seen in the schlieren images helped to explain why the thermal profiles differed so greatly for different flow conditions. Mixing between the hot gases and the ambient air can cause lower wall temperatures due to the entrainment of the cool air, whereas mixing between the unburned fuel and ambient air can cause higher wall temperatures due to the increase in laminar flame speed and adiabatic flame temperature for the leaner local compositions. These effects differ for the different fuel and flow conditions, due to differences in molecular and thermal diffusivity, flame stretch and density ratios between the reactants, products and ambient air. A wrinkle scale methodology has been developed in order to attempt to quantify the effect of turbulent structures and mixing on the flame wall interactions, to be used alongside the qualitative observations from the schlieren and direct imaging.

In addition, the temperature profiles differ for different fuels at similar inlet conditions. The direct imaging can help to explain this, since factors such as flame size on the plate and luminosity will affect the wall temperature. CHEMKIN was used to calculate the effect of equivalence ratio on the laminar flame speeds and adiabatic temperatures, which also affect the wall temperature profiles for different fuels at similar nozzle exit conditions.

High speed schlieren imaging was also used to study the ignition and flame propagation characteristics in the impinging flame configuration. The upwards and downwards propagation of the flame were analysed for various fuels and nozzle exit velocities. Delays in initial propagation were observed when the flame propagated against the fuel stream and various factors affected this delay, including the position of the impingement plate and mixing between the hot gases and ambient air. The competing factors of the upstream propagation, causing decelerations of the flame front as the opposing flow velocity increased, and heat production, causing accelerations of the flame front as more heat was produced, differed significantly for different fuels, flow conditions and ignition locations. The propagation of the flame front immediately after ignition was observed to be very complex, changing significantly for relatively small changes in the conditions at the nozzle.

This thesis has presented interesting results on the flame wall interactions of impinging flames of hydrogen, syngas, propane and methane, combining various visualisation and diagnostic techniques. However, improvements can still be made on the accuracy of these techniques, more extensive experimentation could be performed and additional parameters could be studied. The next chapter will discuss the scope for future work that has arisen from the work in this thesis.

8. Scope for Future Work

8.1. Introduction

This chapter details some improvements that could be made on the techniques and presents some scope for further research. Firstly the wall temperature work will be discussed, related to Chapter 5, followed by improvements and future work for the flame propagation studies (Chapter 6).

8.2. Wall Temperature

8.2.1. Accuracy

Steel Plate

The thermal imaging camera readings depend heavily upon the emissivity values. Therefore, the accuracy could be improved by measuring the emissivity of the steel plate and in addition, by comparing to other temperature measurement readings, such as thermocouples. This was beyond the scope of this thesis due to time restraints. In addition, the holes drilled in the surface could cause uneven conduction through the plate that could cause uneven heat transfer and might affect the thermal imaging readings. However, two identical plates could be used where one has thermocouples drilled into it to verify the thermal imaging readings at a range of temperatures and calculate the emissivity, and the other used for the thermal profiling so that the thermocouples do not disturb the thermal imaging readings or need to be placed in the flame.

Quartz Plate

For the quartz plate, drilling is not possible. However, an oven could be used to heat the plate to a known temperature and the thermal imaging temperature readings verified that way. In addition, for the temperature dependent emissivity methodology, the oven could be used to calculate the emissivities at a larger range of temperatures, with many points on the T - ε curve, so that the temperature-emissivity curve could be more accurately approximated. This was beyond the scope of this thesis as an oven was not available for the current research.

8.2.2. Further Research

Temperature Dependent Emissivity Methodology

The temperature dependent emissivity methodology could be improved and developed for use with other materials. Using an oven to heat the materials with temperature dependent emissivity (for example quartz, aluminium, titanium and copper) to a known range of temperatures, the methodology could be implemented so that the thermal imaging camera could be used to study impinging flames for these targets. In addition, the dependence of the emissivity on the viewing angle and plate thickness could also be studied.

Quartz Plate

The schlieren technique could be applied to the transparent quartz plate in the vertical direction, i.e. with the parallel light beam shining through the plate. This could allow the flow structure in line with the plate, in the wall jet region, to be visualised. This would be particularly useful for the ring flames. However, this would present many challenges; for example, the temperature gradients in the plate would cause distortions of the images, there would be convection currents and condensation on the mirrors and the setup would be difficult.

Additional Parameters

A more extensive study of the syngas compositions could be performed, using different nozzle sizes and flow conditions and a larger range of equivalence ratios. In addition, an angled plate could be used to study the effects of buoyancy on the flame wall interactions and wall temperature. Using a different seeder that would allow the flow of fuel, PIV could be used to evaluate the effects of local flow velocity and vorticity on the wall temperatures. It would also be interesting to test the effects of using different initial plate temperatures or different ambient temperatures on the wall temperature and radiation losses. In addition, the effects of coflow on the wall temperature could be further studied using the larger nozzle burner to produce swirling coflow.

8.3. Flame Propagation

8.3.1. Accuracy

The accuracy and repeatability of the flame propagation results could be improved by taking large amounts of data for each composition (i.e. repeating each case several

times) and finding the averages of the flame propagation behaviours. However, this would remove the instantaneous behaviour that can be studied by evaluating the cases separately. A fixed igniter could be used that does not need to be removed from the flow so that the effects of small changes in igniter position could be minimalised.

8.3.2. Further Research

Plate Effects

A larger plate could be used to test the effects of the horizontal propagation, since in this thesis the flame escaped around the edges of the plate. In addition, an angled plate could be used to test the buoyancy effects, and to see the differences when igniting in the uphill or downhill sections of the wall jet regions. A larger range of plate heights and ignition locations could be used to further examine the effects of the plate on the initial downwards propagation and a free flame could be used to test the effects of the impingement plate on the flame propagation in more detail.

Additional Parameters

Again PIV could be useful for the flame propagation studies, in order to properly evaluate the initial flow velocity profiles and their effects on the flame propagation. PIV could also be used to examine the flow velocity profiles during the ignition process, although this would cause difficulties in the synchronisation of the PIV and the ignition.

A larger range of Reynolds numbers could be used to further test the effects of turbulence on the flame propagation. In addition, hydrogen could be tested without nitrogen dilution, and the syngas compositions could be used for these experiments. However, this presented safety issues in the current work and was therefore not attempted.

8.4. Conclusions

The scope for future work presented in this chapter could not be attempted in the current work due to time, experimental and safety restraints. However, they would provide additional interesting opportunities for further research if these restraints could be overcome. Nevertheless, many interesting results have been presented in this thesis over a wide range of experimental conditions using advanced optical diagnostics. The techniques that have been developed will be useful for future research into the flame wall interaction of impinging flames.

References

[1] W. C. Strahle, *An Introduction to Combustion*. Langhorne: Gordon and Breach Science Publishers, 1993.

[2] C. E. Baukal Jr., "Preface," in *The John Zinc Combustion Handbook*, C. E. Baukal Jr., Ed., Boca Raton: CRC Press, 2001, p. ix.

[3] F. J. Weinberg, "The first half-million years of combustion research and today's burning problems," *Progress in Energy and Combustion Science*, vol. 1, pp. 17-31, 1975.

[4] K. Hunecke, *Jet Engines: Fundamentals of Theory, Design and Operation*, 6th ed. Osceola: Motorbooks International Publishers & Wholesalers, 2003.

[5] C. L. Wadhwa, *Generation, Distribution and Utilization of Electrical Energy*. New Delhi: New age International (P) Ltd., 2005.

[6] M. P. Boyce, *Gas Turbine Engineering Handbook*, 4th ed. Oxford: Elsevier Inc., 2012.

[7] M. L. Perry and T. F. Fuller, "A historical perspective of fuel cell technology in the 20th century," *Journal of the Electrochemical Society*, vol. 149, pp. S59-S67, 2002.

[8] S. Thompson and K. Li, "Modelling of NOx emissions in coal-fired plant," in *Thermal Power Plant Simulation and Control*, D. Flynn, Ed., London: The Institution of Engineering and Technology, 2003.

[9] C.-C. Cormos, "Evaluation of energy integration aspects for IGCC-based hydrogen and electricity co-production with carbon capture and storage," *International Journal of Hydrogen Energy*, vol. 35, pp. 7485-7497, 2010.

[10] J. S. Rhodes and D. W. Keith, "Engineering economic analysis of biomass IGCC with carbon capture and storage," *Biomass and Bioenergy*, vol. 29, pp. 440-450, 2005.

[11] R. Viskanta, "Heat transfer to impinging isothermal gas and flame jets," *Experimental Thermal and Fluid Science*, vol. 6, pp. 111-134, 1993.

[12] N. Chigier, "Preface," in *Combustion Measurements*, N. Chigier, Ed., New York: Hemisphere Publishing Corporation, 1991.

[13] I. Glassman, *Combustion*. New york: Academic Press Inc., 1977.

[14] Hydrogen Association. (2010, 11/02/2010). *Hydrogen Safety Fact Sheet*. Available: http://www.hydrogenassociation.org/general/factSheet_safety.pdf

[15] G. A. Karim, "Hydrogen as a spark ignition engine fuel," *International Journal of Hydrogen Energy*, vol. 28, pp. 569-577, 2003.

[16] E. Brandes, S. Dietlen, H. Hieronymus, I. U. Krause, B. Plewinsky, T. Redeker, et al., "Properties of Reactive Gases and Vapours," in *Handbook of Explosion Prevention and Protection*, M. Hattwig and H. Steen, Eds., Weinheim: Wiley-VCH, 2004, pp. 271-377.

[17] G. Bottrill, D. Cheyne, and G. Vijayaraghavan, *Practical Electrical Equipment and Installations in Hazardous Areas*. Oxford: Newnes, 2005.

[18] Texene LLC. (2013, 11/02/2013). *CROHMIQ Type D FIBC Static Dissipative Antistatic Bulk Bag Fabric*. Available: http://crohmiq.com/mie-fibc-minimum-ignition-energy-antistatic-big-bags.html

[19] Fire Safety Advice Centre. (2011, 07/08/2011). *Information about the Fire Triangle/Tetrahedron and Combustion*. Available: http://www.firesafe.org.uk/information-about-the-fire-triangletetrahedron-and-combustion/

[20] T. Dark and C. E. Baukal Jr., "Combustion Safety," in *The John Zink Combustion Handbook*, C. E. Baukal Jr., Ed., Boca Raton: CRC Press, 2001, pp. 327 - 350.

[21] A. E. Cote, *Fundamentals of Fire Protection*. Massachusetts: National Fire Protection Association Inc., 2004.

[22] K. Kuo, *Principles of Combustion*, 2nd ed. Hoboken, NJ: John Wiley and Sons, 2005.

[23] K. Alex Francis, R. Sreenivasan, and V. Raghavan, "Investigation of structures and reaction zones of methane-hydrogen laminar jet diffusion flames," *International Journal of Hydrogen Energy*, vol. 36, pp. 11183-11194, 2011.

[24] M. R. Davis and P. Rerkshanandana, "Schlieren measurement of turbulent structure in a diffusion flame," *Experimental Thermal and Fluid Science*, vol. 6, pp. 402-416, 1993.

[25] X. Jiang and K. H. Luo, "Dynamics and structure of transitional buoyant jet diffusion flames with side-wall effects," *Combustion and Flame*, vol. 133, pp. 29-45, 2003.

[26] V. R. Katta and W. M. Roquemore, "Role of inner and outer structures in transitional jet diffusion flame," *Combustion and Flame*, vol. 92, pp. 274-282, 1993.

[27] S. Noda, H. Mori, and Y. Hongo, "An investigation of flame base structures of turbulent lifted diffusion flames (1st report, measurements of temperature fields by the Rayleigh scattering method)," *Transactions of the Japan Society of Mechanical Engineers, Part B*, vol. 68, pp. 1295-1301, 2002.

[28] A. Su and Y. C. Liu, "Investigation of impinging diffusion flames with inert gas," *International Journal of Heat and Mass Transfer*, vol. 45, pp. 3251-3257, 2002.

[29] P. S. Kolhe and A. K. Agrawal, "Role of buoyancy on instabilities and structure of transitional gas jet diffusion flames," *Flow, Turbulence and Combustion*, vol. 79, pp. 343-360, 2007.

[30] B. W. Albers and A. K. Agrawal, "Schlieren analysis of an oscillating gas-jet diffusion flame," *Combustion and Flame*, vol. 119, pp. 84-94, 1999.

[31] J. Li and Y. Zhang, "Fuel variability effect on flickering frequency of diffusion flames," *Frontiers of Energy and Power Engineering in China*, vol. 3, pp. 134-140, 2009.

[32] T. S. Cheng, Y. C. Chang, Y. C. Chao, G. B. Chen, Y. H. Li, and C. Y. Wu, "An experimental and numerical study on characteristics of laminar premixed H2/CO/CH4/air flames," *International Journal of Hydrogen Energy*, vol. 36, pp. 13207-13217, 2011.

[33] C. Y. Wu, Y. C. Chao, T. S. Cheng, C. P. Chen, and C. T. Ho, "Effects of CO addition on the characteristics of laminar premixed CH4/air opposed-jet flames," *Combustion and Flame*, vol. 156, pp. 362-373, 2009.

[34] T. Foat, K. P. Yap, and Y. Zhang, "The visualization and mapping of turbulent premixed impinging flames," *Combustion and Flame*, vol. 125, pp. 839-851, 2001.

[35] B. Renou, A. Mura, E. Samson, and A. Boukhalfa, "Characterization of the local flame structure and the flame surface density for freely propagating premixed flames at various Lewis numbers," *Combustion Science and Technology*, vol. 174, pp. 143-179, 2002.

[36] Y. Ichikawa, Y. Otawara, H. Kobayashi, Y. Ogami, T. Kudo, M. Okuyama, et al., "Flame structure and radiation characteristics of CO/H2/CO2/air turbulent premixed flames at high pressure," *Proceedings of the Combustion Institute*, vol. 33, pp. 1543-1550, 2011.

[37] J. Kiefer, Z. S. Li, J. Zetterberg, X. S. Bai, and M. Aldén, "Investigation of local flame structures and statistics in partially premixed turbulent jet flames using simultaneous single-shot CH and OH planar laser-induced fluorescence imaging," *Combustion and Flame*, vol. 154, pp. 802-818, 2008.

[38] J. W. Park and C. B. Oh, "Flame structure and global flame response to the equivalence ratios of interacting partially premixed methane and hydrogen flames," *International Journal of Hydrogen Energy*, vol. 37, pp. 7877-7888, 2012.

[39] T. K. Mishra, A. Datta, and A. Mukhopadhyay, "Comparison of the structures of methane-air and propane-air partially premixed flames," *Fuel*, vol. 85, pp. 1254-1263, 2006.

[40] M. S. Mansour, "A study of turbulent partially premixed flames based on simultaneous imaging of velocity field and OH radical," *Combustion Science and Technology*, vol. 174, pp. 47-78, 2002.

[41] J. M. Cha and S. H. Sohrab, "Stabilization of premixed flames on rotating Bunsen burners," *Combustion and Flame*, vol. 106, pp. 467-477, 1996.

[42] D. Thibaut and S. Candel, "Numerical study of unsteady turbulent premixed combustion: Application to flashback simulation," *Combustion and Flame*, vol. 113, pp. 53-65, 1998.

[43] A. Nauert, P. Petersson, M. Linne, and A. Dreizler, "Experimental analysis of flashback in lean premixed swirling flames: Conditions close to flashback," *Experiments in Fluids*, vol. 43, pp. 89-100, 2007.

[44] Y. Wu, Y. Lu, I. S. Al-Rahbi, and G. T. Kalghatgi, "Prediction of the liftoff, blowout and blowoff stability limits of pure hydrogen and

hydrogen/hydrocarbon mixture jet flames," *International Journal of Hydrogen Energy*, vol. 34, pp. 5940-5945, 2009.

[45] M. Linck, K. H. Yu, and A. K. Gupta, "Dynamics of unconfined and confined methanol and kerosene spray flames," in *2nd International Energy Conversion Engineering Conference*, Providence, Rhode Island, 2004, pp. 38-46.

[46] R. A. Kach and A. A. Adamczyk, "Effects of thermal loading on pressure measurement in a combustion bomb," *Review of Scientific Instruments*, vol. 56, pp. 1274-1278, 1985.

[47] A. R. Noori and M. Rashidi, "Computational fluid dynamics study of heat transfer in a spark-ignition engine combustion chamber," *Journal of Heat Transfer*, vol. 129, pp. 609-616, 2007.

[48] The Engineering ToolBox. (2010, 16/06/2010). *Fuels - Higher Calorific Values*. Available: http://www.engineeringtoolbox.com/fuels-higher-calorific-values-d_169.html

[49] L. D. Berg, W. Bussman, and M. Henneke, "Fundamentals of Fluid Dynamics," in *The John Zinc Combustion Handbook*, C. E. Baukal Jr., Ed., Boca Raton: CRC Press LLC, 2001, pp. 117 - 155.

[50] M. Fairweather, J. K. Kilham, and A. Mohebi-Ashitiani, "Stagnation point heat transfer from turbulent methane-air flames," *Combustion Science and Technology*, vol. 35, pp. 225-238, 1984.

[51] I. Boxx, C. Heeger, R. Gordon, B. Böhm, M. Aigner, A. Dreizler, et al., "Simultaneous three-component PIV/OH-PLIF measurements of a turbulent lifted, C3H8-argon jet diffusion flame at 1.5 kHz repetition rate," *Proceedings of the Combustion Institute*, vol. 32, pp. 905-912, 2009.

[52] A. A. Burluka, A. M. T. El-Dein Hussin, C. G. W. Sheppard, K. Liu, and V. Sanderson, "Turbulent combustion of hydrogen-CO mixtures," *Flow, Turbulence and Combustion*, vol. 86, pp. 735-749, 2011.

[53] H. J. Moon, "Analysis of flame shapes in turbulent hydrogen jet flames with coaxial air," *Journal of Mechanical Science and Technology*, vol. 23, pp. 1743-1750, 2009.

[54] M. Shimura, T. Ueda, G. M. Choi, M. Tanahashi, and T. Miyauchi, "Simultaneous dual-plane CH PLIF, single-plane OH PLIF and dual-plane stereoscopic PIV measurements in methane-air turbulent premixed flames," *Proceedings of the Combustion Institute*, vol. 11, pp. 775-782, 2011.

[55] A. Veser, M. Kuznetsov, G. Fast, A. Friedrich, N. Kotchourko, G. Stern, et al., "The structure and flame propagation regimes in turbulent hydrogen jets," *International Journal of Hydrogen Energy*, vol. 36, pp. 2351-2359, 2011.

[56] G. Balakrishnan, M. D. Smooke, and F. A. Williams, "A numerical investigation of extinction and ignition limits in laminar nonpremixed counterflowing hydrogen-air streams for both elementary and reduced chemistry," *Combustion and Flame*, vol. 102, pp. 329-340, 1995.

[57] S. Chander and A. Ray, "Heat transfer characteristics of laminar methane/air flame impinging normal to a cylindrical surface," *Experimental Thermal and Fluid Science*, vol. 32, pp. 707-721, 2007.

[58] M. F. G. Cremers, M. J. Remie, K. R. A. M. Schreel, and L. P. H. De Goey, "Heat transfer mechanisms of laminar flames of hydrogen + oxygen," *Combustion and Flame*, vol. 139, pp. 39-51, 2004.

[59] M. Fairweather, J. K. Kilham, and S. Nawaz, "Stagnation point heat transfer from laminar, high temperature methane flames," *International Journal of Heat and Fluid Flow*, vol. 5, pp. 21-27, 1984.

[60] J. Natarajan and J. M. Seitzman, "Laminar flame properties of H2/CO mixtures," in *Synthesis Gas Combustion: Fundamentals and Applications*, T. Lieuwen, V. Yang, and R. Yetter, Eds., Boca Raton, FL: CRC Press, 2010, pp. 71-98.

[61] Z. Zhao, T. T. Wong, and C. W. Leung, "Impinging premixed butane/air circular laminar flame jet - Influence of impingement plate on heat transfer characteristics," *International Journal of Heat and Mass Transfer*, vol. 47, pp. 5021-5031, 2004.

[62] M. Thirumaleshwar, *Fundamentals of Heat and Mass Transfer*, Delhi: Dorling Kindersley (India) Pvt. Ltd, 2006.

[63] J. K. Kilham and N. Kirmani, "The effect of turbulence on premixed flame noise," *Symposium (International) on Combustion*, vol. 17, pp. 327-336, 1979.

[64] E. R. Subbarao and B. J. Cantwell, "Investigation of a co-flowing buoyant jet: experiments on the effect of Reynolds number and Richardson number," *Journal of Fluid Mechanics*, vol. 245, pp. 69-90, 1992.

[65] X. Q. Huang, C. W. Leung, C. K. Chan, and S. D. Probert, "Thermal characteristics of a premixed impinging circular laminar-flame jet with induced swirl," *Applied Energy*, vol. 83, pp. 401-411, 2006.

[66] L. L. Dong, C. S. Cheung, and C. W. Leung, "Heat transfer from an impinging premixed butane/air slot flame jet," *International Journal of Heat and Mass Transfer*, vol. 45, pp. 979-992, 2002.

[67] T. K. Ng, C. W. Leung, and C. S. Cheung, "Experimental investigation on the heat transfer of an impinging inverse diffusion flame," *International Journal of Heat and Mass Transfer*, vol. 50, pp. 3366-3375, 2007.

[68] S. Chander and A. Ray, "A combined experimental and numerical study of heat transfer characteristics for methane/air flame impinging normally on a flat surface," in *Ht2008: Proceeding of the Asme Summer Heat Transfer Conference*. vol. 3, New York: Amer Soc Mechanical Engineers, 2009, pp. 235-242.

[69] LMNO Engineering. (2003, 22/06/2010). *Gas Viscosity Calculator*. Available: http://www.lmnoeng.com/Flow/GasViscosity.htm

[70] P. A. Davidson, *Turbulence: An Introduction for Scientists and Engineers*. Oxford: Oxford university Press, 2004.

[71] H. Tennekes and J. L. Lumley, *A First Course in Turbulence*. Massachusetts: The Massachusetts Institute of Technology, 1972.

[72] P. Boudier, S. Henriot, T. Poinsot, and T. Baritaud, "A model for turbulent flame ignition and propagation in spark ignition engines," *Symposium (International) on Combustion*, vol. 24, pp. 503-510, 1992.

[73] Y. Xiong, "Investigation of a spark ignition flame kernel interacting with a laminar vortex toroid," PhD, Mechanical Engineering, North Carolina State Univeristy, 2002.

[74] H. Xiao, D. Makarov, J. Sun, and V. Molkov, "Experimental and numerical investigation of premixed flame propagation with distorted tulip shape in a closed duct," *Combustion and Flame*, vol. 159, pp. 1523-1538, 2012.

[75] S. S. Grossel, *Deflagration and Detonation Flame Arrestors*. New York: American Institute of Chemical Engineers, 2002.

[76] J. P. Holman, *Heat Transfer*, 8th ed. New York: McGraw-Hill, Inc., 1997.

[77] J. M. Samaniego and T. Mantel, "Fundamental mechanisms in premixed turbulent flame propagation via flame-vortex interactions. Part I: Experiment," *Combustion and Flame*, vol. 118, pp. 537-556, 1999.

[78] A. Lipatnikov, *Fundamentals of Premixed Turbulent Combustion*. Boca Raton: CRC Press, 2013.

[79] W. D. Hsieh, S. S. Hou, and T. H. Lin, "Methane flames in a jet impinging onto a wall," *Proceedings of the Combustion Institute*, vol. 30, pp. 267-275, 2005.

[80] Y. Zhang and K. N. C. Bray, "Characterization of impinging jet flames," *Combustion and Flame*, vol. 116, pp. 671-674, 1999.

[81] P. Singh, M. Henneke, J. D. Jayakaran, R. Hayes, and C. E. Baukal Jr, "Heat Transfer," in *The John Zink Combustion Handbook*, C. E. Baukal Jr, Ed., Boca Raton: CRC Press, 2001, pp. 69-114.

[82] M. F. Koseoglu and S. Baskaya, "Experimental and numerical investigation of natural convection effects on confined impinging jet heat transfer," *International Journal of Heat and Mass Transfer*, vol. 52, pp. 1326-1336, 2009.

[83] L. Burmeister, *Convective Heat Transfer*. New York: John Wiley and Sons, 1983.

[84] S. Chander and A. Ray, "Flame impingement heat transfer: A review," *Energy Conversion and Management*, vol. 46, pp. 2803-2837, 2005.

[85] J. M. Beér and N. A. Chigier, "Impinging jet flames," *Combustion and Flame*, vol. 12, pp. 575-586, 1968.

[86] C. O. Popiel, T. H. van der Meer, and C. J. Hoogendoorn, "Convective heat transfer on a plate in an impinging round hot gas jet of low Reynolds number," *International Journal of Heat and Mass Transfer*, vol. 23, pp. 1055-1068, 1980.

[87] A. Milson and N. A. Chigier, "Studies of methane and methane-air flames impinging on a cold plate," *Combustion and Flame*, vol. 21, pp. 295-305, 1973.

[88] G. K. Hargrave, M. Fairweather, and J. K. Kilham, "Forced convective heat transfer from premixed flames. -Part 1: Flame structure," *International Journal of Heat and Fluid Flow*, vol. 8, pp. 55-63, 1987.

[89] R. W. Lewis, P. Nithiarasu, and S. Kankanhalli, *Fundamentals of the Finite Element Method for Heat and Fluid Flow*. Chichester: John Wiley and Sons Ltd., 2004.

[90] B. V. N. R. Kumar and B. V. S. S. S. Prasad, "Computational flow and heat transfer of a row of circular jets impinging on a concave surface," *Heat and Mass Transfer*, vol. 44, pp. 667-678, 2008.

[91] K. Ichimiya, H. Matsumoto, and K. Okumura, "Heat transfer characteristics of an annular turbulent impinging jet," *Transactions of the Japan Society of Mechanical Engineers, Part B*, vol. 62, pp. 2737-2744, 1996.

[92] V. A. Chiriac and A. Ortega, "A numerical study of the unsteady flow and heat transfer in a transitional confined slot jet impinging on an isothermal surface," *International Journal of Heat and Mass Transfer*, vol. 45, pp. 1237-1248, 2002.

[93] L. Sang-Joon, L. Jung-Ho, and L. Dae-Hee, "Local heat transfer measurements from an elliptic jet impinging on a flat plate using liquid crystal," *International Journal of Heat and Mass Transfer*, vol. 37, pp. 967-976, 1994.

[94] E. Vishnuvardhanarao and M. K. Das, "Computational study of heat transfer in a conjugate turbulent wall jet flow with constant heat flux," *International Journal of Numerical Methods for Heat and Fluid Flow*, vol. 19, pp. 39-52, 2009.

[95] J. Y. San and W. Z. Shiao, "Effects of jet plate size and plate spacing on the stagnation Nusselt number for a confined circular air jet impinging on a flat surface," *International Journal of Heat and Mass Transfer*, vol. 49, pp. 3477-3486, 2006.

[96] T. H. van der Meer, "Stagnation point heat transfer from turbulent low reynolds number jets and flame jets," *Experimental Thermal and Fluid Science*, vol. 4, pp. 115-126, 1991.

[97] J. Lee and S. J. Lee, "The effect of nozzle aspect ratio on stagnation region heat transfer characteristics of elliptic impinging jet," *International Journal of Heat and Mass Transfer*, vol. 43, pp. 555-575, 2000.

[98] S. Chander and A. Ray, "An experimental and numerical study of stagnation point heat transfer for methane/air laminar flame impinging on a flat surface," *International Journal of Heat and Mass Transfer*, vol. 51, pp. 3595-3607, 2008.

[99] N. Celik, "Effects of the surface roughness on heat transfer of perpendicularly impinging co-axial jet," *Heat and Mass Transfer*, vol. 47, pp. 1209-1217, 2011.

[100] M. Ashok kumar and B. V. S. S. S. Prasad, "Computational flow and heat transfer of multiple circular jets impinging on a flat surface with effusion," *Heat and Mass Transfer*, vol. 47, pp. 1-12, 2011.

[101] C. E. Baukal Jr and B. Gebhart, "A review of empirical flame impingement heat transfer correlations," *International Journal of Heat and Fluid Flow*, vol. 17, pp. 386-396, 1996.

[102] M. F. G. Cremers, M. J. Remie, K. R. A. M. Schreel, and L. P. H. de Goey, "Thermochemical heat release of laminar stagnation flames of fuel and oxygen," *International Journal of Heat and Mass Transfer*, vol. 53, pp. 952-961, 2010.

[103] C. E. Baukal Jr and B. Gebhart, "Surface Condition Effects on Flame Impingement Heat Transfer," *Experimental Thermal and Fluid Science*, vol. 15, pp. 323-335, 1997.

[104] F. Soldatini, P. Mahonen, M. Saaranen, and C. S. Regazzoni, "Network Management Within an Architecture for Distributed Hierarchial Digital Surveillance Systems," in *Multimedia Video-Based Surveillance Systems: Requirements Issues and Solutions*, G. L. Foresti, P. Mahonen, and C. S. Regazzoni, Eds., Dordrecht: Kluwer Academic Publishers, 2000.

[105] A. Banerji and A. M. Ghosh, *Multimedia Technologies*. New Delhi: The Tata McGraw Hill Education Private Ltd., 2010.

[106] K. Balch. (1999) (2012, 1/11/2012). *High Frame Rate Electronic Imaging*. Available: http://www.motionvideoproducts.com/MVP%20papers/HSV%20White%20Paper.pdf

[107] Photron USA Inc. (2012, 1/11/2012). *Photron - High Speed Camera Products*. Available: http://www.photron.com/

[108] M. Raffel, C. Willert, and J. Kompenhans, *Particle Image Velocimetry: A Practical Guide*. Berlin: Springer, 1998.

[109] A. Moghaddas, K. Eisazadeh-Far, and H. Metghalchi, "Laminar burning speed measurement of premixed n-decane/air mixtures using spherically expanding flames at high temperatures and pressures," *Combustion and Flame*, vol. 159, pp. 1437-1443, 2012.

[110] D. L. Chen, J. H. Sun, Q. S. Wang, and Y. Liu, "Combustion behaviors and flame structure of methane/coal dust hybrid in a vertical rectangle chamber," *Combustion Science and Technology*, vol. 180, pp. 1518-1528, 2008.

[111] K. E. Far, F. Parsinejad, and H. Metghalchi, "Flame structure and laminar burning speeds of JP-8/air premixed mixtures at high temperatures and pressures," *Fuel*, vol. 89, pp. 1041-1049, 2010.

[112] S. Torii, B. K. Jung, and T. Yano, "Reignition phenomenon of high-speed hydrogen jet diffusion flame," *International Journal of Energy Research*, vol. 26, pp. 1045-1053, 2002.

[113] H. Gohari Darabkhani, Q. Wang, L. Chen, and Y. Zhang, "Impact of co-flow air on buoyant diffusion flames flicker," *Energy Conversion and Management*, vol. 52, pp. 2996-3003, 2011.

[114] H. W. Huang and Y. Zhang, "Analysis of the ignition process using a digital image and colour processing technique," *Measurement Science and Technology*, vol. 22, 075401, 2011.

[115] Y. Yu, Y. Zhou, D. Liu, and X. Lu, "Study on Explosion and Combustion Properties of Liquid Propellant Droplets in High Pressure," in *International*

Autumn Seminar on Propellants, Explosives and Pyrotecnics, Beijing, 2003, pp. 604-609.

[116] Y. Yang, X. He, L. An, and B. Nie, "Experimental study on width of flame front of methane/air explosion," in *International Symposium on Safety Science and Technology*, Beijing, 2004, pp. 1587-1591.

[117] N. Chigier, "Measurements in Combustion Systems," in *Combustion Measurements*, N. Chigier, Ed., New York: Hemisphere Publishing Corporation, 1991, pp. 1-20.

[118] W. Merzkirch, *Flow Visualization*, 2nd ed. Orlando: Academic Press, Inc., 1987.

[119] M. Aldén, J. Bood, Z. Li, and M. Richter, "Visualization and understanding of combustion processes using spatially and temporally resolved laser diagnostic techniques," Proceedings of the Combustion Institute, vol. 33, pp. 69-97, 2011.

[120] S. Jarvis and G. K. Hargrave, "A temporal PIV study of flame/obstacle generated vortex interactions within a semi-confined combustion chamber," *Measurement Science and Technology*, vol. 17, pp. 91-100, 2006.

[121] A. M. Steinberg and J. F. Driscoll, "Straining and wrinkling processes during turbulence-premixed flame interaction measured using temporally-resolved diagnostics," *Combustion and Flame*, vol. 156, pp. 2285-2306, 2009.

[122] K. Yamamoto, S. Inoue, H. Yamashita, D. Shimokuri, S. Ishizuka, and Y. Onuma, "PIV measurement and turbulence scale in turbulent combustion," *Heat Transfer - Asian Research*, vol. 35, pp. 501-512, 2006.

[123] M. Tanahashi, S. Murakami, G.-M. Choi, Y. Fukuchi, and T. Miyauchi, "Simultaneous CH–OH PLIF and stereoscopic PIV measurements of turbulent premixed flames," *Proceedings of the Combustion Institute*, vol. 30, pp. 1665-1672, 2005.

[124] R. P. Lindstedt, D. S. Luff, and J. H. Whitelaw, "Velocity fields of fuel lean premixed turbulent opposed jet flames," *Proceedings of the Combustion Institute*, vol. 31, pp. 1459-1466, 2007.

[125] N. Fujisawa and K. Nakashima, "Simultaneous measurement of three-dimensional flame contour and velocity field for characterizing the flickering motion of a dilute hydrogen flame," *Measurement Science and Technology*, vol. 18, pp. 2103-2110, 2007.

[126] Y. Cho, J. H. Kim, T. Cho, I. Moon, Y. Yoon, and C. Lee, "Analysis of Turbulent Fremixed Flame Structure using Simultaneous PIV-OH PLIF," *Journal of Visualization*, vol. 7, pp. 43-54, 2004.

[127] R. Siegel and J. Howell, *Thermal Radiation Heat Transfer*, 4th ed. New York: Taylor and Francis, 2002.

[128] M. Vollmer and K.-P. Möllmann, *Infrared thermal Imaging: Fundamentals, Research and Applications*. Weinheim: John Wiley and Sons, 2010.

[129] F. Kreith, R. M. Manglik, and M. S. Bohn. (2011, 18/09/2012). *Principles of Heat Transfer*, 7th ed. Stamford: Cengage Learning, 2011.

[130] M. F. Modest, *Radiative Heat Transfer*. New York: McGraw-Hill, 1993.

[131] M. M. Rathore and R. Kapuno, *Engineering Heat Transfer*. Sudbury: Jones and Bartlett Learning, LLC, 2011.

[132] F. P. Incropera and D. P. DeWitt, *Fundamentals of Heat and Mass Transfer*, 4th ed. New York: John Wiley and Sons, 1996.

[133] B. F. Levine, "Quantum-well infrared photodetectors," *Journal of Applied Physics*, vol. 74, pp. R1-R81, 1993.

[134] A. Rogalski, "Quantum Well Infrared Photoconductors in Infrared Detectors Technology," in *Intersubband Infrared Photodetectors*, V. Ryzhii, Ed., ed London: Worls Scientific Publishing Co. Pte. Ltd., 2003, pp. 1-66.

[135] Systems Flir, *ThermaCAM SC 3000* vol. 2012. Boston: FLIR systems, 2012.

[136] L. Wright. (2011, 7/01/2011). *EPSRC EIP Loan Pool - Section G: Thermal Imagers*. Available: http://www.eip.rl.ac.uk/sectg.htm#FLIRThermaCAMSC640

[137] R. A. Wood, "Monolithic Silicon Microbolometer Arrays," in *Uncooled Infrared Imaging Systems*. vol. 47, P. W. Kruse and D. D. Skatrud, Eds., London: Academic Press, 1997, pp. 45-122.

[138] R. A. Wood, "Uncooled Microbolometer Infrared Sensor Arrays," in *Infrared Detectors and Emitters: Materials and Devices*, P. Capper and C. T. Elliott, Eds., Dordrecht: Kluwer Academic Publishers, 2001, pp. 149-176..

[139] J. Boyd, "Using hands-free thermal imaging cameras," *Fire Engineering*, vol. 160, pp. 95-97, 2007.

[140] P. J. Riggan and J. W. Hoffman, "Field applications of a multi-spectral, thermal imaging radiometer," *IEEE Aerospace Applications Conference Proceedings*, vol. 3, pp. 443-449, 1999.

[141] F. Amon, A. Hamins, and J. Rowe, "First responder thermal imaging cameras: Establishment of representative performance testing conditions," *Proceedings of the Thermosense XXVIII, Proceedings of SPIE*, vol. 6205, 62050Y, 2006.

[142] E. F. J. Ring, "Beyond human vision: the development and applications of infrared thermal imaging," *The Imaging Science Journal*, vol. 58, pp. 254-260, 2010.

[143] N. N. Akif'eva, B. P. Zhilkin, R. S. Zaikov, A. Y. Kisel'Nikov, and V. Y. Mirenskii, "On thermal imaging application to control burning processes," *Automation and Remote Control*, vol. 71, pp. 1946-1954, 2010.

[144] G. C. Stanton and W. A. Ellingson, "In-Service Infrared Thermal Imaging of Coal-Gasification Plant Components.," Argonne National Lab., Lemont: US Energy Research and Development Administration, 1977.

[145] V. Vijayan and A. K. Gupta, "Combustion and heat transfer at meso-scale with thermal recuperation," *Applied Energy*, vol. 87, pp. 2628-2639, 2010.

[146] C. J. Evans and D. C. Kyritsis, "Experimental investigation of the effects of flame phenomenology on the wall temperature distribution of mesoscale nonadiabatic ducts," *Combustion Science and Technology*, vol. 183, pp. 847-867, 2011.

[147] D. Manca and M. Rovaglio, "Infrared thermographic image processing for the operation and control of heterogeneous combustion chambers," *Combustion and Flame,* vol. 130, pp. 277-297, 2002.

[148] M. Nirmalkumar, V. Katti, and S. V. Prabhu, "Local heat transfer distribution on a smooth flat plate impinged by a slot jet," *International Journal of Heat and Mass Transfer,* vol. 54, pp. 727-738, 2011.

[149] V. Katti and S. V. Prabhu, "Experimental study and theoretical analysis of local heat transfer distribution between smooth flat surface and impinging air jet from a circular straight pipe nozzle," *International Journal of Heat and Mass Transfer,* vol. 51, pp. 4480-4495, 2008.

[150] W. T. Chan, "Modelling and Measurements of Turbulent Flames," PhD, Mechanical Engineering, The University of Manchester Institute of Science and Technology, Manchester, 2000.

[151] D. Blunck, S. Basu, Y. Zheng, V. Katta, and J. Gore, "Simultaneous water vapor concentration and temperature measurements in unsteady hydrogen flames," *Proceddings of the Combustion Institute,* vol. 32, pp. 2527-2534, 2009.

[152] W. M. G. Malalasekera, H. K. Versteeg, and K. Gilchrist, "A review of research and an experimental study on the pulsation of buoyant diffusion flames and pool fires," *Fire and Materials,* vol. 20, pp. 261-271, 1996.

[153] P. A. Strakey and G. Eggenspieler, "Development and validation of a thickened flame modeling approach for large eddy simulation of premixed combustion," *Journal of Engineering for Gas Turbines and Power-transactions of The Asme,* vol. 132, pp. 833-844, 2009.

[154] ASTM Committee E-20, *Manual on the use of Thermocouples in Temperature Measurement*. Philadelphia: American Society for Testing and Materials, 1981.

[155] D. D. Pollock, *The Theory and Properties of Thermocouple elements*. Philadelphia: American Society for Testing and Materials, 1975.

[156] G. S. Settles, *Schlieren and Shadowgraph Techniques: Visualizing Phenomena in Transport Media*. Berlin: Springer-Verlag, 2001.

[157] K. Phalnikar, R. Kumar, and F. Alvi, "Experiments on free and impinging supersonic microjets," *Experiments in Fluids,* vol. 44, pp. 819-830, 2008.

[158] Q. Wang and Y. Zhang, "High speed stereoscopic shadowgraph imaging and its digital 3D reconstruction," *Measurement Science and Technology,* vol. 22, 065302, 2011.

[159] N. P. Sullivan, M. C. Branch, M. Strobel, and M. Ulsh, "Transport issues when impinging laminar premixed flame jets on a rotating cylinder," *Symposium (International) on Combustion,* vol. 28, pp. 1405-1411, 2000.

[160] Q. Wang, H. Gohari Darabkhani, L. Chen, and Y. Zhang, "Vortex dynamics and structures of methane/air jet diffusion flames with air coflow," *Experimental Thermal and Fluid Science,* vol. 37, pp. 84-90, 2012.

[161] V. P. Karpov, A. N. Lipatnikov, and P. Wolanski, "Finding the markstein number using the measurements of expanding spherical laminar flames," *Combustion and Flame,* vol. 109, pp. 436-448, 1997.

[162] M. Ilbas, A. P. Crayford, I. Yilmaz, P. J. Bowen, and N. Syred, "Laminar-burning velocities of hydrogen-air and hydrogen-methane-air mixtures: An experimental study," *International Journal of Hydrogen Energy,* vol. 31, pp. 1768-1779, 2006.

[163] F. Liu, X. Bao, J. Gu, and R. Chen, "Onset of cellular instabilities in spherically propagating hydrogen-air premixed laminar flames," *International Journal of Hydrogen Energy,* vol. 37, pp. 11458-11465, 2012.

[164] C. K. Chan, "Collision of a shock wave with obstacles in a combustible mixture," *Combustion and Flame,* vol. 100, pp. 341-348, 1995.

[165] J. Kompenhans, "Modern image based experimental methods for applications in fluid dynamics," in *Flow Phenomena in Nature: Inspiration, Learning and Application*. vol. 2, R. Liebe, Ed., Gateshead: WIT Press, 2007, pp. 669-697.

[166] M. Stegmeir and T. Strand, "Introduction to PIV: Fundamentals, Hardware Control, and Collecting Valuable Data (Part I)," in *TSI Webinar Training Series*, TSI Fluids Team, Ed., 2010.

[167] TSI Inc. (2006, 4/10/2012). *Laser Diagnostics: Seed particles for LDV and PIV*. Available: http://www.tsi.com/uploadedFiles/Product_Information/Literature/Spec_Sheets/SeedParticles_2980461.pdf

[168] B. J. McKeon, G. Comte-Bellot, j. Foss, J. Westerweel, F. Scarano, C. Tropea, *et al.*, "Velocity, Vorticity and Mach Number," in *Springer Handbook of Experimental Fluid Mechanics*. vol. 1, C. Tropea, A. Yarin, and J. Foss, Eds., Berlin: Springer, 2007, pp. 215-473.

[169] A. Melling, "Tracer particles and seeding for particle image velocimetry," *Measurement Science and Technology,* vol. 8, pp. 1406-1416, 1997.

[170] SCITEK Consultants Ltd. (2012, 4/10/2012). *Power Seeders*. Available: http://www.scitekconsultants.co.uk/7/Powder-Seeders

[171] J. M. Foucaut, S. Coudert, and M. Stanislas, "Unsteady characteristics of near-wall turbulence using high repetition stereoscopic particle image velocimetry (PIV)," *Measurement Science and Technology,* vol. 20, 074004, 2009.

[172] V. Di Sarli, A. Di Benedetto, G. Russo, S. Jarvis, E. J. Long, and G. K. Hargrave, "Large eddy simulation and PIV measurements of unsteady premixed flames accelerated by obstacles," *Flow, Turbulence and Combustion,* vol. 83, pp. 227-250, 2009.

[173] D. Zhang, H. Qu, J. Lan, J. Chen, and Y. Xie, "Flow and heat transfer characteristics of single jet impinging on protrusioned surface," *International Journal of Heat and Mass Transfer,* vol. 58, pp. 18-28, 2013.

[174] A. Koched, M. Pavageau, and F. Aloui, "Vortex structure in the wall region of an impinging plane jet," *Journal of Applied Fluid Mechanics,* vol. 4, pp. 61-69, 2011.

[175] M. J. Tummers, J. Jacobse, and S. G. J. Voorbrood, "Turbulent flow in the near field of a round impinging jet," *International Journal of Heat and Mass Transfer,* vol. 54, pp. 4939-4948, 2011.

[176] M. El Hassan, H. H. Assoum, V. Sobolik, J. Vétel, K. Abed-Meraim, A. Garon, *et al.*, "Experimental investigation of the wall shear stress and the vortex dynamics in a circular impinging jet," *Experiments in Fluids,* vol. 52, pp. 1475-1489, 2012.

[177] K. J. Hammad and I. M. Milanovic, "A time-resolved PIV study of vortical structures in the near-wall region of an impinging round jet," in *ASME International Mechanical Engineering Congress and Exposition,* Florida, 2010, pp. 371-381.

[178] G. L. Pellett, K. M. Isaac, W. M. Humphreys Jr, L. R. Gartrell, W. L. Roberts, C. L. Dancey, *et al.*, "Velocity and thermal structure, and strain-induced extinction of 14 to 100% hydrogen-air counterflow diffusion flames," *Combustion and Flame,* vol. 112, pp. 575-592, 1998.

[179] E. J. Stevens, K. N. C. Bray, and B. Lecordier, "Velocity and scalar statistics for premixed turbulent stagnation flames using PIV," *Symposium (International) on Combustion,* vol. 1, pp. 949-955, 1998.

[180] L. F. G. Geers, M. J. Tummers, and K. HanjaliÄ‡, "Experimental investigation of impinging jet arrays," *Experiments in Fluids,* vol. 36, pp. 946-958, 2004.

[181] P. Gulati, V. Katti, and S. V. Prabhu, "Influence of the shape of the nozzle on local heat transfer distribution between smooth flat surface and impinging air jet," *International Journal of Thermal Sciences,* vol. 48, pp. 602-617, 2009.

[182] N. S. Kim and A. Giovannini, "Experimental study of turbulent round jet flow impinging on a square cylinder laid on a flat plate," *International Journal of Heat and Fluid Flow,* vol. 28, pp. 1327-1339, 2007.

[183] Y. Ozmen and E. Baydar, "Flow structure and heat transfer characteristics of an unconfined impinging air jet at high jet Reynolds numbers," *Heat and Mass Transfer,* vol. 44, pp. 1315-1322, 2008.

[184] M. Yaga, K. Ueda, T. Ohshiro, I. Senaha, and K. Oyakawa, "Experimental and three-dimensional numerical study on under-expanded impinging jets," *Journal of Thermal Science,* vol. 9, pp. 316-321, 2000.

[185] G. K. Agrawal, S. Chakraborty, and S. K. Som, "Heat transfer characteristics of premixed flame impinging upwards to plane surfaces inclined with the flame jet axis," *International Journal of Heat and Mass Transfer,* vol. 53, pp. 1899-1907, 2010.

[186] S. Chander and A. Ray, "Experimental and numerical study on the occurrence of off-stagnation peak in heat flux for laminar methane/air flame impinging on a

flat surface," *International Journal of Heat and Mass Transfer,* vol. 54, pp. 1179-1186, 2011.

[187] F. Dabireau, B. Cuenot, O. Vermorel, and T. Poinsot, "Interaction of flames of H2 + O2 with inert walls," *Combustion and Flame,* vol. 135, pp. 123-133, 2003.

[188] G. K. Hargrave, M. Fairweather, and J. K. Kilham, "Forced convective heat transfer from premixed flames --Part 2: Impingement heat transfer," *International Journal of Heat and Fluid Flow,* vol. 8, pp. 132-138, 1987.

[189] G. K. Malikov, D. L. Lobanov, K. Y. Malikov, V. G. Lisienko, R. Viskanta, and A. G. Fedorov, "Direct flame impingement heating for rapid thermal materials processing," *International Journal of Heat and Mass Transfer,* vol. 44, pp. 1751-1758, 2001.

[190] D. Mira Martinez, X. Jiang, C. Moulinec, and D. R. Emerson, "Numerical investigation of the effects of fuel variability on the dynamics of syngas impinging jet flames," *Fuel,* vol. 103, pp. 646-662, 2013.

[191] D. Mira Martinez and X. Jiang, "Numerical investigations of a hydrogen impinging flame with different finite-rate chemical kinetic mechanisms," *Fuel,* vol. 109, pp. 285-296, 2013.

[192] R. Owston, V. Magi, and J. Abraham, "Interactions of hydrogen flames with walls: Influence of wall temperature, pressure, equivalence ratio, and diluents," *International Journal of Hydrogen Energy,* vol. 32, pp. 2094-2104, 2007.

[193] K. K. J. Ranga Dinesh, X. Jiang, and J. A. Van Oijen, "Numerical simulation of hydrogen impinging jet flame using flamelet generated manifold reduction," *International Journal of Hydrogen Energy,* vol. 37, pp. 4502-4515, 2012.

[194] K. K. J. Ranga Dinesh, X. Jiang, J. A. Van Oijen, R. J. M. Bastiaans, and L. P. H. De Goey, "Influence of fuel variability on the characteristics of impinging non-premixed syngas burning," *Proceedings of the Combustion Institute,* vol. 34, pp. 3219-3229, 2013.

[195] M. J. Remie, M. F. G. Cremers, K. R. A. M. Schreel, and L. P. H. de Goey, "Analysis of the heat transfer of an impinging laminar flame jet," *International Journal of Heat and Mass Transfer,* vol. 50, pp. 2816-2827, 2007.

[196] M. J. Remie, G. Särner, M. F. G. Cremers, A. Omrane, K. R. A. M. Schreel, L. E. M. Aldén, *et al.*, "Heat-transfer distribution for an impinging laminar flame jet to a flat plate," *International Journal of Heat and Mass Transfer,* vol. 51, pp. 3144-3152, 2008.

[197] T. Takagi, Y. Yoshikawa, K. Yoshida, M. Komiyama, and S. Kinoshita, "Studies on strained non-premixed flames affected by flame curvature and preferential diffusion," *Symposium (International) on Combustion,* vol. 26, pp. 1103-1110, 1996.

[198] D. G. Vlachos, L. D. Schmidt, and R. Aris, "Ignition and extinction of flames near surfaces: Combustion of H2 in air," *Combustion and Flame,* vol. 95, pp. 313-335, 1993.

[199] W. G. Weng and Y. Hasemi, "Heat transfer to an unconfined ceiling from an impinging buoyant diffusion flame," *Heat and Mass Transfer,* vol. 42, pp. 652-659, 2006.

[200] B. P. Xu, J. X. Wen, and V. H. Y. Tam, "The effect of an obstacle plate on the spontaneous ignition in pressurized hydrogen release: A numerical study," *International Journal of Hydrogen Energy,* vol. 36, pp. 2637-2644, 2011.

[201] K. Yoshida and T. Takagi, "Transient local extinction and reignition behavior of diffusion flames affected by flame curvature and preferential diffusion," *Symposium (International) on Combustion,* vol. 1, pp. 685-692, 1998.

[202] C. E. Baukal and B. Gebhart, "A review of semi-analytical solutions for flame impingement heat transfer," *International Journal of Heat and Mass Transfer,* vol. 39, pp. 2989-3002, 1996.

[203] C. E. Baukal and B. Gebhart, "Heat transfer from oxygen-enhanced/natural gas flames impinging normal to a plane surface," *Experimental Thermal and Fluid Science,* vol. 16, pp. 247-259, 1998.

[204] S. Chander and A. Ray, "Heat transfer characteristics of three interacting methane/air flame jets impinging on a flat surface," *International Journal of Heat and Mass Transfer,* vol. 50, pp. 640-653, 2007.

[205] L. L. Dong, C. W. Leung, and C. S. Cheung, "Heat transfer characteristics of premixed butane/air flame jet impinging on an inclined flat surface," *Heat and Mass Transfer,* vol. 39, pp. 19-26, 2002.

[206] L. L. Dong, C. W. Leung, and C. S. Cheung, "Heat transfer of a row of three butane/air flame jets impinging on a flat plate," *International Journal of Heat and Mass Transfer,* vol. 46, pp. 113-125, 2003.

[207] L. L. Dong, C. W. Leung, and C. S. Cheung, "Heat transfer and wall pressure characteristics of a twin premixed butane/air flame jets," *International Journal of Heat and Mass Transfer,* vol. 47, pp. 489-500, 2004.

[208] L. L. Dong, C. S. Cheung, and C. W. Leung, "Heat transfer characteristics of an impinging inverse diffusion flame jet. Part II: Impinging flame structure and impingement heat transfer," *International Journal of Heat and Mass Transfer,* vol. 50, pp. 5124-5138, 2007.

[209] D. Durox, T. Schuller, and S. Gandel, "Self-induced instability of a premixed jet flame impinging on a plate," *Proceedings of the Combustion Institute,* vol. 29, pp. 69-75, 2002.

[210] S.-S. Hou and Y.-C. Ko, "Effects of heating height on flame appearance, temperature field and efficiency of an impinging laminar jet flame used in domestic gas stoves," *Energy Conversion and Management,* vol. 45, pp. 1583-1595, 2004.

[211] S. S. Hou and Y. C. Ko, "Influence of oblique angle and heating height on flame structure, temperature field and efficiency of an impinging laminar jet flame," *Energy Conversion and Management,* vol. 46, pp. 941-958, 2005.

[212] H. W. Huang, J. Yang, Q. Wang, and Y. Zhang, "Variation of hydrocarbon compositions and ignition locations on the radiative flame initiation characteristics through multi-dimensional DFCD incorporated image analysis," *Fuel,* vol. 103, pp. 334-346, 2013.

[213] V. R. Katta, C. D. Carter, G. J. Fiechtner, W. M. Roquemore, J. R. Gord, and J. C. Rolon, "Interaction of a vortex with a flat flame formed between opposing jets of hydrogen and air," *Symposium (International) on Combustion,* vol. 1, pp. 587-594, 1998.

[214] V. R. Katta, T. R. Meyer, M. S. Brown, J. R. Gord, and W. M. Roquemore, "Extinction criterion for unsteady, opposing-jet diffusion flames," *Combustion and Flame,* vol. 137, pp. 198-221, 2004.

[215] S. Kim, H. J. Lee, J. H. Park, and I. S. Jeung, "Effects of a wall on the self-ignition patterns and flame propagation of high-pressure hydrogen release through a tube," *Proceedings of the Combustion Institute,* vol. 34, pp. 2049-2056, 2013.

[216] L. C. Kwok, "Heat transfer characteristics of slot and round premixed impinging flame jets," *Experimental Heat Transfer,* vol. 16, pp. 111-137, 2003.

[217] L. C. Kwok, C. W. Leung, and C. S. Cheung, "Heat transfer characteristics of an array of impinging pre-mixed slot flame jets," *International Journal of Heat and Mass Transfer,* vol. 48, pp. 1727-1738, 2005.

[218] H. B. Li, H. S. Zhen, C. W. Leung, and C. S. Cheung, "Effects of plate temperature on heat transfer and emissions of impinging flames," *International Journal of Heat and Mass Transfer,* vol. 53, pp. 4176-4184, 2010.

[219] U. Makmool, S. Jugjai, S. Tia, Y. Laoonual, P. Vallikul, and B. Fungtammasan, "Laser-based investigations of flow fields and OH distributions in impinging flames of domestic cooker-top burners," *Fuel,* vol. 90, pp. 1024-1035, 2011.

[220] J. W. Mohr, J. Seyed-Yagoobi, and R. H. Page, "Combustion measurements from an impinging Radial Jet Reattachment flame," *Combustion and Flame,* vol. 106, pp. 69-80, 1996.

[221] W. B. Ng and Y. Zhang, "Stereoscopic imaging and computer vision of impinging fires by a single camera with a stereo adapter," *International Journal of Imaging Systems and Technology,* vol. 15, pp. 114-122, 2005.

[222] M. Niu, Z. Yan, Q. Guo, Q. Liang, G. Yu, F. Wang, *et al.*, "Experimental measurement of gas concentration distribution in an impinging entrained-flow gasifier," *Fuel Processing Technology,* vol. 89, pp. 1060-1068, 2008.

[223] G. Singh, S. Chander, and A. Ray, "Heat transfer characteristics of natural gas/air swirling flame impinging on a flat surface," *Experimental Thermal and Fluid Science,* vol. 41, pp. 165-176, 2012.

[224] S. G. Tuttle, B. W. Webb, and M. Q. McQuay, "Convective heat transfer from a partially premixed impinging flame jet. Part I: Time-averaged results," *International Journal of Heat and Mass Transfer,* vol. 48, pp. 1236-1251, 2005.

[225] S. G. Tuttle, B. W. Webb, and M. Q. McQuay, "Convective heat transfer from a partially premixed impinging flame jet. Part II: Time-resolved results," *International Journal of Heat and Mass Transfer,* vol. 48, pp. 1252-1266, 2005.

[226] J. A. Wehrmeyer, Z. Cheng, D. M. Mosbacher, R. W. Pitz, and R. Osborne, "Opposed jet flames of lean or rich premixed propane-air reactants versus hot products," *Combustion and Flame,* vol. 128, pp. 232-241, 2002.

[227] Z. Zhao, T. T. Wong, C. W. Leung, and S. D. Probert, "Wok design: thermal-performance influencing parameters," *Applied Energy,* vol. 83, pp. 387-400, 2006.

[228] Z. Zhao, D. W. Yuen, C. W. Leung, and T. T. Wong, "Thermal performance of a premixed impinging circular flame jet array with induced-swirl," *Applied Thermal Engineering,* vol. 29, pp. 159-166, 2009.

[229] H. S. Zhen, C. W. Leung, and C. S. Cheung, "Heat transfer from a turbulent swirling inverse diffusion flame to a flat surface," *International Journal of Heat and Mass Transfer,* vol. 52, pp. 2740-2748, 2009.

[230] H. S. Zhen, C. W. Leung, and C. S. Cheung, "Heat transfer characteristics of an impinging premixed annular flame jet," *Applied Thermal Engineering,* vol. 36, pp. 386-392, 2012.

[231] E. P. Keramida, H. H. Liakos, M. A. Founti, A. G. Boudouvis, and N. C. Markatos, "Radiative heat transfer in natural gas-fired furnaces," *International Journal of Heat and Mass Transfer,* vol. 43, pp. 1801-1809, 2000.

[232] L. J. Saeys, M. Zumer, and J. M. Dealy, "Criteria for recirculation in confined jet flames," *Combustion and Flame,* vol. 17, pp. 367-377, 1971.

[233] C. E. J. Baukal, *Heat Transfer in Industrial Combustion*. Boca Raton: CRC Press LLC, 2000.

[234] R. Conolly and R. M. Davies, "A study of convective heat transfer from flames," *International Journal of Heat and Mass Transfer,* vol. 15, pp. 2155-2172, 1972.

[235] M. Fishenden and O. Saunders, *An Introduction to Heat Transfer*. Oxford: Clarendon Press, 1957.

[236] C. P. Randolph and M. J. Overholser, "The Emissivity of Oxidized Metallic Surfaces," *Physical Review,* vol. 2, pp. 144-152, 1913.

[237] Everest Interscience Inc. (2013, 10/3/2013). *Theory of Emissivity*. Available: http://www.ictinternational.com.au/brochures/everest/emissivity-theory.pdf

[238] Mikron Instrument Company Inc. (2013, 10/3/2013). *Table of Emissivity of Various Surfaces*. Available: http://www-eng.lbl.gov/~dw/projects/DW4229_LHC_detector_analysis/calculations/emissivity2.pdf

[239] I. M. Taufiq, A. W. Mazlan, and A. M. Ibthisham, "Characteristics of impinging reacting jet flow on flat surface," in *The 10th Asian International Conference on Fluid Machinery*, Kuala Lumpur: 2010, pp. 1050-1056.

[240] K. Mizuno, R. Mital, and R. Viskanta, "An experimental study of premixed flame impingement heat transfer," *American Society of Mechanical Engineers, Heat Transfer Division, (Publication) HTD,* vol. 335, pp. 245-252, 1996.

[241] S. Chander and A. Ray, "Investigation of effect of burner diameter on heat transfer characteristics of methane/ air flame impinging on a flat surface," *ASME 2005 Summer Heat Transfer Conference collocated with the ASME 2005 Pacific Rim Technical Conference and Exhibition on Integration and Packaging of MEMS, NEMS, and Electronic Systems,* San Francisco: 2005, pp. 213-220.

[242] C. Saha, R. Ganguly, and A. Datta, "Heat transfer and emission characteristics of impinging rich methane and ethylene jet flames," *Experimental Heat Transfer,* vol. 21, pp. 169-187, 2008.

[243] S. Jerzembeck, N. Peters, P. Pepiot-Desjardins, and H. Pitsch, "Laminar burning velocities at high pressure for primary reference fuels and gasoline: Experimental and numerical investigation," *Combustion and Flame,* vol. 156, pp. 292-301, 2009.

[244] Z. Huang, Y. Zhang, K. Zeng, B. Liu, Q. Wang, and D. Jiang, "Measurements of laminar burning velocities for natural gas-hydrogen-air mixtures," *Combustion and Flame,* vol. 146, pp. 302-311, 2006.

[245] X. Wu, Z. Huang, C. Jin, X. Wang, B. Zheng, Y. Zhang, *et al.*, "Measurements of laminar burning velocities and Markstein lengths of 2, 5dimethylfuran-air-diluent premixed flames," *Energy and Fuels,* vol. 23, pp. 4355-4362, 2009.

[246] E. Hu, Z. Huang, J. He, C. Jin, H. Miao, and X. Wang, "Measurement of laminar burning velocities and analysis of flame stabilities for hydrogen-air-diluent premixed mixtures," *Chinese Science Bulletin,* vol. 54, pp. 846-857, 2009.

[247] D. Bradley, M. Lawes, and K. Liu, "Turbulent flame speeds in ducts and the deflagration/detonation transition," *Combustion and Flame,* vol. 154, pp. 96-108, 2008.

[248] M. F. Ivanov, A. D. Kiverin, and M. A. Liberman, "Flame acceleration and DDT of hydrogen-oxygen gaseous mixtures in channels with no-slip walls," *International Journal of Hydrogen Energy,* vol. 36, pp. 7714-7727, 2011.

[249] C. Y. Wu, Y. H. Li, and T. W. Chang, "Effects of CO addition on the propagation characteristics of laminar CH 4 triple flame," *Combustion and Flame,* vol. 159, pp. 2806-2816, 2012.

[250] S. H. Chung, "Stabilization, propagation and instability of tribrachial triple flames," *Proceedings of the Combustion Institute,* vol. 31, pp. 877-892, 2007.

[251] J. Lee, S. H. Won, S. H. Jin, S. H. Chung, O. Fujita, and K. Ito, "Propagation speed of tribrachial (triple) flame of propane in laminar jets under normal and micro gravity conditions," *Combustion and Flame,* vol. 134, pp. 411-420, 2003.

[252] R. W. Schefer, M. Namazian, E. E. J. Filtopoulos, and J. Kelly, "Temporal evolution of turbulence/chemistry interactions in lifted, turbulent-jet flames," *Symposium (International) on Combustion,* vol. 25, pp. 1223-1231, 1994.

[253] E. Mastorakos, "Ignition of turbulent non-premixed flames," *Progress in Energy and Combustion Science,* vol. 35, pp. 57-97, 2009.

[254] A. Upatnieks, J. F. Driscoll, and S. L. Ceccio, "Cinema particle imaging velocimetry time history of the propagation velocity of the base of a lifted turbulent jet flame," *Proceedings of the Combustion Institute,* vol. 29, pp. 1897-1903, 2002.

[255] J. Oh, Q. S. Khan, and Y. Yoon, "Nitrogen dilution effect on flame stability in a lifted non-premixed turbulent hydrogen jet with coaxial air," *Fuel,* vol. 89, pp. 1492-1498, 2010.

[256] U. D. Lee, C. S. Yoo, J. H. Chen, and J. H. Frank, "Effects of H2O and NO on extinction and re-ignition of vortex-perturbed hydrogen counterflow flames," *Proceedings of the Combustion Institute,* vol. 32, pp. 1059-1066, 2009.

[257] Y. Zhang, K. N. C. Bray, and B. Rogg, "Temporally and spatially resolved investigation of flame propagation and extinction in the vicinity of walls," *Combustion Science and Technology,* vol. 113-114, pp. 255-271, 1996.

[258] W. T. Ashurst and I. G. Shepherd, "Flame front curvature distributions in a turbulent premixed flame zone," *Combustion Science and Technology,* vol. 124, pp. 115-144, 1997.

[259] Aalborg. (2013, 14/02/2013). *GFC Mass Flow Controller: Aalborg, Manufacturer of High Quality Flow Instrumentation*. Available: http://www.aalborg.com/index.php/main_page/product_overview/id_product_overview/21

[260] Casio America. Inc. (2012, 20/08/2012). *EX-F1 - High-Speed - Best, Compact, High Speed, GPS, Digital Camera | CASIO America, Inc.* Available: http://www.casio.com/products/archive/Digital_Cameras/High-Speed/ex-f1/

[261] C. Engelhard, A. Scheffer, T. Maue, G. M. Hieftje, and W. Buscher, "Application of infrared thermography for online monitoring of wall temperatures in inductively coupled plasma torches with conventional and low-flow gas consumption," *Spectrochimica Acta - Part B Atomic Spectroscopy,* vol. 62, pp. 1161-1168, 2007.

[262] A. J. Ede, *An Introduction to Heat Transfer Principles and Calculations* vol. 2. Oxford: Pergamon Press, 1967.

[263] P. Sagaut, *Large Eddy Simulation for Incompressible Flows: An Introduction*, 2nd ed. Berlin: Springer, 2006.

[264] X. Jiang and C.-H. Lai, *Numerical Techniques for Direct and Large-Eddy Simulations*. Boca Raton: CRC Press, 2009.

[265] P. A. Rock, *Chemical Thermodynamics*. Sausalito: University science Books, 1983.

[266] C. Morley. (2005, 30/10/2012). *Gaseq Chemical Equilibrium Program*. Available: www.gaseq.co.uk

[267] CHEMKIN. (2011, 30/10/2012). *CHEMKIN Tutorials Manual*. Available: http://www.ems.psu.edu/~radovic/ChemKin_Tutorial_2-3-7.pdf

[268] J. Seitzman. (2005, 18/3/2013). *Flame Structure and Flame Speed Measurements*. Available: http://soliton.ae.gatech.edu/people/jseitzma/classes/ae6766/FlameStructureSpeedMeasurements.pdf

[269] R. J. Kee, J. F. Grcar, J. A. Miller, and E. Meeks, (1998, 19/3/2013). *PREMIX: A FORTRAN Program for Modeling Steady Laminar One-Dimensional Premixed Flames*, San Diego: Reaction Design, 1998. Available: http://www.scc.acad.bg/ncsa/articles/library/Computational%20%20Fluid%20Dynamics/PREMIX%20code%20Sandia.pdf

[270] B. Serauskas, M. Frenklach, T. Bowman, G. Smith, and B. Gardiner. (2013, 19/3/2013). *Project Overview*. Available: http://www.me.berkeley.edu/gri_mech/overview.html

[271] H. Wang, X. You, A. V. Joshi, S. G. Davis, A. Laskin, F. Egolfopoulos, *et al.* (2007, 19/3/2013). *USC Mech Version II. High-Temperature Combustion Reaction Model of H2/CO/C1-C4 Compounds*. Available: http://ignis.usc.edu/Mechanisms/USC-Mech%20II/USC_Mech%20II.htm

[272] G. Maag, C. Falter, and A. Steinfeld, "Temperature of a quartz/sapphire window in a solar cavity-receiver," *Journal of Solar Energy Engineering, Transactions of the ASME*, vol. 133, 014501, 2011.

[273] W. Potze, "Radiation heat transfer in axisymmetric quartz glass tubes," *Journal of Quantitative Spectroscopy and Radiative Transfer*, vol. 84, pp. 575-586, 2004.

[274] Y. Wu, I. S. Al-Rahbi, Y. Lu, and G. T. Kalghatgi, "The stability of turbulent hydrogen jet flames with carbon dioxide and propane addition," *Fuel*, vol. 86, pp. 1840-1848, 2007.

[275] S. Mukhopadhyay and J. Abraham, "Influence of compositional stratification on autoignition in n-heptane/air mixtures," *Combustion and Flame*, vol. 158, pp. 1064-1075, 2011.

[276] C. R. Wilke, "A viscosity equation for gas mixtures," *The Journal of Chemical Physics*, vol. 18, pp. 517-519, 1950.

Appendix A: LabVIEW Block Diagram

A.1. Introduction

This chapter presents the LABVIEW block diagram used for calculating the parameters of the fuel mixtures. The block diagram (i.e. the programming space) of the LabVIEW VI is shown in Fig. A1. The front panel has been shown in Chapter 3 and the block diagram is explained here for the purposes of completion.

The block diagram begins at the top left hand corner of Fig. A1 and flows toward the right and downwards. Each 'wire', shown by an orange or blue line, connects one command to the next. In the block diagram, the initial input is the individual fuel flow rate of each gas (shown to the far left of the diagram). These are connected to a flow rate output signal on the front panel (see Chapter 3, Fig. 3.4). The grey border is a 'While loop' which is necessary so that the commands will be executed until the 'stop' button is pressed on the front panel. While the VI is running, only commands on the front panel such as the 'stop' button or the execution controls can be changed. As the block diagram is very complicated to look at, smaller diagrams, which are shown in Figs. A2 to A10, have been constructed from it in order to illustrate the use of the equations for the calculations, which are given in Eqs. A1 to A7. The equations and their relevance to the combustion properties of the various fuels have been given in Chapter 2 but have been repeated here for illustrative purposes. The block diagram for the nozzle exit velocity has been described in Chapter 3.

Since the methane and propane were not used at the same time, and in fact one flow controller was used for both gases and recalibrated, the VI was used for either methane or propane. The calculations shown here are for propane but when methane was used the values in the block diagram were changed to correspond to methane instead of propane.

Appendix A: LabVIEW Block Diagram

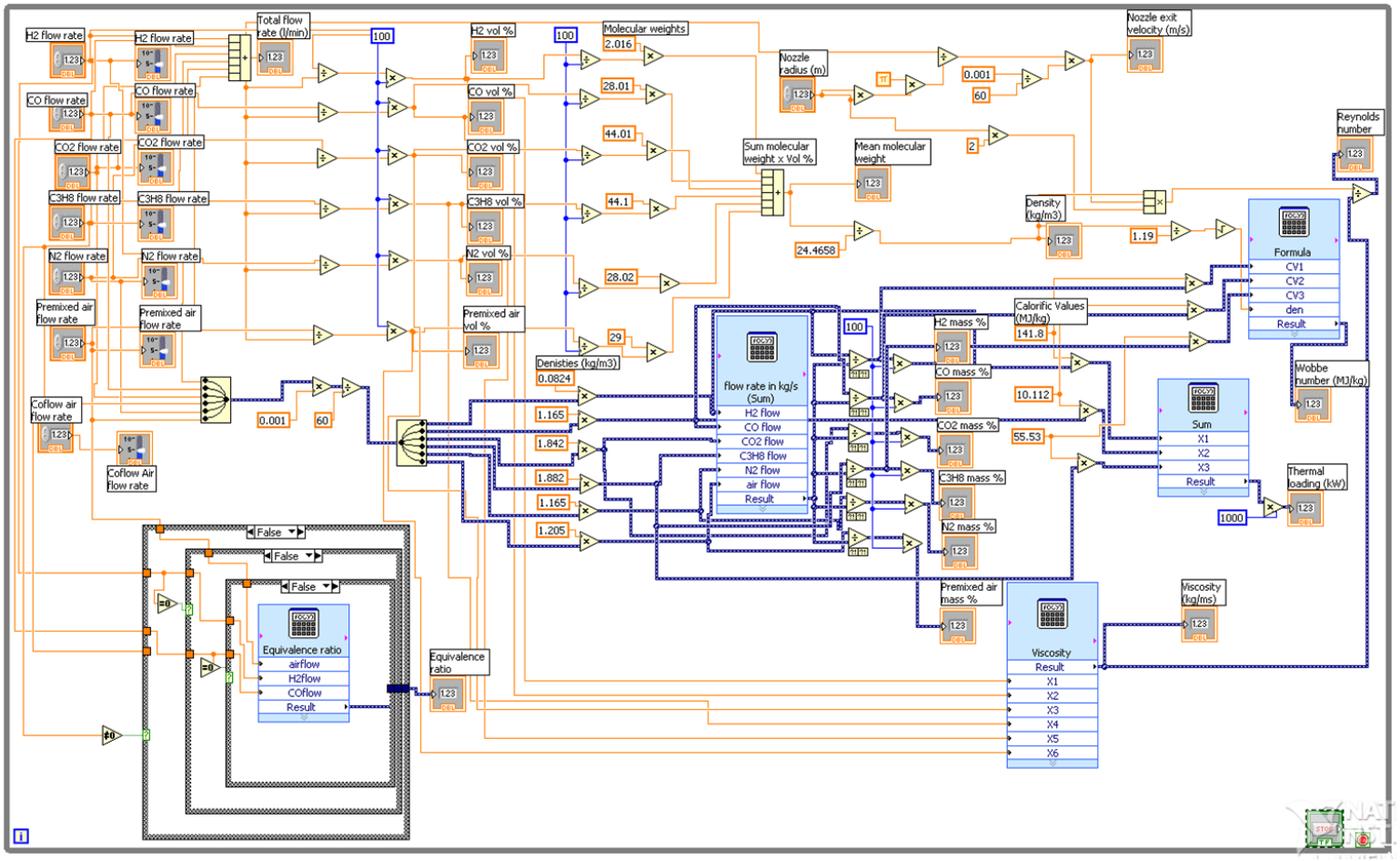

Figure A1: Block diagram of the LabVIEW VI.

A.2. Density Calculations

The density of the mixture was calculated from:

$$\rho = p\sum_i {x_i M_i}/{RT}\,, \tag{A1}$$

where p is atmospheric pressure, equal to 1 atm, x_i is the volume fraction of component i. M_i is the molecular weight of component i, R is the universal gas constant, equal to 0.082057 litre atm K^{-1} mol^{-1}, and T is the temperature, equal to 298 K. Equation A1 gives the density in units of g $litre^{-1}$, which are equal to kg m^{-3}.

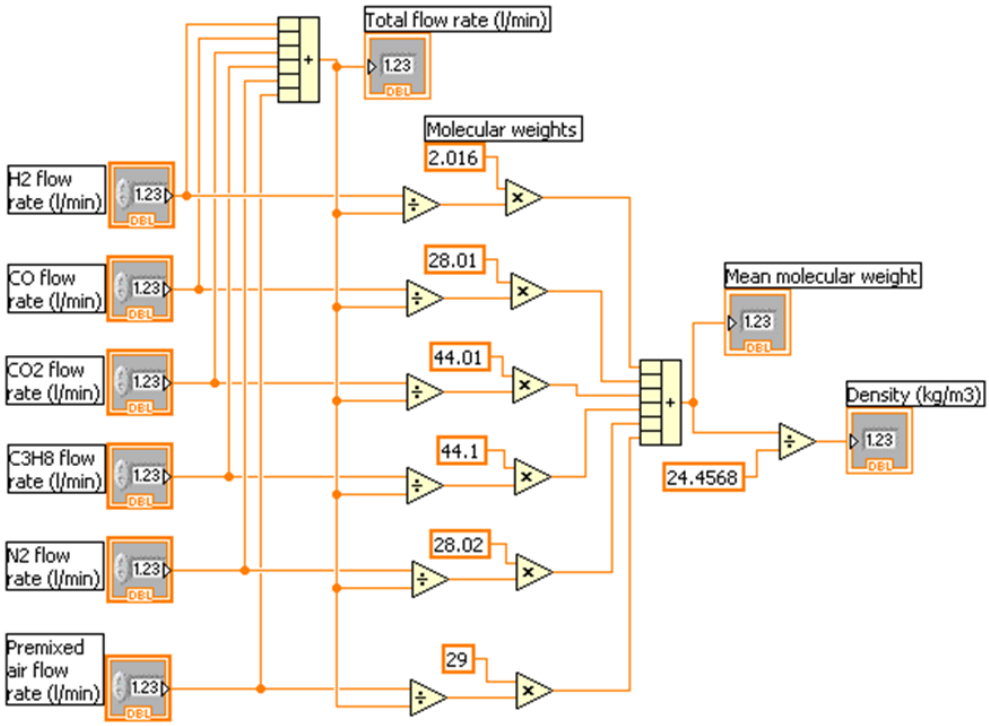

Figure A2: Density calculations using LabVIEW.

Figure A2 shows the density calculations using LabVIEW. The individual flow rates at the left (which are controlled by the user) are connected to a summation command which calculates the 'total flow rate' output on the top of the diagram. Each flow rate is then divided by this total to give the flow rate as a fraction of the total flow rate. In the larger block diagram these values are then multiplied by 100 (first vertical blue line connected to a 100 input on the block diagram in Fig. A1) to give the individual volume flow rate percentages, which are shown on the front panel (Fig. 3.4). This division is missed out in Fig. A2 as it is only needed to calculate the volume percentages, which

are then re-divided by 100 before continuing (Fig. A1). Moving further to the right in Fig. A2, the individual volume fractions are then multiplied by the molecular weights of the respective components (shown by the orange boxes) and summed to give the mean molecular weight, which is then divided by (R x T) = 24.4658 to give the density of the mixture as specified by Eq. A1. When methane was used, the value 44.1 was substituted for the molecular weight of methane (equal to 16.04). The density values were used along with the viscosity values to calculate the Reynolds numbers quoted in the results of this thesis.

A.3. Viscosity Calculations

The viscosities of the gas mixtures were calculated using Eqs. A2 and A3:

$$\mu_{\text{mix}} = \sum_{i=1}^{N} \frac{\mu_i}{1 + \frac{1}{x_j} \sum_{\substack{j=1 \\ j \neq i}}^{N} x_j \varphi_{ij}}, \tag{A2}$$

where

$$\varphi_{ij} = \frac{\left[1 + \left(\mu_i / \mu_j\right)^{1/2} \left(M_j / M_i\right)^{1/4}\right]^2}{\left(4/\sqrt{2}\right)\left[1 + \left(M_i / M_j\right)\right]^{1/2}}, \tag{A3}$$

and where μ_{mix} is the viscosity of the mixture, μ_i is the viscosity of component i, x_i is the volume fraction of component i, M_i is the molecular weight of component i, the values of which are shown in Fig. A2, and N is the total number of components. Wilke [276] found the equations (Eqs. A2 and A3) to be within 1.9 % of the experimental values for thirteen tested mixtures which was stated to be of sufficient accuracy for general multi-component systems.

Figure A3 shows the VI used to calculate the viscosity. X1 to X6 were the inputs for the volume fraction in the blue equation box labelled viscosity. The equation boxes allow complex equations to be calculated based on the input signals without having to have the separate wires in the block diagram. The equation is shown at the bottom of Fig. A3. It uses Eq. A2 with calculated values of φ_{ij} from Table A1. For methane, the fuel was

not mixed with any other fuel or with air in this thesis, and so the viscosity was taken as 1.03×10^{-5}, without using the equation in the blue box in Fig. A3.

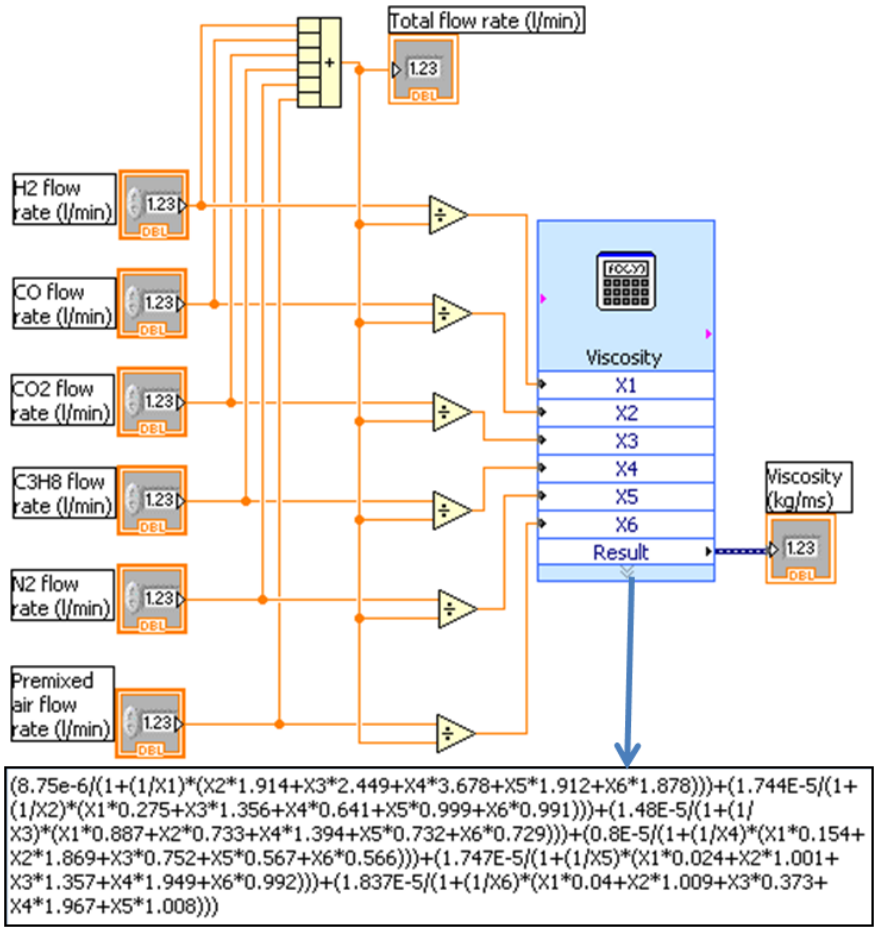

Figure A3: Viscosity calculation in LabVIEW with equation shown below.

Gas *i*	Gas *j*	*ij*	φ_{ij}	φ_{ji}
H_2	CO	12	1.914	0.275
H_2	CO_2	13	2.449	0.887
H_2	C_3H_8	14	3.678	0.154
H_2	N_2	15	1.912	0.024
H_2	Air	16	1.878	0.04
CO	CO_2	23	1.356	0.733
CO	C_3H_8	24	0.641	1.869
CO	N_2	25	0.999	1.001
CO	Air	26	0.991	1.009
CO_2	C_3H_8	34	1.394	0.752
CO_2	N_2	35	0.732	1.357
CO_2	Air	36	0.729	1.373
C_3H_8	N_2	45	0.567	1.949
C_3H_8	Air	46	0.566	1.967
N_2	Air	56	0.992	1.008

Table A1: Viscosity parameters φ_{ij} for each combination of gas for use in the viscosity equation.

A.4. Reynolds Number Calculations

The Reynolds number was calculated from:

$$\mathrm{Re} = \frac{\rho v d}{\mu}, \tag{A4}$$

where ρ is the density of the mixture (calculated from Eq. A1), v is the nozzle exit velocity (calculated from Eq. 3.1 see Chapter 3), d is the nozzle diameter and μ is the viscosity of the mixture (calculated from Eqs. A2 and A3). Fig. A4 shows how the Reynolds number was calculated using LabVIEW, but with the inputs used from Figs. A2, A3 and 3.5.

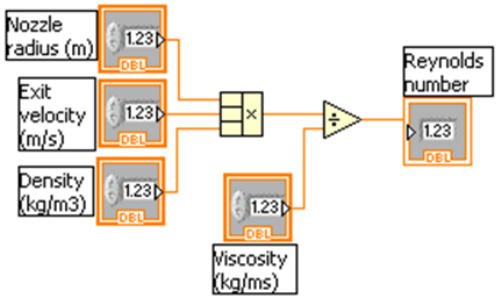

Figure A4: Reynolds number calculations using LabVIEW.

A.5. Thermal Loading Calculations

In order to calculate the thermal loading (Eq. A5) the mass flow rates needed to be known.

$$\text{Thermal loading} = \sum_i \left(CV_i \times \text{mass flow rate}_i \right), \qquad \text{(A5)}$$

where *CV* is the calorific value of the fuel, whose values are shown in Fig. A5, and *i* is the fuel type.

Figure A5 shows the calculation of the thermal loading. First the mass flow rates of the fuel components were calculated using the volume flow rates (which were changed into $m^3 s^{-1}$ using the conversion factor 0.001/60) multiplied by the individual densities. The box with the three orange flow rate inputs and one blue output merges the signals so that the same calculation (converting to $m^3 s^{-1}$ in this case) can be performed simultaneously on each value. Then the signals are split again, with the output wires in the same order as the previous input wires. This changes the orange wire to a blue wire.

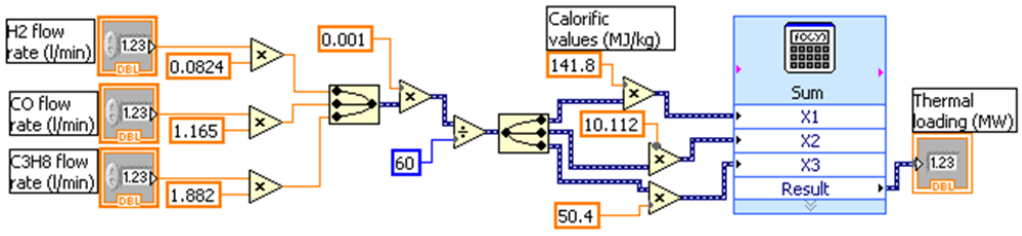

Figure A5: Thermal loading calculations using LabVIEW.

The thermal loading was then calculated by summing the fuel component mass flow rates multiplied by the individual calorific values of the fuel components as shown in Eq. A5. When methane was used, the CV was set to 55.53 instead of 50.4. The simple

addition tool used in Figs. A2 and A3 cannot be used on the blue multi value wires and so a formula box must be used. The formula box is a simple summation of the three input values.

A.6. Wobbe Number Calculations

The Wobbe number of the fuel can be calculated from Eq. A6:

$$\text{Wobbe No.} = \frac{\text{Gross } CV}{\sqrt{\rho / \rho_a}}, \tag{A6}$$

where Gross *CV* is the gross calorific value of the fuel, shown in Fig. A6, ρ is the density, calculated from Eq. A1, and ρ_a is the density of air, taken as 1.19 kg m^{-3}.

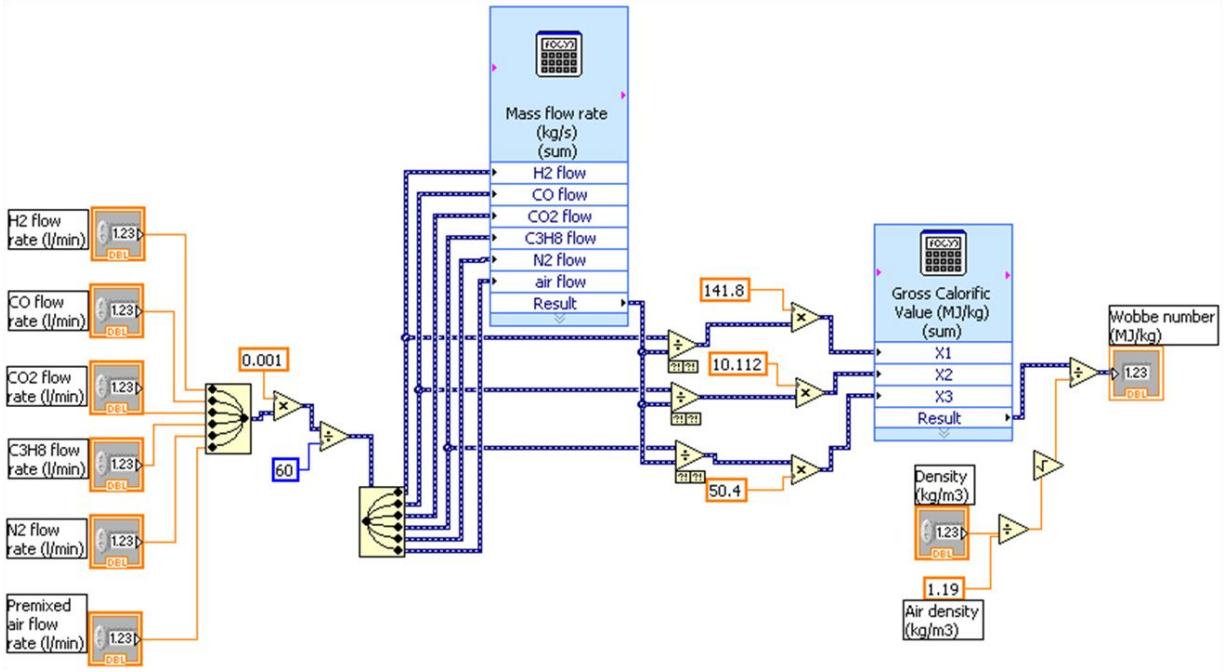

Figure A6: Wobbe number calculations using LabVIEW.

Similar to the thermal loading calculations, the mass flow rates of the fuel components were calculated using the volume flow rates (which were changed into $m^3 s^{-1}$ using the conversion factor 0.001/60) multiplied by the individual densities. The individual values were then divided by the total mass flow rate, which is the result from the formula box in Fig. A6, to give the mass fractions. The mass fractions for the fuel components were then multiplied by the individual calorific values and summed. Again a CV of 55.53 was used when methane was used as a fuel instead of propane. This value was then

divided by the specific gravity, which is the square root of the fuel density/air density (Fig. A6).

A.7. Equivalence Ratio Calculations

The equivalence ratio (Eq. A7) had to be calculated using a case structure. This is because the equation is different depending on the fuel mixture. For a single fuel it is calculated using Eq. A7 (see Chapter 2, Eqs. 2.1 to 2.3):

$$\phi = \frac{m_f / m_a}{M_f / 29.0(\alpha + \beta/4 - \gamma/2)(4.76)}, \tag{A7}$$

where ϕ is the equivalence ratio, m_f and m_a represent the mass of the actual fuel and air respectively, M_f is the molecular weight of the fuel, the values of which are shown in Fig. A2, and the bottom line on the right hand side of the equation is calculated from the stoichiometric atom balance, shown in Chapter 2. The values of m_f and m_a were calculated using the mass flow rate of fuel or air respectively multiplied by the respective densities. The conversion factor of 0.001/60 was omitted since it appears in both m_f and m_a.

Equation A7 was used to calculate the equivalence ratio when only a single gas was used. Since the values of M_f (shown in Fig. A2) and (α + β/4 – γ/2) (equal to 0.5, 0.5, 5, and 2 for H_2, CO, C_3H_8 and CH_4 respectively) were different for the different gases, a case structure was used in the VI. A case structure is such that if the input (shown by the green box with the '?' symbol) is 'true' then the calculations shown inside the true structure are performed. If 'false', then the corresponding calculations shown in the 'false' box are performed. Each composition in this work is either a single fuel; C_3H_8, H_2 or CO, or a mixture of H_2 and CO fuel parts. For the H_2 and CO mixture, the value of (α + β/4 – γ/2) is still 0.5 since 0.5 moles of oxygen are need to react 1 mole of hydrogen, and again for the CO. Therefore, 0.5 + 0.5 = 1 mole of oxygen is needed to react 2 moles of fuel (hydrogen plus CO). If carbon dioxide or nitrogen were used then they were assumed to be non-reacting and so did not carry any weight in the equivalence ratio calculations. Methane was only used as a diffusion flame and so equivalence ratio calculations were not necessary. Therefore, four cases were defined:

Case 1 is pure C_3H_8, case 2 is pure CO, case 3 is pure H_2 and case 4 is a mixture of H_2 and CO.

For case 1, the input to the case structure was 'true' if the flow of C_3H_8 did not equal zero (Fig. A7). Since C_3H_8 was not mixed with any other gases, this means that Eq. A7 should be calculated for pure C_3H_8, as is shown in the equation in Fig. A7. If the input was false (Fig. A8), then the calculation will be made for compositions of H_2 and CO. Therefore another case structure was placed inside the 'false' structure and the 'true' input was set to the condition that the H_2 flow rate was zero. This means that case 2 (Fig. A8) was for gases with only CO as the fuel content and so Eq. A7 was calculated for pure CO, as shown in Fig. A8. The third case is pure H_2, and is shown in Fig. A9. This case uses the false input for the second case structure and a true input for a third structure whose input command is that the flow of CO is zero.

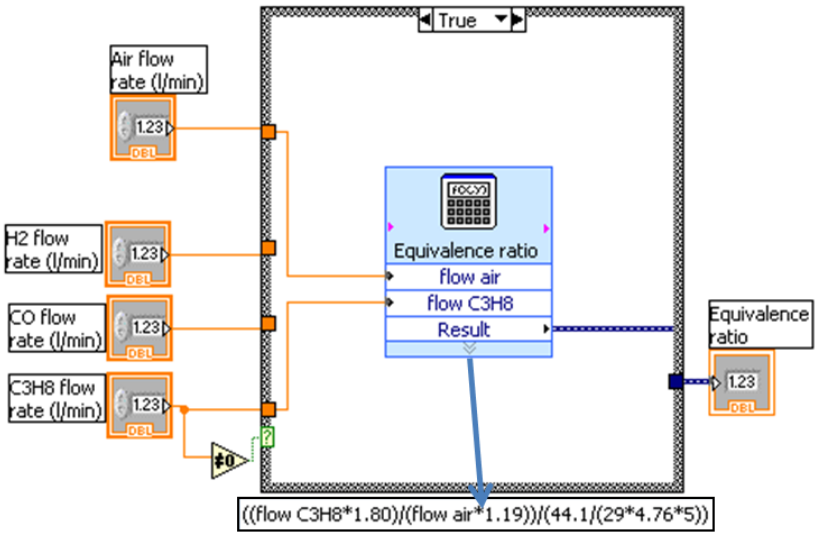

Figure A7: Equivalence ratio calculations for C3H8 using LabVIEW.

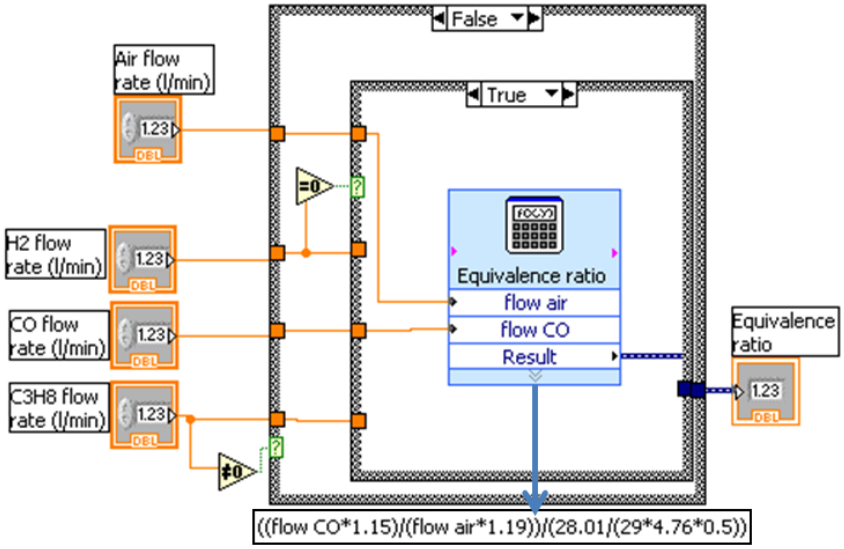

Figure A8: Equivalence ratio calculations for CO using LabVIEW.

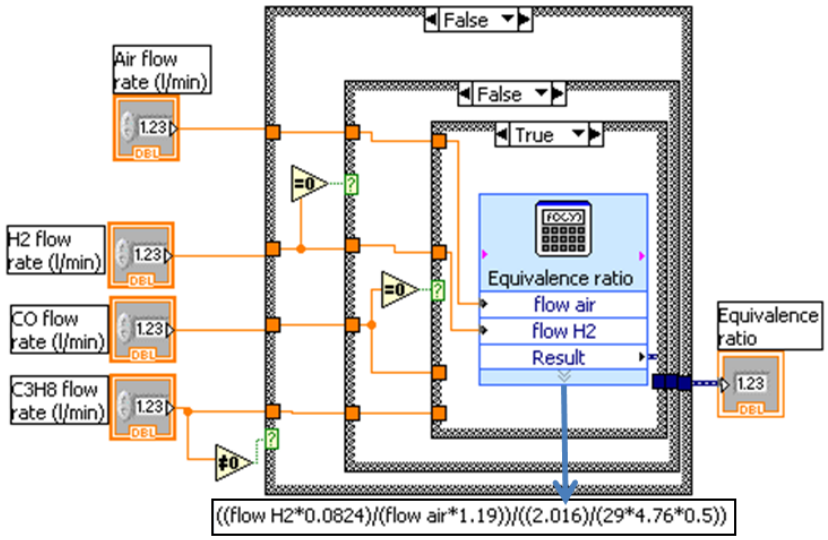

Figure A9: Equivalence ratio calculations for H_2 using LabVIEW.

The final case is for a mixture of H_2 and CO, which uses the final 'false' box (Fig. A10), meaning that the inputs for all three case structures are false, so neither the flow rates of H_2 or CO are zero but the flow rate of C_3H_8 is zero. When this is true the equation box for the equivalence ratio in Fig. A10 is used, such that in Eq. A7, m_f was calculated using the sum of the mass flow rates of H_2 and CO and M_f was calculated using the sum of the molecular weights of H_2 and CO equal to (2.016 + 28.01).

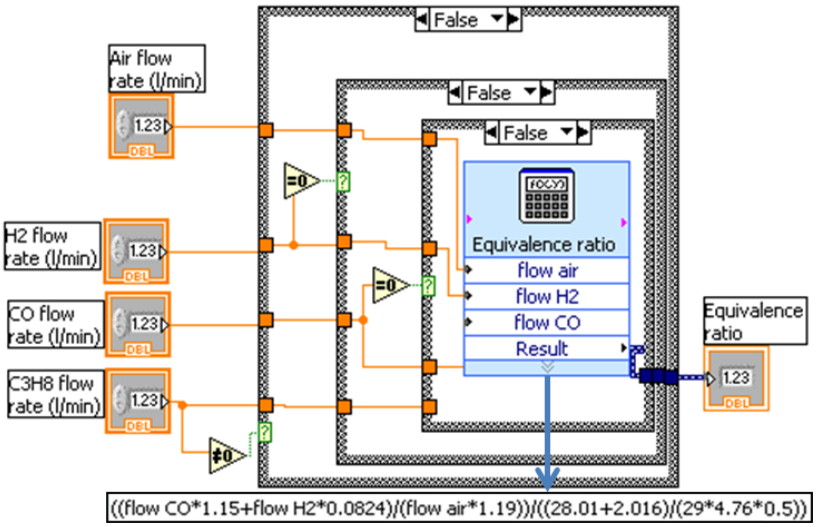

Figure A10: Equivalence ratio calculations for H_2 plus CO mixtures using LabVIEW.

A.8. Conclusions

This Chapter has shown how LabVIEW was used to calculate the fuel properties for the mixture compositions. The LabVIEW system was used so that mixtures with a given thermal loading, equivalence ratio or Reynolds number could be used. A trial and error method was used to determine the flow rates of the fuels that would give mixtures with the certain properties. Otherwise, the flow rates were inputted into the VI to calculate the fuel properties corresponding to the given flow rates. LabVIEW has been very useful in the aim of comparing fuels by given parameters.